



# Kent Academic Repository

**Fowler, Ronald Francis (1985) *Computer simulation of microscopic liquid drops.* Doctor of Philosophy (PhD) thesis, University of Kent.**

## Downloaded from

<https://kar.kent.ac.uk/94355/> The University of Kent's Academic Repository KAR

## The version of record is available from

<https://doi.org/10.22024/UniKent/01.02.94355>

## This document version

UNSPECIFIED

## DOI for this version

## Licence for this version

CC BY-NC-ND (Attribution-NonCommercial-NoDerivatives)

## Additional information

This thesis has been digitised by EThOS, the British Library digitisation service, for purposes of preservation and dissemination. It was uploaded to KAR on 25 April 2022 in order to hold its content and record within University of Kent systems. It is available Open Access using a Creative Commons Attribution, Non-commercial, No Derivatives (<https://creativecommons.org/licenses/by-nc-nd/4.0/>) licence so that the thesis and its author, can benefit from opportunities for increased readership and citation. This was done in line with University of Kent policies (<https://www.kent.ac.uk/is/strategy/docs/Kent%20Open%20Access%20policy.pdf>). If you ...

## Versions of research works

### Versions of Record

If this version is the version of record, it is the same as the published version available on the publisher's web site. Cite as the published version.

### Author Accepted Manuscripts

If this document is identified as the Author Accepted Manuscript it is the version after peer review but before type setting, copy editing or publisher branding. Cite as Surname, Initial. (Year) 'Title of article'. To be published in **Title of Journal**, Volume and issue numbers [peer-reviewed accepted version]. Available at: DOI or URL (Accessed: date).

### Enquiries

If you have questions about this document contact [ResearchSupport@kent.ac.uk](mailto:ResearchSupport@kent.ac.uk). Please include the URL of the record in KAR. If you believe that your, or a third party's rights have been compromised through this document please see our [Take Down policy](https://www.kent.ac.uk/guides/kar-the-kent-academic-repository#policies) (available from <https://www.kent.ac.uk/guides/kar-the-kent-academic-repository#policies>).

**Computer Simulation of Microscopic  
Liquid Drops**

by

Ronald Francis Fowler

Thesis submitted for the degree of  
Doctor of Philosophy  
at the  
University of Kent at Canterbury  
1985

The Physics Laboratory  
The University  
Canterbury  
Kent

For Mum and Dad

## Acknowledgements

I would like to express my sincere thanks to my supervisor, Professor J.G.Powles, whose constant help and guidance has been invaluable throughout the course of this work. I also thank my co-supervisor, Dr. W.A.B.Evans, who has provided a great deal of advice and encouragement as well as unravelling many mathematical problems.

I am greatly indebted to a number of friends and colleagues whom I have met during the course of this work. In particular I would like to thank two fellow computer "hackers", Andy Augousti and Mark Williams. Their generosity and friendship, not to mention numerous useful and stimulating discussions, is greatly appreciated.

I am grateful to Professors J.B.Brown and J.H.Strange for the facilities provided within the physics laboratory. Extensive use has been made of the excellent services provided by the university computing laboratory, and this is also acknowledged.

I thank the Science and Engineering Research Council for their support in the form of a research studentship.

## Table of Contents

Abstract .....	i
Chapter 1: Introduction - Computer simulation of liquids .....	1
1.1: Introduction .....	1
1.2: Computer simulations of the liquid state .....	2
1.2.1: Molecular dynamics .....	2
1.2.2: Monte carlo .....	4
1.2.3: Simulation of inhomogeneous systems .....	4
1.3: Organisation of the thesis .....	6
1.4: Reduced units .....	7
Chapter 2: Simulation methods for liquid drops .....	9
2.1: Introduction .....	9
2.2: Simulations of LJ12-6 systems .....	9
2.2.1: Boundary conditions to contain the system .....	9
2.2.2: Cut-off in the LJ12-6 potential .....	11
2.2.3: Integration method .....	13
2.2.4: The initial configuration .....	16
2.2.5: Programming details .....	17
2.2.6: Definition for the location of the cluster .....	18
2.3: Stockmayer systems .....	19
2.3.1: The Stockmayer potential .....	19
2.3.2: Integration method for the Stockmayer potential .....	21
2.3.3: Cut-off for the Stockmayer potential .....	24

2.3.4: Programming details .....	24
Chapter 3: Stability and structure of LJ and Stockmayer drops .....	28
3.1: Introduction .....	28
3.2: Equilibration .....	28
3.3: States studied and their properties .....	32
3.3.1: Range of state points .....	32
3.3.2: Properties of LJ drops .....	34
3.3.3: Properties of Stockmayer drops .....	49
3.4: Accuracy of results .....	59
3.5: Discussion .....	61
Chapter 4: Surface tension in microscopic drops .....	65
4.1: Introduction .....	65
4.2: The thermodynamic treatment of surface tension .....	65
4.2.1: The planar liquid gas interface .....	65
4.2.2: The spherical liquid gas interface .....	67
4.3: The mechanical definition of surface tension .....	72
4.3.1: The planar interface .....	72
4.3.2: The spherical interface .....	73
4.4: Calculation of $\gamma$ by computer simulation .....	73
4.4.1: Calculations for the plane surface .....	74
4.4.2: Calculating $\gamma$ in liquid drops .....	75
4.4.3: The accuracy of the Kelvin equation .....	80
4.4.4: Predictions of the Tolman equation .....	82
4.5: Liquid densities within small drops .....	83
4.6: Conclusions .....	83
Chapter 5: Surface width of microscopic drops .....	88

5.1: Introduction .....	88
5.2: Critical exponents and the surface width .....	88
5.3: Temperature dependence of the surface width .....	90
5.4: Theoretical calculations of the LJ surface width .....	93
5.5: The effects of capillary waves on surface width .....	95
5.6: Discussion .....	100
Chapter 6: Dielectric theory and computer simulation .....	102
6.1: Introduction .....	102
6.2: The Static dielectric constant .....	102
6.2.1: Polarization and the dielectric constant .....	102
6.2.2: Simple theories of the dielectric constant .....	104
6.2.3: The Kirkwood $g$ factor and the mean square moment .....	106
6.3: The frequency dependent dielectric constant .....	109
6.3.1: The debye equation .....	109
6.3.2: Relation of $\epsilon(\omega)$ to the CF $\langle \mathbf{M}(0) \cdot \mathbf{M}(t) \rangle$ .....	111
6.4: Computer simulation of dipolar fluids .....	112
Chapter 7: Results for the static dielectric constant .....	116
7.1: Introduction .....	116
7.2: Measuring the MSM within the drops .....	116
7.3: The generalized MSM for a macroscopic dielectric sphere .....	117
7.3.1: Derivation of the formula .....	117
7.3.2: Comparison with simulation data .....	121
7.3.3: Importance of surface width .....	121
7.4: The MSM for a continuous dielectric profile .....	125
7.4.1: MSM within the surface .....	125
7.4.2: The general form of the dielectric constant .....	127

7.4.3: Fitting $\epsilon_s(r)$ to the $\langle M^2(r) \rangle$ data .....	127
7.4.4: An alternative form for $\epsilon_s(r)$ .....	136
7.5: Comparison with previous dielectric measurements .....	137
7.6: The MSM at small $r$ .....	143
7.7: Conclusions .....	144
Chapter 8: The dynamic dielectric constant .....	146
8.1: Introduction .....	146
8.2: Calculation of the correlation functions .....	146
8.2.1: The total moment correlation function .....	146
8.2.2: The single particle correlation function .....	147
8.3: Results for the correlation functions .....	147
8.3.1: The radial dependence of $\Phi_r^s(t)$ .....	147
8.3.2: The radial dependence of $\Phi_r(t)$ .....	149
8.3.3: Trends in the correlation functions .....	149
8.4: Calculation of $\epsilon(\omega)$ .....	155
8.5: Discussion .....	158
Conclusion .....	162
Appendix A: Listing of the LJ simulation programme .....	165
Appendix B: Listing of the Stockmayer programme .....	173
Appendix C: Determination of the drop location .....	185
Appendix D: Method of calculating the MSM .....	190

## Abstract

Molecular dynamics computer simulations of small liquid drops are reported. Systems of between 60 and 1300 particles have been studied, each comprising of a central drop that is allowed to come to equilibrium with its surrounding vapour. Two common potential models have been used for the interactions between particles, the Lennard-Jones 12-6 form and the Stockmayer potential (LJ 12-6 plus a point dipole moment). Simulations for the Stockmayer fluid have been performed with  $\mu^2/\epsilon\sigma^3 = 1$  and  $\mu^2/\epsilon\sigma^3 = 3$ . For both potentials, relatively long cut-offs have been employed so that "tail" corrections are unnecessary.

Results are given for the size and density profiles of such drops over a range of temperatures. The Kelvin equation for the excess vapour pressure outside a curved interface is investigated as a means of determining the surface tension,  $\gamma$ , for a given fluid. Calculations using simulation results, in conjunction with the known coexistence vapour pressure, lead to a value of  $\gamma$  which is consistent with previous measurements of this quantity. This technique is seen to work best with large drops near the triple point, and though such simulations are currently quite expensive the increasing power of computers could make this a viable method for finding the surface tension.

The surface width of the liquid vapour interface in these systems is analysed as a function of temperature. Comparisons of the width with theoretical calculations for this quantity show that a significant discrepancy exists. This difference can be explained in terms of the contribution of surface oscillations (capillary waves) to the width.

The dielectric properties of Stockmayer drops have been studied via measurements of the mean square moment within spheres about the centre of mass of the system. It is found that values of the static dielectric constant,  $\epsilon_s$ , for the "bulk" liquid within the drops are consistent with previous results obtained by Adams and Adams for homogeneous systems, at least for  $\mu^2/\epsilon\sigma^3 = 1$ . For the more strongly polar fluid, with  $\mu^2/\epsilon\sigma^3 = 3$ , it may be that systems of more than 450 particles are necessary to determine the liquid value of  $\epsilon_s$ , but more work is required on this point.

In addition to determining  $\epsilon_s$  within the drops, it is shown that measured data for the mean square moment as a function of radius can be explained in terms of a (scalar) dielectric constant that depends on  $r$ . A dielectric profile of similar width and position to the density profile is obtained.

Measurements have also been made of the time dependent correlations of the total moment within spherical volumes about the centre of mass. In principle the dynamic dielectric constant can be obtained from these functions. However, it has not been possible to obtain consistent results for  $\epsilon(\omega)$  from the data reported here and some of the reasons for this are examined.

# Chapter One: Introduction - Computer simulation of liquids

## 1.1. Introduction

From a theoretical point of view the liquid state represents a very difficult topic to treat satisfactorily. Statistical mechanics can provide expressions for many important properties of a liquid in terms of the partition function,  $Z$ , which is related to the interaction potential,  $\Phi_N$ , of the  $N$  molecules comprising the sample. However, the direct evaluation of these expressions is impossible, due to the vast number of integrations that would have to be performed and the complexity of the interaction potential for real liquids.

Despite the problems, a great deal of progress has been made in the understanding of liquid behaviour through various approximate theories. Perhaps the best known, and most useful, are those based on integral equations, such as the Percus-Yevick (PY) and hypernetted chain (HNC) approximations. Even these methods can become virtually intractable when the actual many-body form of the interaction potential in real liquids is considered, and further approximations still have to be made.

An alternative (though often complementary) method to relate physical properties of a liquid to the molecular interaction potential is that of computer simulation. The advent of high speed digital computers has made it possible to take a given form for  $\Phi_N$  and calculate typical configurations for a (very small) sample of such a “theoretical” fluid. Properties of this liquid can be found from averages over these configurations.

This thesis is concerned with computer simulations that have been performed on small liquid drops in equilibrium with surrounding vapour. These systems allow us to study properties of the highly curved liquid vapour interface, and results on the stability and structure of the drops are reported, along with calculations of the surface

tension by an unusual route.

One of our prime considerations in choosing to study drops was, however, to yield an effectively isolated liquid sample (the coexistence vapour density being very low). This has some potential advantages for the calculation of the properties of dielectric fluids, which we investigate.

In this introductory chapter a very brief review is given of computer simulation methods, and some of the previous work that has been made on the liquid vapour interface and free clusters of molecules. This is followed by an outline of the organization of the whole thesis. The chapter is concluded by a section on the reduced units that have been employed throughout this work.

## 1.2. Computer simulations of the liquid state

### 1.2.1. Molecular dynamics

The molecular dynamics (MD) method that we have used here dates back to the work of Alder and Wainwright<sup>1</sup> in 1957, and is described in a number of books and review articles<sup>2,3</sup>. Basically, the positions, and other relevant coordinates, of a small number of molecules are set up in some chosen initial configuration by the computer programme. Using the given form of the interaction potential,  $\Phi_N$ , the forces acting on each molecule can then be calculated and the equations of motion integrated to find the time evolution of the system. Properties of the liquid are then calculated as time averages over this system (effectively a micro-canonical ensemble).

The above outline of the method omits the various difficulties involved, not the least of which is the form to be used for the molecular interaction potential. It is nearly always assumed that this can be expressed as a sum over pair potentials,

$$\Phi_N = \sum_{i < j} \phi(\mathbf{r}_i - \mathbf{r}_j, \mathbf{\Omega}_i - \mathbf{\Omega}_j) \quad (1.1)$$

where the  $\mathbf{r}_i$  and the  $\mathbf{\Omega}_i$  are respectively the position and orientation of molecule  $i$ .

This ignores the effect of many-body contributions, such as the triple dipole (Axilrod-Teller) dispersion potential<sup>4</sup>, which have been shown to be non-negligible for real liquids. However, the high cost (in computer time) of including such terms has limited their use. Instead it is common to use an “effective” pair potential for  $\phi(\mathbf{r}, \mathbf{\Omega})$ . For example, the LJ12-6 potential,  $\phi(r) = 4\epsilon[(\sigma/r)^{12} - (\sigma/r)^6]$ , is used as a model for a liquid of simple spherical molecules, such as argon. The true potential between two argon atoms is, in fact, known to differ significantly from the LJ12-6 form<sup>5</sup>, but by choosing suitable values for the parameters  $\epsilon$  and  $\sigma$ , quite good agreement can be achieved between simulation and measured data for the real liquid. The reason for this is that the LJ potential used happens to approximate the effective interaction that is really the sum of the pair interactions plus the contributions of higher order terms. For argon the values usually taken for the potential are<sup>6</sup>  $\epsilon = 119.8\text{K}$  and  $\sigma = 0.3405\text{nm}$ , determined from data on the second virial coefficient (other methods give slightly different values, with  $\epsilon$  in the range<sup>7</sup> 116 - 119.8K).

The most time consuming part of MD simulations is usually the calculation of the forces from the potential, so it is advantageous to use as simple a form for  $\Phi_N$  as possible, from this point of view. Even using the LJ12-6 potential with the fastest computers presently available it is unreasonable to use more than a few thousand molecules, and systems sizes of 256 or 512 are more common. To compensate for the limited number of particles, periodic boundary conditions (PBCs) are normally applied in simulations, whereby the basic cell (e.g. a cube,  $L \times L \times L$ ) is replicated to fill all space, to give a uniform liquid sample. Of course any correlations beyond half the cell length,  $L$ , are meaningless, and the interactions between molecules have to be cut-off at or before  $L/2$ . This causes some unwanted side effects, especially when the interactions are of long range, as is the case for dipolar liquids (this is discussed further in chapters two and six).

The actual integration of the equations of motions also has to be treated with

some care, as there is a need to balance the requirements of accurately following the system's evolution against the amount of computer time used. A stepwise algorithm, like the Verlet method<sup>6</sup>, or the so-called "leapfrog" variation, is usually employed.

### 1.2.2. Monte carlo

Though we have only used MD in this work, another important technique frequently used in computer simulations of liquids is the Monte Carlo (MC) method. Instead of calculating the time evolution of a set of molecules, new configurations of the system are generated by making small random moves of individual particles. The key to this method is to accept or reject the new configurations in such a way that the likelihood of it occurring is proportional to the Boltzmann factor for that state. A criterion for this was first given by Metropolis *et al*<sup>8</sup>.

This technique has a number of advantages, which partly compensate for the fact that it cannot be used to study any time dependent properties of liquids. For example, normal MC gives a canonical ensemble system, so that the temperature, rather than the total energy, is a fixed quantity (though methods for constant temperature MD simulations have recently been developed<sup>9</sup>). Additionally, other ensembles can be studied by MC, such as the Grand canonical ensemble (GCMC) where the actual number of particles within the system is also allowed to vary. This form has been used by Yao *et al*<sup>10</sup> to examine the thermodynamic properties (including the chemical potential) of dipolar fluids, using the same potential (the Stockmayer potential) that is employed in some of our simulations. Such measurements are useful in the prediction of coexistence densities for the fluid.

### 1.2.3. Simulation of inhomogeneous systems

In addition to the work on properties of the "bulk" homogeneous liquid, there is growing interest in the behaviour of liquids near interfaces and surfaces. For example,

Chapela *et al*<sup>11</sup>, among others, have performed extensive simulations of two phase liquid-vapour systems with planar interfaces. They have employed up to 4096 particles, interacting via the LJ12-6 potential, using both MD and MC methods. This provides information on the structure of the interface and allows calculation of various important surface properties, such as the surface tension.

Small clusters of molecules have been studied by a number of workers, often to determine data concerning the nucleation of liquid drops from the vapour. McGinty<sup>12</sup> has investigated the stability of groups of up to 100 LJ particles, using the MD technique. Rao *et al*<sup>13</sup> have examined the formation of liquid drops from an “over-expanded” liquid and also from the super-saturated vapour. Systems were of 108 or 256 molecules, again with the LJ interaction.

Drops of liquid in equilibrium with their own vapour have been simulated by Rusanov and Brodskaya<sup>14</sup>, though again only for very limited systems of up to 256 particles. Their results cover a number of aspects of the behaviour of such microscopic drops, but their runs were quite short and this leads to large uncertainties in the conclusions. This paper only came to our attention after much of our work on the LJ potential had been completed, and does examine a similar technique to that used in chapter four (for the surface tension). However, our work uses larger samples, with better statistics, to provide more comprehensive data.

It is worth noting here that a great deal of theoretical work has been performed on liquid interfaces. Many calculations exist for the structure and surface tension of planar interfaces, but of particular relevance to the data presented in this work are the results of Falls *et al*<sup>15</sup>. They have used a gradient-theory approach to predict the structure and stress within small drops in equilibrium with surrounding vapour. An interaction potential similar to the LJ12-6 form was used.

### 1.3. Organisation of this thesis

In this work we report a range of results for the simulation of drops in equilibrium with their own vapour. The first studies that were made used the simple LJ form for the interaction potential. This has the advantages of being relatively straightforward to deal with and fairly fast to compute. There is also a large amount of data in existence for this particular model, with which comparisons can be made. In fact an empirical equation of state has been derived for this fluid from simulation data, by McDonald and Singer<sup>7</sup>. A more comprehensive equation has since been given by Nicolas *et al*<sup>16</sup>.

Our later drop studies were extended to use the Stockmayer potential, as a simple model of a dipolar fluid. As well as examining the thermodynamics of these systems we attempt to calculate dielectric properties of both the bulk liquid within the drop and of the surface region.

In chapter two the technical details of the MD simulations employed in this work are discussed. The chosen boundary conditions are explained and the effects of truncation of the interaction potential considered in inhomogeneous systems.

The states that have been studied are summarised in chapter three. Results for the temperature, size and stability of the drops are given and some conclusions drawn.

Chapter four examines the calculation of the surface tension from the data of the preceding chapter. The Kelvin equation for the excess vapour pressure outside a drop is used as an alternative to the more complex and time consuming process of evaluating the pressure tensor.

The surface width of liquid drops, and also planar interfaces, is known to rise rapidly with the temperature. Chapter five is devoted to this topic, and the effect that surface oscillations (capillary waves) have on the observed width in drops.

The final three chapters of the thesis are concerned with the dielectric properties of the Stockmayer drops. Chapter six is simply a review of some relevant background

theory of dielectrics. Results for the static dielectric constant within the bulk liquid are presented in chapter seven, and an effective dielectric profile for the interface region calculated.

Some efforts have been made to find the dynamic dielectric constant from measurements on these Stockmayer drops, but with unsatisfactory results. The methods used and the problems that were encountered are discussed in chapter eight.

#### 1.4. Units used in this thesis

We conclude this introductory chapter with a note on the reduced units which are used throughout this thesis. In common with many simulators we use dimensionless units and these are defined by  $r^* = r/\sigma$  and  $\phi^* = \phi/\epsilon$  for the lengths and energies, respectively.  $\sigma$  and  $\epsilon$  are the parameters in the LJ potential, which becomes  $\phi^* = 4(r^{*-12} - r^{*-6})$ . Similar reductions are made for other units, but some ambiguity arises in the choice of the units of mass and time. We follow Verlet in taking the unit of time to be  $\left(\frac{m\sigma^2}{48\epsilon}\right)^{1/2}$ , and hence the reduced mass of each molecule is 48. A number of other workers use a time unit without the factor of 48, so that conversions have to be made in comparisons with their results.

While it is usual to distinguish these reduced units with the superscript “\*”, this is not done in the remainder of this work since all our results are expressed in this form.

In the treatment of the dielectric properties of polar fluids we make use of Gaussian units, in that the constant  $\epsilon_0 = 1/4\pi$ . This results in slightly simpler equations.

#### References

1. B.J.Alder and T.E.Wainwright, *J. Chem. Phys.*, vol. 27, p. 1208, 1957.

2. W.W.Wood, *Physics of simple liquids*, North-Holland, Amsterdam, 1968. H.N.V.Temperley, J.S.Rowlinson, G.S.Rushbrooke eds.
3. F.H.Ree, *Physical chemistry, an advanced treatise*, Academic press, New York, 1971. H.Eyring, D.Henderson, W.Jost eds.
4. B.M.Axilrod and E.Teller, *J. Chem. Phys.*, vol. 11, p. 299, 1943.
5. J.A.Barker, *Rare gas solids*, Academic press, London, 1976. M.L.Klein and J.A.Venables, eds.
6. L.Verlet, *Phys. Rev.*, vol. 159, p. 98, 1967.
7. I.R.McDonald and K.Singer, *Molec. Phys.*, vol. 23, p. 29, 1972.
8. M.Metropolis, A.W.Rosenbluth, M.N.Rosenbluth, A.N.Teller, and E.Teller, *J. Chem. Phys.*, vol. 21, p. 1087, 1957.
9. D.J.Evans and G.P.Morriss, *Chem. Phys.*, vol. 77, p. 63, 1983.
10. J.Yao, R.A.Greenkorn, and K.C.Chao, *J. Chem. Phys.*, vol. 76, p. 4657, 1982.
11. G.A.Chapela, G.Saville, S.M.Thompson, J.S.Rowlinson, *J. Chem. Soc. Faraday Trans. 2*, vol. 73, p. 1133, 1977.
12. D.J.McGinty, *J. Chem. Phys.*, vol. 58, p. 4733, 1972.
13. M.Rao, B.J.Berne, and M.H.Kalos, *J. Chem. Phys.*, vol. 68, p. 1325, 1978.
14. A.I.Rusanov and E.N.Brodskaya, *J. Colloid Interface Sci.*, vol. 62, p. 542, 1977.
15. A.H.Falls, L.E.Scriven, and H.T.Davis, *J. Chem. Phys.*, vol. 75, p. 3986, 1981.
16. J.J.Nicolas, K.E.Gubbins, W.B.Streett, D.J.Tildesley, *Molec. Phys.*, vol. 37, p. 1429, 1979.

## Chapter Two: Simulation methods for liquid drops

### 2.1. Introduction

The technique of molecular dynamics has been in use for many years now and the basic principles of the method are reviewed in a number of articles<sup>1,2</sup>. In this chapter we shall discuss the particular MD methods that have been employed in our work, but with more emphasis on any differences between these methods and the “standard” homogeneous simulations.

Our initial work on drops was performed with the simple Lennard-Jones (LJ) 12-6 potential, and the techniques used for these systems are described first, and an outline given of the computer programmes that were employed.

The modifications necessary to study non-spherically symmetric molecules are then considered, using the quaternion representation of orientation. This algorithm is used with the Stockmayer potential as a simple model for linear polar molecules, and the technical details of these simulations are given.

### 2.2. Simulations of LJ12-6 systems

#### 2.2.1. Boundary conditions to contain the system

In the simulation of homogeneous liquids the use of periodic boundary conditions is accepted as being the best way of containing the system, and avoiding surface effects. For inhomogeneous systems, such as liquid-vapour interfaces, the situation is not so clear, and there are various ways in which boundary conditions can be applied.

Studies of the planar liquid-vapour interface usually employ a rectangular cell that is periodic in at least the  $x$  and  $y$  directions, the plane in which the surface lies. If the system is also made periodic in the  $z$  direction, then two interfaces are obtained, on either side of a thin liquid film. Alternatively, hard or soft wall potentials may be used at the  $z$  boundaries, to give just one interface, as was done by Chapela *et al*<sup>3</sup>.

With spherical liquid-vapour interfaces, different boundary conditions again are required. At very low temperatures it would be possible to simulate a totally free system; the lack of any boundary constraints allowing particles to escape from the cluster, and not return. However this would be a rare occurrence if the system were cool enough, and so the clusters could be stable over long periods. Obviously, this method is not suitable for our study, where we are interested in the higher temperatures of the liquid state, as the drops would then evaporate too rapidly.

Let us consider three other possibilities to contain a liquid drop:

- (i) Place the system in the usual type of cubic periodic boundary conditions, but simply make the cell size much larger than the diameter of the cluster so that it is possible to form a vapour region that separates the cluster from its periodic images.
- (ii) Surround the system with a spherical wall of some nature, with the volume of this container being much greater than that of the cluster. Thus particles may freely evaporate from the cluster to form a vapour region between it and the wall.
- (iii) Use a constraining potential (or wall) that tightly confines the system within a spherical region. The volume of the container would be the same as that of the cluster, so that no significant vapour phase can exist.

Initially we employed boundary conditions of type (ii), with a simple spherical hard wall with a radius of about two or three times that of the cluster. However, it was found that clusters would drift away from the center of the system at such a rate that very long simulations of small systems could run into the problem of the drop reaching the wall<sup>†</sup>. To avoid this, the radius of the wall could be increased, but this increases the amount of vapour that has to be simulated, and also the time for the system to reach equilibrium.

---

<sup>†</sup> To minimize the drift, the linear momentum of each system was set to zero at the start of any simulation, as was the angular momentum. This was the case with the hard wall containment, as well as with the periodic boundary conditions. Thus any drift was due to Brownian motion, rather than the initial configuration.

A wall closely confining the system, as in (iii), was not investigated as it prevents any study of the liquid-gas interface, and may also introduce density oscillations near the surface of the cluster<sup>4,5</sup> (it would, however, have the advantage of reducing the equilibration needed for the system). Instead, almost all the cluster simulations reported in this work have been conducted in large periodic systems, as in (i). As long as the cluster does not split into two, there is no problem with drift since it can not get any closer to its periodic images. In such a system it is important that the cell size is large enough to prevent significant interaction between the cluster and its images, so the cell size must still be quite large.

Variations on the methods mentioned above have been used by some workers in this field. Thompson *et al*<sup>6</sup>, use a soft wall spherical container, as in (ii), though in some runs they move the wall so as to keep the cluster at the center. Hesse-Brot *et al*<sup>7</sup>, have recently published results for a Stockmayer system constrained by a soft wall, as in (iii).

### 2.2.2. Cut-off in the LJ12-6 potential

As was explained in chapter one, it is common to truncate the usual LJ12-6 potential,  $\phi_{LJ}(r)$ , at some separation  $r_c$ , partly because the periodic boundary conditions limit the meaningful range of forces, and partly to save computer time. To avoid a discontinuity in  $\phi(r)$  at  $r_c$ , a constant is added to give the so-called shifted potential (sp),

$$\begin{aligned} \phi(r) &= \phi_{LJ}(r) - \phi_{LJ}(r_c) & r \leq r_c \\ &= 0 & r > r_c \end{aligned} \quad (2.1)$$

The value of  $r_c$  is usually  $2.5$  or  $3.0\sigma$ , and these forms of the LJ potential will be referred to as *sp2.5* and *sp3* respectively.

This still leaves a discontinuity in the force,  $f(r) = d\phi/dr$  at  $r = r_c$ , and this may effect the accuracy of the dynamics<sup>8</sup>. A constant term may be added to the force for  $r < r_c$ , to eliminate this, and this is known as the shifted force potential. Typically

the cut-off is set to  $3.0\sigma$  in this case, and this potential will be denoted  $sf3$ .

Though these modified forms of the potential may be considered as defining new fluids in their own right, it is usual to correct the results back to the full LJ12-6, at least for homogeneous simulations. Even in simulations of non-homogeneous systems attempts have been made to correct for the truncation, as for example with the surface tension calculation of Chapela *et al*<sup>3</sup>. Correction terms in the case of homogeneous liquids are usually calculated on the assumption that the radial distribution function,  $g(r)$ , is unaffected by the truncation of the potential and that  $g(r) = 1$  beyond  $r_c$ . Thus the correction to internal energy for an  $sp\{r_c\}$  fluid is<sup>9</sup>,

$$\Delta U = \frac{1}{2}\rho\int_{r_c}^{\infty}\phi_{LJ}(r)4\pi r^2dr \quad (2.2)$$

A similar expression is obtained for the pressure correction. In the case of the  $sf3$  form of the potential a slightly more complex correction is required<sup>10</sup>.

However it is only possible to make such corrections to these simulation results because the average force on a given particle, due to the fluid beyond  $r_c$ , is zero and the most important source of *fluctuating* force comes from particles within  $r_c$ . In the case of a liquid-gas interface the contribution to the force on a molecule near the surface, due to particles at distances greater than  $r_c$ , is clearly non-zero. The magnitude of the long range part of the force may be estimated from a similar analysis used to find  $\Delta U$ , and at typical liquid densities  $\Delta f \sim 0.8$  for  $r_c = 2.5$ . Such a force will be directed into the liquid and must affect the resulting density profile obtained. Work on the equations of state for these modified potentials has shown that there are significant differences in the coexistence curves<sup>11</sup>.

Due to these considerations, we chose to use an unusually long cut-off, with  $r_c = 9$  or  $10\sigma$ . This is feasible since the periodic cell size is very large, but it will of course, increase the computer time required. In fact, due to numerical accuracy (most calculations are in single precision  $\sim 7$  decimal digits), the *effective* cut-off, at least in

the liquid, may be more like  $8\sigma$ . The importance of the long range corrections (such as eqn. (2.2)) vary as  $\sim 1/r_c^3$ , so that our corrections will be about thirty times smaller than those needed for the sp2.5 potential. Thus our results are effectively for the full LJ potential, without making any corrections.

### 2.2.3. Integration Method

Various algorithms have been used to integrate the  $N$  coupled equations of motion that arise in MD simulations,

$$\mathbf{r}_i^{(2)} = (1/m) \sum_{j \neq i} \mathbf{f}_{ij}(\mathbf{r}_{ij}) \quad (i=1, N) \quad (2.3)$$

where  $\mathbf{r}_i^{(2)}$  is the acceleration,  $m$  the mass, and  $\mathbf{f}_{ij}$  the force between particles  $i$  and  $j$ . They all depend on a stepwise integration, advancing the system by a time  $\Delta t$  over each cycle. The well known method of Verlet<sup>12</sup>, for example, calculates the next positions of the particles from their current positions and forces, along with previous positions,

$$\mathbf{r}_i(t + \Delta t) = -\mathbf{r}_i(t - \Delta t) + 2\mathbf{r}_i(t) + (\Delta t)^2 \sum_{i \neq j} \mathbf{f}_{ij}/m \quad (2.4)$$

which is correct to order  $(\Delta t)^3$ , so it is a third order method.

The particle velocities,  $\mathbf{r}_i^{(1)}$  are obtained from the equation,

$$\mathbf{r}_i^{(1)}(t) = \frac{\mathbf{r}_i(t + \Delta t) - \mathbf{r}_i(t - \Delta t)}{2\Delta t} \quad (2.5)$$

which is correct to order  $(\Delta t)^2$ .

Though this method is well established, we chose to use a more recent method employing a Gear<sup>13</sup> predictor-corrector algorithm. This numerical scheme has been used in a large number of simulations, though it has by no means replaced other methods, such as Verlet's, and the relative merits of each technique are still the subject of debate.

In the prediction step of the Gear method a Taylor series is used to estimate the new position and higher derivatives at the time  $(t + \Delta t)$ , from the values at time  $t$  only.

For the fifth order Gear algorithm that we use, this is simply,

$$\begin{aligned} \mathbf{r}_p^{(0)}(t+\Delta t) &= \mathbf{r}^{(0)}(t) + \Delta t \mathbf{r}^{(1)}(t) + \frac{\Delta t^2}{2!} \mathbf{r}^{(2)}(t) + \frac{\Delta t^3}{3!} \mathbf{r}^{(3)}(t) + \frac{\Delta t^4}{4!} \mathbf{r}^{(4)}(t) + \frac{\Delta t^5}{5!} \mathbf{r}^{(5)}(t) \\ \mathbf{r}_p^{(1)}(t+\Delta t) &= \mathbf{r}^{(1)}(t) + \Delta t \mathbf{r}^{(2)}(t) + \frac{\Delta t^2}{2!} \mathbf{r}^{(3)}(t) + \frac{\Delta t^3}{3!} \mathbf{r}^{(4)}(t) + \frac{\Delta t^4}{4!} \mathbf{r}^{(5)}(t) \\ &\dots \\ \mathbf{r}_p^{(5)}(t+\Delta t) &= \mathbf{r}^{(5)}(t) \end{aligned} \quad (2.6)$$

The subscript  $p$  is used here to indicate the predicted values and the label for the  $i^{\text{th}}$  particle has been dropped. For the correction step of the Gear method, the actual values of the second derivatives, which we denote as  $\mathbf{r}_a^{(2)}(t+\Delta t)$ , are evaluated from the predicted positions, using eqn. (2.3). From these results we obtain the vector  $\Delta \mathbf{A}$ , defined by,

$$\Delta \mathbf{A} = \frac{\Delta t^2}{2!} \left[ \mathbf{r}_a^{(2)}(t+\Delta t) - \mathbf{r}_p^{(2)}(t+\Delta t) \right] \quad (2.7)$$

If the prediction step had given the exact solution then this term would vanish. This will not usually be the case, and so the size of this term is a measure of the error incurred in the step. The Gear corrector is of the following form,

$$\mathbf{r}_c^{(n)}(t+\Delta t) = \mathbf{r}_p^{(n)}(t+\Delta t) + \alpha_n \Delta \mathbf{A} \frac{n!}{\Delta t^n} \quad (2.8)$$

where we have used the subscript  $c$  to denote the corrected value. The terms  $\alpha_n$  ( $n=0,5$ ) are the Gear coefficients which depend on the orders of the differential equation and the method being used. For a second order equation and a fifth order algorithm these are,

$$\alpha_i = \left\{ \frac{3}{20}, \frac{251}{360}, 1, \frac{11}{18}, \frac{1}{6}, \frac{1}{60} \right\} \quad (2.9)$$

The detailed determination of these values is given in Gear's book<sup>13</sup>, where it is shown that the requirements of a solution that will be both stable and accurate are fulfilled by these values. Note that the particular coefficients given above are for a general second order equation in which the first derivative may also appear explicitly. If, as is the case with the LJ potential,  $\mathbf{r}^{(1)}$  is not present then it is possible to achieve higher accuracy

by changing the value of  $\alpha_0$  from  $\frac{3}{20}$  to  $\frac{3}{16}$ <sup>14</sup>. While this could be done for the LJ simulations, the equations of angular re-orientation for Stockmayer molecules require the more general coefficients. Due to the numerical accuracy of the computations, the advantage of such an increase in the order of the method will be very slight.

The Gear method has a number of potential advantages over other integration schemes, such as that of Verlet. Firstly, it allows a higher order method to be used and hence a more accurate solution should be obtained, at least when a sufficiently small time step is used. The fact that we only require the derivatives at one point in time (a multivalued method) means that a simple scaling operation is all that is required to change the time step (a leapfrog algorithm usually requires interpolation when the step is altered). Furthermore, the method is 'self-starting', in that it is not necessary to calculate all the higher derivatives for the initial configuration; they may be set to zero and a small value of  $\Delta t$  used for the first few steps. The time step can then be increased when the higher derivatives have stabilized.

On the negative side, a fifth order Gear method requires significantly more computer memory than Verlet's scheme. This is not usually a problem with machines that have large virtual memories, such as the ones used for this work.

Possibly more worrying is the fact that Verlet's method is found to give smaller energy fluctuations than higher order methods<sup>15</sup>, at least for very long time steps e.g.  $\Delta t \sim 0.1$  (approximately  $3 \times 10^{-14}$  sec. for argon). A time step of about half this length was used in the LJ simulations.

It has been pointed out by Janzen and Leech<sup>16</sup> that certain methods, such as that of Verlet, have the property of conserving energy to very high accuracy, at least when the time step is less than a certain critical value. In particular these methods give energy conservation that is only limited by numerical round-off errors, when applied to simple oscillator problems. The fifth order Gear method is not of this type, so it might be expected that the energy conservation will be inferior to the Verlet method, for

large  $\Delta t$ . Even when smaller time steps are used it is common to ‘renormalise’ the velocities such that the total energy is kept constant. This is done every ten steps in our simulations. The factor by which the velocities have to be scaled is, of course, very close to unity, but this procedure prevents any net drift building up during the run. It may be shown in simple systems, such as the Morse oscillator problem used by Janzen and Leech, that rescaling to keep the total energy constant gives a more accurate solution, in addition to improving the energy conservation.

The conclusions of the two papers mentioned above suggest that fifth order methods may not offer much advantage over third order ones, such as that of Verlet, in MD simulations. However, many questions are still unanswered, such as just how accurate trajectories need to be to measure a given property. This topic is of fundamental significance to simulators, and undoubtably warrants much more research.

#### 2.2.4. The initial configuration

To generate an initial configuration for our system, we first performed a normal homogeneous simulation, with the molecules starting from a face-centred cubic lattice. Each particle was given a random velocity, chosen from a Boltzmann distribution. A very short run was then performed on the system, at a high temperature, to ensure that the structure was melted. A spherical region was then excised from the centre of this sample, containing the number of molecules required for the drop simulation. The density of the liquid was chosen to be close to the coexistence value for the desired temperature of the drop, so that the sample would not be under excessive pressure when placed on its own at the centre of the large periodic cell.

Both the linear and angular momentum of the newly formed cluster were set to zero by making small changes in the velocity of each particle (however, the angular momentum, at least within a given periodic cell, is not conserved with these boundary conditions).

### 2.2.5. Programming details

A complete listing of the programming used for simulating LJ drops is given in the appendices. The language used is Fortran-77. Most of the coding is fairly standard, and is based on an earlier version used by Dr. W.A.B. Evans for simulations of homogeneous liquid systems.

The Gear method is implemented by three subroutines, with reasonably self-explanatory names; PREDIC, to predict the values at the next step, FORCES, which calculates the actual forces and CORREC, which applies the correction. By far the most time consuming of these is the forces calculation, which has a loop over all pairs of particles, giving  $N_p(N_p - 1)/2$  separate terms. Due to the very long cut-off employed here and the inhomogeneous nature of the system, almost all of these pair interactions must be evaluated explicitly at each step. This is why truncated forms of the potential (e.g. sp2.5) can offer significant computational time savings in large systems, since neighbour lists<sup>12</sup> may be utilised to vastly decrease the number of interactions that have to be calculated.

The multiple time step technique of Street *et al*<sup>17</sup> could well have offered significant time savings in the particular LJ simulations performed in this work. However, this was not noted until most of the LJ simulations had been completed, at which point the necessary modifications and testing to use it would not have been economic. Furthermore, the multiple time step algorithm appears to be unsuitable for use with angular dependent potentials such as the Stockmayer one.

Due to the very limited disk and tape storage space, all measurements were performed during the course of the simulations, rather than saving velocity and trajectory data for later analysis. The various averages are calculated in the subroutine called DATA. The basic quantities calculated are the temperature of the system and the distribution of particles within the periodic cell. The first of these is obtained directly from the mean kinetic energy<sup>†</sup>.

---

† Note that due to the constraints on the linear and angular momentum in such a system, the

The most convenient way of measuring the density distribution is via the density profile,  $\rho(r)$ , about the center of the drop. The assumption we make in this work is that the drop is on average spherically symmetrical. The only checks that were made for this involved visual inspection of the clusters on a graphics terminal. This serves only as a very crude test, but it showed that no gross distortions were present. As long as there is a reasonable separation between the periodic images, there is no reason to expect a non-spherical average distribution of particles.

We measure  $\rho(r)$  by counting the number of particles within shells from radius  $r_i$  to  $r_{i+1}$ , about the center of the drop. For simplicity, the shells are taken to be of equal width, even though this gives a wide variation in the volume and expected number of particles for each one. The 'corners' of the periodic box, the region between the largest inscribed sphere and the boundaries, are treated as a whole and the mean density within it measured.

#### 2.2.6. Definition for the location of the cluster

It is important that the location of the center of the drop is known accurately during the course of a simulation, if quantities such as  $\rho(r)$  are to be measured. Even though the total linear momentum is set to zero at the start of each simulation, the drop may drift by several molecular diameters during the course of a run.

The center of mass of all particles is a fair guide to the location of the cluster center, but it is sensitive to the distribution of particles in the vapour. To avoid this, a definition is required to decide which particles are actually in the cluster and which are in the vapour. Then density profiles, etc., may be measured about the center of mass of the cluster only. The definition of the cluster we use may be stated as follows: Any two particles whose center-to-center separation is less than some value,  $R_n$ , are said to

---

mean temperature,  $T$ , is related to the mean kinetic energy,  $\langle KE \rangle$ , by the equation  $T = (2/3)[3N_p/(3N_p - 6)]\langle KE \rangle$ . This is only important for very small drops.

be neighbours. All particles that may be connected by an unbroken chain of such neighbours are said to be in the same cluster. A similar method was used by Stoddard<sup>18</sup>. While micro-clusters of two or three atoms may exist in the vapour there should be only one large cluster, which is the liquid drop.

Appendix C gives details of the particular computational method used to implement this definition in an economic manner during the course of the simulations. The best value of  $R_n$  is found to be about  $1.9\sigma$ . This value proved adequate over the range of temperatures studied in this work, but it is likely that a smaller value would be necessary if states much closer to the critical point are simulated. This is due to the increasing density of the vapour, which approaches that of the liquid.

## 2.3. Stockmayer systems

### 2.3.1. The Stockmayer potential

The Stockmayer potential is simply an LJ 12-6 potential with the addition of an (ideal) dipole, located at the centre. On physical grounds this is a less realistic model than the basic LJ one, which has proved a fair approximation for the heavier inert gases. Permanent dipole moments are only found in molecules composed of two or more non-identical atoms, and higher order moments (quadrupole, octapole etc.) are usually quite significant. Hence the use of just one LJ site, coincident with the dipole, is unrealistic. Additionally, the Stockmayer form ignores the polarizability of molecules. Nevertheless, this is a relatively simple potential that offers a good 'first approximation' to a real dielectric liquid, with long range dipolar interactions.

The reduced dipole moment is given by,

$$\mu^* = \mu/(\epsilon\sigma^3)^{1/2} \quad (2.10)$$

where reduction is w.r.t. the parameters used for the LJ part of the potential. As with other reduced quantities, we shall drop the superscript, and use  $\mu$  for the reduced moment.

The interaction energy of two dipoles,  $\mu_1$  and  $\mu_2$ , is,

$$\phi_{dd}(\mathbf{r}_1, \mu_1, \mathbf{r}_2, \mu_2) = \frac{\mu_1 \cdot \mu_2}{r_{12}^3} - 3 \frac{(\mu_1 \cdot \mathbf{r}_1)(\mu_2 \cdot \mathbf{r}_2)}{r_{12}^5} \quad (2.11)$$

using an obvious notation. The strength of the interaction varies as  $\mu^2$ , rather than as  $\mu$ , and the properties of the fluid will, of course, depend on the value chosen. Most of our Stockmayer simulations were performed with  $\mu^2 = 1$ , and we refer to this as the *S1* potential. Rowlinson<sup>19</sup> has calculated the effective Stockmayer parameters for a number of organic polar molecules, using data on the second virial coefficients. A value of  $\mu^2 = 1$  lies between that of chloromethane ( $\text{CH}_3\text{Cl}$ ,  $\mu^2 \sim 1.7$ ) and trichloromethane ( $\text{CHCl}_3$ ,  $\mu^2 \sim 0.3$ ), according to his data. These values must be treated with caution, since they derive from vapour phase results. For example, Rowlinson found  $\sigma = 0.336\text{nm}$  for  $\text{CH}_3\text{F}$ , where as the best value for liquid simulations of methane (a smaller molecule) is found to be<sup>20</sup>  $\sigma = 0.388\text{nm}$ . The reduced dipole moment is very sensitive to the reduction parameter  $\sigma$ .

A few simulations have been made with  $\mu^2 = 3$ , which represents a very strongly polar fluid, which we denote as the *S3* potential. Rowlinson's parameters give fluoromethane a reduced moment of  $\mu^2 \sim 3$ . The *S1* and *S3* potentials have been widely used by other workers.

The force between two dipoles can be expressed in vector notation as,

$$\mathbf{f}_{12} = 3 \left[ \mathbf{r} \frac{(\mu_1 \cdot \mu_2)}{r^5} - 5\mathbf{r} \frac{(\mu_1 \cdot \mathbf{r})(\mu_2 \cdot \mathbf{r})}{r^7} + \mu_1 \frac{(\mu_2 \cdot \mathbf{r})}{r^5} + \mu_2 \frac{(\mu_1 \cdot \mathbf{r})}{r^5} \right] \quad (2.12)$$

where  $\mathbf{F}_{12}$  is the force on 2 due to 1, and  $\mathbf{r} = \mathbf{r}_{12} = \mathbf{r}_2 - \mathbf{r}_1$ . The torque is given by,

$$\mathbf{T}_{21} = 3 \frac{(\mu_1 \cdot \mathbf{r})(\mu_2 \times \mathbf{r})}{r^5} - \frac{(\mu_2 \times \mu_1)}{r^3} \quad (2.13)$$

The Stockmayer potential is considered to represent a linear molecule, in so far as it has non-zero moments of inertia about its  $x$  and  $y$  axes only, with the dipole moment,  $\mu$ , along the  $z$  axis, so that,

$$\mathbf{I} = \begin{pmatrix} I_x & 0 & 0 \\ 0 & I_y & 0 \\ 0 & 0 & 0 \end{pmatrix} \quad (2.14)$$

where  $I_x = I_y = I$ . Hence each molecule has only two degrees of rotational freedom.

Using the same reduced units as for the LJ simulations (in particular,  $m = 48$ ), we chose the moment of inertia to be  $I = 1$ . Again it is difficult to compare this value with the moments of real molecules due to the ambiguity in the choice of reduction parameters. Nevertheless, this value is greater than that of a molecule such as HCl, with any reasonable choice of  $\epsilon$  and  $\sigma$ . Hesse-Bezot *et al*<sup>7</sup> used a value of  $I \approx 1.56$  in a recent Stockmayer simulation. The static properties of Stockmayer fluids are, however, independent of the actual value of  $I$  used. Only dynamical properties should be effected by the chosen value of inertia. It is desirable to avoid an excessively small value of  $I$ , since this increases the mean angular velocity at a given temperature, so that smaller time steps are required.

### 2.3.2. Integration method for the Stockmayer potential

The translational forces due to the dipole moment can be treated by the same algorithm used in the LJ simulations, just by adding the additional terms from equation (2.12).

To include the orientations and torques that arise with the Stockmayer potential requires the use of additional coordinates. Due to the symmetry of this molecule, it is in fact only necessary to use a further two coordinates (such as the spherical polar angles  $\theta$  and  $\phi$ ) to fully specify the position and orientation of the dipole. For more complex molecules that are not linear, at least three additional coordinates are needed to completely define the orientation, such as the *Euler angles* ( $\theta, \psi, \phi$ ), as described by Goldstein<sup>21</sup>. In practice it is found to be convenient to use more coordinates than are strictly necessary, for reasons discussed below.

Though Cheung and Powles<sup>9</sup> have given a method for simulating linear molecules, such as we have here, it was decided that a more recent generalization of this technique (due to Evans<sup>22</sup>) should be used. This would allow the code to be

easily adapted for non-linear molecules, if required.

While it is perfectly possible to accurately represent the orientation of a body in terms of the three Euler angles  $(\theta, \psi, \phi)$ , it is found that numerical integration schemes based these angles are not satisfactory. These difficulties are due to singularities that arise when one or more of the angles are undefined (see Evans, reference[22]). The alternative method given by Evans, actually uses a set of four coordinates, known as quaternions, to describe the orientation of each molecule. In terms of the Euler angles these four parameters are,

$$\begin{aligned}\chi &= \cos\theta/2 \cos((\psi+\phi)/2) \\ \eta &= \sin\theta/2 \cos((\psi-\phi)/2) \\ \xi &= \sin\theta/2 \sin((\psi-\phi)/2) \\ \zeta &= \cos\theta/2 \sin((\psi+\phi)/2)\end{aligned}\tag{2.15}$$

The fact that these are not independent is illustrated by the relation,

$$\chi^2 + \eta^2 + \xi^2 + \zeta^2 = 1\tag{2.16}$$

Thus the quaternions allow any given orientation of a solid body to be represented by a vector in four-dimensional space, with unit magnitude.

Evans shows that these new coordinates avoid the singularities that are inherent in the Euler angle representation, and that they may be simply related to physical quantities. For example, the angular velocity vector  $(\omega_p)$  in the principal coordinate system (i.e. the coordinate system of the molecule, as opposed to the fixed laboratory frame) is related to the quaternion derivatives by the equation,

$$\begin{pmatrix} \dot{\xi} \\ \dot{\eta} \\ \dot{\zeta} \\ \dot{\chi} \end{pmatrix} = \frac{1}{2} \begin{pmatrix} -\zeta & -\chi & \eta & \xi \\ \chi & -\zeta & -\xi & \eta \\ \xi & \eta & \chi & \zeta \\ -\eta & \xi & -\zeta & \chi \end{pmatrix} \begin{pmatrix} \omega_{px} \\ \omega_{py} \\ \omega_{pz} \\ 0 \end{pmatrix}\tag{2.17a}$$

which may be written in the more compact form,

$$\dot{Q} = \frac{1}{2} B \omega_p\tag{2.17b}$$

with  $\omega_p$  made into a four component vector. It is also easy to obtain the rotation matrix to transform from the laboratory frame to the principal coordinate system.

Within the laboratory frame we have the basic equation of angular motion,

$$\mathbf{T} = \frac{d}{dt}(\mathbf{L}) = \frac{d}{dt}(\mathbf{I}\boldsymbol{\omega}) \quad (2.18)$$

where  $\mathbf{L}$  is the angular momentum. This equation can be transformed into the principal set of coordinates, but it must be remembered that the transformation matrix is time dependent. This leads to the appearance of additional terms when the time derivative of the angular momentum is taken. Thus the torque about the principal  $x$  axis is,

$$T_{px} = I_{px} \frac{d\omega_{px}}{dt} + (I_{pz} - I_{py})\omega_{py}\omega_{pz} \quad (2.19)$$

with similar expressions for the  $y$  and  $z$  torques. In the case of linear molecules with  $I_{px} = I_{py}$  we can set  $\omega_{pz} = 0$  so that the second order terms in  $\omega$  can be ignored. This is not the case for more general polyatomic molecules, as was highlighted recently<sup>23</sup>. Hence, for the Stockmayer molecules we may write the equations of motion as,

$$\frac{d\omega_{px}}{dt} = T_{px}/I_{px} \quad (2.20)$$

with a similar expression for the  $y$  component and  $d\omega_{pz}/dt = 0$ .

The two coupled first order differential equations, (2.17) and (2.20), may be integrated directly, but it is more convenient to combine them into a single second order equation, as was done by Powles *et al*<sup>24</sup>. The result of doing this is,

$$\ddot{\mathcal{Q}} = \frac{1}{2}B \begin{pmatrix} T_{px}/I_{px} \\ T_{py}/I_{py} \\ 0 \\ -2|\dot{\mathcal{Q}}|^2 \end{pmatrix} \quad (2.21)$$

where  $|\dot{\mathcal{Q}}|^2 = \dot{\chi}^2 + \dot{\xi}^2 + \dot{\eta}^2 + \dot{\zeta}^2$ .

This second order differential equation may be solved by the same type of Gear algorithm that is used for the translational motion, but it is now necessary to choose coefficients that cater for the appearance of  $\dot{\mathcal{Q}}$  in the expression for  $\ddot{\mathcal{Q}}$ . As was pointed out earlier, this is easily allowed for in the choice of Gear coefficients.

A more detailed discussion of the use of quaternions with a second order equation is given by Allen<sup>25</sup>.

### 2.3.3. Cut-off for the Stockmayer potential

In the case of the Stockmayer potentials we have again employed a simple cut-off at  $r_c \approx 10\sigma$ . For the LJ part of the interaction this may be justified, as before, by the fact that  $\phi_{LJ}(r)$  is almost negligible at the radius of  $r_c$ , since it varies as  $r^{-6}$  at large  $r$ . The dipolar part of the interaction potential, on the other hand, only decreases as  $\sim r^{-3}$ . Thus there will be a more significant jump in the potential for two atoms at this separation, though it is still quite small for  $r_c = 10$  (and dependent on orientation).

As the drop diameter is generally less than  $10\sigma$ , the vast majority of liquid-liquid interactions will be fully accounted for. The main effect of the cut-off is on the forces between the particles in the vapour and others in the drop or the vapour. Since the vapour density is always quite low, the numbers involved will be small. Furthermore, the dielectric constant of the vapour is, in any case, very close to unity, so there is no need for special treatment of the interactions with dipoles beyond the cut-off length, as is the case for homogeneous simulations, i.e. despite the periodic boundary conditions, the drop appears to be surrounded by a vapour region with a dielectric constant  $\epsilon \approx 1$ , beyond which is an effective vacuum.

### 2.3.4. Programming details

The programme used for the Stockmayer drops is a modified version of the LJ programme, and a listing is given in the appendices. While the prediction and correction steps use the quaternions, plus their derivatives, to represent dipole orientation and motion, the more comprehensible direction cosines and angular velocities are also calculated from these, for use in the FORTOR and DATA subroutines.

The initial configurations were generated in the same way as the LJ ones, except that random orientations and angular velocities have to be generated at the start. The total linear and angular momentum of the initial configuration was set to zero before each run. Though the angular momentum is not conserved, at least within a given periodic cell, it was thought best to ensure there was no net rotation to start with.

In most of the Stockmayer simulations a timestep of  $\Delta t = 0.05$  has been used, which is the same as the value used for the LJ runs. This is quite large considering the moment of inertia of the particles. From equipartition, the RMS rotational velocity is given by  $\frac{2}{2}kT = \frac{1}{2}I\langle|\omega|^2\rangle$ , with  $k$  and  $I$  both unity in this case. A typical temperature of  $T \sim 0.8$  then gives  $\langle|\omega|^2\rangle^{1/2} = 1.5$ , which corresponds to a reorientation of about 0.06 radians, or 3.5 degrees, per integration step with  $\Delta t = 0.05$ .

As a check on the adequacy of our value of  $\Delta t$ , a few runs were performed with a step length of  $\Delta t = 0.025$  instead. No significant difference was observed in the data obtained with the shorter step length. Since these simulations are very time consuming, and require quite long equilibration periods, it was felt that a reasonably large step size should be employed. Our value of  $\Delta t$  is about 50% greater than the value used by Hesse-Bezot *et al*<sup>7</sup> in a recently published study of Stockmayer systems. They also had a slightly larger moment of inertia, but their state points were at higher temperatures. A few of the Stockmayer runs in this work have been performed with  $\Delta t = 0.04$  instead of 0.05, when higher temperatures were required.

As with the LJ simulations, the total energy was kept constant by rescaling the total kinetic energy every ten steps. The values were again very close to unity, and indicated a drift of the order of 2% per 10000 steps.

## References

1. F.H.Ree, *Physical chemistry, an advanced treatise*, Academic press, New York, 1971. H.Eyring, D.Henderson, W.Jost eds.
2. W.W.Wood, *Physics of simple liquids*, North-Holland, Amsterdam, 1968. H.N.V.Temperley, J.S.Rowlinson, G.S.Rushbrooke eds.
3. G.A.Chapela, G.Saville, S.M.Thompson, J.S.Rowlinson, *J. Chem. Soc. Faraday Trans. 2*, vol. 73, p. 1133, 1977.
4. J.G.Powles, G.Rickayzen, and M.L.Williams, *J. Chem. Phys.*, vol. 83, p. 293, 1985.
5. D.Nicholson and N.G.Parsonage, *Computer simulation and the statistical mechanics of adsorption*, Academic press, London, 1982. Chapter 6
6. S.M.Thompson, K.E.Gubbins, J.P.R.B.Walton, R.A.R.Chantry, J.S.Rowlinson, *J. Chem. Phys.*, vol. 81, p. 530, 1984.
7. C.Hesse-Bezot, G.Bossis, and C.Brot, *J. Chem. Phys.*, vol. 80, p. 3399, 1983.
8. J.G.Powles, W.A.B.Evans, N.Quirke, *Molec. Phys.*, vol. 46, p. 1347, 1982.
9. P.S.Y.Cheung and J.G.Powles, *Molec. Phys.*, vol. 30, p. 921, 1975.
10. J.J.Nicolas, K.E.Gubbins, W.B.Streett, D.J.Tildesley, *Molec. Phys.*, vol. 37, p. 1429, 1979.
11. J.G.Powles, *Physica*, vol. 126A, p. 289, 1984.
12. L.Verlet, *Phys. Rev.*, vol. 159, p. 98, 1967.
13. C.W.Gear, *Numerical initial value problems in ordinary differential equations*, Prentice-Hall, 1971.
14. C.W.Gear, *Argonne national laboratory report, ANL-7126*, 1966.
15. D.Fincham, D.M.Heyes, *Information Quarterly for MD and MC Simulations*, vol. 6, p. 4, 1982.
16. A.R.Janzen and J.W.Leech, *Comp. Phys. Comm.*, vol. 32, p. 349, 1984.

17. W.B.Street, D.J.Tildesley, and G.Saville, *Molec. Phys.*, vol. 35, p. 639, 1978.
18. S.D.Stoddard, *J. Comp. Phys.*, vol. 27, p. 291, 1978.
19. J.O.Hirschfelder, C.F.Curtis, and R.B.Bird, *Molecular theory of liquids and gases*, John Wiley, New York, 1954.
20. L.G.Alsson and K.E.Larsson, *Physica*, vol. 72, p. 300, 1974.
21. H.Goldstein, *Classical mechanics*, Addison-Wesley, New York, 1971.
22. D.J.Evans, *Molec. Phys.*, vol. 34, p. 317, 1977.
23. D.J.Tildesley and M.P.Allen, *Information Quarterly for Computer Simulation of Condensed Phases*, vol. 16, p. 46, 1985.
24. J.G.Powles, W.A.B.Evans, E.McGrath, K.E.Gubbins, and S.Murad, *Molec. Phys.*, vol. 38, p. 893, 1979.
25. M.P.Allen, *Information Quarterly for MD and MC simulators*, vol. 5, p. 18, 1982.

## Chapter Three: Stability and structure of LJ and Stockmayer drops

### 3.1. Introduction

This chapter presents the results obtained for the size, shape and stability of the series of LJ and Stockmayer drops that have been studied. The approach of these systems to liquid-vapour equilibrium is first discussed (section (3.2)), since an adequate portion of each run must first be discarded before meaningful averages can be obtained. We then describe the range of drop size and temperature over which simulations have been performed, and present the basic data obtained, i.e. density profiles, pressures etc. In the final section some discussion of these results is given along with an estimate of the uncertainty in the data.

### 3.2. Equilibration

The equilibration period required in these simulations is clearly greater than that needed in more usual ones (e.g. of homogeneous liquid), due to the larger size of the periodic cell. For example, assuming a reduced temperature of unity, a particle with the RMS velocity would take  $\sim 1500$  time steps to travel from one drop to its nearest neighbour image (assuming no other interactions occur). This is a lower bound on the initialization period, and it is likely that a rather longer time will be necessary in practice.

To study the evolution from a cluster in vacuum to one in equilibrium with its vapour we can observe the cluster size as a function of time. The definition used for  $N_c$  has been discussed in the previous chapter. In figure (3.1a) the variation of the cluster size with time is shown for a typical system. These results are for an S1 simulation with  $N_p = 260$ , a total energy per particle of  $E = -2.0$  and a cell size of  $S = 20\sigma$ , state (D1)<sup>†</sup>. The run extends over almost 25000 time steps of  $\Delta t = 0.05$ ,

---

<sup>†</sup> This is just a reference number to help identify the particular run in the tables that are presented later. The letter 'D' indicates dipolar systems, while LJ states will be labelled L1, L2.. etc.

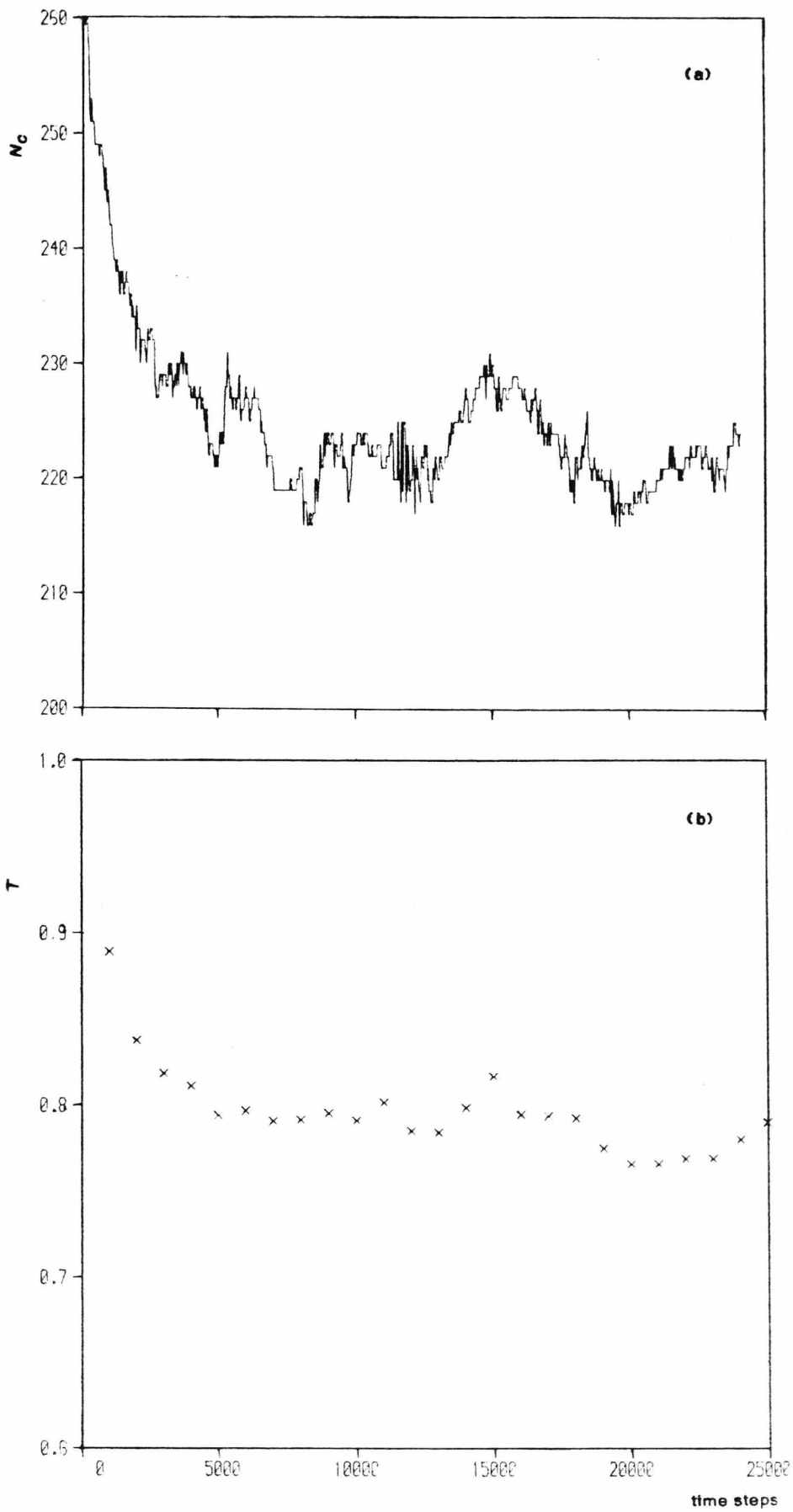


**Figure 3.1:** (a) The number of particles within the cluster against time (in units of the simulation integration time step,  $\Delta t = 0.05$ ). These results are for state (D1), a Stockmayer S1 drop, with  $N_p = 260$  and  $T = 0.79$ .

(b) The mean temperature of the above system as a function of time, given by subaverages of the total kinetic energy over intervals of 1000 time steps.

starting from an initial configuration obtained from an homogeneous simulation (see chapter two).

The mean temperature of the system may also be used as a guide to the approach to equilibrium. However, in MD simulations the temperature can only be obtained from the time average of the kinetic energy, the instantaneous value of which is subject to large fluctuations. Nevertheless, subaverages can be made to estimate the temperature over small portions of the run. Values of  $T$  obtained by averaging over periods of 1000 steps are plotted in figure (3.1b), again for state (D1).

Comparing figures (3.1a) and (3.1b) it can be seen that there is some correlation between them, as might be expected since evaporation of particles from the cluster leads to a reduction in the kinetic energy of the system. It can be seen that the greatest part of the change in  $N_c$  occurs in the first  $\sim 2000$  steps of the run, in agreement with the rough estimate made above. After about 3000 steps the cluster size is within the band  $216 < N_c < 230$ , and it fluctuates within these approximate limits for the remainder of the run.

The behaviour of the temperature during the run also suggests that a minimum of  $\sim 3000$  equilibration steps are required for this system. Similar results to these are observed in the other simulations, for both Stockmayer and LJ drops. In very large systems the cluster size takes slightly longer to 'level-out', but the increased number of particles within the drop means that variations in quantities, such as the sub-averages of the temperature, are much less. In such cases it is likely that the central cluster is very close to its equilibrium state after a few thousand time steps, but that the gas density in the furthest corners of the periodic cell may take longer to reach its true equilibrium value.

In view of the above observations a minimum equilibration period of 3000 steps was generally adopted for these simulations. However, the results of each run were inspected individually and, if it was felt that the initialization period was inadequate,

sufficient data was recorded to allow averages to be made over smaller parts of the run. For example, the averages could be calculated from only the last 6000 steps of a run of, say, 13000 steps, if required.

After equilibration, systems were usually run for at least 10000 further integration steps to obtain data. As is apparent in figures (3.1a,b) the fluctuations in  $T$ ,  $N_c$  etc. take place over long periods, and hence we need to average over many steps. With very big drops ( $N_p \sim 1000$ ), it was not usually possible to use 10000 steps due to the high cost in computing time, and shorter runs were sometimes made. Thompson *et al*<sup>1</sup>, in their recent study of LJ (sp2.5) drops, have used extremely long MD simulations of between 16000 and 350000 time steps. However their main concern is the calculation of the pressure tensor, and this appears to require such enormous runs.

To test the adequacy of using 10000 steps, the measured properties obtained from two consecutive runs of this length can be compared. This has been done for the data for the run shown in figures (3.1a,b) and the findings are given in table (3.1).

Table 3.1						
Run	$T$	$N_c$	$\rho_l$	$\rho_g$	$R_h$	$D$
First	0.793	222.5	0.855	0.0052	3.83	1.62
Second	0.785	222.8	0.849	0.0050	3.83	1.71

Table 3.1: A comparison of averages over the first and second 10000 step periods of run (D1).

The temperatures measured in the two segments differ by about 1%, which is acceptable, considering the small number of particles and inhomogeneous nature of the system. The mean cluster sizes are almost identical, while the densities and virial pressure values are not in quite such good agreement, but they have larger uncertainties (which we estimate later).

### 3.3. States studied and their properties.

#### 3.3.1. Range of state points

The upper bound on temperatures at which free drops may be observed is  $T_c$ , the critical temperature of the fluid. For the full LJ 12-6 potential it is found that  $T_c$  lies within the range 1.30 - 1.35 (e.g. see Nicolas<sup>2</sup> or Adams<sup>3</sup>). Hence, with the almost complete LJ interaction used in our simulations, we must have  $T < \sim 1.3$ . In practice it was found to be difficult to obtain drops at temperatures above  $T \sim 1.0$ , and the most energetic LJ state we ran had  $T=1.05$ . This significantly lower limitation is imposed by the finite number of particles that can be used and the requirement that the cell size,  $S$ , remains 'sufficiently large'. As the temperature of a drop is increased the density in the surrounding gas also increases very rapidly. Due to the very large volume of the cell, the proportion of particles within the gas phase rises sharply, so that the drop can evaporate well before  $T_c$  is reached. To obtain states at higher temperature it would be necessary to either reduce the size of the periodic cell (but this may lead to interactions between images, which is very undesirable), or increase the number of particles in the simulation (which requires more computing time).

The Stockmayer fluids (S1 and S3) have not been studied in as great a detail as has the LJ fluid. However, some data is available and Powles<sup>4</sup> has analysed this, in conjunction with some basic perturbation theory, to allow the coexistence curve to be predicted for the S1 fluid, and estimates made of its critical parameters. He finds that  $T_c \approx 1.45$  in this case. The highest temperature S1 system we have used is at  $T \sim 0.95$ , despite the increase in  $T_c$  over the LJ value. This is partly due to the fact that slightly larger periodic cells were used to ensure the isolation of images in the presence of long-ranged dipole-dipole interactions.

We are not aware of any estimates of the critical parameters for the S3 fluid, but the value of  $T_c$  will be greater than 1.45. The S3 drops used in this work were

simulated at temperatures of  $T \sim 1.2 - 1.25$ .

At the other extreme of very low temperatures, there is no real difficulty in obtaining clusters in equilibrium with surrounding gas. However we are mainly interested in the properties of liquid systems and the liquid-vapour interface, rather than solids and the solid-vapour interface, so that most state points simulated had temperatures above the triple point value,  $T_t$ , for the fluid. For the LJ potential it is known that<sup>5</sup>,  $T_t \approx 0.68$ , while the value for S1 and S3 fluids is less well known. Powles<sup>6</sup> suggests the value of  $T_t \sim 0.77$  for the S1 fluid. Nevertheless, we have performed some runs for  $T < T_t$ , but they are not very far below it, and are mainly small clusters. It has been shown by McGinty<sup>7</sup> that a sharp liquid-solid phase transition does not occur in very small clusters. His work was performed with LJ clusters of between 30 and 100 particles. By measuring the diffusion constant in the center of these clusters the transition from liquid to solid state can be detected. It is found that drops of  $\sim 100$  particles remain essentially fluid down to  $T \approx 0.6$  or so. When the transition does occur it is a gradual one. In their work on drops of  $\sim 256$  particles, Rusanov and Brodskaya<sup>8</sup> find that the solid liquid transition may not occur until  $T \sim 0.32$  (sp3 potential).

The diffusion constant was not calculated in our simulations, though it is observed that the central densities obtained are generally closer to the coexisting liquid values than to the density of the solid phase. It seems unlikely that any of the drops we simulated would have had a solid core, though further investigation of the melting transition in large clusters may be warranted

Within the above temperature ranges a series of states have been studied for the LJ and S1 potentials, along with two S3 states. Tables (3.2a) and (3.2b) give details of the important parameters used for each system; the total energy, cell size, number of particles and the length of the run. The majority of runs are of 260 or 450 particles, larger systems proving to be very expensive in computer time. The few very

small systems studied ( $N_p = 60 - 100$ ) were only stable at low temperatures.

Run no.	Run parameters			Length of run	
	$N_p$	$S$	$E$	Init.	Prod.
(L1)	60	17.0	-1.0	10000	40000
(L2)	100	17.0	-1.0	10000	40000
(L3)	100	17.0	-0.5	10000	40000
(L4)	260	18.0	-2.0	3000	20000
(L5)	260	18.0	-1.1	3000	20000
(L6)	260	24.0	-2.0	20000	12000
(L7)	260	24.0	-1.3	15000	20000
(L8)	260	24.0	-1.0	10000	10000
(L9)	260	24.0	-0.6	10000	25000
(L10)	320	18.0	-2.4	3000	20000
(L11)	320	18.0	-2.0	3000	10000
(L12)	320	18.0	-1.2	3000	10000
(L13)	320	18.0	-1.0	3000	10000

Table 3.2a: The details of the LJ systems that have been studied with between 60 and 320 molecules.  $N_p$  is the number of molecules,  $S$  is the side length for the periodic cell and  $E$  is the set total energy per particle. The final two entries are the run lengths, in time steps of 0.05.

A range of cell sizes have been used in the search for a satisfactory compromise between ensuring that periodic images are isolated from each other and keeping the equilibration time down. The results are discussed later.

### 3.3.2. Properties of LJ drops

A typical LJ drop density profile,  $\rho(r)$ , is shown in fig. (3.2a) for the state (L21). This is a 450 particle system with  $E = -1.0$ , and a periodic cell size of  $S/\sigma = 20$ .

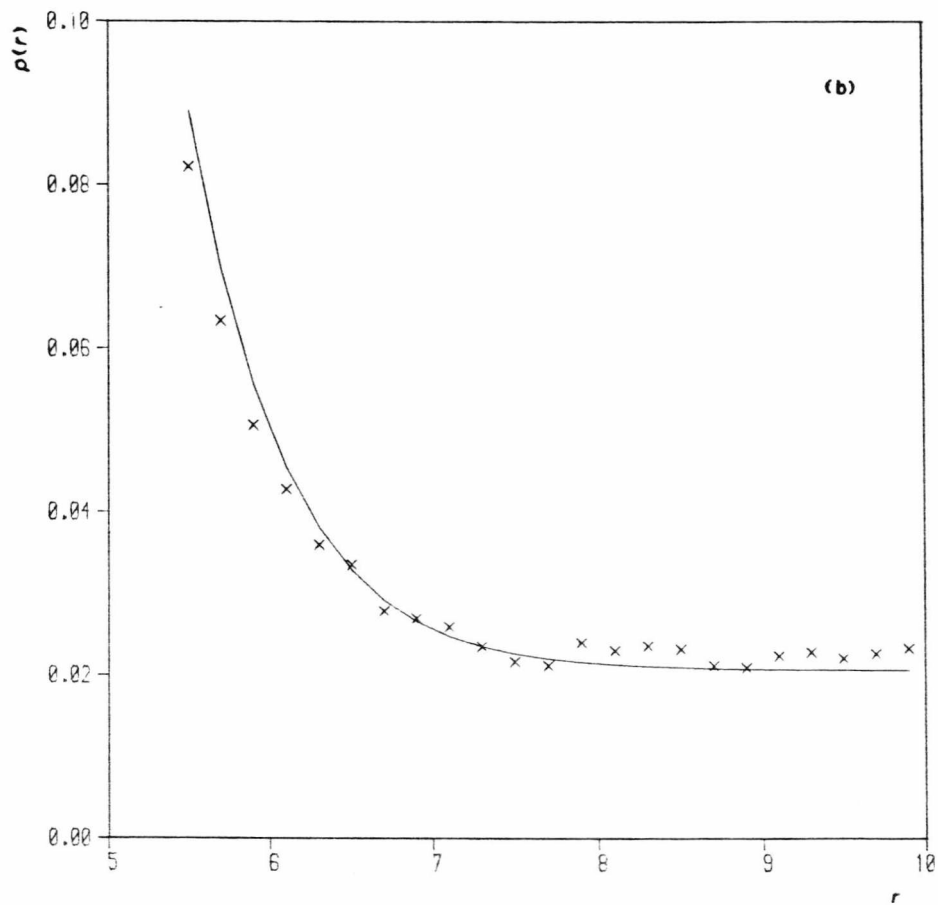
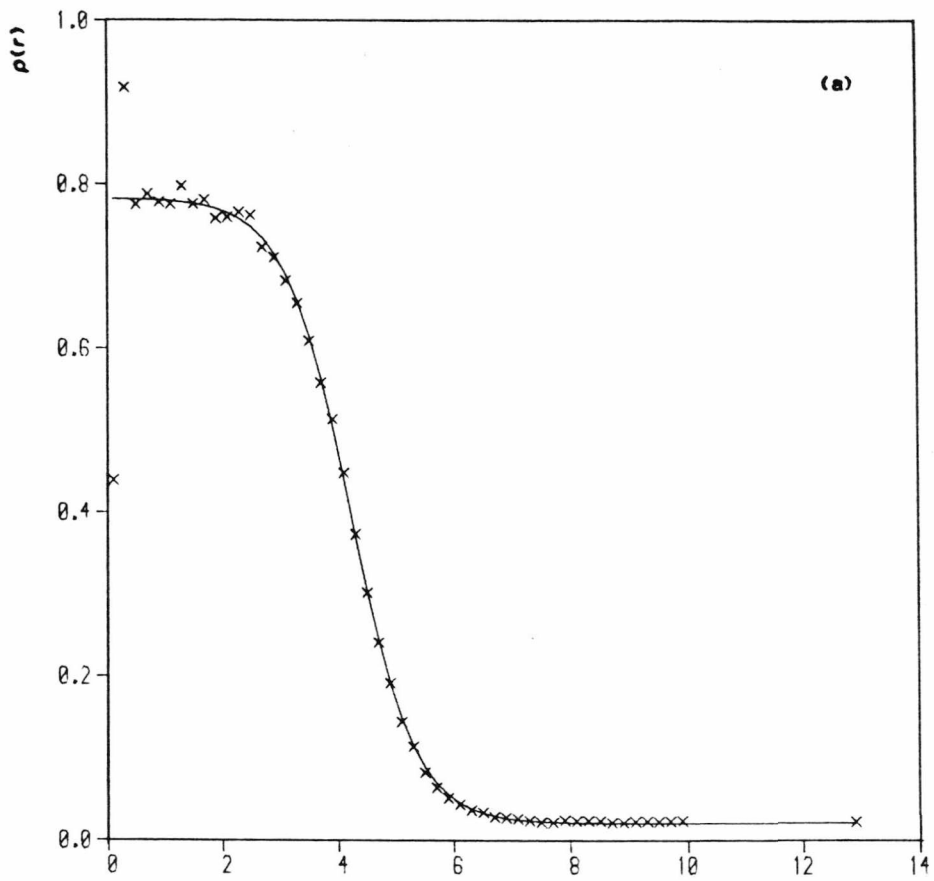


Figure 3.2: (a) The density profile,  $\rho(r)$ , (data shown as (x)) measured for the LJ state (L21), with  $N_p = 450$  and  $T = 0.86$ . The solid curve shows the tanh function (described in the text) that has been obtained by a "least squares" fit to the simulation data.

(b) As above, but on an enlarged scale to show the density profile within the vapour region.

Table 3.2a (continued)					
Run no.	Run parameters			Length of run	
	$N_p$	$S$	$E$	Init.	Prod.
(L14)	450	16.0	-0.2	6000	8000
(L15)	450	18.0	-2.8	3000	10000
(L16)	450	18.0	-2.0	4000	18000
(L17)	450	18.0	-1.0	4000	10000
(L18)	450	20.0	-3.1	3000	12000
(L19)	450	20.0	-2.8	3000	10000
(L20)	450	20.0	-2.0	4000	12000
(L21)	450	20.0	-1.0	3000	10000
(L22)	450	20.0	-0.5	2000	10000
(L23)	450	20.0	-0.3	2500	10000
(L24)	450	20.0	0.0	3000	5000
(L25)	800	17.5	-0.8	2000	8000
(L26)	1300	25.0	-3.7	4000	5000
(L27)	1300	25.0	-2.5	2000	5000
(L28)	1300	23.0	-0.8	2000	4000

Table 3.2a (Cont.): Data on the LJ states that used between 450 and 1300 particles. Column entries as before.

The temperature of this system was found to be  $T = 0.86$  with the average number of particles within the cluster  $N_c = 303$ . The general appearance of the liquid-vapour interface is qualitatively similar to that obtained in other studies, such as that for the planar interface<sup>9</sup>. The increasing fluctuations in  $\rho(r)$  as  $r \rightarrow 0$  are due to the decrease in shell volumes (the width of shells is kept constant). For a planar interface the coexisting liquid density at this temperature is<sup>4</sup>  $\rho_l = 0.78$  and  $\rho(r)$  is very close to this

Run no.	Run parameters					Length of run	
	$N_p$	$S$	$E$	$\Delta t$	$\mu^2$	Init.	prod.
(D1)	260	20.0	-2.0	0.050	1	4000	20000
(D2)	260	20.0	-1.0	0.050	1	2000	5000
(D3)	260	24.0	-2.0	0.025	1	10000	16640
(D4)	260	24.0	-1.0	0.025	1	7000	6400
(D5)	450	18.0	-1.0	0.050	1	2000	10000
(D6)	450	24.0	-3.0	0.050	1	2500	15000
(D7)	450	24.0	-2.0	0.050	1	10000	20500
(D8)	450	24.0	-1.5	0.040	1	2500	5000
(D9)	450	24.0	-0.4	0.050	1	2000	10000
(D10)	800	27.0	-3.1	0.050	1	2000	5000
(D11)	900	27.0	-3.0	0.050	1	3000	3000
(D12)	900	27.0	-1.5	0.040	1	3000	11900
(D13)	450	24.0	-2.6	0.040	3	5000	20000
(D14)	450	24.0	-1.6	0.040	3	10000	22000

Table 3.2b: Details of all the Stockmayer states simulated in this work. Parameters are as for table (3.2a), plus the time step,  $\Delta t$ , and the squared dipole moment,  $\mu^2$ .

value for  $r < 2.5\sigma$ . A more complete analysis of the liquid densities obtained will be made in chapter four.

The surface region, where  $\rho$  changes rapidly with  $r$ , has a width of  $\sim 2-3\sigma$ . Due to the spherical geometry a large proportion of the particles lie within this region of varying density. Beyond the surface region the density profile levels off to a gas density of  $\rho_g \approx 0.022$  for  $r$  greater than  $\sim 7\sigma$ . This compares with a coexistence vapour density of  $\rho_v = 0.0086$  for planar surfaces. This discrepancy is due to the difference

surface tension and will also be treated in more detail in chapter four.

Also shown in fig. (3.2a) is a hyperbolic tangent of the form,

$$\rho(r) = A - B \tanh(2(r - R_h)/D) \quad (3.1)$$

This curve has been fitted to the data by a least squares method. Each data point was given a weight proportional to the square root of the number of particles found within that shell. This gives a good fit in the surface and dense liquid regions, where there are many particles. Such a choice of weights is quite arbitrary, and may not be the best choice. The use of equal width shells leads to great variations in the mean number of particles within each one, so it is clearly unsatisfactory to give all the  $\rho$  values the same weight.

Due to the large fluctuations in the density at small  $r$ , the estimate of the liquid density<sup>†</sup>,  $\rho_l = A + B$ , is adopted as the most convenient way of obtaining  $\rho_l$ . The estimate of the gas density,  $\rho_g = A - B$ , on the other hand, is not very reliable with the given weighting, particularly when  $\rho_g$  is very small. Rather than use another set of weights,  $\rho_g$  was measured directly from the  $\rho(r)$  data. Figure (3.2b) shows the same data as (3.2a), but on a larger scale to show the profile within the gas. It can be seen that the tanh curve slightly under estimates the gas density in this case.

Table (3.3a) presents a summary of the temperature and cluster size data for all the LJ simulations. The virial pressure, as measured over the entire periodic cell, is also given for some of the states, along with the  $R_h$  and  $D$  parameters for the fitted tanh curves. In addition, the best estimates of  $\rho_l$  and  $\rho_g$  are included.

Graphs of the density profiles, and the corresponding tanh fits, are shown for a selection of states in figs. (3.3) to (3.8). The first of these represents a drop of only  $\sim 42$  particles (state L1) and it can be seen that is virtually no 'bulk' liquid inside the surface region. At the other extreme is the drop in fig. (3.8) (state L26), with

---

<sup>†</sup> At  $r=0$  the  $\tanh(\dots)$  term in (3.1) is virtually -1.

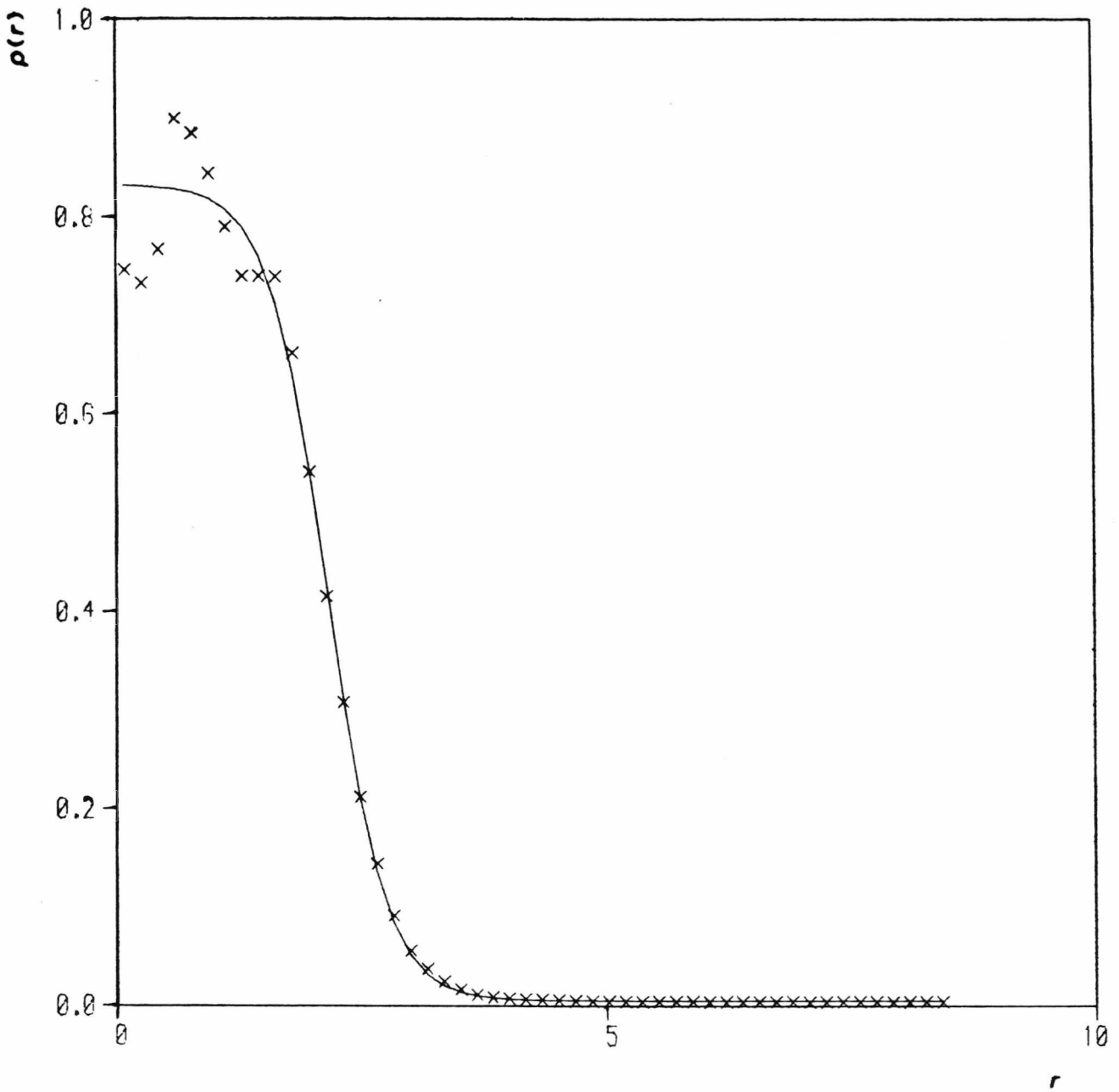


Figure 3.3: The measured density profile (x) and the fitted tanh curve for state (L1).  $N_p = 60$  and  $T = 0.625$ .

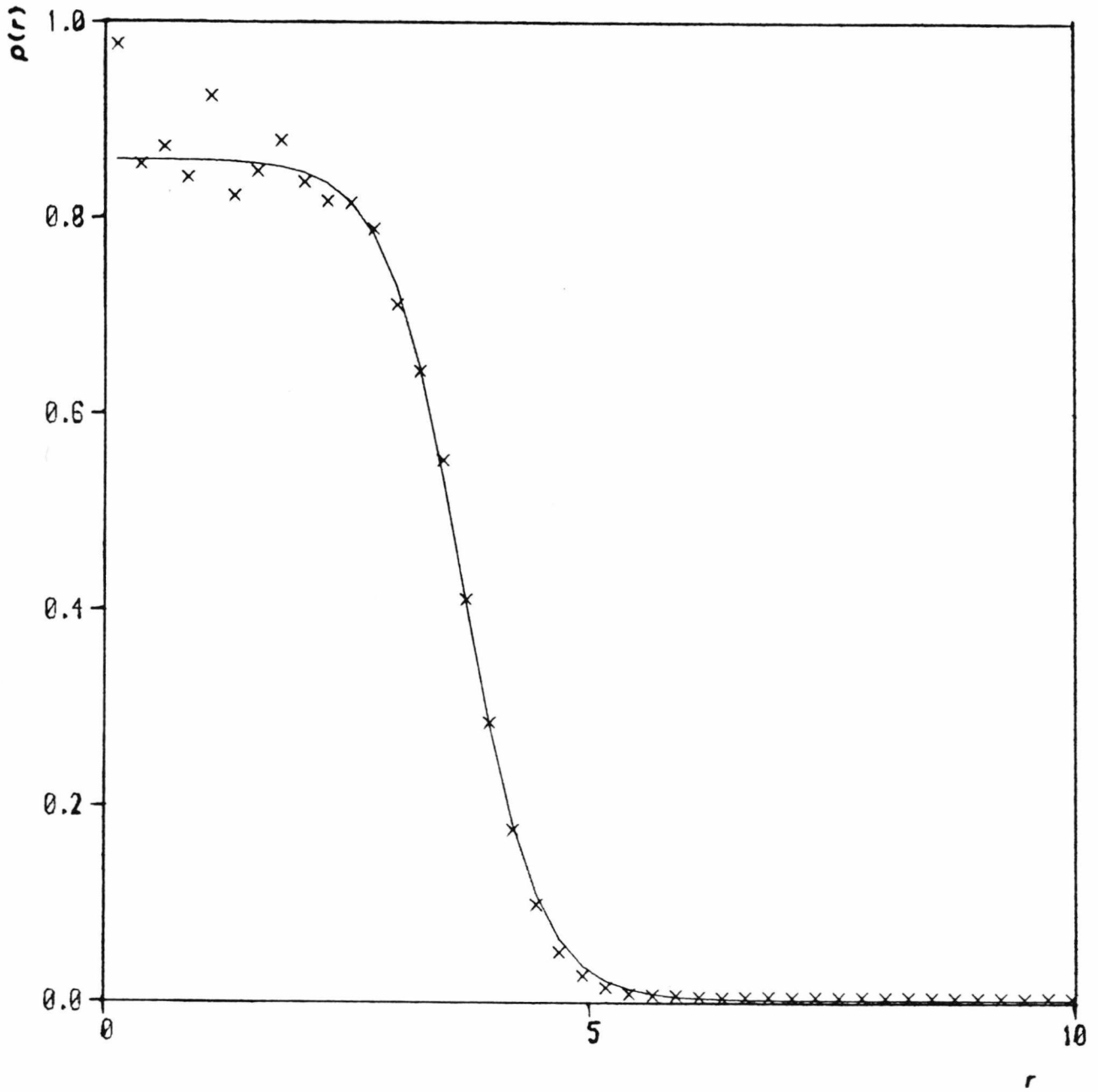


Figure 3.4: As for fig. (3.3), but for state (L6),  $N_p = 260$  and  $T = 0.643$ .

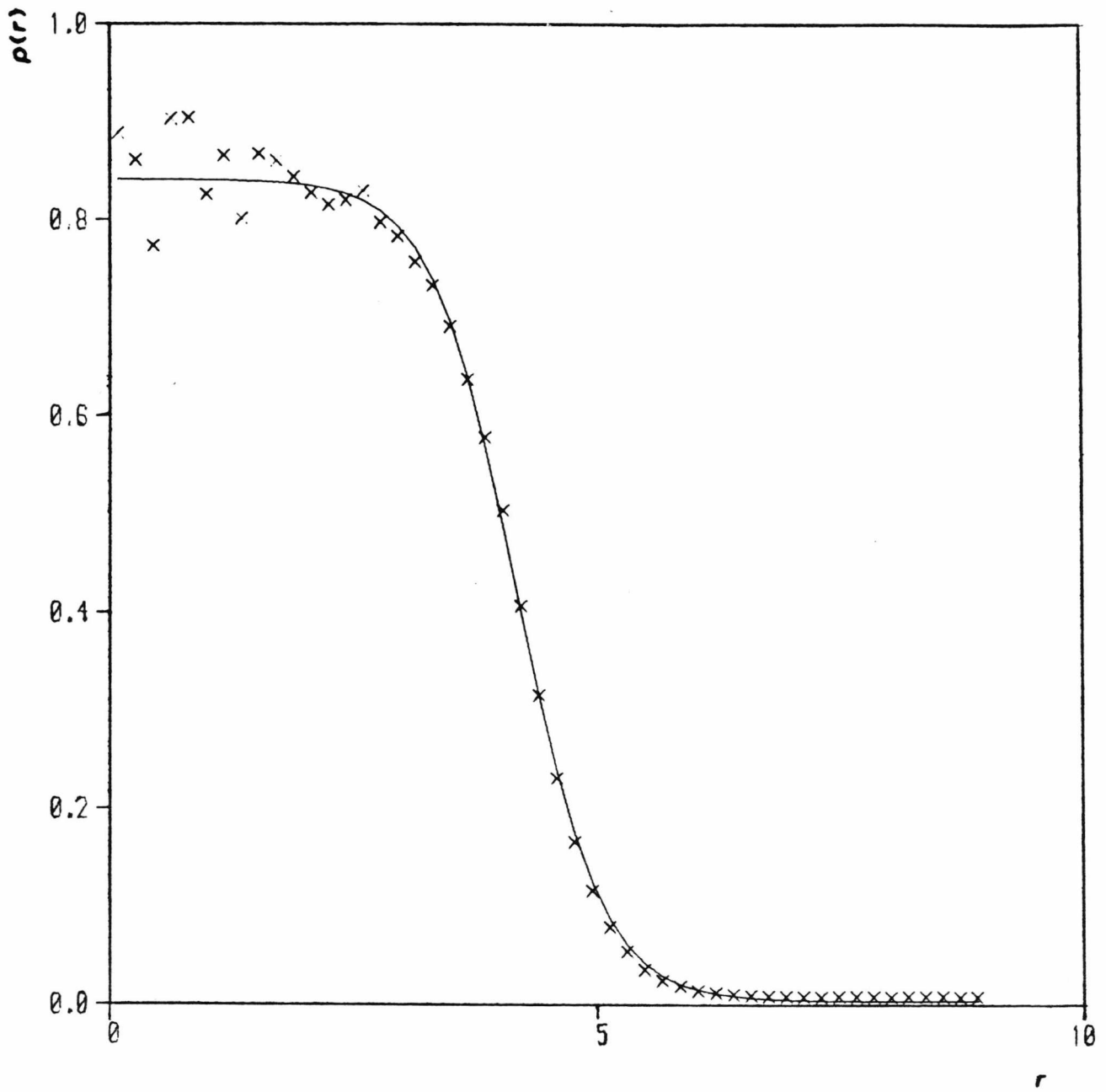


Figure 3.5: As for fig. (3.3), but for state (L10).  $N_p = 320$  and  $T = 0.717$ .

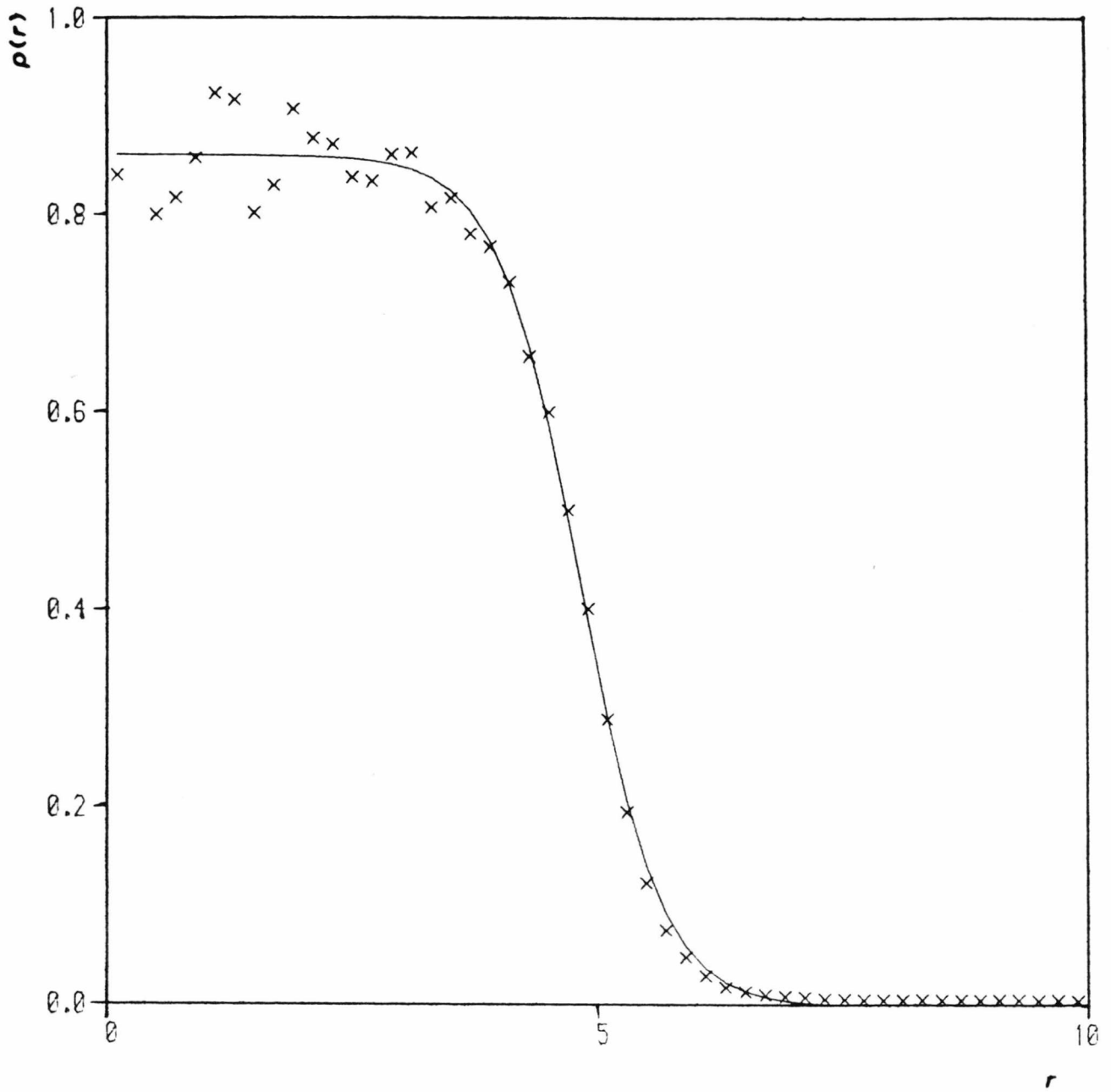


Figure 3.6: As for fig. (3.3), but for state (L18),  $N_p = 450$  and  $T = 0.676$ .

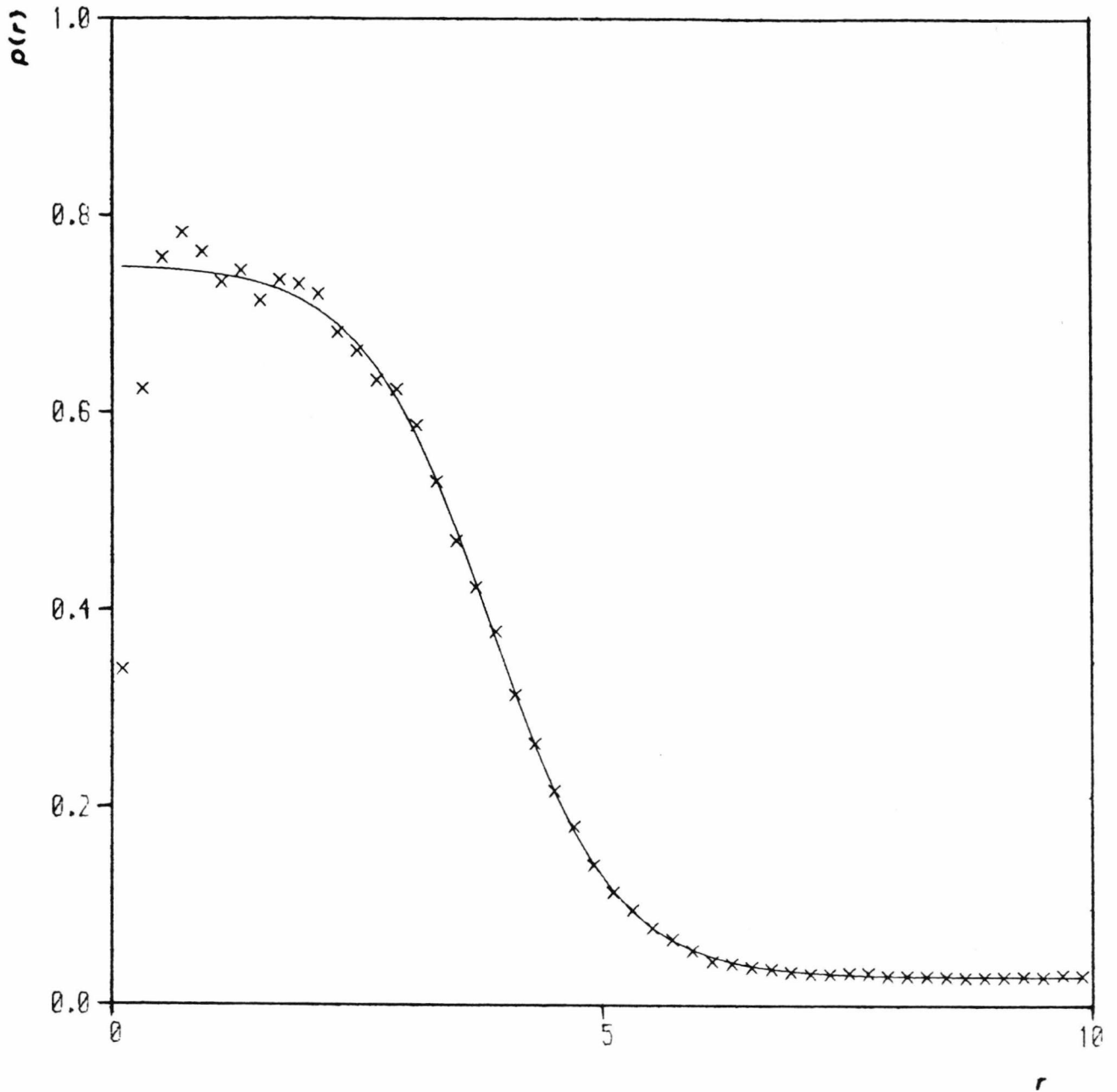


Figure 3.7: As for fig. (3.3), but for state (L23).  $N_p = 450$  and  $T = 0.949$ .

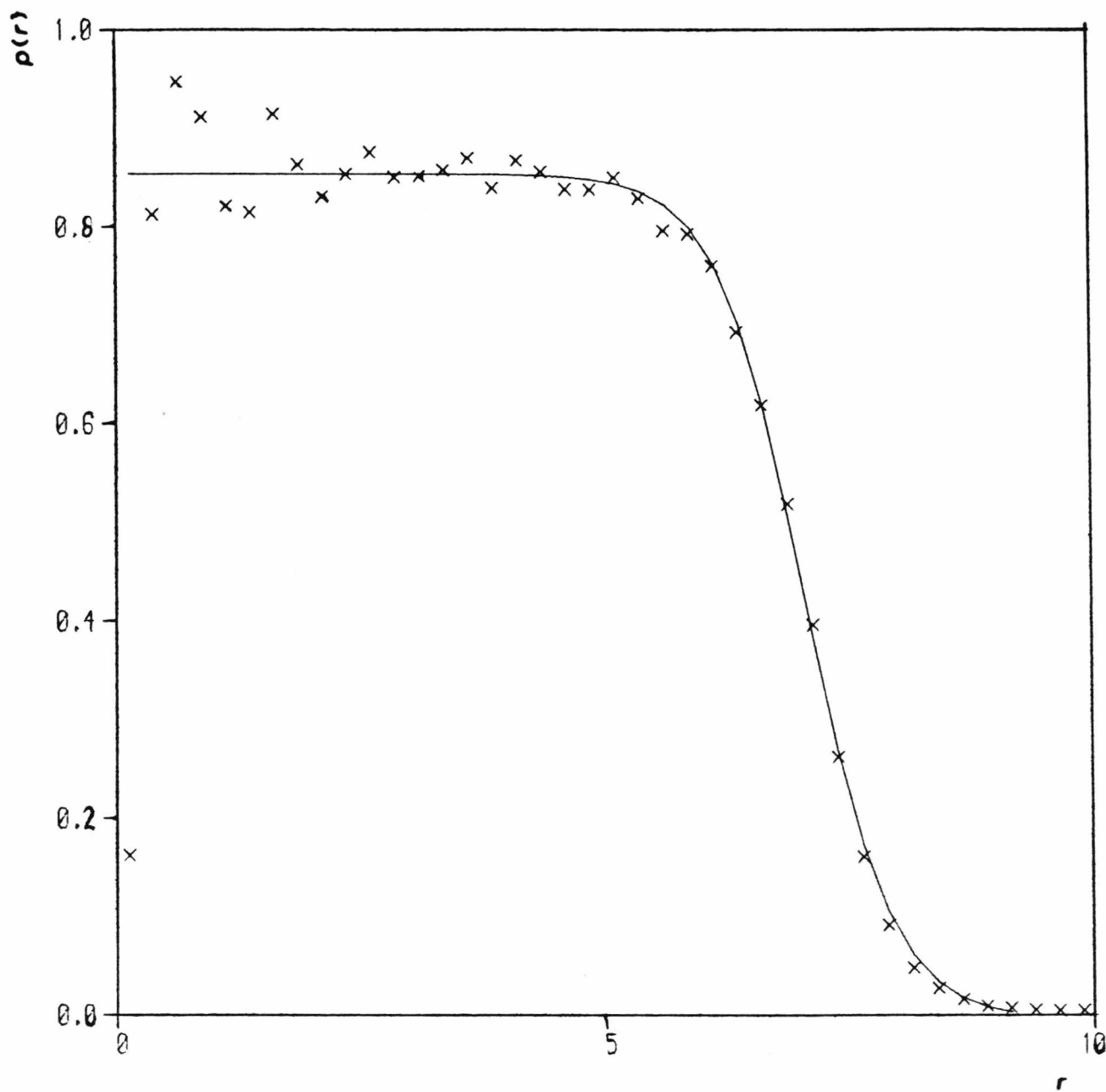


Figure 3.8: As for fig. (3.3), but for state (L26),  $N_p = 1300$  and  $T = 0.69$ .

Table 3.3a							
Run	T	$N_c$	P	$\rho_g$	$\rho_l$	$R_h$	D
(L1)	0.625	42	-	0.0037	0.832	2.14	1.18
(L2)	0.654	67	-	0.0072	0.834	2.49	1.53
(L3)	0.713	56	-	0.0094	0.847	2.29	1.56
(L4)	0.726	219	-	0.0080	0.834	3.80	1.77
(L5)	0.805	183	-	0.0150	0.801	3.54	1.99
(L6)	0.643	197	-	0.0047	0.860	3.68	1.57
(L7)	0.694	168	-	0.0068	0.838	3.48	1.64
(L8)	0.760	158	-	0.0077	0.831	3.47	1.86
(L9)	0.715	132	-	0.0091	0.818	3.19	1.80
(L10)	0.717	286	-	0.0085	0.841	4.19	1.72
(L11)	0.747	268	-	0.0110	0.839	4.04	2.00
(L12)	0.802	238	-	0.0170	0.796	3.88	2.35
(L13)	0.813	222	-	0.0200	0.787	3.76	2.15

**Table 3.3a:** Results for the LJ systems of between 60 and 320 particles.  $T$  is the temperature and  $N_c$  is the mean number of particles within the cluster.  $\rho_l$  and  $\rho_g$  are the liquid and vapour densities respectively,  $D$  is the surface width and  $R_h$  the half radius of the drop.

$N_c = 1250$  and a radius in excess of  $7\sigma$ . There is a substantial central region of liquid at close to the coexistence density for this temperature. The other figures show a range of drops of various temperatures and sizes between these extremes. Most work has been performed with 450 particle simulations which have a significant central region at liquid densities, while not being too expensive in terms of computer time.

The relationship between the final temperature and the preset total energy,  $E$ , was found to be approximately linear for a given number of particles and periodic cell size. This is illustrated in fig. (3.9) for  $N_p = 450$ ,  $S/\sigma = 20$  states. Deviations from

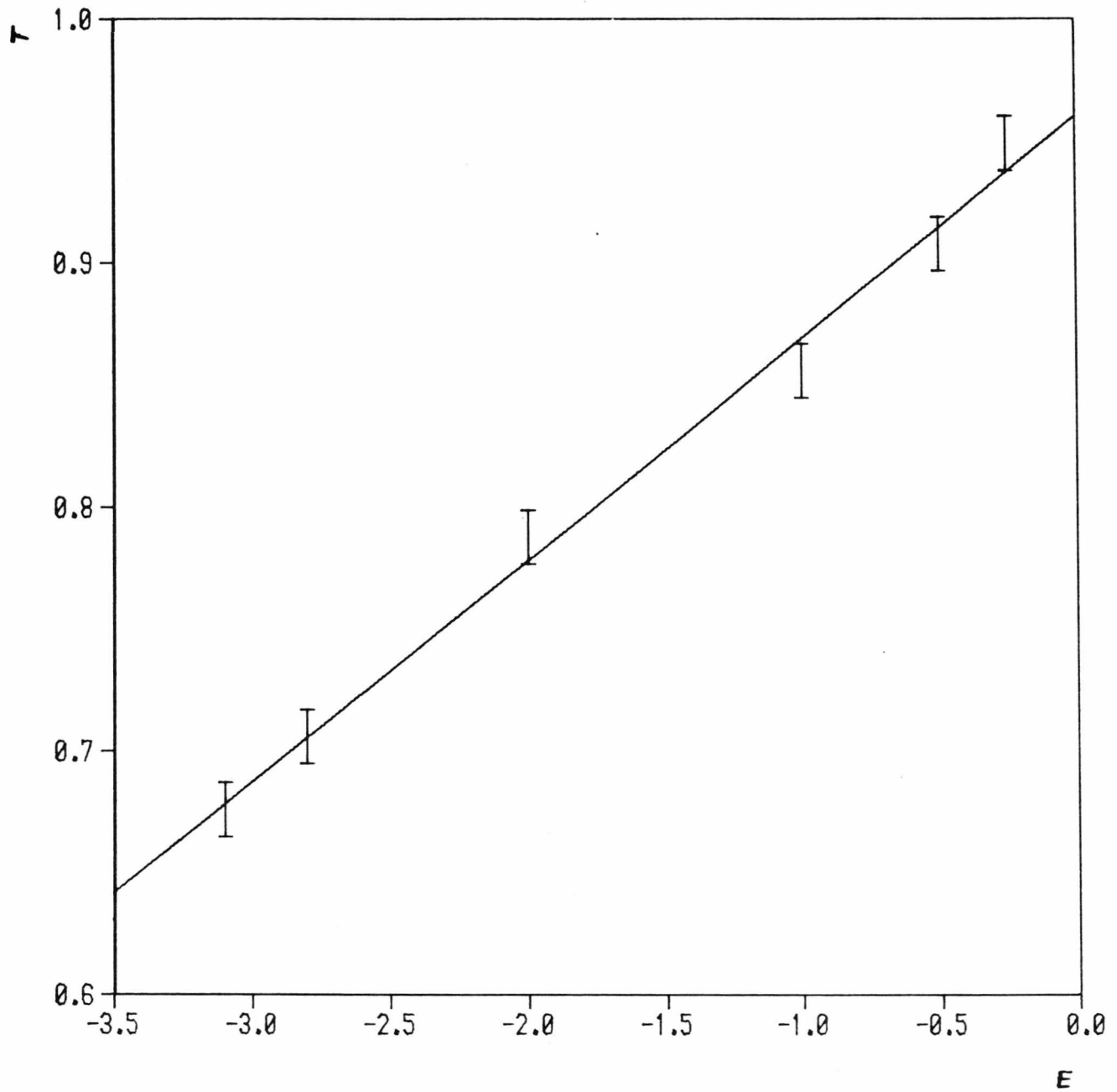


Figure 3.9: The mean temperature, as measured for the LJ drops with  $N_p = 450$  and periodic cell side  $S = 20$ , as a function of the set total energy per particle,  $E$ . The line is a least squares fit to the data.

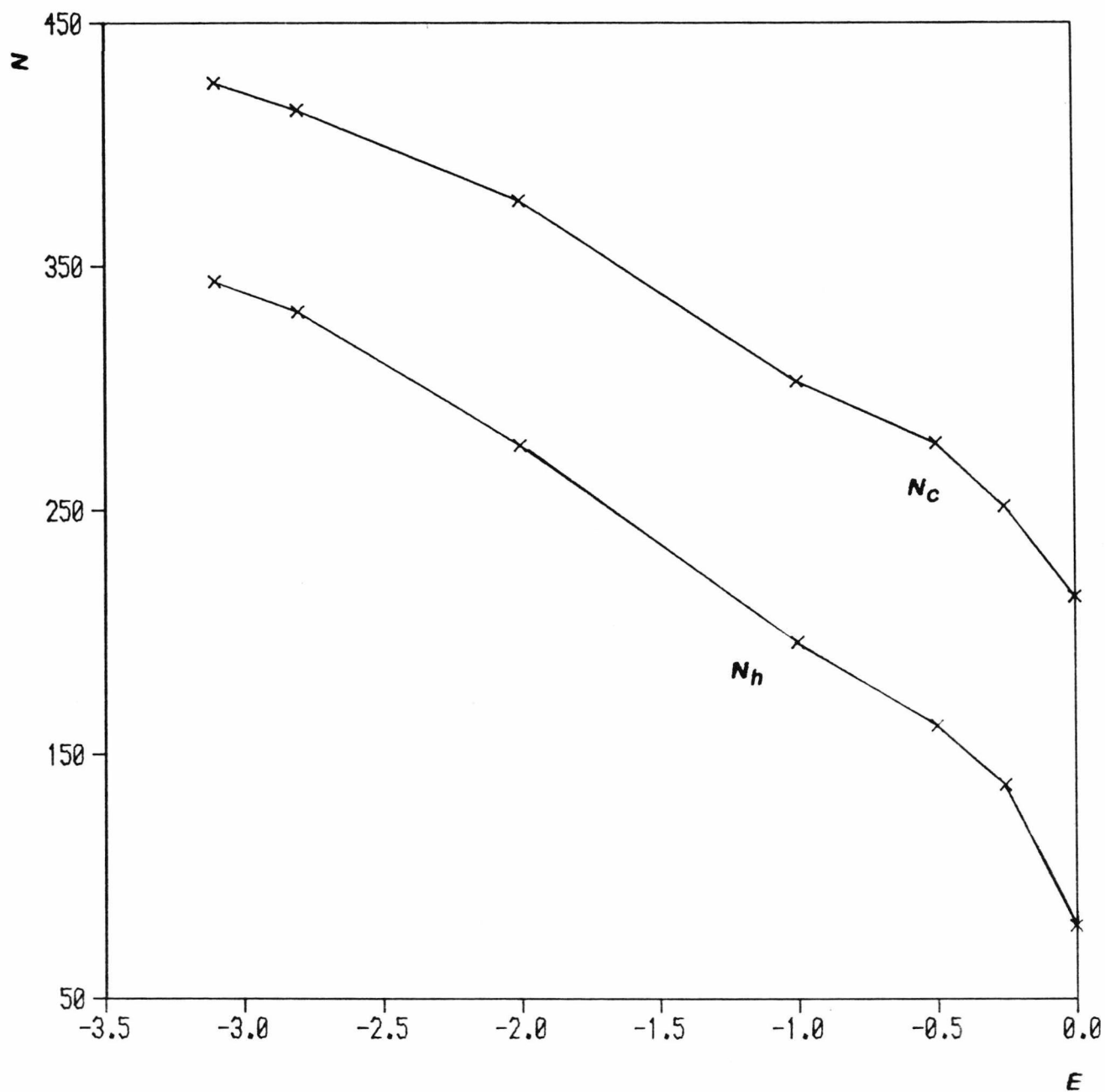


Figure 3.10: The mean number of particles within the cluster as a function of the total energy per particle of the system. The data is again for the series of LJ drops with  $N_p = 450$  and  $S = 20$ . The method used in this work to define the cluster size gives the results marked as  $N_c$ , while an alternative method (described in the text) gives the values marked as  $N_h$ .

Table 3.3a (continued)							
Run	T	$N_c$	P	$\rho_g$	$\rho_l$	$R_h$	D
(L14)	0.989	325	.039	0.0630	0.664	3.80	3.44
(L15)	0.721	422	-	0.0065	0.840	4.80	1.79
(L16)	0.811	392	-	0.0140	0.812	4.62	2.16
(L17)	0.888	329	-	0.0280	0.762	4.29	2.45
(L18)	0.676	425	.0023	0.0034	0.860	4.82	1.68
(L19)	0.706	414	-	0.0050	0.840	4.79	1.65
(L20)	0.788	377	-	0.0110	0.814	4.62	2.06
(L21)	0.856	303	-	0.0220	0.782	4.21	2.24
(L22)	0.908	278	-	0.0250	0.741	4.03	2.25
(L23)	0.949	252	.0247	0.0300	0.749	3.84	2.55
(L24)	0.900	215	.023	0.0350	0.764	3.25	3.07
(L25)	1.056	690	.042	0.0600	0.679	5.30	4.10
(L26)	0.688	1265	-	0.0028	0.856	7.02	1.74
(L27)	0.838	1162	-	0.0140	0.796	6.86	2.26
(L28)	1.033	1063	-	0.0340	0.700	6.57	3.49

Table 3.3a (Cont.): Results for LJ systems of 450 to 1300 particles. Column entries as before.

linearity occur as  $E \rightarrow 0$ , and it was generally found that clusters become unstable for  $E \approx 0$ . Systems run with  $E=0$  were found to slowly evaporate, without any sign of reaching equilibrium and the results of one such state, (L24), are included in the tables, though the values obtained are not expected to be dependable.

Fig. (3.10) shows how the cluster size,  $N_c$ , depends on  $E$  for the same series of  $N_p = 450$ ,  $S/\sigma = 20$  systems. As  $E \rightarrow 0$  it can be seen that  $N_c$  begins to decline quite rapidly as more and more particles are lost to the vapour. Also shown in the figure are

values of an alternative cluster size definition, which we call  $N_h$ . This is just the number of particles that lie within the radius  $R_h$ , and it can be seen that  $N_h$  declines faster than  $N_c$  as  $E \rightarrow 0$ . In fact both  $N_h$  and  $N_c$  are fairly arbitrary definitions, but the latter is more useful to locate the drop during computations.  $N_h$  has the advantage that it is clearly defined even when the density of surrounding vapour is approaching that of the liquid ( $T \rightarrow T_c$ ). The definition of  $N_c$  will fail in such cases, unless the nearest neighbour criteria,  $R_n$  (see chap. two), is chosen very carefully.  $N_c$  declines less rapidly than  $N_h$  because some 'vapour particles' are included in the former method. It must be said though, that the number of 'vapour' particles counted as belonging to the cluster is quite small for all our simulations (since  $\rho_l \gg \rho_g$ ) and the location of the center of the cluster is not impaired.

### 3.3.3. Properties of Stockmayer drops.

The density profiles obtained for S1 and S3 systems are very similar to the LJ ones, with the density decreasing monotonically from the liquid to the vapour. However, with similar temperature and size of cluster the Stockmayer potentials give lower  $\rho_g$  and higher  $\rho_l$  than observed with the LJ potential. This is as would be expected from the shifts in  $T_c$  and  $T_l$ .

Density profiles for a few typical S1 drops are shown in figures (3.11) - (3.14), and an S3 result is given in (3.15), along with the fitted hyperbolic tangents. The measured parameters of these states and others are listed in tables (3.3b) and (3.3c).

In addition to the average temperature of the whole system, the separate rotational ( $T_r$ ) and translational ( $T_t$ ) contributions are listed. It can be seen that the two components differ by up to 2% in some cases. This is believed to be due to the random fluctuations within the system, and it is independent of the time step used to integrate the equations of motion.

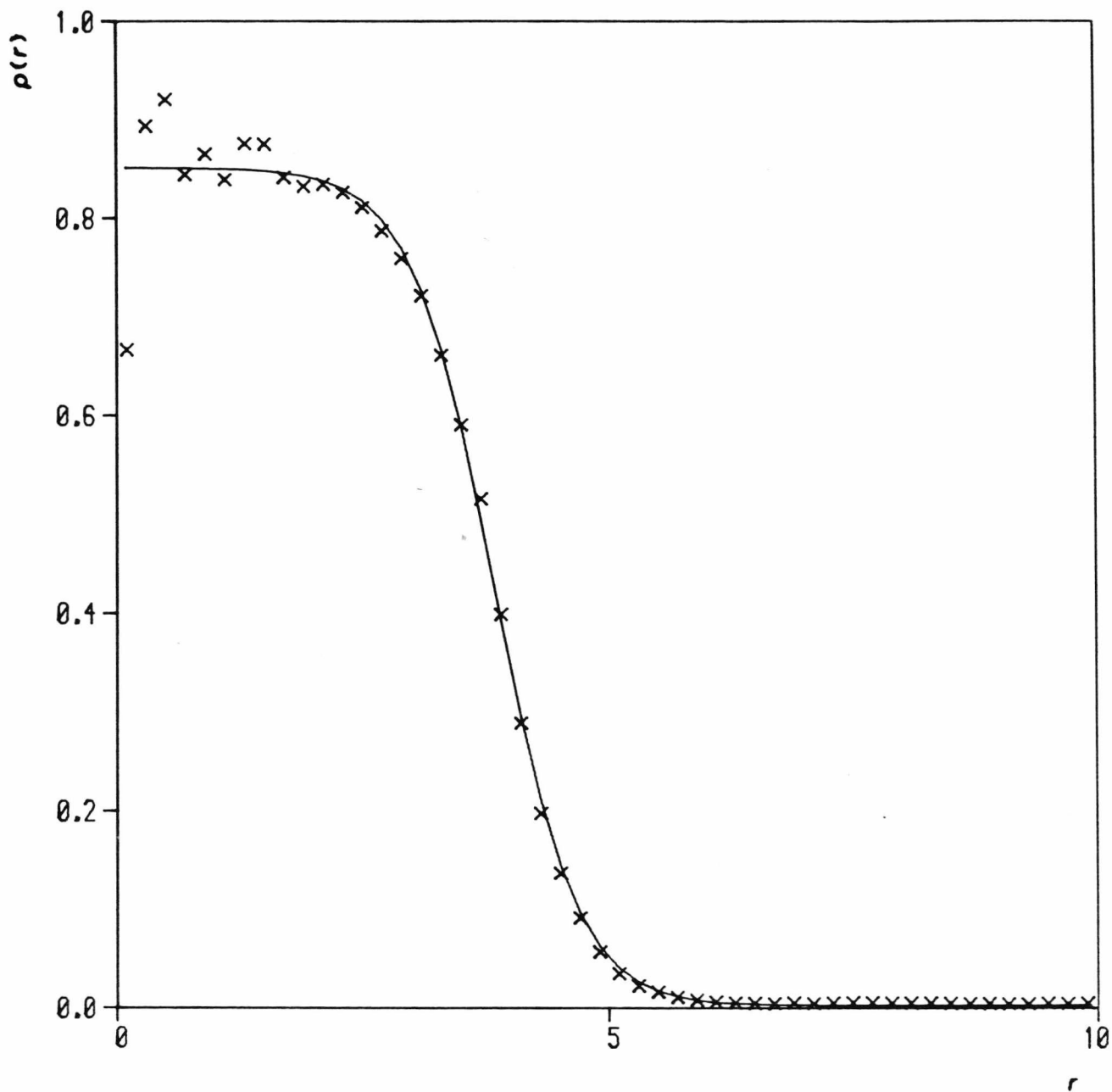


Figure 3.11: The measured density profile (x) for a Stockmayer drop. This data is for state (D1), an S1 system with  $N_p = 260$  and  $T = 0.79$ . The solid curve shows the fitted tanh profile.

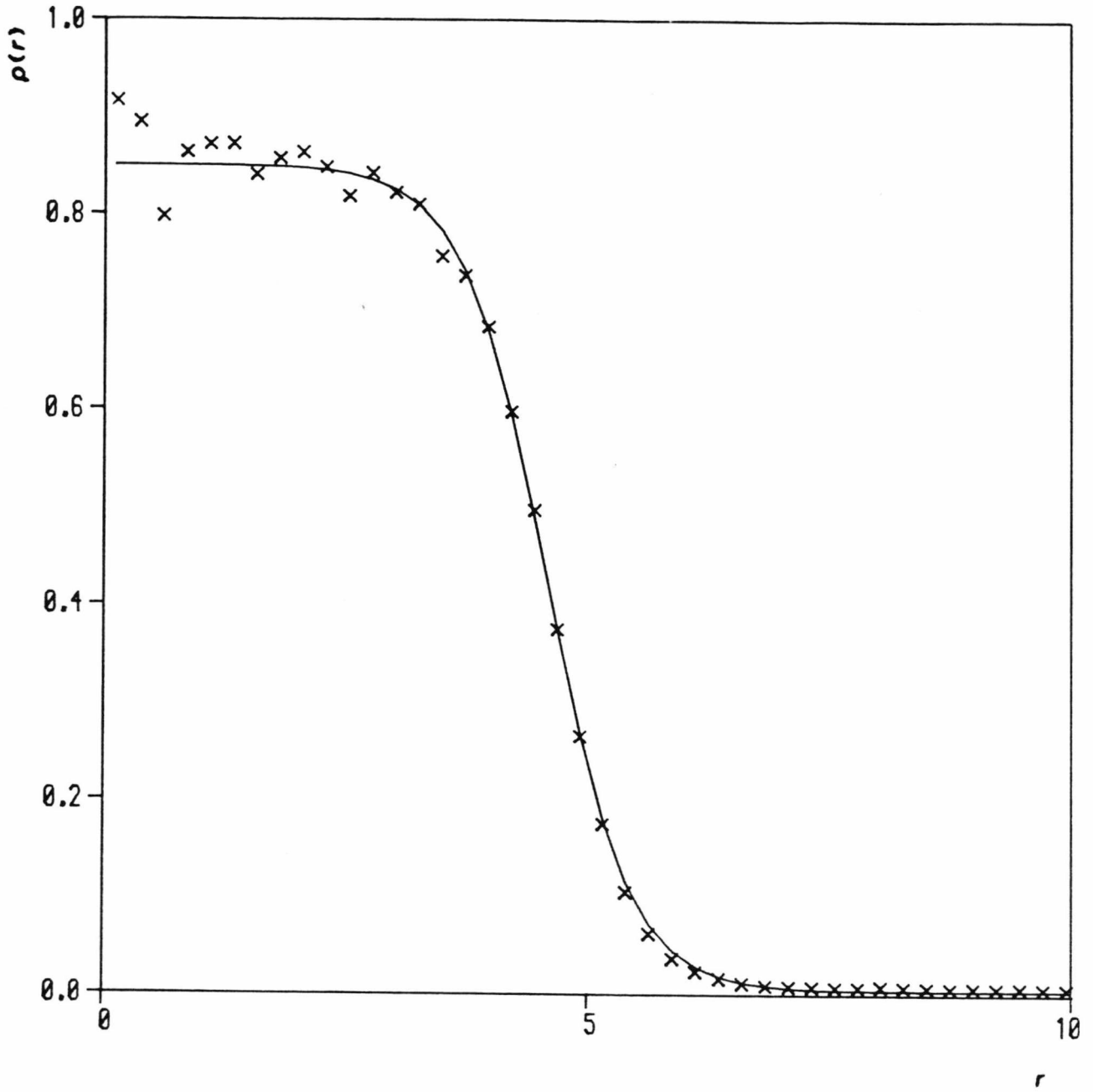


Figure 3.12: As for fig. (3.11), but for the state (D6), with  $N_p = 450$  and  $T = 0.734$ .

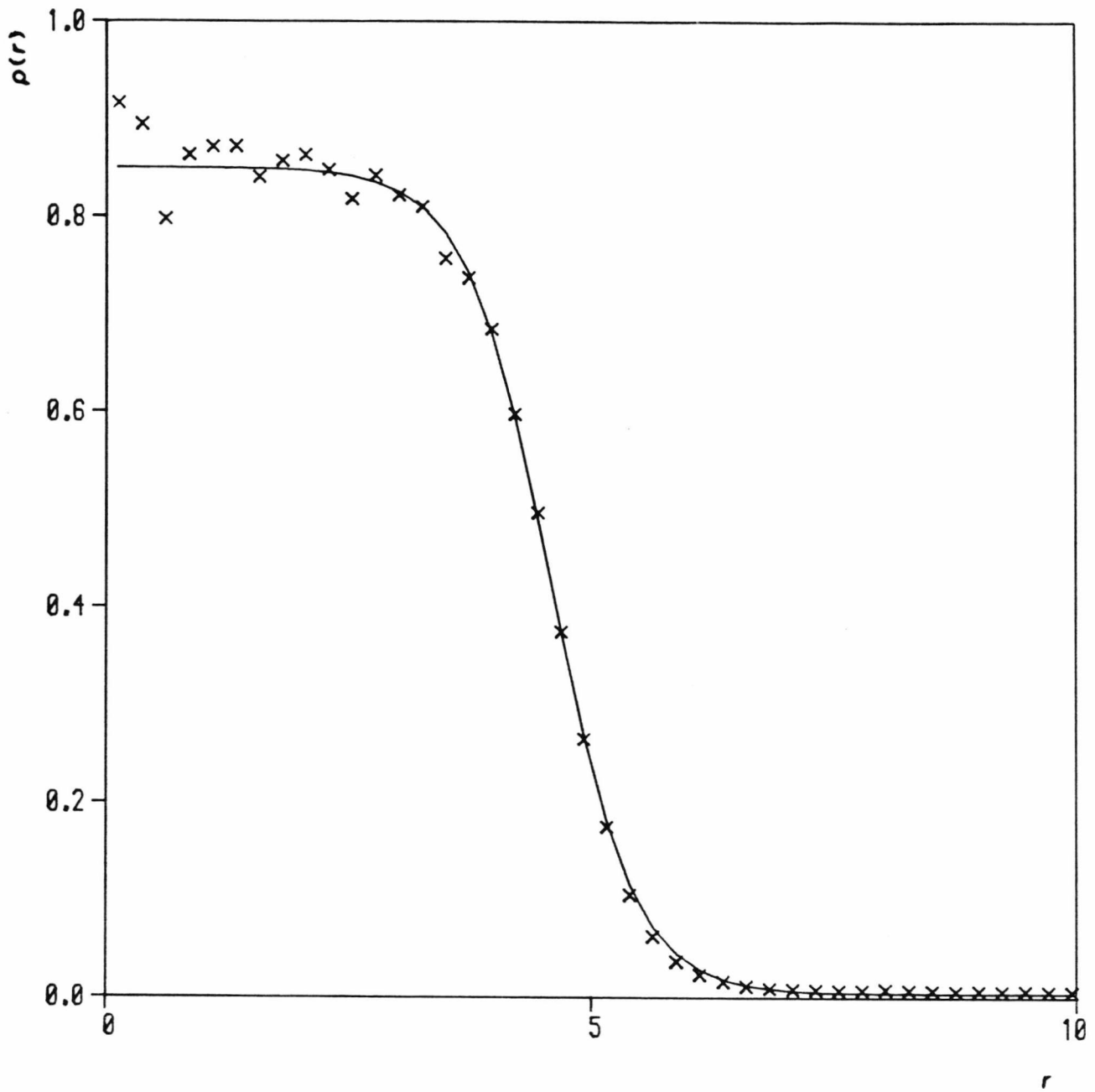


Figure 3.13: As for fig. (3.11), but for the state (D7), with  $N_p = 450$  and  $T = 0.809$ .

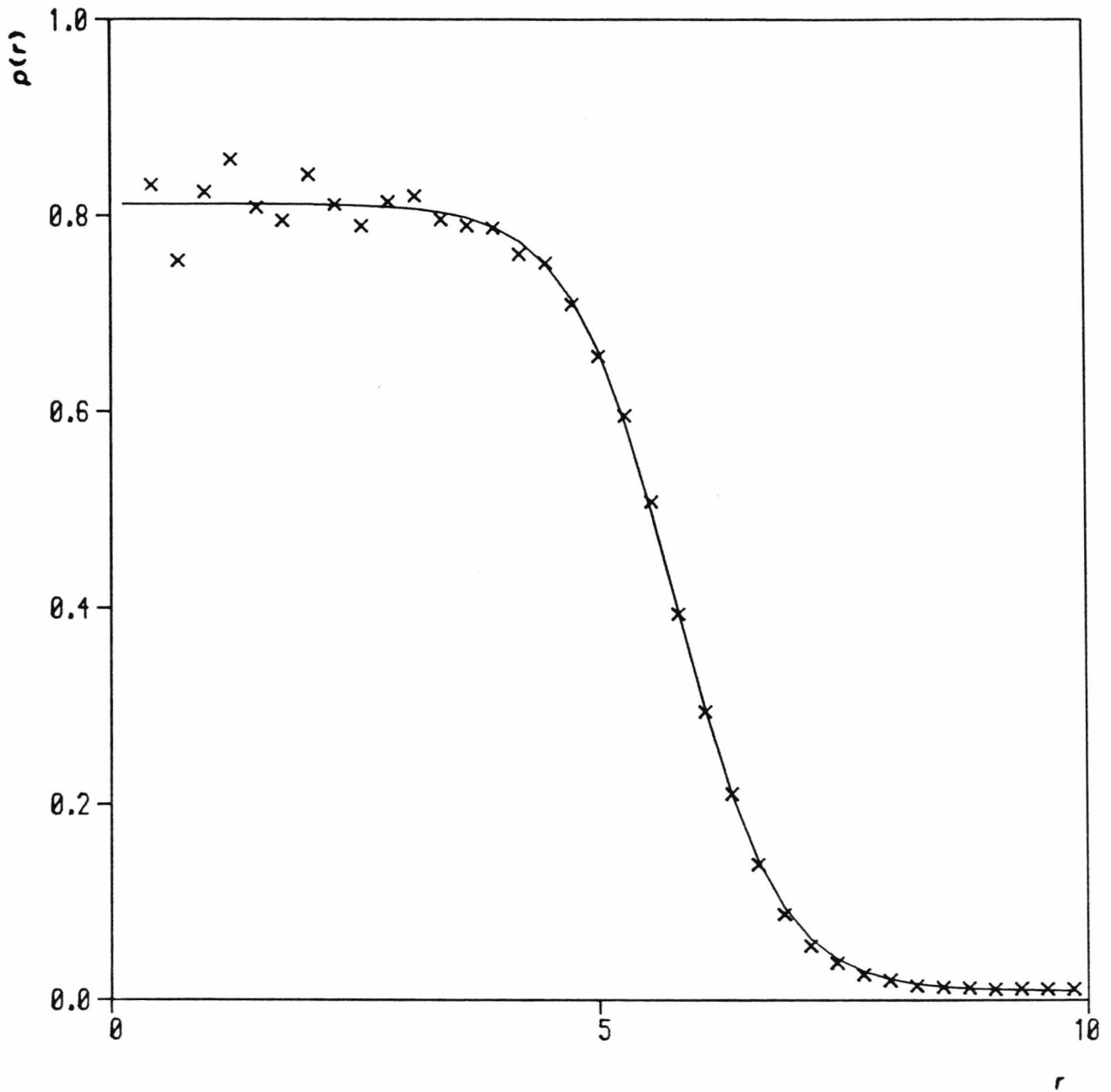


Figure 3. 14: As for fig. (3. 11) , but for the state (D12) , with  $N_p = 900$  and  $T = 0.913$ .

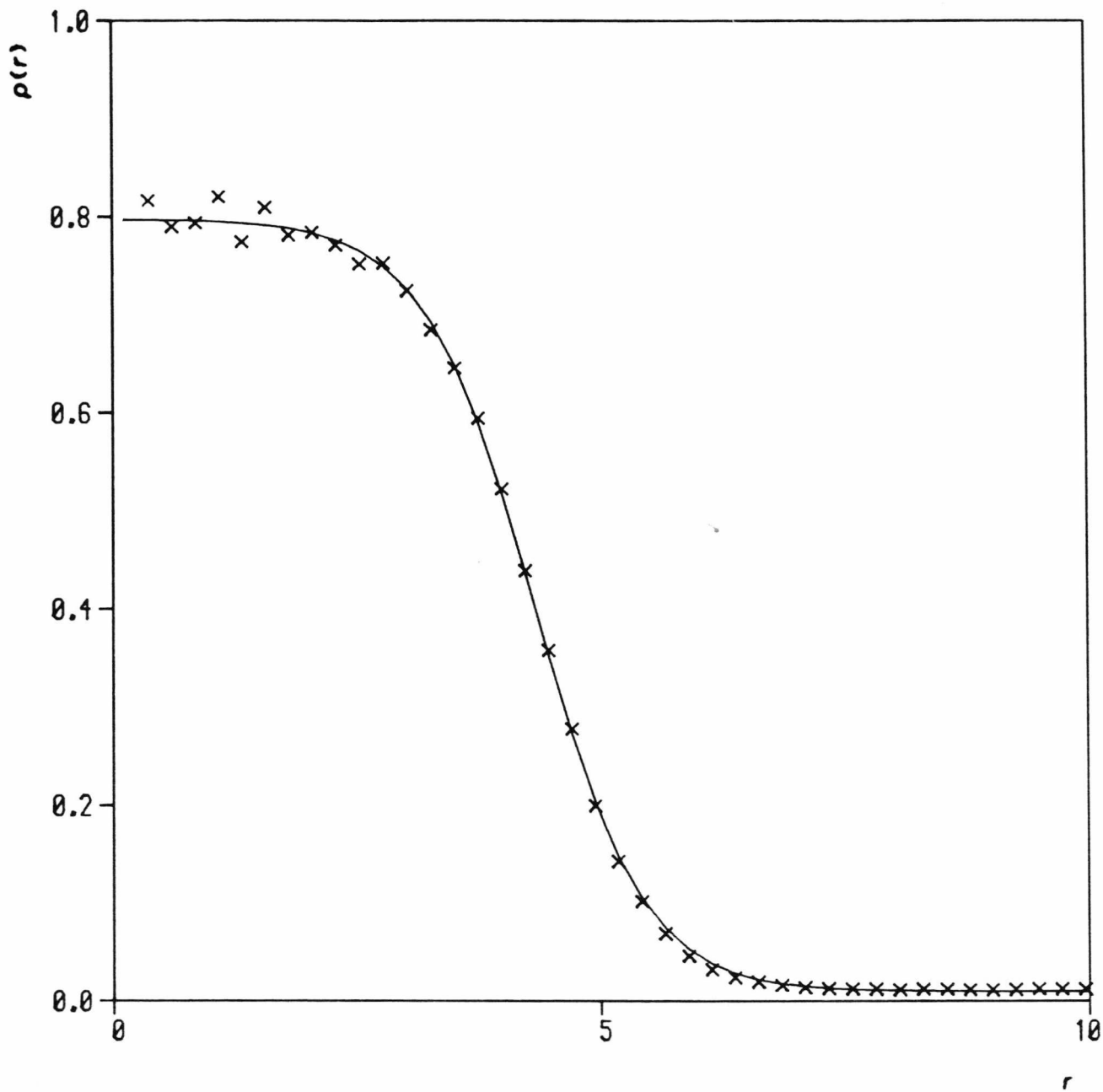


Figure 3.15: As for fig. (3.11), but for the S3 potential. This data data refers to state (D14), with  $N_p = 450$  and  $T = 1.25$ .

Run	$T$	$T_t$	$T_r$	$N_c$	$P$	$U_{LJ}$	$U_{dip}$
(D1)	0.790	0.797	0.781	223	0.0037	-0.74	-3.23
(D2)	0.839	0.836	0.842	189	0.0078	-0.57	-2.52
(D3)	0.751	0.749	0.754	210	0.0029	-0.72	-3.15
(D4)	0.835	0.825	0.850	177	0.0058	-0.57	-2.51
(D5)	0.948	0.946	0.950	366	0.0160	-0.59	-2.79
(D6)	0.734	0.729	0.742	407	0.0025	-0.88	-3.96
(D7)	0.809	0.807	0.812	367	0.0048	-0.70	-3.30
(D8)	0.869	0.876	0.858	359	0.0060	-0.65	-3.03
(D9)	0.944	0.933	0.959	288	0.0119	-0.49	-2.28
(D10)	0.744	0.740	0.749	715	0.0024	-0.88	-4.08
(D11)	0.820	0.818	0.823	872	0.0028	-0.89	-4.24
(D12)	0.913	0.906	0.925	710	0.0105	-0.65	-3.16
(D13)	1.203	1.195	1.214	348	0.0094	-2.97	-2.63
(D14)	1.251	1.252	1.249	312	0.0117	-2.54	-2.18

**Table 3.3b:** Thermodynamic results for the Stockmayer drops.  $T$ ,  $T_t$  and  $T_r$  are the mean, translational and rotational temperatures respectively.  $N_c$  is the cluster size and  $P$  is the virial pressure of the whole system.  $U_{LJ}$  and  $U_{dip}$  are the potential energy contributions due to the LJ and dipole-dipole interactions.

To observe the fluctuations in the two components of  $T$ , the subaverages of  $T_r$  and  $T_t$  can be calculated and this has been done for state (D7), see fig. (3.16). The subaverages are over intervals of 500 time steps, so there is a large amount of noise. No particular bias in the distribution of kinetic energy between modes can be observed. The statistical uncertainties in the averages are dealt with in section (3.4.1).

The tables of results also give the separate contributions to the internal energy due to dipolar ( $U_{dip}$ ) and LJ ( $U_{LJ}$ ) interactions. For the S1 potential  $U_{LJ}$  is the larger

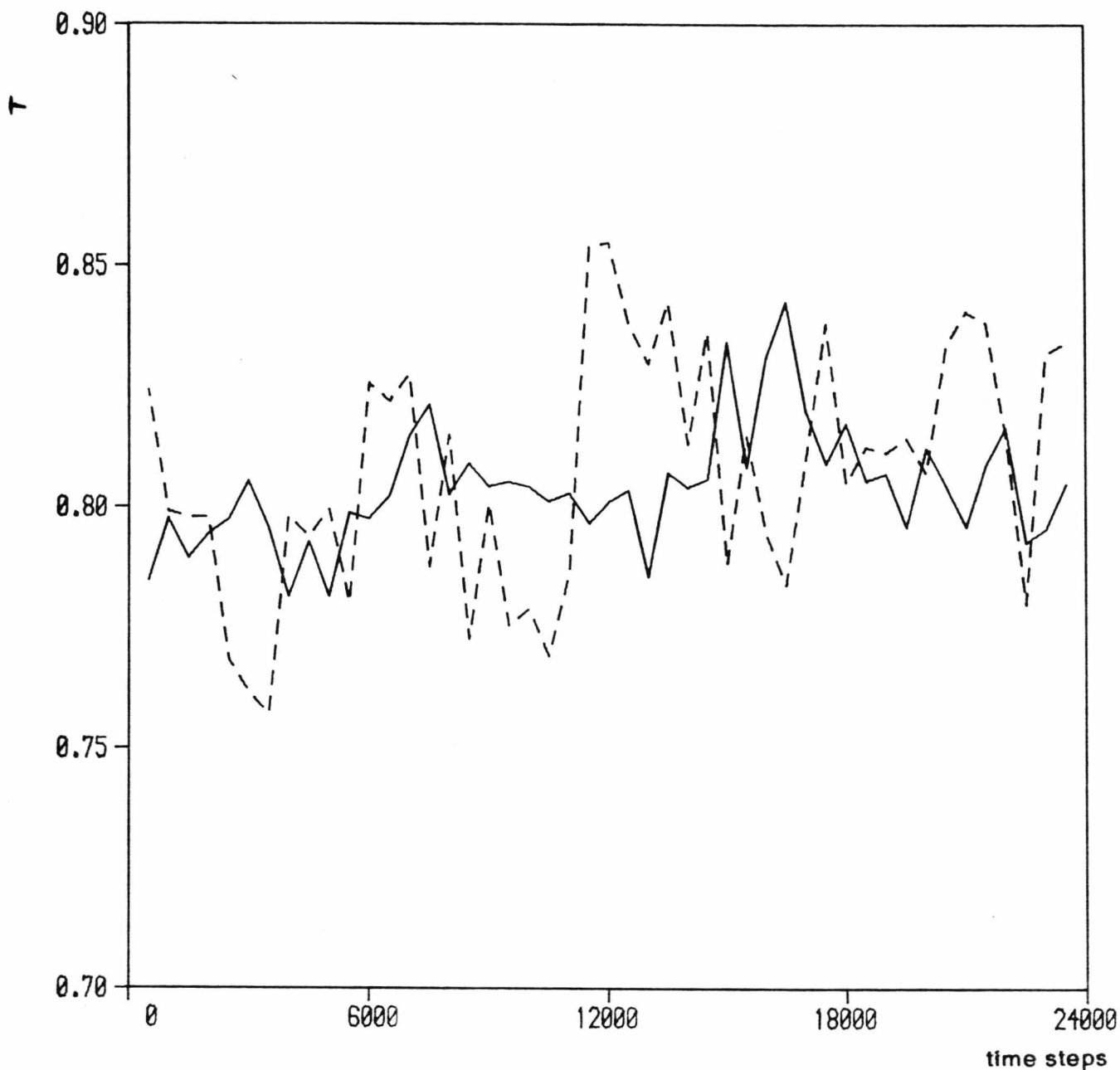


Figure 3.16: The separate rotational ( $T_{rot}$ , dashed line) and the translational ( $T_{trans}$ , solid line) temperatures, as measured for a Stockmayer drop, state (D7),  $N_p=450$  and  $T=0.81$ . The values shown are averages over periods of 500 time steps during the course of the simulation.

Table 3.3c				
Run	$\rho_g$	$\rho_l$	$R_h$	$D$
(D1)	0.0053	0.855	3.83	1.62
(D2)	0.0100	0.838	3.60	1.81
(D3)	0.0036	0.875	3.76	1.46
(D4)	0.0060	0.845	3.57	1.54
(D5)	0.0180	0.808	4.49	2.36
(D6)	0.0037	0.879	4.72	1.52
(D7)	0.0062	0.850	4.57	1.76
(D8)	0.0083	0.825	4.55	1.96
(D9)	0.0125	0.819	4.15	1.99
(D10)	0.0048	0.866	5.74	1.62
(D11)	0.0026	0.847	6.13	1.81
(D12)	0.0110	0.812	5.77	2.10
(D13)	0.0083	0.828	4.48	2.05
(D14)	0.0101	0.797	4.30	2.24

Table 3.3c: Results for the density profiles of the Stockmayer drops. Columns as in table (3.3a).

term, and  $U_{dip}$  represents only  $\sim 18\%$  of the total internal energy. A similar ratio is found in homogeneous liquid results<sup>10</sup>. For the S3 states the  $U_{dip}$  contribution accounts for  $\sim 55\%$  of the total, which underlines the fact that the S3 fluid is much more polar than the S1 fluid.

As for the LJ states, an approximately linear relationship is found between the total energy  $E$  and  $T$ , as is shown in fig. (3.17) for a series of states ( $N_p = 450$ ,  $S = 24$ ).

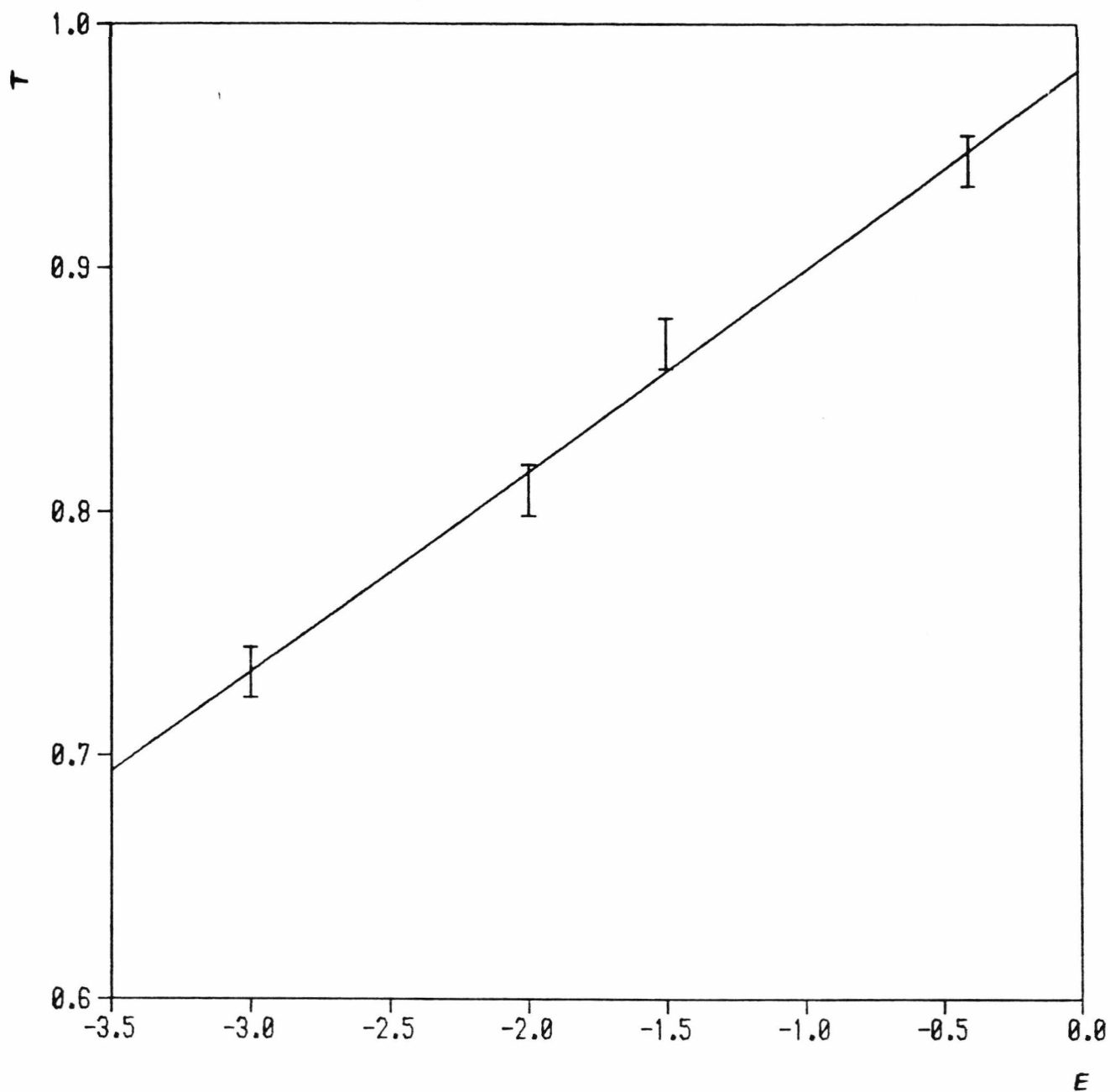


Figure 3. 17: The mean temperature of the S1 systems, with  $N_p = 450$  and  $S = 24$ , as a function of the set total energy per molecule.

### 3.4. Accuracy of results

The usual method of estimating the statistical uncertainty in computer simulations is from the inspection of subaverages calculated within a given run<sup>11</sup>. Taking the system temperature, for example, the standard deviation (s.d.) of the mean can be estimated from the equation,

$$(\Delta\bar{T}) = \left\{ \sum_{s=1}^k (T_s - \bar{T})^2 / (k(k-1)) \right\}^{1/2} \quad (3.2)$$

where  $\{T_s\}$  are the subaverages of the temperature, each measured over a fixed period of  $L_k$  steps (as in fig. (3.16), where  $L_k = 500$ ). An important condition on this is that the subaverages must be independent, i.e.  $L_k$  is large enough to ensure that there is no correlation between values of  $T_s$ <sup>12</sup>. As is indicated by figures (3.1a) and (3.1b), the fluctuations in T can occur over long periods of time due to the large cell size. To investigate the dependence of  $(\Delta\bar{T})$  on the length of subaverages, eqn. (3.2) was used with a range of  $L_k$  values. Taking, for example, data from state (D14) it was found that the s.d. of the mean increased with  $L_k$ , up until  $L_k \sim 2000$  steps. Above this  $(\Delta\bar{T})$  is insensitive to  $L_k$ , and hence  $L_k \geq 2000$  should give a fair estimate of the statistical error. For this particular run ( $N_p = 450$ , 22000 steps) it was found that  $(\Delta\bar{T}) \approx \pm 0.005$ . Similar values were found for other systems of comparable size and length of run. With  $N = 260$  the uncertainty was estimated as  $(\Delta\bar{T}) \approx \pm 0.01$ , again for a run of  $\sim 20000$  steps. For the larger systems the increased number of particles is offset by rather shorter runs, so that  $(\Delta\bar{T}) \sim \pm 0.01$  for state (D12) ( $N_p = 900$ , 11900 steps) for example.

Thus statistical fluctuations give rise to uncertainties of the order of  $\pm 0.01$  in the temperature for the longer simulations. Since the s.d. of the mean is roughly inversely proportional to the square root of the length of the run, the errors may be of the order of  $\pm 0.02$  for the temperature, when less than  $\sim 10000$  steps have been used. If the rotational and translational components of the temperature in the dipolar simulations

are assumed to fluctuate in the same way, then the uncertainty in each one will be greater than that in the mean  $T$  by factors of  $\sim 1.6$  and  $\sim 1.3$  respectively.

The above estimates are, of course, only based on the statistical fluctuations observed during the simulations. There may also be non-random sources of error. The most obvious possibility is that a system has not reached complete equilibrium in the allotted initialization time. Due to limitations in the computer time available, some of the larger drops were run for fewer steps than would have been used otherwise.

In addition to the uncertainty in the temperature of each system, all the other quantities that are obtained as time averages are subject to some statistical error. The virial pressures that are calculated in many simulations appear accurate to within  $\pm 5\%$  in longer runs, and perhaps  $\pm 10\%$  in the others.

It was noted in fitting the  $\rho(r)$  curve that the uncertainty in each value of the density profile is proportional to the square root of the number of particles counted. However, since  $\rho(r)$  is computed at each step in the simulation, the samples are not independent and we have the same difficulty in estimating  $(\Delta\bar{\rho}(r))$  as for  $(\Delta\bar{T})$ . Instead of trying to estimate the error for each value of  $\rho(r)$  it is more useful and convenient to estimate the uncertainties in the fitted parameters  $\rho_l$ ,  $\rho_g$ ,  $R_h$  and  $D$ . By observing the variations in these parameters that are obtained during the course of a run, and the quality of the fit, an idea of the reliability may be found. In very small systems at low temperatures, like state (L1) with  $N_c = 42$ , the value of  $\rho(r)$  is very poorly defined in the liquid and the error in the fitted value may be  $\pm 10\%$ . In more realistically sized systems ( $N_p \geq 260$ ), the increased liquid region allows more confidence to be placed in the fitted value of  $\rho_l$ , and the uncertainty is of the order  $\pm 1\%$  -  $\pm 2\%$ , depending on the length of run and number of particles used.

The gas density estimate obtained from the tanh fit is not reliable, for reasons that have already been elaborated, and this value was taken directly from  $\rho(r)$  at large

r. Due to the low number of particles in this region the values of  $\rho_g$  are not much better than  $\pm 10\%$  in general.

The radius of the drops,  $R_h$ , can be obtained to within  $\pm 1\%$ , since it is determined by the surface region of the drop, where the statistics are good. By contrast the surface width,  $D$ , is not so well defined. The reason for this may be that small changes in the parameter  $D$  can be partly compensated for by variations in  $\rho_l$  and  $\rho_g$  such that the tanh curve still fits the (more heavily weighted) central portion of the data quite well. The estimated uncertainty is typically  $\pm 5\%$  for values of  $D$ .

In summary, it appears that the fluctuations inherent in these inhomogeneous drop-vapour systems leads to greater uncertainties than would be found in the more usual homogeneous simulations. It would have been desirable to have made longer runs on some of our drops to improve the accuracy of the data, had the extra computer time been available.

### 3.5. Discussion

Falls *et al*<sup>13</sup> have calculated the density profile of drops of varying size by means of density gradient theory. The model used is based on the LJ fluid, but a number of approximations are made, such as replacing the 12-6 form of the potential by a Gaussian expression and using the van der Waals equation of state. This prevents any quantitative comparison being made with our simulation results. Qualitatively, their results are similar to ours, with  $\rho(r)$  profiles that appear to be of tanh form. Further comparisons of our results with this paper will be made in chapters four and five.

Several references have already been made to the simulations of Thompson *et al*<sup>1</sup> who have also studied liquid drops. Again it is not possible to directly compare our results because Thompson *et al* have used the LJ sp2.5 model, while we chose to use the virtually complete LJ potential. Nevertheless, their profile results are qualitatively similar to ours.

One way to make a more quantitative comparison between these results is to use the theory of corresponding states, whereby all quantities are reduced with respect to the critical parameters (thus we use  $\rho' = \rho/\rho_c$ ,  $T' = T/T_c$  and  $P' = P/P_c$  where  $T_c = 1.35$  for full LJ and 1.119 for sp2.5, etc.). However, if the corresponding states principle is valid, the coexistence curves of the two fluids should be very similar to each other when plotted in these units. This can be checked quite easily, using the data of Powles<sup>4</sup> and doing so reveals that the agreement is not very good, especially in the liquid region well below  $T_c$ , where the reduced densities differ by  $\sim 16\%$ .

Table (3.4) compares the data obtained for one of our simulations with that of a similarly sized state from Thompson *et al*'s paper. Both runs have the same value of  $T' = T/T_c$ , and the enclosing volumes are very nearly identical, though the shape of the containers differs. The agreement is not very good, as would be expected from the difference between the equations of state. This emphasizes the fact that using a truncated potential in an inhomogeneous system alters the state in a way that makes it very difficult, if not impossible, to 'correct' results back to those for the full potential.

Run	T	$T/T_c$	$N_c$	$R_h$	D	$\rho_l$	$\rho_g$	$\rho_l/\rho_c$	$\rho_g/\rho_c$
(L21)	.856	.634	303	4.22	2.24	.856	.022	2.45	.063
Th.	.71	.634	321	4.43	2.50	.764	.024	1.87	.059

Table 3.4: A comparison of data from state (L21) with results due to Thompson *et al* (denoted as "Th.").

We note that the addition of dipolar interactions does not change the general form of the drop profiles, though the actual densities and widths are different due to the different equations of state.

The virial pressure has also been evaluated in a number of the drops studied. The meaning of this quantity in an inhomogeneous system is far from clear. For

example, Powles *et al*<sup>14</sup> have shown that it is not possible to find the pressure within a drop by measurements of the virial for just molecules within the central (liquid) region. It is thought that the virial for the whole periodic cell, which we have measured here, may give the vapour pressure outside the drop. A simple comparison of  $\rho T$  with  $P$  (i.e. assuming perfect gas behaviour) gives a ratio that is usually within 20 or 30% of unity, though rather worse in a few cases. This is reasonable agreement, considering the uncertainty in both quantities and the fact that the perfect gas assumption is not exact. However, we shall take the measured vapour density as being the more reliable indicator of the state of the coexisting gas.

### References

1. S.M.Thompson, K.E.Gubbins, J.P.R.B.Walton, R.A.R.Chantry , J.S.Rowlinson, *J. Chem. Phys.*, vol. 81, p. 530, 1984.
2. J.J.Nicolas, K.E.Gubbins, W.B.Streett, D.J.Tildesley, *Molec. Phys.*, vol. 37, p. 1429, 1979.
3. D.J.Adams, *Molec. Phys.*, vol. 32, p. 647, 1976.
4. J.G.Powles, *Physica*, vol. 126A, p. 289, 1984.
5. L.Verlet, *Phys. Rev.*, vol. 159, p. 98, 1967.
6. J.G.Powles, R.F.Fowler, and W.A.B.Evans, *Chem. Phys. Let.*, vol. 96, p. 289, 1983.
7. D.J.McGinty, *J. Chem. Phys.*, vol. 58, p. 4733, 1972.
8. A.I.Rusanov and E.N.Brodskaya, *J. Colloid Interface Sci.*, vol. 62, p. 542, 1977.
9. G.A.Chapela, G.Saville, S.M.Thompson, J.S.Rowlinson, *J. Chem. Soc. Faraday Trans. 2*, vol. 73, p. 1133, 1977.
10. J.Yao, R.A.Greenkorn, and K.C.Chao, *J. Chem. Phys.*, vol. 76, p. 4657, 1982.

11. W.W.Wood, *Physics of simple liquids*, North-Holland, Amsterdam, 1968.  
H.N.V.Temperley, J.S.Rowlinson, G.S.Rushbrooke eds.
12. E.Friedberg and J.E.Cameron, *J. Chem. Phys.*, vol. 52, p. 6049, 1970.
13. A.H.Falls, L.E.Scriven, and H.T.Davis, *J. Chem. Phys.*, vol. 75, p. 3986, 1981.
14. J.G.Powles, G.Rickayzen, and M.L.Williams, *J. Chem. Phys.*, vol. 83, p. 293, 1985.

## Chapter Four: Surface tension in microscopic drops

### 4.1. Introduction

In this chapter we examine some of the effects of surface tension (which we denote by  $\gamma$ ) on the LJ drops that have been simulated. Due to the very small size of these systems, the surface tension might be expected to make a considerable contribution to the pressure within the drops ( $\Delta p = 2\gamma/R$ , the Laplace eq.). Other effects, particularly the enhancement of the vapour pressure predicted by the Kelvin equation, may also be present, but both these results depend on macroscopic thermodynamics and must eventually fail as the size of a drop approaches that of a single molecule. We shall compare our results with some of the predictions of the Kelvin and Laplace equations.

The thermodynamic and mechanical methods of treating surface tension are briefly discussed for planar and spherical interfaces in §4.2 and §4.3. In section 4.4 we look at methods of calculating  $\gamma$  by computer simulation, and how the excess pressure outside small drops may be useful in this respect. Finally, some observations are made on the effect of the Laplace equation on the liquid densities inside drops.

### 4.2. The thermodynamic treatment of surface tension

#### 4.2.1. The planar liquid gas interface

Surface tension is treated in many books on thermodynamics, to varying degrees. A particularly detailed and up to date review of surface phenomenon is given in a book by Rowlinson and Widom<sup>1</sup> and we have made frequent references to this work in the following discussion of surface tension.

We first consider the case of a planar liquid-gas interface of area  $A$ . The temperature, volume and total number of particles ( $T, V, n$ ) are all held constant, so we have a canonical ensemble. The change in the Helmholtz free energy of the system is

given in general by the equation,

$$dF = -SdT - PdV + \gamma dA + \mu dn \quad (4.1)$$

for a system of only one species of molecule, where  $S$  is the entropy,  $P$  the pressure and  $\mu$  the chemical potential (as  $n$  is constant for the whole system the last term is normally omitted, but it is useful to retain it here to treat the separate liquid and vapour phases later).

Hence a thermodynamic expression for the surface tension is,

$$\gamma = \left( \frac{\partial F}{\partial A} \right)_{T,V,n}, \quad (4.1')$$

the rate of change of free energy with surface area. Due to the extensive nature of  $F, V, A$  and  $n$ , we may integrate (4.1) to give,

$$F = -PV + \gamma A + n\mu \quad (4.2)$$

To allow properties of the surface to be calculated, it is usual to introduce a *Gibbs dividing surface*, which is simply any surface such that its normal (at all points) lies in the direction of  $\nabla\rho(\mathbf{r})$ . For the flat interface these are just planes of constant  $z$ , assuming that the density varies only in the  $z$  direction. The particular dividing surface chosen is quite arbitrary, since no measurable property should depend on it. It is often found to be most convenient to use the so-called equimolar dividing surface, which is located at a height  $z_e$  such that,

$$\int_{-\infty}^{z_e} [\rho_l - \rho(z)] dz = \int_{z_e}^{\infty} [\rho(z) - \rho_g] dz \quad (4.3)$$

where  $\rho_l$  and  $\rho_g$  are the limiting values of the density in the liquid and vapour regions respectively. This surface divides the system into liquid and gas regions with volumes of  $V_l$  and  $V_g$ . It is then possible to define the surface value of an extensive thermodynamic quantity as the difference between the actual value for the whole system and the total value expected for two homogeneous regions of  $(\rho_l, V_l)$  and  $(\rho_g, V_g)$ . For example, the surface number of molecules for a given dividing surface

is,

$$\begin{aligned} n_s &= n - n_l - n_g \\ &= n - \rho_l V_l - \rho_g V_g \end{aligned} \quad (4.4)$$

(=0 for the equimolar surface), and the surface free energy which is,

$$\begin{aligned} F_s &= -PV + \mu n + \gamma A - (-PV_l + \mu n_l) - (-PV_g + \mu n_g) \\ &= \gamma A + \mu n_s \end{aligned} \quad (4.5)$$

(note that this only reduces to  $F_s = \gamma A$  for the equimolar dividing surface). Thus quantities such as  $F_s$  are dependent on the dividing surface chosen, but measurable values, such as  $\gamma$ , should be invariant to this. The thermodynamic definition of  $\gamma$  avoids any consideration of the structure within the interface.

#### 4.2.2. The spherical liquid gas interface

The surface tension in a spherical interface can also be treated thermodynamically, though it turns out to be rather more complicated than the previous case. The original theory of this (as well as of the planar surface) is due to Gibbs, but with further development by other workers, most notably Tolman<sup>2</sup>.

It is convenient to consider a small section of a liquid drop in equilibrium with its vapour, as illustrated in figure (4.1). The section is defined by a solid angle,  $\Omega$ , and the two spherical surfaces at  $R_g$  and  $R_l$ . As before, we can define a series of dividing surfaces that are everywhere normal to  $\nabla\rho(r)$  (i.e. concentric spheres about the origin), and the radius of the equimolar surface,  $R_e$ , is given by,

$$\int_{R_l}^{R_e} (\rho_l - \rho(r)) dr = \int_{R_e}^{R_g} (\rho(r) - \rho_g) dr \quad (4.6)$$

Note that, unlike the planar case, an antisymmetric profile for  $\rho(r)$  does not have  $R_e = R_h$ , where  $R_h$  is the radius such that  $\rho(R_h) = (\rho_l + \rho_g)/2$ . It is also assumed that  $R_l$  and  $R_g$  are far enough from the interface that  $\rho(R_g) = \rho_g$  and  $\rho(R_l) = \rho_l$ .

The general form for the change in free energy of this system is,

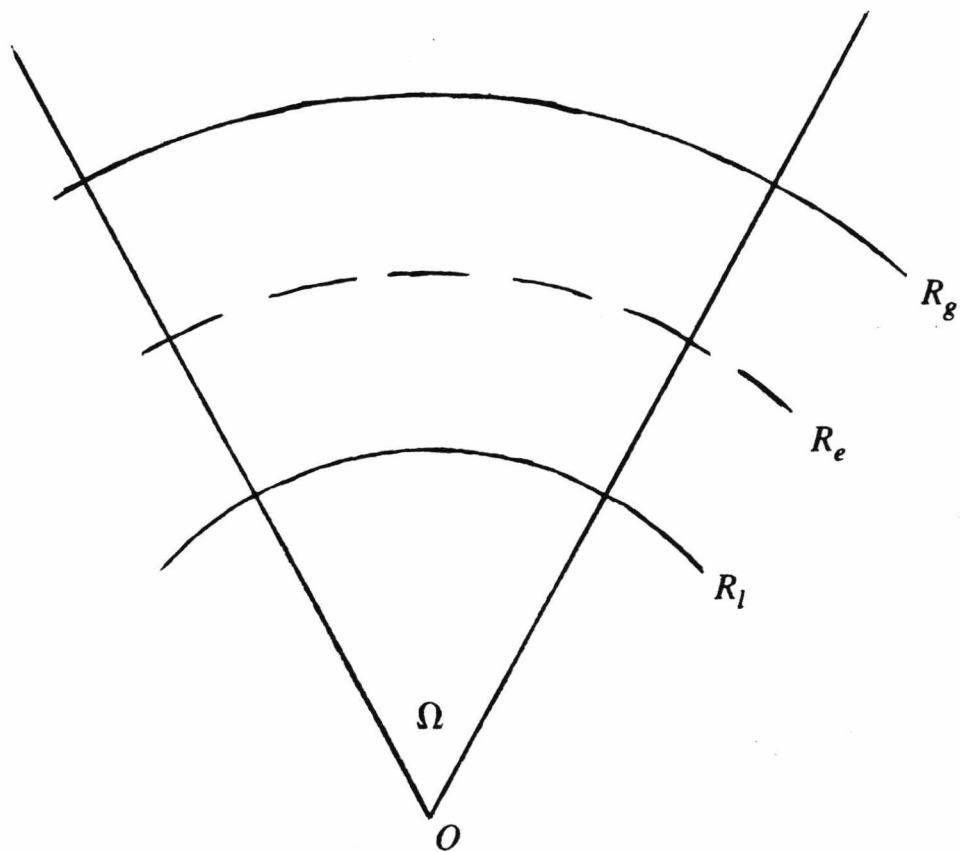


Figure 4.1: Diagram of a spherical interface. The centre of the drop is located at 'O' and the equimolar surface is at  $R_e$ . The subsystem defined by the solid angle  $\Omega$  and the surfaces  $R_g$  and  $R_l$  is considered in the text.

$$dF = -S dT - P_l dV_l - P_g dV_g + \gamma dA + C dR + \mu dn \quad , \quad (4.7)$$

where this equation is taken as the definition of the surface tension,  $\gamma$ , and of the curvature dependence, given by the term  $C dR$ .

The total free energy of the system must be invariant to the choice of dividing surface so that, on changing this from  $R$  to  $R + dR$ , we require that,

$$\begin{aligned} dF &= -(P_l - P_g) dV_l + \gamma dA + C dR \\ &= -(P_l - P_g) \Omega R^2 dR + \gamma 2\Omega R dR + C dR = 0 \end{aligned} \quad (4.8)$$

Keeping  $R$  and  $T$  fixed, the first of these equations can be integrated with respect to  $\Omega$  to give the expression for the free energy,

$$F = -P_l V_l - P_g V_g + \gamma A + \mu n \quad (4.9)$$

If the condition that this free energy should be invariant to the choice of  $R$  is then used, as in ref. [3], it can be shown that the curvature term is given by  $C = A d\gamma/dR$ .

Using this in (4.8) gives the result that,

$$\Delta P \equiv P_l - P_g = \frac{2\gamma}{R} + \frac{d\gamma}{dR} \quad (4.10)$$

Hence the surface tension is, in general, dependent on the dividing surface at which it is measured. In the limit of large drops, where the surface width and curvature effects may be neglected, we obtain the well known Laplace equation,

$$\Delta P = \frac{2\gamma}{R} \quad (4.11)$$

For any drop we can define a dividing surface of radius  $R = R_s$ , such that,

$$\left. \frac{d\gamma}{dR} \right|_{R=R_s} = 0 \quad ,$$

and this is referred to as the *surface of tension*. Thus, Laplace's equation holds exactly for this choice of dividing surface,

$$\Delta P = \frac{2\gamma[R_s]}{R_s} \quad (4.12)$$

It is possible to integrate equation (4.10) by putting it in the form,

$$\frac{d}{dR} (R^2 \gamma[R]) = R^2 \Delta P \quad (4.13)$$

to give variation of  $\gamma$  with the choice of dividing surface as

$$\frac{\gamma[R]}{\gamma[R_s]} = 1 + \left( \frac{R - R_s}{R} \right)^2 \left( \frac{R_s + 2R}{3R_s} \right) \quad (4.14)$$

It is thought that the fact that the surface tension is not invariant to the choice of dividing surface implies that  $\gamma$  is not physically meaningful in very small drops<sup>1</sup>.

We now consider the dependence of  $\gamma$  ( $= \gamma[R_s]$ ) on the drop size, i.e. how the surface tension varies with  $R_s$ . The equimolar surface and the surface of tension are not in general equal even in the case of a planar interface. The difference between these two surfaces is important in Tolman's treatment of the curvature dependence of surface tension. This separation is denoted by  $\delta$ ,

$$\begin{aligned} \delta &= R_e - R_s \\ &= z_e - z_s \quad (\text{as } R \rightarrow \infty) \end{aligned} \quad (4.15)$$

Tolman<sup>2</sup> has shown that the surface tension in a drop ( $\gamma_R = \gamma[R_s]$ ) is related to the planar value ( $\gamma_\infty$ ) by the equation,

$$\frac{\gamma_R}{\gamma_\infty} = 1 - \frac{2\delta}{R_s} + \dots, \quad (4.16)$$

to first order in  $(\delta/R_s)$ . To this accuracy we may take  $\delta = R_e - R_s \approx z_e - z_s$ . Tolman was able to calculate the higher order terms in (4.16), but it is thought that these are not useful, due to the ambiguity in  $\gamma_R$  at small  $R$  mentioned above<sup>1,3</sup>.

While the Laplace equation gives the difference in pressure between the liquid and vapour phases of a drop, the actual vapour pressure outside the drop also differs from the coexistence value that is found for the planar case. The relationship between the drop vapour pressure,  $P_g(R)$ , and the planar value,  $P_g(\infty)$ , is usually known as the Kelvin equation. This equation may be derived (again, after Rowlinson and Widom) as follows: Since the chemical potential is the same in both phases for the drop and for the planar interface, we have  $\mu_l(R) = \mu_g(R)$  and  $\mu_g(\infty) = \mu_l(\infty)$  so that,

$$\mu_g(R) - \mu_g(\infty) = \mu_l(R) - \mu_l(\infty) \quad (4.17)$$

This may be rewritten as,

$$\int_{\mu_g(\infty)}^{\mu_g(R)} d\mu = \int_{\mu_l(\infty)}^{\mu_l(R)} d\mu \quad (4.18)$$

and since  $dP = \rho d\mu + \frac{\sigma}{A} dT = \rho d\mu$ , at constant  $T$ ,

$$\int_{P_g(\infty)}^{P_g(R)} \frac{dP}{\rho_g(P)} = \int_{P_l(\infty)}^{P_l(R)} \frac{dP}{\rho_l(P)} \quad (4.19)$$

To obtain the usual form of the Kelvin equation it is necessary to make three approximations, as follows:

(i) The liquid phase is effectively incompressible, so that the RHS of (4.19) becomes,

$$\begin{aligned} \int_{P_l(\infty)}^{P_l(R)} \frac{dP}{\rho_l(P)} &= \frac{1}{\rho_l} \int dP = \frac{1}{\rho_l} (P_l(R) - P_l(\infty)) \\ &= \frac{1}{\rho_l} \left( P_g(R) + \frac{2\gamma}{R} - P_g(\infty) \right), \end{aligned} \quad (4.20)$$

using the Laplace equation.

(ii) The vapour is assumed to behave as a perfect gas, so that  $P = \rho kT$ , and the LHS of (4.19) becomes,

$$\int_{P_g(\infty)}^{P_g(R)} \frac{dP}{\rho_g(P)} = kT \int \frac{dP}{P} = kT \ln \left( \frac{P_g(R)}{P_g(\infty)} \right) \quad (4.21)$$

(iii) If  $\frac{2\gamma}{R} \gg P_g(R) - P_g(\infty)$  then (4.20) and (4.21) may be combined to give the Kelvin formula,

$$\frac{P_g(R)}{P_g(\infty)} = \exp \left( \frac{2\gamma}{R \rho_l kT} \right) \quad (4.22)$$

Since  $\gamma$  only varies slowly with  $R$ , at least for  $R \gg \delta$ , the equilibrium vapour pressure outside a drop increases as the size is reduced (this makes small drops unstable w.r.t. larger ones in a condensing vapour).

The excess vapour pressure outside some of the drops simulated in this work will be used to obtain an estimate of  $\gamma$ , using the Kelvin equation. The effects of the above approximations are discussed later. Before this method is employed, we shall

briefly review the mechanical definition of surface tension, and the other methods by which  $\gamma$  may be obtained in a simulation.

### 4.3. The mechanical definition of surface tension

#### 4.3.1. The planar interface

The thermodynamic treatment of  $\gamma$  can be made without having to define the “local” values of the pressure, temperature or chemical potential within the surface region. The mechanical definition of  $\gamma$  on the other hand requires knowledge of the pressure through the surface. For the planar case, the pressure is a tensor of the form,

$$P(z) = P_N(z)\hat{k}\hat{k} + P_T(z)(\hat{i}\hat{i} + \hat{j}\hat{j}) \quad (4.23)$$

where  $P_T(z)$  and  $P_N(z)$  are the tangential and normal components of the pressure, assuming an interface in the  $x-y$  plane. The mechanical condition for equilibrium, that  $\nabla \cdot P = 0$ , leads to the result that  $P_N$  is constant, and hence equal to the bulk pressure,  $P$ .

By considering the work done at constant  $T$  and  $V$ , when the surface area is increased by  $dA$ , the surface tension can be written as,

$$\gamma = \int_{-\infty}^{\infty} (P - P_T(z)) dz \quad (4.24)$$

The surface of tension,  $z_s$ , can then be defined by,

$$z_s = \int_{-\infty}^{\infty} z (P - P_T(z)) dz \quad (4.25)$$

Thus  $\gamma$  and  $z_s$  can be obtained if  $P_T(z)$  is known. Unfortunately it is found that  $P_T$  is not uniquely defined within the surface<sup>4,5</sup>. This occurs because the non-kinetic part of the stress on a given surface arises from the forces that act between the particles on opposite sides. The ambiguity is in deciding on the path along which the force acts. The two most common definitions for the pressure tensor are the Irving-Kirkwood<sup>6</sup> and the Kirkwood-Buff/Harasima<sup>7</sup> formulas, which have been shown to give measurably

different results for  $P_T$  in the planar interface<sup>8</sup>.

It is found that, though  $P_T$  is not unique, the value of  $\gamma$  given by (4.24) is invariant to the choice of pressure tensor. However, the surface of tension, given by (4.25), is not invariant to this, so that it can not be precisely defined by mechanical arguments, even in the planar case.

#### 4.3.2. The spherical interface

For a spherical drop in equilibrium with its vapour the pressure tensor within the surface is of the form,

$$P(r) = P_N(r)\hat{e}_r\hat{e}_r + P_T(r)(\hat{e}_\theta\hat{e}_\theta + \hat{e}_\phi\hat{e}_\phi) \quad (4.26)$$

The condition that  $\nabla \cdot P = 0$  now leads to a set of differential equations relating  $P_T$  and  $P_N$ , and both of these components vary through the interface. To calculate  $\gamma$  it is again necessary to define a dividing surface and the surface of tension,  $R_s$ , is the usual choice. Considering the forces across a strip of width  $d\theta$  leads to,

$$\begin{aligned} \gamma_s R_s d\theta &= d\theta \left( \int_{R_l}^{R_s} r dr P_l + \int_{R_s}^{R_g} r dr P_g - \int_{R_l}^{R_g} r dVP_T(r) \right) \\ \gamma_s R_s &= \int_{R_l}^{R_g} r dr \left[ P_{l,g}(r; R_s) - P_T(r) \right] \end{aligned} \quad (4.27)$$

where  $P_{l,g}(r; R_s) = P_l$  if  $r < R_s$  and  $P_g$  otherwise and  $\gamma_s = \gamma[R_s]$ .

Using the condition that  $\nabla \cdot P = 0$  allows several different versions of the equation for  $\gamma_s$  to be obtained, such as that due to Buff<sup>9</sup>,

$$\gamma_s = \int_{R_l}^{R_g} \left( \frac{r}{R_s} \right) dr \left[ P_N(r) - P_T(r) \right] \quad (4.28)$$

It is found that  $R_s$  depends on the choice of the pressure tensor, as it does for a plane surface. However, the expressions for  $\gamma_s$  are not now invariant to the choice of  $P$ , so that there is no unique mechanical definition for the surface tension of a drop.

#### 4.4. Calculation of $\gamma$ by computer simulation

##### 4.4.1. Calculations for the plane surface

The surface tension in the planar liquid-gas interface has been evaluated by a number of techniques, both in MC and MD simulations. Most of this work has been based on the LJ12-6 potential. A few of these methods, and the results, are discussed here.

The direct simulations of the planar interface have already been mentioned in chapter two. The most convenient method of calculating  $\gamma$  in such a system is from the expression,

$$\gamma = \frac{1}{4} \int_{-\infty}^{\infty} dz_1 \int d\mathbf{r}_{12} \left( r_{12} - \frac{3z_1^2}{r_{12}} \right) \phi'(r_{12}) \rho^{(2)}(\mathbf{r}_1, \mathbf{r}_2) \quad (4.29)$$

where  $\rho^{(2)}(\mathbf{r}_1, \mathbf{r}_2)$  is the pair density distribution function and  $\phi'$  is the derivative of the interaction potential (this expression may be obtained starting from either the thermodynamic or pressure tensor forms of  $\gamma$ , with the use of some statistical mechanics<sup>1</sup>).

In terms of a simulation average, this is evaluated as,

$$\gamma = \frac{1}{A} \left\langle \sum_{i>j} (r_{ij} - 3z_{ij}^2/r_{ij}) \phi'(r_{ij}) \right\rangle \quad (4.30)$$

and this has been used several workers<sup>10,11</sup>.

An alternative is to actually evaluate the tangential pressure,  $P_T(z)$ , through the surface, and then to use equation (4.24). Such a calculation is much more time-consuming than use of (4.30), and the result for  $P_T$  is dependent on the definition used for the pressure tensor. Rao and Berne<sup>12</sup>, for example, have performed MC simulations in which  $P_T$  and  $P_N$  are obtained for a 2048 particle planar system (sp2.5 interaction). A total of over 3 million moves were made, which is only about 1400 per particle. Their results for these components are quite ragged, and it appears to be very expensive to find the pressure tensor accurately. In addition to finding  $\gamma$  it is also

possible to calculate the location of the surface of tension, using (4.25), though this is not uniquely defined. The Harasima form of  $P$  was used in this case. While the surface tension result of  $\gamma = 0.42$  at  $T = 0.92$  is invariant to the form of  $P$ , it is not expected to be highly accurate.

Chapela *et al*<sup>11</sup> use equation (4.30) to calculate  $\gamma$  for a range of states using MD and MC for the sp2.5 fluid with planar systems of 255 to 4048 particles. In addition, correction terms are derived so that the surface tension for the complete LJ potential can be obtained. This process is rather suspect though, since the use of the sp2.5 potential gives different coexisting densities and surface widths to those of the full potential, and the coexistence curves can not be simply scaled onto each other, as was noted in chapter three. This was one of the main reasons for our decision to use the virtually full LJ interaction in our simulations. The accuracy of the values of  $\gamma$  obtained in this way for the full potential is estimated as  $\pm 10\%$ , or worse.

Possibly the most accurate simulation results for  $\gamma$  are those due to Miyazaki *et al*<sup>13</sup>. They use MC with the full LJ potential to calculate the total change in free energy of a homogeneous liquid that is cut in two. This forms two surfaces which are allowed to relax to equilibrium. The surface tension is then given from equation (4.1'). In this method an estimated accuracy of  $\sim \pm 2\%$  is achieved.

#### 4.4.2. Calculating $\gamma$ in liquid drops

It has been seen that the definitions of surface tension in a spherical system are more complex than for the planar case, and it appears that there is no direct analogue of equation (4.30) for curved interfaces. The alternative method of direct evaluation of the pressure tensor during the simulation can, however, still be employed. We made investigations of this possibility, using the Irving-Kirkwood definition to find  $P_N(r)$  through the surface. This calculation is very time consuming as it necessary to resolve all the force components acting across each shell at which  $P_N(r)$  is required ( $P_T(r)$  can be obtained by differentiation of this result, since the condition that

$\nabla \cdot \mathbf{P} = 0$  leads to  $P_T(r) = P_N(r) + (r/2)(dP_N(r)/dr)$ . The very long cut-off that we use with the LJ potential makes this much slower than, for example, if the sp2.5 model had been used.

The results obtained were not very encouraging, particularly for the pressure towards the centre of the drop, where the shell areas become very small, due to poor statistics. Because of the very long and time consuming runs that would be necessary, and since other workers<sup>14</sup> were already exploring the possibility of calculating  $P$ , we chose instead to investigate the use of the Kelvin equation to measure  $\gamma$ . The expression in equation (4.22) can be written as,

$$\ln \left( \frac{P_g(R)}{P_g(\infty)} \right) = \frac{2\gamma}{R \rho_l T} , \quad (4.31)$$

since  $k = 1$  in our reduced units. If  $\gamma$  is assumed to be independent of drop size, then at fixed temperature, a plot of  $\ln P_g(R)$  against  $R^{-1}$  should give a straight line, the gradient of which would allow the determination of  $\gamma$ . This, of course, ignores the variation of  $\gamma$  with  $R$ , predicted by equation (4.16), and the approximations in the derivation of the Kelvin equation. The importance of these effects can also be investigated.

The only remaining problem with using the Kelvin equation in this way, is what value to use for the drop radius,  $R$ , in (4.31). From the derivation, it appears that the appropriate value is  $R_s$ , the radius of the surface of tension. However the calculation of this quantity is not easy, and to do so from the mechanical definition would require  $P$ , which is unknown in our simulations. Instead, the equimolar radius  $R_e$  will be used, which is a quantity that may easily be obtained from the simulations. This is equivalent to assuming  $\delta = 0$  ( $\delta$  is dependent on the choice of pressure tensor anyway, at least from mechanical definitions).

Figure (4.2) shows a graph a graph of  $\ln[P_g(R_e)]$  against  $R_e^{-1}$  for a series of states at  $T = 0.69$ . This temperature is very close to the triple point and the assumptions of

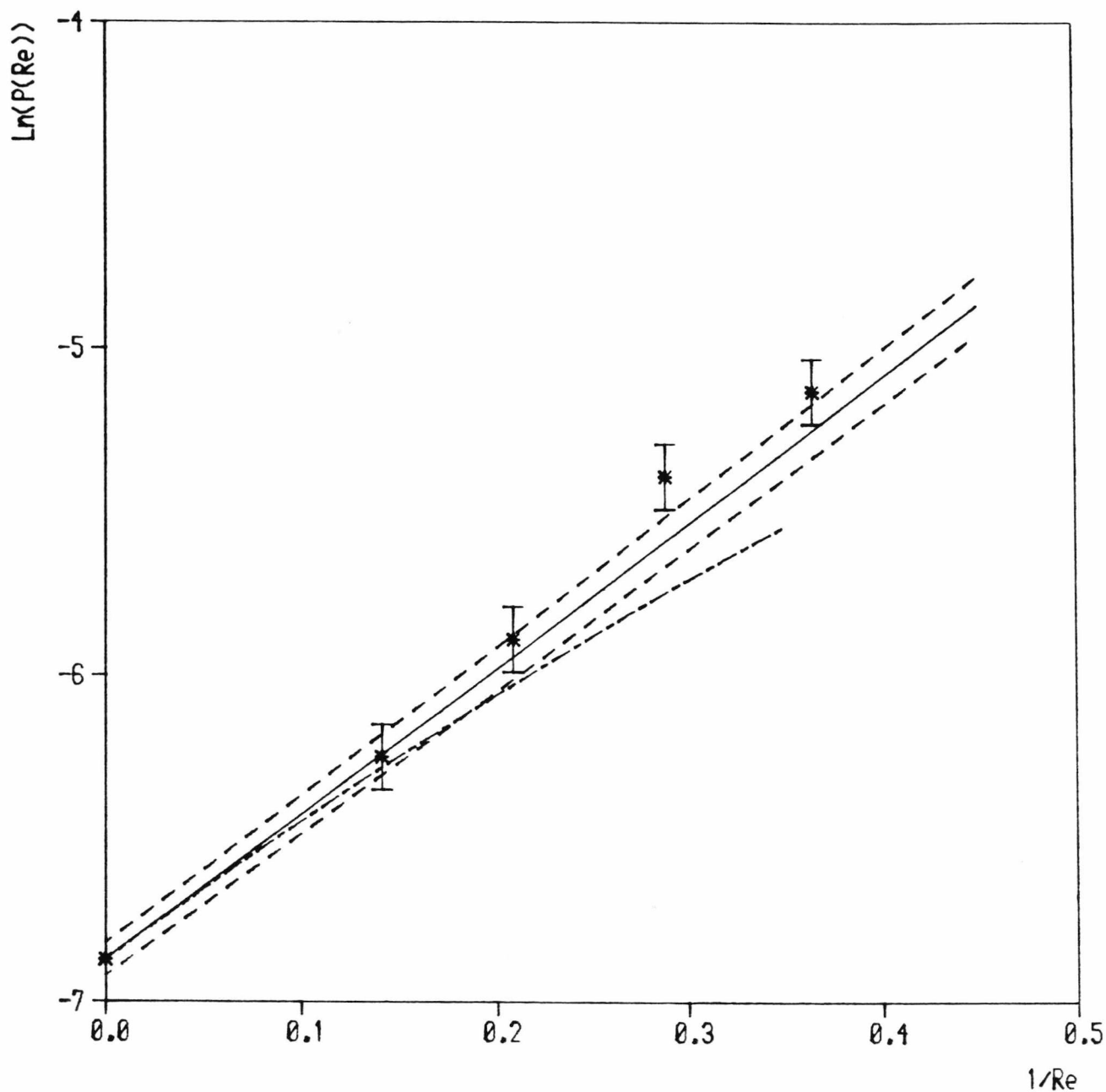


Figure 4.2: Logarithm of the reduced vapour pressure against  $R_c^{-1}$ , the reciprocal of the drop equimolar radius, at  $T = 0.69$ . The points, from right to left, correspond to systems of 100, 260, 450 and 1300 LJ particles. The latter is state (L26), while some interpolation has been used for the other results. The solid line corresponds to the Kelvin equation with the planar value of  $\gamma$ , and the two dashed lines estimate the possible variation due to the uncertainty in  $T$ , etc. Assuming  $\delta = 0.5$  in Tolman's equation gives the curvature shown by the chained line.

the Kelvin equation (incompressibility, “perfect gas” vapour and  $2\gamma/R \gg P_g(R) - P_g(\infty)$ ) are expected to be more accurate here than at higher temperatures.

The straight line shows the result that is predicted by the Kelvin equation. The  $R_e^{-1} = 0$  intercept is the coexistence pressure for the planar fluid that is given by Powles<sup>15</sup> (from the Nicholas equation of state). This gives  $P_g(\infty) = 0.00105 \pm .00005$  at this temperature. The gradient is given by  $2\gamma/\rho_l T \approx 4.47$ , where the value of  $\gamma = 1.31 (\pm 0.02)$  has been obtained from the data of Miyazaki *et al*<sup>13</sup> for the planar surface, and  $\rho_l = 0.85$  at  $T = 0.69$ .

Due to the uncertainty in the temperature of the simulations, and also in the values of  $\gamma$ ,  $P_g(\infty)$  and  $\rho_l$ , two other lines have been marked around the Kelvin result, as an indication of the possible error. The four data points shown correspond to systems of the following sizes; (i)  $N_p = 1300$  (run L26), (ii)  $N_p = 450$  (runs L18/L19), (iii)  $N_p = 260$  (L7) and (iv)  $N_p = 100$  (L2/L3). It is difficult to achieve a given temperature in constant energy molecular dynamics, so some interpolation of the data was necessary in cases (ii) and (iv).

The agreement of the simulation data with the Kelvin line is very good for the largest drop, (i). In fact this must be fortuitously so, considering the uncertainty in the measured vapour density. For drops with fewer particles the vapour pressure tends to rise faster than that predicted by the Kelvin equation, until we get to the 100 particle systems. Clearly,  $P_g(R_e)$  cannot increase indefinitely as  $R_e \rightarrow 0$ , and there must be some critical size at which  $P_g$  reaches a maximum. The 100 particle systems may be close to this point.

In figure (4.3) a similar analysis has been performed for systems with a temperatures of  $T \approx 0.84$ , but only for sizes of  $N_p = 1300$  and  $N_p = 450$ . In this case the divergence from the Kelvin result is much more marked, even for the 1300 particle system. The planar value for the surface tension that has been used in this case is

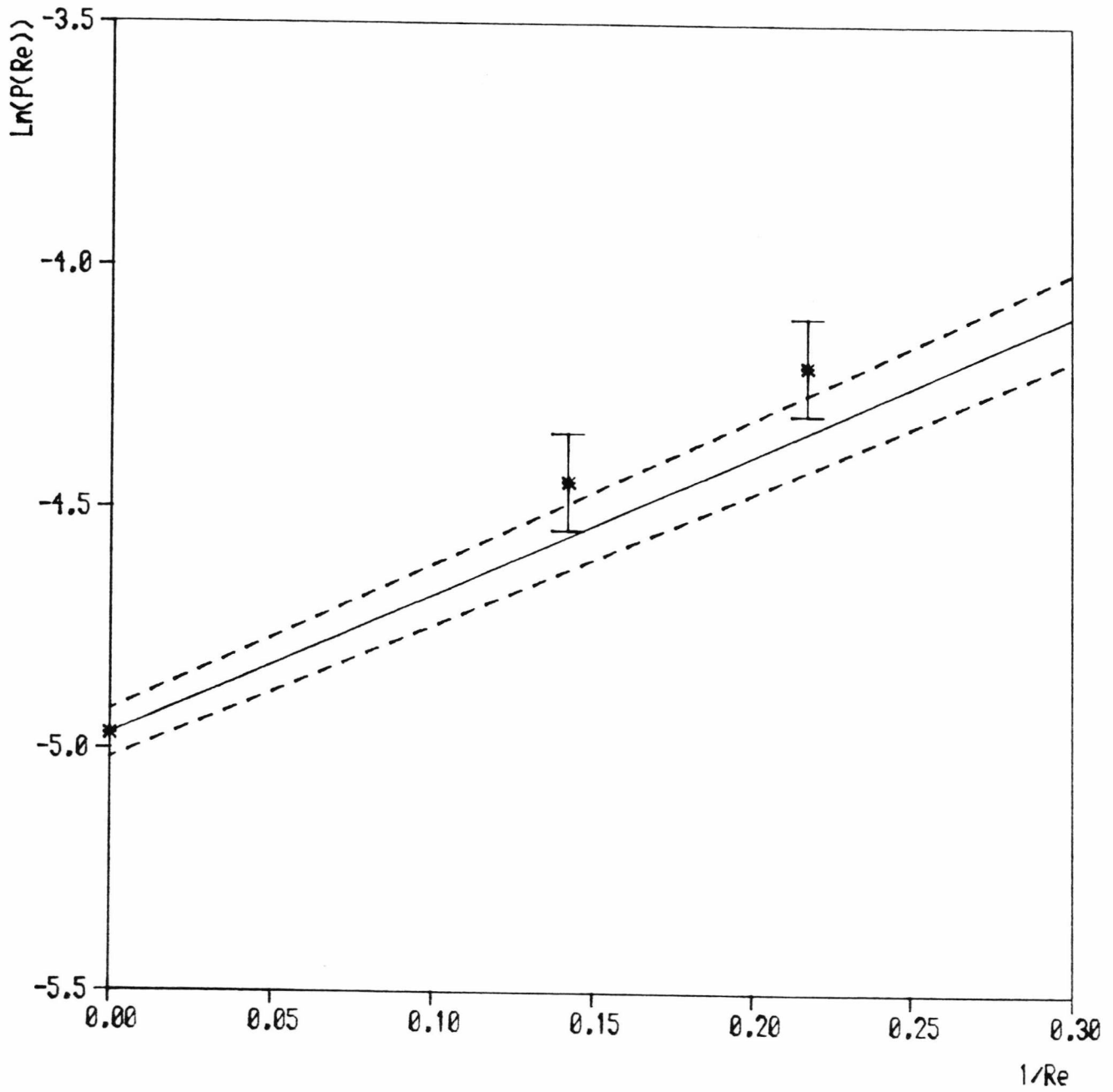


Figure 4.3: As for figure (4.2), except at the temperature of  $T = 0.838$ . note that results are only available for the two larger system ( $N_p = 1300$  and  $N_p = 450$ ) at this particular state.

$\gamma = 0.95$ , which is based on the Miyazaki *et al* value at  $T = 0.7$ , and using the empirical relation<sup>1</sup>  $\gamma(T) \propto (T_c - T)^{1.26}$ . Hence it is not as reliable as before. However, the  $N_p = 1300$  drop gives a gradient corresponding to  $\gamma = 1.2$  which is rather high, considering the result at  $T = 0.69$ . Thus the Kelvin equation seems to over-estimate the value of  $\gamma$  at this higher temperature, though the uncertainty in  $\gamma$  obtained in this way is still quite large ( $\sim 15\%$ ) and longer simulations would be helpful.

Figure (4.4) shows the variation of the measured vapour densities with temperature, for systems of varying size. The plane surface (coexistence) values are plotted for comparison. It can be seen that the vapour density is generally greater in the smaller drops, as predicted by the Kelvin equation<sup>†</sup>. However, the vapour densities of the 320 particle simulations (L10-L13) lie above some of the 260 particle results (periodic box side,  $S=18$ ). This anomaly may be due to a fall in the surface tension of small drops.

#### 4.4.3. The accuracy of the Kelvin equation

Due to the approximations needed to obtain the kelvin equation, there is some doubt about its usefulness at any temperature significantly above  $T_t$ . This problem has recently been analysed by Powles<sup>16</sup>. He has shown that the three approximations involved in the derivation of (4.22) are still quite good for higher temperatures. Using the Nicolas equation of state and planar values of  $\gamma$ , the vapour pressure outside an LJ drop is calculated without using these approximations. The accuracy of  $\ln P_g(R)$  from the Kelvin equation is found to be quite good, even for temperatures well above  $T_t$ , though it tends to overestimate this quantity more for smaller drops. However, even at  $T = 1.0$  and for drops as small as  $R = 3$ , the error is still only  $\sim 15\%$ , so the accuracy is rather better than might be expected at higher temperatures. It should be noted though that this analysis is in terms of the surface of tension,  $R_s$ , and that any

---

<sup>†</sup> Note that vapour density is proportional to vapour pressure in the Kelvin approximation.

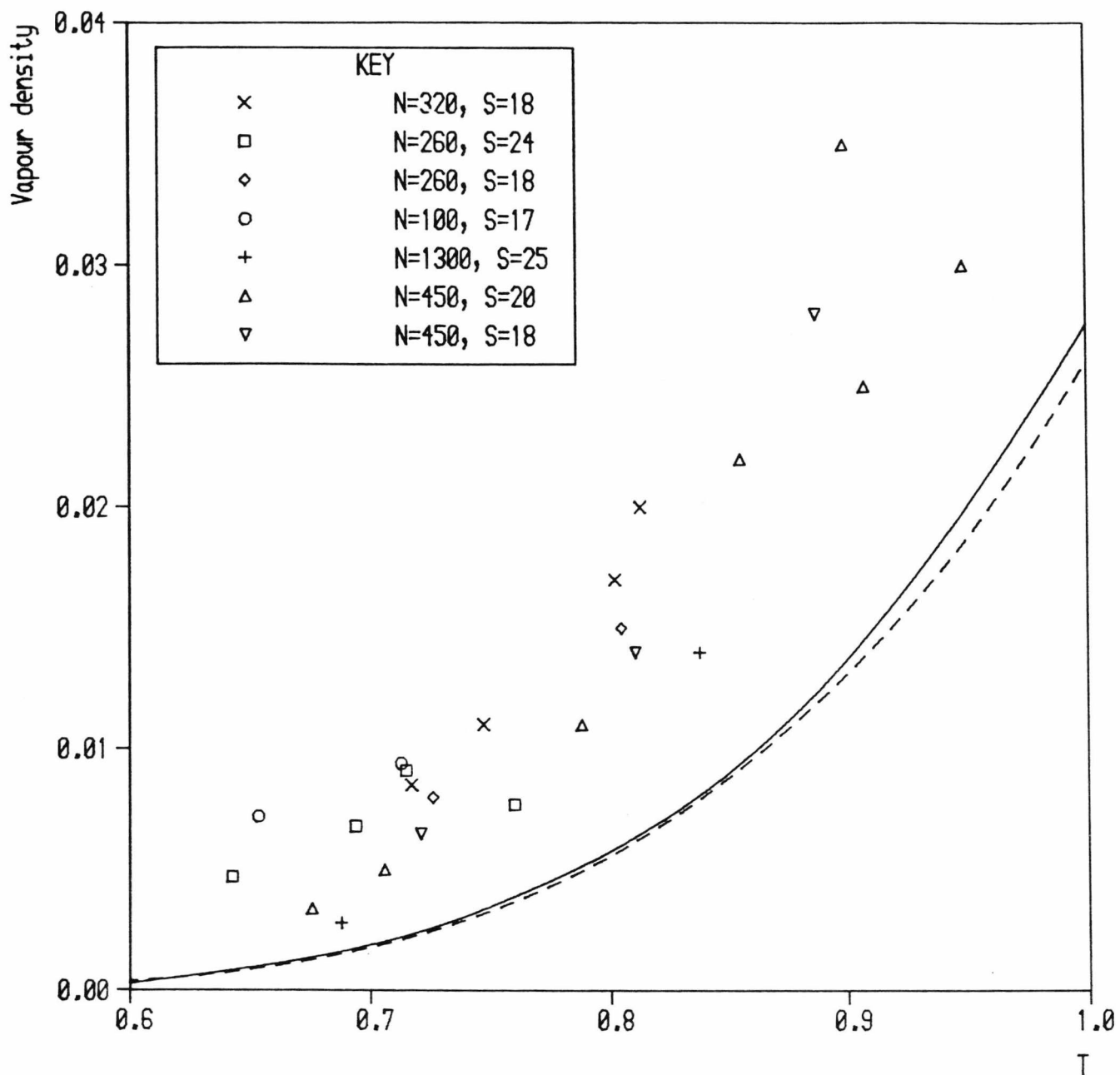


**Figure 4.4:** Vapour densities for the LJ drops as a function of temperature. The solid line represents the coexistence values predicted by the Nicolas equation of state, while the dashed line is due to Adams.

variation of  $\gamma$  with radius is ignored.

Thompson *et al* have reported results for the vapour pressure outside sp2.5 drops. They have used constant temperature MD (as described by Haile and Gupta<sup>17</sup>) to study several drops at  $T = 0.71$ , which corresponds to  $T/T_c = 0.634$ . This compares with  $T/T_c = 0.838/1.35 = 0.62$  for the higher temperature state used here (fig. 4.3), so the Kelvin equation will not be so accurate for their state. Their MD results appear rather scattered considering the lengths of the runs employed.

#### 4.4.4. Predictions of the Tolman equation

The Tolman equation, (4.16), gives the first order variation of  $\gamma$  with radius, but knowledge of  $\delta = R_e - R_s$  is poor, particularly for drops. In their plane surface simulation, Rao and Berne<sup>12</sup> found a value of  $\delta = 0.96 \pm 0.12$  (sp2.5,  $T = 0.92$ ), using the Harasima form for P.

Thompson *et al*<sup>14</sup> have calculated  $\delta$  for a range of sp2.5 drops, using a thermodynamic route, and also via the two common forms for the pressure tensor. For larger drops ( $N_p \sim 1000$ ) they find  $\delta$  to be in the range 0.05 - 0.4, rising to the order of unity for smaller systems.

If a value of  $\delta = 0.5$  is assumed, then equation (4.16) can be used with  $\gamma_\infty$  in the Kelvin equation to find  $\ln[P_g(R)/P_g(\infty)]$ . This has been done for  $T = 0.69$ , and the resulting curve is also shown in figure (4.2). The agreement with the simulated values is worse than without this correction which may indicate that the drops are too small for (4.16) to be useful, or that the value of  $\delta$  used is not appropriate for the full LJ potential. A negative value of  $\delta$  would be required to explain the rise above the Kelvin line, while most calculations suggest a positive value for this quantity. However, the uncertainty in our data is quite significant, and if the value of  $\gamma_\infty$  was in fact slightly higher, the results could be consistent with a small positive  $\delta$ .

#### 4.5. Liquid densities within small drops

Finally in this chapter on surface tension, the central liquid densities of the simulated drops are examined. This section is included here because the Laplace equation predicts increased pressure within the drops that should lead to densities above the coexistence values expected for a planar system.

Figures (4.5) and (4.6) show the measured values of  $\rho_l$  as a function of temperature for the LJ and S1 drops respectively. The coexistence values of  $\rho_l$ , from ref.[15], are also shown, as continuous lines.

The results for LJ drops are scattered about the coexistence line, with the majority lying above it. Since an equation of state is available for this fluid and the surface tension,  $\gamma_\infty$ , is known, we may calculate the expected liquid density under a pressure of  $P = P_g(R) + 2\gamma/R$ . This has been done for  $R = 7$  and the resulting curve is also marked in figure (4.3). The value of  $R = 7$  corresponds roughly to the size of the 1300 particle systems, assuming that  $R_e \approx R_s$ . While all three such results fall below this line, the uncertainty in these  $\rho_l$  values ( $\sim \pm 3\%$ ) is such that they could still be consistent with the Laplace equation. However, as the drop radius is decreased further there is no evidence of a general rise in the liquid densities, and indeed the very small drops have rather lower values of  $\rho_l$ .

Falls *et al*<sup>18</sup> find a qualitatively similar behaviour in their gradient theory treatment of drops. The central density of their drops increases with  $R_e^{-1}$  at first, and then decreases for very small drops.

#### 4.6. Conclusions

The results presented here indicate that moderately accurate values of  $\gamma$  can be obtained by use of the Kelvin equation for drops of the order of  $\sim 1000$  particles. This avoids the calculation of the pressure tensor through the surface, which would slow the simulation be a factor of at least two, even when only evaluated at every tenth time

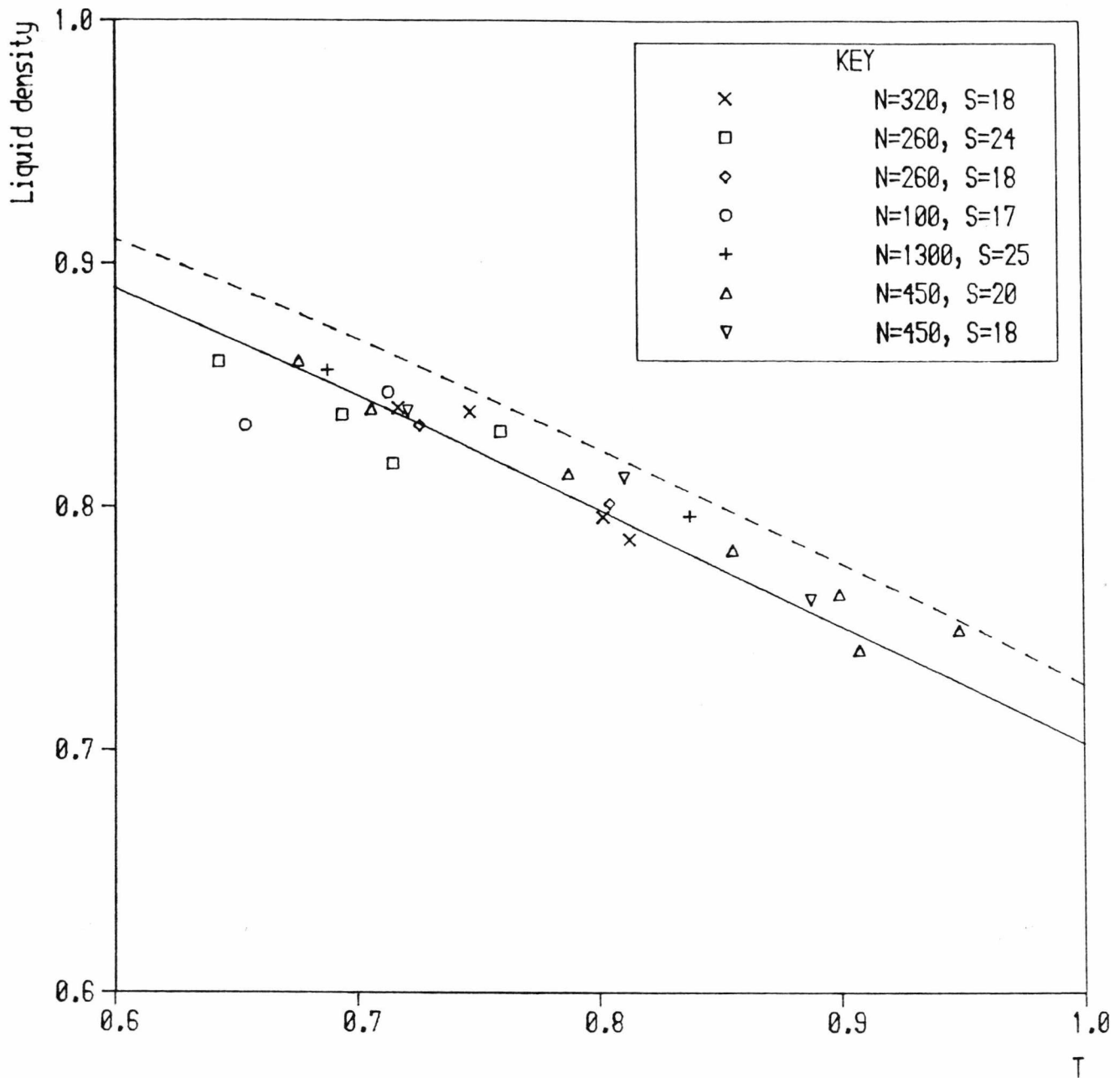


Figure 4.5: Liquid densities inside the LJ drops as a function of temperature. The solid line shows the liquid coexistence densities given by the Nicolas equation of state. The dashed line shows the density that would be found inside a drop of  $R_s = 7$ , using the planar surface tension, along with the Laplace equation for the pressure difference, and the equation of state.

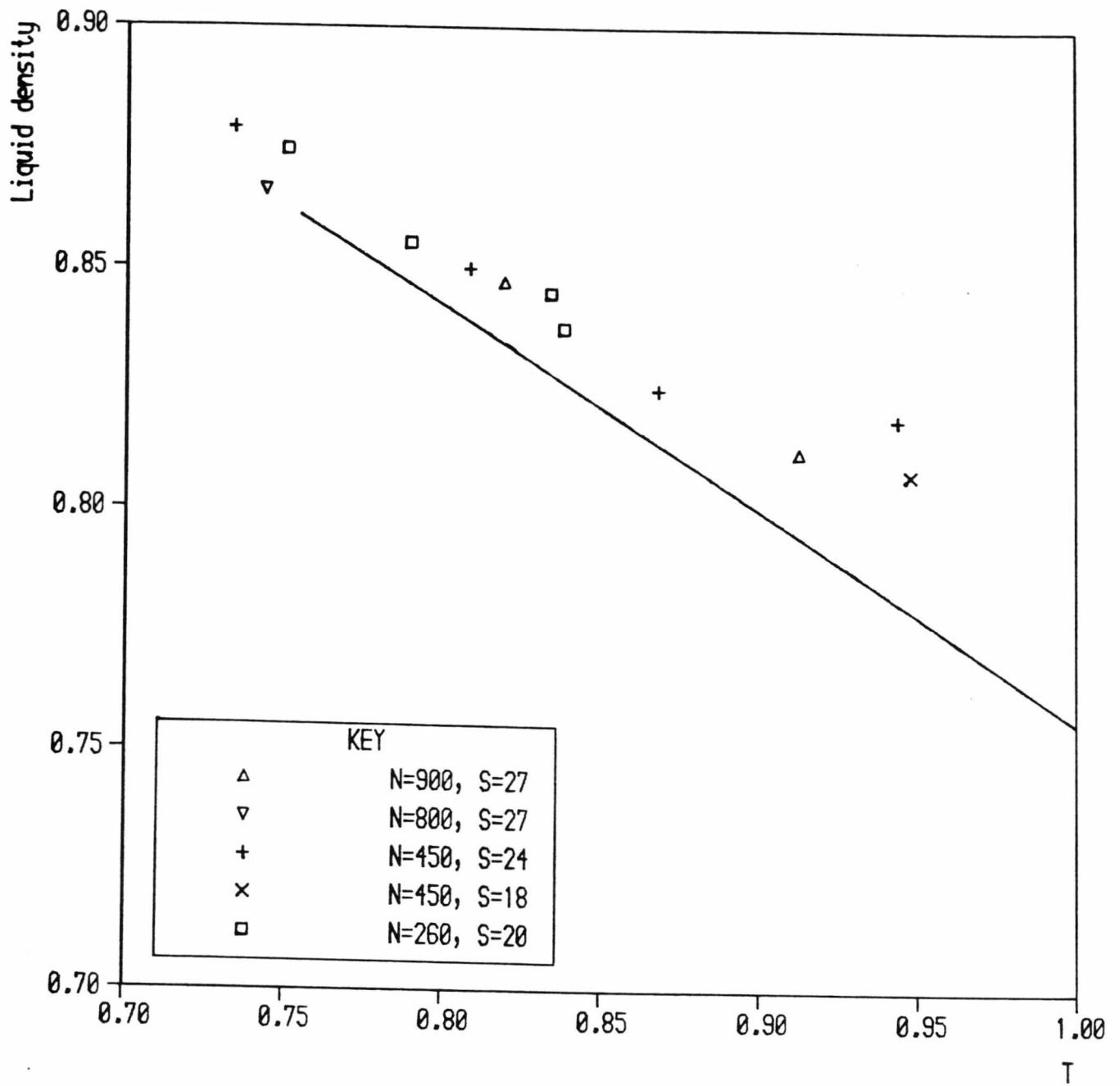


Figure 4.6: Liquid densities of the S1 Stockmayer drops. The expected planar values (shown as a solid line) are those due to Powles (see text).

step<sup>14</sup>. However it is necessary to know the density of the coexisting vapour for the potential. The method is also restricted to temperatures near  $T_l$ , though corrections using the second virial coefficients, as in reference[16], might extend this range.

This method has not been applied to find  $\gamma$  for the S1 data since the coexisting vapour curve is less well known for this potential, and fewer large systems were simulated. Quite long runs are required to get sufficiently accurate values of the vapour density, and the Stockmayer simulations are much more expensive (in computer time) than the LJ ones.

### References

1. J.S.Rowlinson and B.Widom, *Molecular theory of capillarity*, Clarendon, Oxford, 1982.
2. R.C.Tolman, *J. Chem. Phys.*, vol. 17, p. 333, 1949.
3. S.J.Hemingway, J.R.Henderson, and J.S.Rowlinson, *Faraday Symp. Chem. Soc.*, vol. 19, p. 33, 1981.
4. P.Schofield and J.R.Henderson, *Proc. R Soc. London, A*, vol. 379, p. 231, 1982.
5. J.R.Henderson and P.Schofield, *Proc. R. Soc. London, A*, vol. 382, p. 211, 1982.
6. J.H.Irving and J.G.Kirkwood, *J. Chem. Phys.*, vol. 18, p. 817, 1950.
7. A.Harasima, *Adv. Chem. Phys.*, vol. 1, p. 203, 1958.
8. J.P.R.B.Walton, D.J.Tildesley, and J.S.Rowlinson, *Molec. Phys.*, vol. 48, p. 1357, 1983.
9. F.P.Buff, *J. Chem. Phys.*, vol. 23, p. 419, 1955.
10. M.Rao and D.Levesque, *J. Chem. Phys.*, vol. 65, p. 3233, 1976.
11. G.A.Chapela, G.Saville, S.M.Thompson, J.S.Rowlinson, *J. Chem. Soc. Faraday Trans. 2*, vol. 73, p. 1133, 1977.

12. M.Rao and B.J.Berne, *Molec. Phys.*, vol. 37, p. 455, 1979.
13. J.Miyazaki, J.A.Barker, and G.M.Pound, *J. Chem. Phys.*, vol. 64, p. 3364, 1976.
14. S.M.Thompson, K.E.Gubbins, J.P.R.B.Walton, R.A.R.Chantry, J.S.Rowlinson, *J. Chem. Phys.*, vol. 81, p. 530, 1984.
15. J.G.Powles, *Physica*, vol. 126A, p. 289, 1984.
16. J.G.Powles, *J. Phys. A*, vol. 18, p. 1551, 1985.
17. J.M.Haile and S.Gupta, *J. Chem. Phys.*, vol. 79, p. 3067, 1983.
18. A.H.Falls, L.E.Scriven, and H.T.Davis, *J. Chem. Phys.*, vol. 75, p. 3986, 1981.

## Chapter Five: Surface width of microscopic drops

### 5.1. Introduction

The behaviour of liquid-vapour systems as the critical temperature is approached, has been extensively studied, by both experimental and theoretical methods. Of particular interest is the manner in which certain physical properties either diverge or vanish as  $T \rightarrow T_c$ . This is usually characterised by a so-called *critical exponent* for the given property<sup>1,2</sup>. In the preceding chapter it was noted that the surface tension near the critical point is known to be proportional to  $(T_c - T)^\nu$ , and that the critical exponent,  $\nu$ , in this case is  $\nu \approx 1.26$ .

In this chapter the surface width of the simulated drops is considered, and an estimate of the critical exponent for this property obtained, albeit for data well below  $T_c$ . This is compared with the predicted value of this exponent, and with actual theoretical calculations of the surface width, in the temperature range used in the simulations. The contribution of surface oscillations (*capillary waves*) to the surface width is evaluated to enable a better comparison to be made between theory and simulation. This analysis is due to Powles (private communication).

### 5.2. Critical exponents and the surface width

A critical exponent describes the behaviour of a given thermodynamic property in the limit as the system approaches the critical point,  $(T_c, P_c, \rho_c)$ . A typical example is the isothermal compressibility,  $\chi_T$ , which diverges at the critical point. It is found that its behaviour may be represented by the equation,

$$\chi_T = c |T_c - T|^{-\gamma} \quad (\text{as } T \rightarrow T_c) \quad (5.1)$$

where  $c$  is a constant and  $\gamma$  is the appropriate critical exponent (it is conventional to use  $\gamma$ , which is not to be confused with the surface tension). It is found from experiment that the same exponent is obtained if  $T_c$  is approached from above (along  $\rho = \rho_c$ ) or below (along the coexistence curve). Moreover the same value of  $\gamma$

(experimentally<sup>2</sup>,  $\gamma = 1.2 \pm .04$ ) is obtained independent of the liquid been studied, so it is a 'universal' constant.

Other important critical exponents govern the heat capacity, ( $C_v \propto |T_c - T|^{-\alpha}$ ,  $\alpha \approx 0.1$ ), the difference between liquid and vapour densities ( $\rho_l - \rho_g \propto |T_c - T|^\beta$ ,  $\beta \approx 0.355$ ) and the pressure along the isotherm  $T = T_c$  ( $P - P_c \propto |\rho - \rho_c|^{\delta-1}(\rho - \rho_c)$ ,  $\delta \approx 4.35$ ). The values quoted here are derived from experiments on real liquids or advanced theoretical methods, such as renormalization theory<sup>2,3</sup>.

The surface width of both drops and planar interfaces is expected to diverge, as the critical point is approached along the coexistence curve. A value for the critical exponent in this case may be derived from, for example, the van der Waals equation of state. Using such an equation, in conjunction with a Taylor expansion about the critical point leads, to the 'mean field' results for the exponents<sup>4</sup>. In fact these values are only approximations of the experimental results, for reasons discussed below. Nevertheless, within this approximate treatment it is possible to show that the density profile of a planar interface takes on a hyperbolic tangent form as the critical temperature is approached, such that,

$$\rho(z) - \rho_c = \frac{1}{2}(\rho_l - \rho_g) \tanh(z/2D) \quad (5.2)$$

The parameter  $D$  is immediately identifiable with the width parameter that was fitted to the simulation profiles in chapter three. In the mean-field theories it is found that the width diverges as  $D \propto |T_c - T|^{-\nu}$ , with  $\nu = 1/2$ . In fact the parameter  $D$  is thought to be equivalent to the coherence length of density fluctuations in the bulk phases of the fluid, so that these two properties have the same exponent.

The mean-field calculations may also be used to derive values for other critical exponents, and these results are referred to as the *classical* values of the exponents. In general, these classical values are not in good agreement with experimental values for real liquids. For example, mean-field theory predicts the value of  $\gamma = 1$  for the

compressibility, instead of  $\gamma = 1.2 \pm 0.04$  as is actually found. The failure of mean-field theory is believed to be due to the non-analytic behaviour of the equation of state at the critical point, related to the long range density fluctuations that are possible in the thermodynamic limit. To obtain more accurate values of the critical exponents from theory requires a more sophisticated treatment, such as scaling theory or renormalization theory (see e.g. Hansen and McDonald<sup>2</sup> and references therein).

Computer simulations are necessarily performed with no more than a few thousand particles at most. Such systems cannot realistically reproduce the behaviour at the critical point because the long range fluctuations are suppressed. Hansen and Verlet<sup>5</sup> and Alder *et al*<sup>6</sup> have calculated various critical exponents from MD simulations close to the critical point. They find results that are consistent with the classical mean-field values for the exponents  $\beta$ ,  $\gamma$  and  $\delta$  (defined above), but the exponent for the specific heat at constant volume,  $\alpha$ , is close to the 'real-liquid' value. The exponent  $\nu$  was not calculated in these simulations. Alder *et al* used homogeneous systems of (mainly) 108 particles and with temperatures above  $T = 0.9T_c$ .

### 5.3. Temperature dependence of the surface width

Using the data for all the LJ states that have been studied, a graph of the surface width,  $D$ , as a function of the temperature has been drawn. This is shown in figure (5.1). It can be seen that  $D$  rises from approximately  $1.5\sigma$  near the triple point, to over  $4\sigma$  at the highest temperature used, which was  $T = 1.06$ . The width is clearly rising rapidly as the temperature approaches  $T_c$ , but the limited size of the drops prevents states much closer to the critical point being studied (see chapter three). As it is, the highest temperature simulation that was performed (state L25) had a cell size that was rather small considering the number of particles and the spread of the surface region involved. Even for this state,  $T/T_c \approx 0.79$ , so we are still well below the critical point.

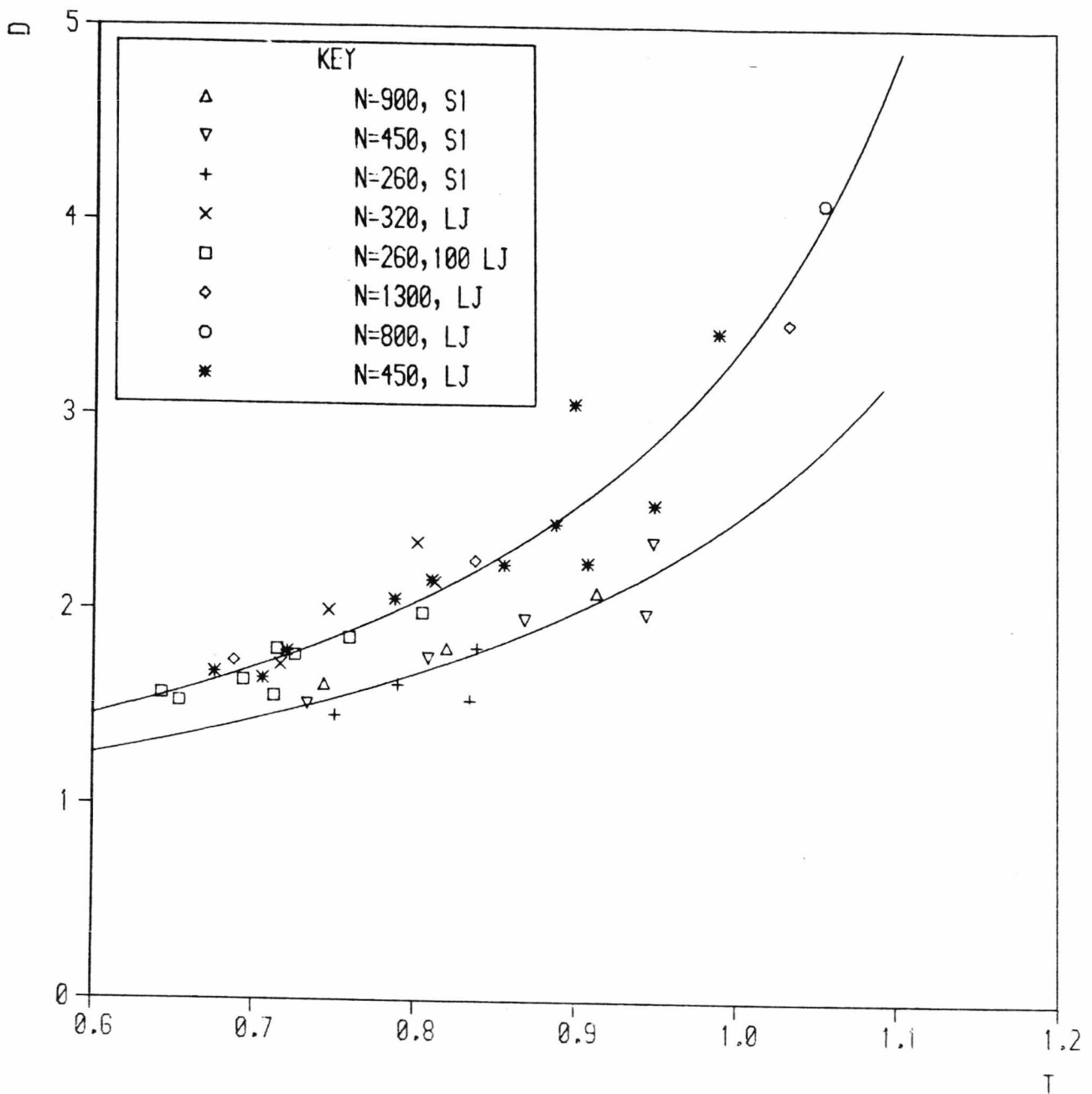


Figure 5.1: The surface widths ( $D$ ) for the LJ and S1 (Stockmayer) drops, as a function of temperature. The upper curve is the result  $D = 1.06(T_c - T)^{-1.0}$ , which was obtained by a least squares to the LJ data ( $T_c = 1.32$ ). The lower curve is a similar fit for the Stockmayer data ( $T_c = 1.45$ ).

The results for  $D(T)$  show a fair amount of scatter, perhaps in part due to the relative insensitivity of the fitting process to the value of  $D$  (see chapter three). Despite this scatter, and the fact that all the data lie well below  $T_c$ , we shall least-squares fit these results to an expression of the form,

$$D(T) = A(T_c - T)^{-\nu} \quad (5.3)$$

An equal weighting was given to all the data points in this fit, and the value of  $T_c = 1.35$  was used, though this is subject to some uncertainty. However the results of the fit are not very sensitive to  $T_c$ , and we obtain the expression,

$$D \approx 1.06(T_c - T)^{-1.0} \quad (5.4)$$

Thus our estimate of the critical exponent in this case is  $\nu \approx 1.0 \pm 0.1$ , though only from data well below  $T_c$ . This is significantly greater than either the mean field value or the prediction of the more sophisticated theory,  $\nu = 1/2$  and  $\nu \approx 0.63$  respectively. If the exponent in equation (5.3) is constrained to be either of these values, then a very poor fit is obtained. Hence it appears that the simulated surface width is diverging more rapidly than would be expected from either value of the critical exponent, assuming that they are still meaningful this far from  $T_c$  †.

It is difficult to discern any clear trend in the surface width of drops as a function of the number of particles. There is some indication that small drops have thinner surfaces than larger drops at the same temperature. This is not as noticeable as the size dependence observed by Chapela *et al*<sup>7</sup> in their simulations of planar interfaces, using the sp2.5 potential. Thompson *et al*<sup>8</sup> have given surface width results for sp2.5 drops, and they also indicate a rather faster divergence of the width of  $N_p = 256$  particle systems compared with  $N_p = 2048$  particle ones. However this is most notable at higher temperatures, and most of our smaller simulations have been made at low  $T$ . It might also be noted that there is some inconsistency between the surface widths

---

† Experimental data<sup>6</sup> for  $\beta$  (the exponent for the density difference) indicates a slow rise in the apparent exponent as the temperature falls below  $T_c$ . For  $T/T_c = 0.8$  the increase is  $\sim 10\%$ .

obtained from the two different simulation methods used by Thompson *et al* (the Oxford (O) and Cornell (C) results in their paper). If the appropriate value of  $T_c$  is used in equation (5.3), a least squares fit to their 2048 particle data yields a critical exponent of  $\nu \approx 1.1$ , that is in reasonable agreement with our results.

Proceeding to the Stockmayer results reported in chapter three, we have also plotted the surface width values for these states in figure (5.1). It can be seen that these values lie below the LJ results, but they diverge in a similar manner as the Stockmayer critical temperature is approached. This is as might be expected from the upwards shift in temperature of the S1 coexistence curve compared to that of the LJ fluid. An exponent of  $\nu \approx 1.0$  is again obtained from a least squares fit. The S1 data are relatively further from  $T_c$  ( $\approx 1.45$ ) than the LJ results.

#### 5.4. Theoretical calculations of the LJ surface width

A number of theoretical calculations of the liquid-vapour surface width have been performed for the LJ fluid. Some recent values will be compared with our simulation results. Henderson and Lekner<sup>9</sup> have obtained a value of  $D$  at one temperature (85K in argon units) using surface tension and energy data due to Shih and U<sup>an</sup>ag. In fact their calculation is based on the BFW potential for argon, rather than the LJ one, but it is not expected that the width should be very sensitive to this.

A range of values have been obtained by Fisher and Methfessel<sup>10</sup> who used the BGY approximation (along with the LJ interaction) and calculate  $D$  for several temperatures up to  $T = 1.1$ . In another calculation, due to Ebner *et al*<sup>11</sup>, the surface width is obtained using a density functional formalism, with an approximation for the direct correlation function.

In figure (5.2) these theoretical values of the surface width have been plotted as a function of temperature. There is reasonable agreement between the various values, even though they are based on different approximations. Also shown in the figure is

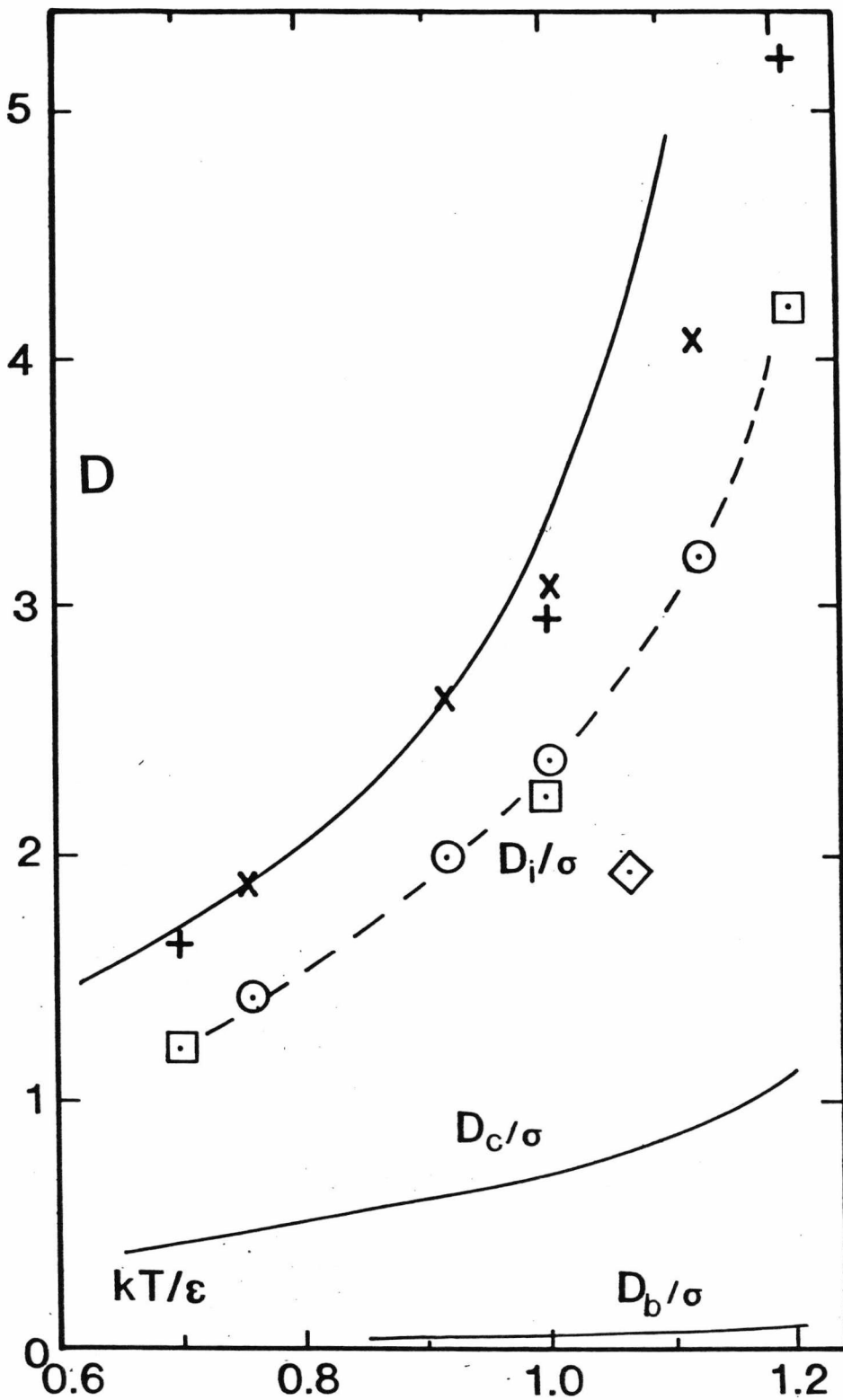


Figure 5.2: Comparison of calculated surface widths with the LJ simulation results. The upper curve again shows the fit to the simulation data. Calculations of the intrinsic surface width ( $D_i$ ) due to Henderson and Lekner ( $\bullet$ ), Ebner *et al* ( $\square$ ) and Fisher and Methfessel ( $\odot$ ) are shown. The value for  $D_i$  due to Falls *et al* ( $\diamond$ ) is seen to lie well below these results. The curve marked  $D_c$  is the calculated capillary contribution to the surface width and  $D_b$  is that due to the "breathing" mode of oscillation. The estimates of the total width due to capillary plus intrinsic parts are marked as (+) and (x).

the curve that was fitted to the LJ simulation data, equation (5.4). Clearly there is a large discrepancy between these two sets of data. A fit to the theoretical values gives a critical exponent of  $\nu \approx 0.7$ , which is much closer to the expected value of  $\sim 0.63$  (or perhaps 0.5), than the simulation results.

The theories referred to above are all applied to planar liquid-vapour surfaces, but it is likely that similar widths should be observed in our case, at least in the larger simulated drops. Some theoretical predictions of the surface width in drops can be obtained from the data of Falls *et al*<sup>12</sup>. One such point is included in the figure (5.2) and it is very much lower than the other theoretical values. However, the approximations used by Falls *et al* are such as to make their results only qualitatively comparable to the actual LJ fluid, and we shall not use this value.

In the next section we examine surface oscillations in drops as a possible explanation of the difference between the simulated and theoretical widths.

### 5.5. The effects of capillary waves on surface width

Ideally, a liquid drop at equilibrium may be considered as having a 'step function' profile, so that the density changes from  $\rho_l$  to  $\rho_g$  discontinuously at the radius  $R$ . The spherical shape of the well defined interface is maintained by the surface tension forces. Such a surface can support oscillations and these are generally referred to as *capillary waves* (they also exist in the planar interface). At any finite temperature each independent mode of the surface will be subject to thermal excitations and, by equipartition (in the classical limit), will have a mean energy of  $kT/2$  ( $k=1$  in reduced units, but we retain it here). We wish to investigate what contribution such oscillations make to the surface width. This problem has been analysed by Henderson and Lekner<sup>9</sup>, who give a detailed description that includes quantum effects. Here we shall give a simpler classical treatment of the problem.

An analysis of capillary wave modes is given in several text books, such as that by

Landau and Lifshitz<sup>13</sup>. It is usual to make the assumption that the liquid is incompressible, in addition to the idealised profile mentioned above. This allows solutions to be obtained in terms of the velocity potential,  $\psi$ , which obeys the equation  $\nabla^2\psi = 0$  for an incompressible fluid. With the further assumption that the oscillations are of small amplitude it can be shown the solutions are spherical harmonics which we write in the form,

$$\psi_{lm} = A_{lm} e^{-i\omega t} r^l P_l^m(\cos\theta) e^{im\phi} \quad (5.5)$$

where  $\omega$  is the angular frequency and  $P_l^m(\cos\theta)$  are associated Legendre functions.

The boundary conditions for the system lead to the condition that,

$$\omega^2 = \gamma l(l-1)(l+2)/\rho_M R^3 \quad (l \geq 2) \quad (5.6)$$

where  $\rho_M$  is the mass density and  $\gamma$  the surface tension. The requirement that  $l \geq 2$  arises since the  $l = 1$  mode corresponds to translation of the whole drop and  $l = 0$  to a 'breathing' mode that is impossible for an incompressible liquid.

Since both our simulations and the theoretical predictions of surface width, shown in figure (5.2), ignore any quantum effects there should not be any inconsistency on these grounds. To check if such capillary waves in real argon drops of this size can still be treated classically, we calculate the ratio  $\hbar\omega/kT$ . It is found that this quantity is much less than unity for argon, at most reasonable values of  $l$ , e.g. for a radius of  $R_{Ar} = 4\sigma \approx 1.36\text{nm}$  and a temperature of  $T_{Ar} = 0.7\epsilon/k \approx 84\text{K}$ , even a large value of  $l = 12$  only gives  $\hbar\omega/kT \approx 0.2$ . It is shown below that higher frequency modes are unimportant, so that it is reasonable to treat argon drops classically. Quantum corrections only become significant for drops of liquids such as neon and helium which are already known to be poorly described by classical calculations.

From equipartition, each such capillary mode will have a mean kinetic energy of  $\frac{1}{2}kT$ . If the displacement of the surface from its mean value in the mode  $(l, m)$  is denoted as  $\zeta_{l,m}(\theta, \phi) \equiv \zeta_{l,m}$ , then the form of this function can be obtained from the velocity potential, (5.5), since the radial velocity satisfies  $\frac{\partial\psi}{\partial r} = v_r = \frac{\partial\zeta}{\partial t}$ . Hence we

obtain,

$$\zeta_{l,m} = a_{l,m} P_l^m(\cos\theta) \cos m\phi \sin\omega t \quad (5.7)$$

where  $a_{l,m}$  is the amplitude of oscillation. It was originally noted by Rayleigh<sup>14</sup> that the mean radius of such an oscillating drop is increased from its value when free of disturbances,  $R$ , to a value  $R_s$ , (not to be confused with the surface of tension in chap. 4) such that the volume is conserved. This gives the condition,

$$\frac{1}{3} \int \int (R_s + \zeta_{l,m})^3 \sin\theta \, d\theta \, d\phi = \frac{4}{3} \pi R^3 \quad (5.8)$$

To order  $\zeta_{l,m}^2$  we get,

$$R^2 - R_s^2 = \frac{a_{l,m}^2}{2\pi} \int \int P_l^m(\cos\theta)^2 \cos^2 m\phi \sin^2\omega t \, d\theta \, d\phi \quad (5.9)$$

The increase in surface area of the drop is (see Landau and Lifshitz, § 61),

$$\Delta A = \int \int \left[ (R_s + \zeta_{l,m})^2 + \left( \frac{\partial \zeta_{l,m}}{\partial \theta} \right)^2 + \frac{1}{2} \frac{1}{\sin^2\theta} \left( \frac{\partial \zeta_{l,m}}{\partial \phi} \right)^2 \right] d\theta \, d\phi \quad (5.10)$$

Substituting (5.7) and using (5.9) in (5.10) leads to the equation,

$$\Delta A = a_{l,m}^2 \pi \sin^2\omega t \int \left[ -P_l^m(\cos\theta)^2 + \frac{1}{2} \left( \frac{dP_l^m(\cos\theta)}{d\theta} \right)^2 + \frac{1}{2} \frac{1}{\sin^2\theta} P_l^m(\cos\theta)^2 m^2 \right] \sin\theta \, d\theta \quad (5.11)$$

This allows the determination of  $a_{l,m}$ , since the mean energy of a mode is just the average of  $\Delta A$  times the surface tension  $\gamma$ , i.e.  $kT/2 = \gamma \langle \Delta A \rangle$ . Using this in equation (5.7), we can then find the mean square amplitude of the thermal capillary waves by taking the average over time and  $(\theta, \phi)$ . This eventually yields,

$$\overline{\zeta_{l,m}^2} = \frac{kT}{4\pi\gamma} \frac{1}{(l-1)(l+2)} \quad (l \geq 2) \quad (5.12)$$

This equation is also obtained by Henderson and Lekner when they treat drops in the classical limit.

Due to the incoherence of the vibrations, the total mean square amplitude is

simply the summation of (5.12) from  $l = 2$  to  $l = L_{\max}$ ,

$$\overline{\xi^2} = \frac{kT}{4\pi\gamma} \sum_{l=2}^{L_{\max}} \frac{(2l+1)}{(l-1)(l+2)} \quad (5.13)$$

The high frequency cut-off arises, in this case, as the wavelength,  $\lambda$ , approaches the value of the mean separation between particles. We shall take the lowest wavelength as  $\lambda_{\min} \approx 2\sigma$ . For the typical sizes of the simulated drops ( $R \sim 4 - 5 \sigma$ ) this corresponds to  $L_{\max} \approx 12 - 16$ .

In the limit as  $R \rightarrow \infty$ , we go over to a planar interface and the upper limit of the summation in (5.13),  $L_{\max} \rightarrow \infty$ . The resulting series is proportional to  $\sum l^{-1}$  for large  $l$ , and this is known to diverge as  $\log(L_{\max})$ . Thus we obtain the usual result that capillary waves lead to an infinite width for an interface of infinite area.

For a drop radius of  $R = 4$  it is found that  $L_{\max} \approx 12$ , for which the summation in (5.13) is  $\sum(\dots) \approx 4.44$  and so the RMS amplitude is,

$$\left(\overline{\xi^2}\right)^{1/2} \approx 2.1 \left(\frac{kT}{4\pi\gamma}\right)^{1/2} \quad (5.14)$$

The leading coefficient is only weakly dependent on the values taken for the cut-off and the drop radius, e.g. for  $R = 7$ , we get 2.35 instead of 2.1. Using values of surface tension for the planar interface (see chapter four), we have plotted equation (5.14) in figure (5.2) (the curved marked  $D_c$ ).

Before the above analysis is compared with the actual surface widths of LJ drops, it must be noted that the assumptions of a sharp interface and of incompressible liquid are only approximately satisfied. Also, the effect of the vapour pressure outside the drops is ignored, and this may be significant at high temperatures.

A check may be made on the importance of the finite compressibility,  $\chi$ , of the LJ fluid by calculating the amplitude of the 'breathing' mode of oscillation, when the surface may be described by the expression,  $r(t) = R + \zeta_b(t)$ , where  $\zeta_b$  is independent of the angles  $\theta$  and  $\phi$ . For a given small amplitude  $a_b$ , the work performed against

the pressure may be calculated from the compressibility at the liquid density, which can be obtained since the equation of state is known. Depending on the time period of such oscillations, either the adiabatic ( $\chi_s$ ) or isothermal ( $\chi_T$ ) value may be more appropriate, but for a rough estimate of the amplitude it is more convenient to calculate the isothermal value. Using this value, and equating the total work for the maximum displacement to  $kT$ , the result is,

$$\left(\overline{\zeta_b^2}\right)^{1/2} = \left(\frac{\chi kT}{12\pi R}\right)^{1/2} \quad (5.15)$$

Taking a radius of  $R = 4$ , this yields the curve shown in figure (5.2) (labelled  $D_b$ ). This is very much smaller in amplitude than the capillary oscillations so it appears that incompressibility is a reasonable approximation.

The assumption of a sharp interface is clearly not very realistic, especially for the smaller drops and at higher temperatures. Nevertheless, the RMS amplitude of thermal capillary waves is only weakly dependent on the actual radius of the system, and the equimolar radius  $R_e$  will be taken as the 'mean' value. Since a significant proportion of all the molecules in a given drop lie in the interface region, where the density is less than the liquid value, this may lead to an increased value of the compressibility. This in turn could enhance the contribution of the breathing mode to the surface width.

Considering the accuracy of the simulation data for  $D$ , the treatment of capillary waves given above is probably adequate. The values shown in figure (5.2) indicate that these oscillations have a significant amplitude in comparison to the total width of the simulated drops.

Now, it is claimed by Lekner and Henderson<sup>9</sup>, and others, that the theoretical widths such as those discussed above are actually for the 'bare' (or intrinsic) profiles, in that they do not contain any contribution due to capillary waves. Thus we need to combine the two effects to find the surface width of real drops. However some doubt

has been cast on this by Evans<sup>15</sup> who has shown that some capillary-like effects may already be included in a van der Waals model of the interface, so that the simple addition of the two effects could be incorrect. Despite this, we shall proceed to calculate the total width due to the intrinsic (theoretical) profiles plus the capillary contribution. As a rough approximation we could simply add the two widths to give a total width of  $D \approx D_i + D_c$ . A more correct analysis is to use the central limits theorem to replace the sum over the capillary waves by a gaussian distribution. This can then be convoluted with the intrinsic profile, which may be represented by a hyperbolic tangent, and the width of the resulting curve obtained. In fact this process yields values very close to the original result of  $D \approx D_i + D_c$  for the values of  $D_i$  and  $D_c$  that we have. These values are also shown in figure (5.2). They are in quite good agreement with the simulation results, except, perhaps, at temperatures above  $T \approx 1.0$ .

## 5.6. Discussion

The surface width results reported here, and the particular theoretical predictions looked at above, are consistent with the assumption of capillary wave broadening of the intrinsic profile. The scatter in the simulation values and the approximations of the capillary theory make it difficult to determine if the discrepancy that occurs at higher temperatures is significant or not.

Further studies of liquid drops would be desirable to get more accurate values of the surface width, and also to obtain data closer to the critical point. This requires more computer time and probably larger systems to achieve the higher temperatures. It would be interesting to see if the predicted weak dependence of  $D_c$  on the radius ( $\approx 10\%$  increase from  $R = 4$  to  $R = 7$ ) could be observed for a series of drops at constant temperature.

It might also be useful to study the actual modes of oscillation of the simulated drops. For example, the method of perturbation-difference (which is mentioned in a later chapter) might be used for this. However the period of the lowest mode of

oscillation is rather long ( $T = 2\pi/\omega \approx 100 \equiv 2000$  integration steps), and problems with noise usually arise after about 100 steps.

### References

1. C.Domb, *Adv. in Phys.*, vol. 9, p. 150, 1960.
2. J.P.Hansen and I.R.McDonald, *Theory of simple liquids*, Academic Press, London, 1976.
3. K.G.Wilson, *Phys. Rev.*, vol. B4, p. 3174, 1971.
4. J.S.Rowlinson and B.Widom, *Molecular theory of capillarity*, Clarendon, Oxford, 1982.
5. J.P.Hansen and L.Verlet, *Phys. Rev.*, vol. 184, p. 151, 1969.
6. B.J.Alder, D.A.Young, and M.A.Mark, *J. Chem. Phys.*, vol. 56, p. 3013, 1972.
7. G.A.Chapela, G.Saville, S.M.Thompson, J.S.Rowlinson, *J. Chem. Soc. Faraday Trans. 2*, vol. 73, p. 1133, 1977.
8. S.M.Thompson, K.E.Gubbins, J.P.R.B.Walton, R.A.R.Chantry, J.S.Rowlinson, *J. Chem. Phys.*, vol. 81, p. 530, 1984.
9. J.Lekner and J.R.Henderson, *Physica*, vol. 94A, p. 545, 1978.
10. J.Fisher and M.Methfessel, *Phys. Rev.*, vol. 22A, p. 2836, 1980.
11. C.Ebner, W.F.Saam, and D.Stroud, *Phys. Rev.*, vol. 14A, p. 2264, 1976.
12. A.H.Falls, L.E.Scriven, and H.T.Davis, *J. Chem. Phys.*, vol. 75, p. 3986, 1981.
13. L.D.Landau and E.M.Lifshitz, *Fluid mechanics*, Pergamon, New York, 1963.
14. Lord Rayleigh, *Theory of sound*, 2, Macmillan, London, 1929.
15. R.Evans, *Molec. Phys.*, vol. 42, p. 1169, 1981.



## Chapter Six: Dielectric theory and computer simulation

### 6.1. Introduction

The remainder of this thesis is concerned with the calculation of dielectric properties of the Stockmayer fluid from the data obtained in the simulation of the S1 and S3 drops. In this chapter a brief review is made of some of the basic dielectric theory that is relevant to the interpretation of our results. The static dielectric constant,  $\epsilon_s$ , is discussed in 6.2 for polar (non-polarizable) fluids, and the frequency dependence of this quantity,  $\epsilon(\omega)$ , is considered in 6.3.

A number of techniques have previously been employed to study the dielectric properties of polar fluids, and some of these are briefly reviewed in the final section of this chapter.

### 6.2. The Static dielectric constant

#### 6.2.1. Polarization and the dielectric constant

When a fluid (or any other material) is placed in an electric field a net dipole moment is induced in it. For a homogeneous and isotropic sample in a field  $E$ , the dipole moment per unit volume (polarization) is found to be given by,

$$\mathbf{P} = \chi \mathbf{E} \quad (6.1)$$

where the constant  $\chi$  is the dielectric susceptibility (this relation breaks down in very intense fields, but is usually adequate).

From basic electrostatics the electric displacement vector  $\mathbf{D}$  is related to  $\mathbf{E}$  and  $\mathbf{P}$  by the equations,

$$\mathbf{D} = \mathbf{E} + 4\pi\mathbf{P} = \mathbf{E}(1 + 4\pi\chi) = \epsilon_s \mathbf{E} \quad (6.2)$$

where  $\epsilon_s = 1 + 4\pi\chi$  is the dielectric constant (we shall use the subscript  $s$  to help distinguish this from the LJ energy parameter).

While it is reasonably straightforward in principle to measure  $\epsilon_s$  in a given

macroscopic sample, it is rather more difficult to calculate the dielectric constant from the microscopic properties of matter, such as the interaction potential between molecules. This is due to the long range correlations that exist in dipolar fluids, which are sensitive to the (macroscopic) shape of the sample and its surroundings. Nevertheless, it has been shown that the dielectric constant can still be expressed in terms of local correlations, and is independent of the macroscopic shape and surroundings of the system<sup>1</sup>.

There are two main sources of the polarization that is induced in the fluid. The first is due to the redistribution of electronic charge within a molecule. In the presence of an electric field the distortion of this charge distribution produces a dipole moment within each molecule. Also, atoms, or groups of atoms, within a molecule can change their relative positions so as to produce a net dipole moment. Secondly, for a dipolar liquid the molecules themselves can reorientate so that the permanent dipoles tend to lie in the direction of the applied field.

The total polarization of a given sample can be expressed as  $\mathbf{P} = \mathbf{P}_\alpha + \mathbf{P}_\mu$ , where  $\mathbf{P}_\alpha$  is the contribution due to the electronic distortion, and  $\mathbf{P}_\mu$  is the part due to reorientation of permanent dipoles.

The degree of electronic polarization is dependent not on the mean field within the liquid (the Maxwell field), but on the mean field that each molecule actually experiences, known as the internal field,  $\mathbf{E}_i$ . It is found that  $\mathbf{P}_\alpha = N\alpha\mathbf{E}_i$ , where  $N$  is the total number of molecules and  $\alpha$  is a constant, the molecular polarizability (in general the molecular polarizability is a tensor,  $\alpha$ , but it is usually adequate to use the scalar value  $\text{tr } \alpha / 3$ ).

The reorientational polarization is given by  $\mathbf{P}_\mu = N\langle\boldsymbol{\mu}\rangle$ , where  $\langle\boldsymbol{\mu}\rangle$  is the expectation value of one molecule's permanent dipole moment in the applied field. The mean electric field acting on such a molecule to produce this alignment is  $\mathbf{E}_d$ , the directing field. This is not the same as either the Maxwell or the internal field<sup>†</sup>.

<sup>†</sup> The fact that the directing field is not equal to the internal field was first noted by Onsager,

Using basic statistical mechanics<sup>2</sup> it can be shown that  $\langle \mu \rangle$  is related to  $E_d$  by the equation  $\langle \mu \rangle = (\mu^2/3kT)E_d$ , and hence,  $P_\mu = N\mu^2E_d/3kT$ .

Thus if the internal and directing fields can be calculated from the microscopic structure of the fluid, the polarization can be determined for a given applied field. Once this is known the dielectric constant can be obtained. However, such calculations are difficult, and usually require drastic approximations, some of which will be discussed later.

There are some important differences between the two main sources of polarization. Most significantly, the response time of the electronic contribution is very much shorter than that of the reorientational part. Thus  $P_\mu$  takes very much longer to reach its equilibrium value than does  $P_\alpha$ , when a static field is applied. Additionally, the electronic polarization, being an intramolecular effect, is only weakly dependent on the density and temperature of the fluid, whereas the reorientational part is extremely sensitive to these parameters. The alignments of molecules that give rise to  $P_\mu$  are subject to greater disruption as the temperature of the system is increased.

The Stockmayer potential that is used in this work is essentially a model of a polar fluid, the molecules of which are non-polarizable, i.e.  $\alpha = 0$ . Hence we shall neglect  $P_\alpha$  and confine our attention to the reorientational contribution only.

### 6.2.2. Simple theories of the dielectric constant

The long range nature of the dipolar interaction, and the fact that the macroscopic sample shape influences the behaviour of molecular correlations makes it difficult to treat  $\epsilon_s$  by theoretical means. One of the first approaches to have some success is the treatment due to Onsager<sup>3</sup>. In this model only one central dipolar

---

who pointed out that the part of  $E_i$  that is due to the reaction field of the permanent dipole should not be included in  $E_d$ .

molecule is considered explicitly, and the surrounding fluid is assumed to behave as a macroscopic dielectric continuum. This drastic approximation ignores all the effects of the short range structure of the fluid. Nevertheless, with these assumptions it is possible to obtain a simple relation between the size of the permanent dipole moment,  $\mu$ , and the dielectric constant, which is the well known Onsager equation (e.g. see reference[2] ),

$$\begin{aligned} \frac{4\pi}{3} \rho \frac{\mu^2}{3kT} &= \frac{(\epsilon_s - \epsilon_\infty)(2\epsilon_s + \epsilon_\infty)}{\epsilon_s(\epsilon_\infty + 2)} \\ &= \frac{(\epsilon_s - 1)(2\epsilon_s + 1)}{3\epsilon_s} \end{aligned} \quad (6.3)$$

where  $\epsilon_\infty$  is the dielectric constant measured at high frequencies. This represents the electronic contribution to  $\epsilon_s$ , and so for the Stockmayer model we have put  $\epsilon_\infty = 1$  in the above expression.

The Onsager equation is found to be a moderately successful approximation for the behaviour of various real dipolar liquids. However it is particularly poor for highly polar liquids, such as water, where hydrogen bonding can occur.

For polar gases at low density, a virial expansion (analogous to that employed for the pressure) can be used for the dielectric constant. This equation is based on the Clausius-Mossotti (CM) formula, but the expansion is made in terms of the density, rather than the polarizability, which appears in the CM expression. This allows the virial form to be used with polar fluids, even when  $\alpha = 0$ . The virial equation in this case can be written as<sup>2</sup>,

$$\frac{\epsilon_s - 1}{\epsilon_s + 2} \frac{1}{\rho} = a_\epsilon(T) + \rho b_\epsilon(T) + \rho^2 c_\epsilon(T) + \dots \quad (6.4)$$

where  $a_\epsilon(T) = 4\pi\mu^2/(9kT)$ , and the higher order coefficients can be expressed as integrals over pairs, triplets, etc. of molecules. While this expression is limited to densities much less than that of the liquid state, it is interesting to note the important effect of molecular shape on the second dielectric virial coefficient,  $b_\epsilon(T)$ . For example,  $b_\epsilon(T)$  is found to be strictly positive for gas phase measurements on  $\text{CHF}_3$ ,

while similar data for a molecule such as  $\text{CH}_3\text{F}$  always gives a negative value for this coefficient. This difference is due to the shape of the molecules, which effects the relative stability of the parallel and anti-parallel alignments that can occur between pairs of molecules. It can be shown that the spherical symmetry of the LJ part of the Stockmayer potential will always lead to a positive value for  $b_\epsilon(T)$ .

### 6.2.3. The Kirkwood $g$ factor and the mean square moment

In dense polar liquids it is necessary to treat the interactions of the fluid by more general statistical mechanics. It is desirable to relate the dielectric constant of a macroscopic sample to the molecular correlation functions within the fluid. Some of the most important pioneering work in this area was performed by Kirkwood<sup>4</sup> with further developments due to Fröhlich<sup>5</sup>.

The treatment given in Fröhlich's book is based on the consideration of the spontaneous polarization fluctuations within a small volume,  $V$ , containing  $N$  molecules, of the total sample. The remainder of the sample is then treated as a continuous dielectric, so that the only molecular interactions that are explicitly treated are those within  $V$ . It is usually stated that  $V$  should be *sufficiently* large to make this a good approximation, without actually specifying the minimum volume. We shall give some of the details of the derivation of the Kirkwood formula here because the method is similar to that used in later calculations.

From equation (6.2) we can write,

$$(\epsilon_s - 1)\mathbf{E} = 4\pi\mathbf{P} = \frac{4\pi\langle\mathbf{M}\rangle_E}{V} \quad (6.5)$$

where  $\langle\mathbf{M}\rangle_E = \langle\sum_i \boldsymbol{\mu}_i\rangle_E$  is the mean moment of the sample of  $N$  particles in the applied field. Introducing a unit vector in the direction of  $\mathbf{E}$ , we can write  $\mathbf{E} = E\hat{\mathbf{e}}$ , and the vector  $\langle\mathbf{M}\rangle_E$  will be parallel to  $\hat{\mathbf{e}}$ . Thus we can take the dot product of (6.5) with  $\hat{\mathbf{e}}$ , and then expand the RHS in a Taylor series about  $E = 0$ , which can be truncated at the first term since we are only interested in the linear response, so that

we get,

$$(\epsilon_s - 1)E = \frac{4\pi}{V} \langle \mathbf{M} \cdot \hat{\mathbf{e}} \rangle_E = \frac{4\pi}{V} E \frac{\partial}{\partial E} \langle \mathbf{M} \cdot \hat{\mathbf{e}} \rangle$$

where the omission of the subscript  $E$  on the angle brackets indicates the average with no applied field. Hence,

$$(\epsilon_s - 1) = \frac{4\pi}{V} \frac{\partial}{\partial E} \langle \mathbf{M} \cdot \hat{\mathbf{e}} \rangle = \frac{4\pi}{V} \left( \frac{\partial E_o}{\partial E} \frac{\partial}{\partial E_o} \langle \mathbf{M} \cdot \hat{\mathbf{e}} \rangle \right) \quad (6.6)$$

The field within the dielectric is the Maxwell field  $E$ , but it is more convenient to introduce the actual field that acts upon the volume under consideration. This value is denoted here as  $E_o$ , and this is the applied, or cavity, field which would exist if all the molecules were removed from  $V$ . Simple electrostatics gives the relation between  $E$  and  $E_o$  as  $E_o = \frac{3\epsilon_s}{2\epsilon_s + 1} E$ , where  $\epsilon_s$  is the static dielectric constant of the fluid.

Applying classical statistical mechanics to the system of  $N$  particles in the applied field, a formal expression can be obtained for the expectation value  $\langle \mathbf{M} \cdot \hat{\mathbf{e}} \rangle$ . If the integral over all positions and orientations is denoted as  $\int dX$  and the energy of the configuration  $X$  in the applied field  $E_o$  by  $U(X, E_o)$ , then

$$\langle \mathbf{M} \cdot \hat{\mathbf{e}} \rangle = \frac{1}{Z} \int dX (\mathbf{M} \cdot \hat{\mathbf{e}}) \exp \left( -U(X, E_o) / kT \right) \quad (6.7)$$

with  $Z = \int dX \exp(-U(X, E_o) / kT)$ . Thus we can write,

$$\begin{aligned} \frac{\partial \langle \mathbf{M} \cdot \hat{\mathbf{e}} \rangle}{\partial E_o} &= \frac{1}{Z} \int dX \frac{\partial}{\partial E_o} (\mathbf{M} \cdot \hat{\mathbf{e}}) \exp(-U(X, 0) / kT) - \frac{1}{Z} \frac{1}{kT} \int dX \mathbf{M} \cdot \hat{\mathbf{e}} \frac{\partial U}{\partial E_o} \exp(-U(X, 0)) \\ &\quad + \frac{1}{Z^2} \frac{1}{kT} \int dX (\mathbf{M} \cdot \hat{\mathbf{e}}) \exp(-U(X, 0) / kT) \int dX \frac{\partial U}{\partial E_o} \exp(-U(X, 0) / kT) \\ &= \left\langle \frac{\partial}{\partial E_o} (\mathbf{M} \cdot \hat{\mathbf{e}}) \right\rangle - \frac{1}{kT} \langle \mathbf{M} \cdot \hat{\mathbf{e}} \frac{\partial U}{\partial E_o} \rangle + \frac{1}{kT} \langle \mathbf{M} \cdot \hat{\mathbf{e}} \rangle \left\langle \frac{\partial U}{\partial E_o} \right\rangle \\ &= \frac{1}{kT} \langle (\mathbf{M} \cdot \hat{\mathbf{e}})^2 \rangle \\ &= \frac{1}{3kT} \langle M^2 \rangle, \end{aligned} \quad (6.8)$$

since we have  $\partial U / \partial E_o = -\mathbf{M} \cdot \hat{\mathbf{e}}$  and also  $\langle \mathbf{M} \cdot \hat{\mathbf{e}} \rangle = 0$ . In the final equation we have used the fact that  $\langle \cos^2 \theta \rangle = 1/3$ . Thus the final relation obtained is,

$$\frac{(\epsilon_s - 1)(2\epsilon_s + 1)}{3\epsilon_s} = \frac{4\pi}{V} \frac{\langle M^2 \rangle}{3kT} \quad (6.9)$$

It can be seen that the mean square fluctuations of the total moment within a sphere immersed in its own medium are directly related to the dielectric constant.

The expectation value  $\langle M^2 \rangle$  can be expressed as,

$$\begin{aligned} \langle M^2 \rangle &= \langle \mathbf{M} \cdot \mathbf{M} \rangle = \langle (\sum_i \boldsymbol{\mu}_i) \cdot (\sum_j \boldsymbol{\mu}_j) \rangle \\ &= \mu^2 \langle \sum_i \sum_j \cos \theta_{ij} \rangle \end{aligned} \quad (6.10)$$

where  $\theta_{ij}$  is the angle between dipoles  $\boldsymbol{\mu}_i$  and  $\boldsymbol{\mu}_j$ . For a sufficiently large volume  $V$ , the value of  $\sum_i \cos \theta_{ij}$  should be virtually independent of the position of the  $j^{\text{th}}$  molecule and so we can write  $\langle M^2 \rangle = \mu^2 N \sum_j \langle \cos \theta_{ij} \rangle$  (for a more complete discussion of this point, see e.g. ref. [2]). Using this, equation (6.9) can be rearranged as,

$$\begin{aligned} \frac{(\epsilon_s - 1)(2\epsilon_s + 1)}{12\pi\epsilon_s} &= \frac{\rho}{3kT} \mu^2 \langle \sum_j \cos \theta_{ij} \rangle \\ &= \frac{\rho}{3kT} \mu^2 g \end{aligned} \quad (6.11)$$

where  $g$  is known as the Kirkwood correlation factor. For  $g = 1$  the Onsager equation is recovered, and so (6.11) can be seen as a generalization of this result.

The Kirkwood  $g$  factor is of course related to the more general pair correlation function for the molecular liquid which is  $h(\mathbf{r}_1, \boldsymbol{\Omega}_1, \mathbf{r}_2, \boldsymbol{\Omega}_2) = h(12)$ . Rather than deal with the whole of this function, it is more convenient to expand it in a series of terms, the coefficients of which are rotationally invariant (i.e. angle independent). This procedure is described in ref. [6], for example, and leads to  $h(12) = h_s(r) + h_\Delta(r)\Delta(12) + h_D(r)D(12) + \dots$ , where the angle dependence is in the functions such as  $\Delta(12) = \hat{\boldsymbol{\mu}}_1 \cdot \hat{\boldsymbol{\mu}}_2$  and  $D(12) = 3(\hat{\boldsymbol{\mu}}_1 \cdot \hat{\mathbf{r}})(\hat{\boldsymbol{\mu}}_2 \cdot \hat{\mathbf{r}}) - (\hat{\boldsymbol{\mu}}_1 \cdot \hat{\boldsymbol{\mu}}_2)$ . We are mainly interested in the function  $h_\Delta(r)$  here because it is this term that determines the value of the Kirkwood  $g$  factor.  $h_\Delta(r)$  is related to the  $h(12)$  by the equation,

$$h_{\Delta}(r) = 3 \int \frac{h(12)\Delta(12)}{\Omega^2} d\Omega_1 d\Omega_2 \quad (6.12)$$

From the above definitions  $g$  may be expressed as,

$$g = \int_0^{\infty} h_{\Delta}(r) 4\pi r^2 dr \quad (6.13)$$

Thus the dielectric constant can be directly related to part of the pair correlation function, but calculation of  $h(12)$  is of course very difficult. Some progress has nevertheless been made in the theoretical treatment polar fluids, such as the important work of Nienhuis and Deutch<sup>1</sup>. More recently Patey *et al*<sup>7,8</sup> have used a quadratic HNC approximation to find  $\epsilon_s$  for a fluid of hard spheres with variable dipole and quadrupole moments at the centre. Some calculations have also been made for the Stockmayer potential.

### 6.3. The frequency dependent dielectric constant

#### 6.3.1. The <sup>D</sup>Debye equation

Since the permanent dipoles within a liquid take a finite time to reorientate when an electric field is applied, the dielectric constant measured in an alternating field, of angular frequency  $\omega$ , is different to that found in the static case. The frequency dependent form of  $\epsilon_s$  is represented as a complex quantity,  $\epsilon(\omega) = \epsilon'(\omega) - i\epsilon''(\omega)$ , where  $\epsilon'(0) = \epsilon_s$  and  $\epsilon''(0) = 0$ <sup>†</sup>.

One of the simplest (and often quite adequate) models for understanding  $\epsilon(\omega)$  is that given by Debye<sup>10</sup>. The Debye equation can be derived starting from the assumption that the rate of change of the polarization at any time ( $P(t)$ ) is simply proportional to the difference between the equilibrium value ( $P_{eqm}$ ) and the current

<sup>†</sup> Note that we assume  $\epsilon(\omega)$  to be independent of the spatial variation of the electric field, i.e.  $\epsilon(\mathbf{k}, \omega) = \epsilon(\omega)$ , at least in the low wave vector ( $\mathbf{k}$ ) limit. This point is discussed in detail by, for example, Madden and Kivelson<sup>9</sup>. At extremely high frequencies the electric field can vary over lengths that are shorter than the range of the correlation functions which are important in the determination of the dielectric constant. It may then be necessary to treat  $\epsilon(\omega)$  as been dependent on  $\mathbf{k}$ , as well as frequency, but we are not interested in this limit.

value,  $\frac{dP}{dt} \propto P(t) - P_{eqm}$ . The resulting differential equation gives an exponential solution for the polarization, such as  $P(t) = P_{eqm}(1 - \exp(-t/\tau))$ , in the case of a constant field applied at  $t = 0$  (we ignore the polarizability which leads to a small, virtually instantaneous, response since this is absent in the Stockmayer model). The time constant  $\tau$  is the macroscopic relaxation time of the system.

The solution for  $P(t)$  in an alternating field,  $E\hat{e}e^{i\omega t}$ , allows the calculation of  $\epsilon(\omega)$ , via the use of equation (6.2). It is found that,

$$\epsilon(\omega) = \epsilon'(\omega) - i\epsilon''(\omega) = 1 + \frac{\epsilon_s - 1}{1 + i\omega^2\tau^2}$$

and hence the two components are,

$$\begin{aligned}\epsilon'(\omega) &= 1 + \frac{\epsilon_s - 1}{1 + \omega^2\tau^2} \\ \epsilon''(\omega) &= \frac{\epsilon_s - 1}{1 + \omega^2\tau^2} \omega\tau\end{aligned}\tag{6.14}$$

These equations give the simple Debye behaviour of the dielectric constant, with  $\epsilon'(\omega)$  falling monotonically from  $\epsilon_s$  to unity at very high frequency, while  $\epsilon''(\omega)$  has its peak value at  $\omega = \tau^{-1}$ , and disappears at low and high  $\omega$ . It is sometimes more convenient to display both parts of  $\epsilon(\omega)$  on the same graph, in a so-called 'Cole-Cole' plot. This is just a graph of  $\epsilon'(\omega)$  against  $\epsilon''(\omega)$ , and for the Debye model this just gives a semi-circle, radius  $(\epsilon_s - 1)/2$  centred at  $\epsilon' = (\epsilon_s + 1)/2$ ,  $\epsilon'' = 0$ . Such a plot is convenient for comparing experimental data with theoretical curves like the Debye result.

While the Debye result is a good approximation to the behaviour of a many simple dielectrics, it has a number of limitations. In particular, at very short times the response of the dipoles to the applied field is limited by their inertia, which is not allowed for in the Debye treatment. More complex materials can also have a range of different relaxation times. Various empirical modifications to the Debye theory have been proposed (e.g. see refs. [11] and [5]) with varying degrees of success, but we shall not discuss these here.

### 6.3.2. Relation of $\epsilon(\omega)$ to the CF $\langle \mathbf{M}(0) \cdot \mathbf{M}(t) \rangle$

It has already been seen that the static dielectric constant can be related to the mean square fluctuations of the total moment within a spherical sub-volume of the fluid. An analogous relation can be derived for the dynamic dielectric constant in terms of the time-dependent extension of  $\langle M^2 \rangle$ , the normalized auto-correlation function of the moment,

$$\Phi(t) = \frac{\langle \mathbf{M}(0) \cdot \mathbf{M}(t) \rangle}{\langle M^2 \rangle} \quad (6.15)$$

The derivation of such a relation can be made using the linear response theory of Kubo<sup>12</sup>. Applying this to the total dipole moment of our spherical sample yields<sup>13</sup> the following expression for  $\langle \mathbf{M}(t) \rangle_{E_o}$  in an applied field  $E_o(t)$ ,

$$\langle \mathbf{M}(t) \rangle_{E_o} = -\frac{1}{3kT} \int_{-\infty}^t dt' E_o(t') \frac{d}{dt'} \langle \mathbf{M}(0) \cdot \mathbf{M}(t') \rangle \quad (6.16)$$

which is just an "after-effect" expression for the moment, except that the response kernel is given. For the case of an immersed sphere the applied field  $E_o(t)$  is just the cavity field, as used in the static formula, (6.9).

Within a homogeneous system the static formula for  $\epsilon_s$ , (6.2), can be extended to express  $\epsilon(\omega)$  as,

$$\epsilon(\omega) - 1 = 4\pi P(\omega)/E(\omega) = 4\pi \frac{\langle M(\omega) \rangle_E}{VE(\omega)} \quad (6.17)$$

where we assume a homogeneous applied field of the form  $E_o e^{i\omega t}$  and have taken the frequency transform of the various terms involved.

The susceptibility of the dielectric to the applied field (rather than the Maxwell field, as in (6.2)) can be defined as,

$$\chi_o(\omega) = \frac{P(\omega)}{E_o(\omega)} = \frac{1}{V} \frac{\langle M(\omega) \rangle_E}{E_o(\omega)} \quad (6.18)$$

Combining this equation with the linear response result, (6.16), eventually gives,

$$\chi_o(\omega) = \frac{\langle M^2 \rangle}{3kTV} \left( 1 - i\omega \int_0^{\infty} \Phi(t) e^{-i\omega t} dt \right) \quad (6.19)$$

Thus  $\epsilon(\omega)$  may be expressed as,

$$\epsilon(\omega)-1 = \frac{4\pi}{3} \frac{\langle M^2 \rangle}{kTV} \left( 1 - i\omega \int_0^\infty \Phi(t) e^{-i\omega t} dt \right) \frac{E_o(\omega)}{E(\omega)} \quad (6.20)$$

Ignoring retardation effects (the “quasi-dielectric” limit) the ratio of the applied field to the Maxwell field at the frequency  $\omega$  is just given by the same formula as for the static case, with  $\epsilon(\omega)$  replacing  $\epsilon_s$ . For a spherical volume immersed in its own medium we get  $E_o(\omega)/E(\omega) = 3\epsilon(\omega)/(2\epsilon(\omega)+1)$ . Using this in (6.20), with the static result from (6.9) yields,

$$\left( 1 - i\omega \int_0^\infty \Phi(t) e^{-i\omega t} dt \right) = \frac{\epsilon_s}{(2\epsilon_s+1)(\epsilon_s-1)} \frac{(2\epsilon(\omega)+1)(\epsilon(\omega)-1)}{\epsilon(\omega)} \quad (6.21)$$

This equation was first obtained by Fatuzzo and Mason<sup>14</sup>.

While the functions  $\epsilon(\omega)$  and  $\chi(\omega)$  are shape independent, the other functions such as  $\langle M^2 \rangle$ ,  $\Phi(t)$  and  $\chi_o(\omega)$  vary according to the boundary conditions of the sample. For example, in the case of a dielectric sphere in vacuo, the above type of analysis gives the result,

$$\left( 1 - i\omega \int_0^\infty \Phi(t) e^{-i\omega t} dt \right) = \frac{\epsilon(\omega)-1}{\epsilon(\omega)+2} \frac{\epsilon_s+2}{\epsilon_s-1} \quad (6.22)$$

so that the correlation function  $\Phi(t)$  must be different from that obtained for the immersed sphere. This topic has been discussed in relation to the computer simulation of homogeneous systems by Neumann and Steinhauser in a recent paper<sup>15</sup>.

#### 6.4. Computer simulation of dipolar fluids

The method that we have used for simulating the Stockmayer fluid (described in chapter two) is based on a simple spherical truncation of the interaction potential, though with a much greater cut-off than usual. Due to the long range nature of the dipolar force, various schemes have been employed in homogeneous simulations to account for the significant interaction that would, in a macroscopic liquid, occur

between an individual dipole and the fluid beyond the cut-off,  $r_c$ . These methods have been reviewed by several authors<sup>16,15</sup> and we shall just mention some of the basic details for comparison. The two most commonly used methods are:

(1) Reaction field techniques, in which a simple spherical truncation of the interaction is used, but it is also assumed that a continuous dielectric exists beyond the cut-off sphere, with a dielectric constant  $\epsilon_{RF}$ . This continuum produces a reaction field on each dipole, like that used in Onsager's calculation of  $\epsilon_s$ , which is proportional to the total moment within  $r_c$ ,  $\mathbf{M} = \sum_{r < r_c} \boldsymbol{\mu}_i$ . Since the response of this reaction field is instantaneous, it corresponds to a frequency independent dielectric constant beyond the cut-off<sup>15</sup>. The value of  $\epsilon_{RF}$  is usually chosen to be as close as possible to the expected value of  $\epsilon_s$  for the fluid. It is also possible to use  $\epsilon_{RF} = \infty$ , which corresponds to "conducting boundary conditions". The reaction field method was first used by Barker and Watts<sup>17</sup>

(2) The Ewald-Kornfeld<sup>18,19</sup> summation technique, where by interactions with all dipoles beyond  $r_c$  (i.e. including all the periodic images) are expressed as two rapidly convergent series which can then be evaluated. This is a more time consuming procedure than the reaction field method, and it is necessary to exercise great care in the accurate evaluation of these series<sup>20</sup>. It has been shown that this method gives similar results to (1), and also effectively corresponds to a frequency independent dielectric constant beyond  $r_c$ .

Other methods used include that due to Ladd<sup>21</sup> who approximated the effect of each image cell by a number of point multipole moments at its centre. These can then be summed over relatively quickly, though the result is effectively similar to that of the Ewald method.

It is known that the use of a simple spherical truncation of the dipolar potential leads to a significantly different form of the function  $h_{\Delta}(r)$  near  $r = r_c$ , compared to

that obtained with any of the above methods<sup>22</sup>. This is for homogeneous simulations with  $r_c \sim 4\sigma$ . However, both lattice summation (e.g. Ewald) and reaction field methods are to some degree artificial and some differences still exist between the results of these methods. The system that has been studied in this work does still involve a simple spherical truncation, but with a value of  $r_c$  several times greater than that possible in more conventional simulations. In addition, the cut-off mainly effects the much less numerous liquid-gas interactions, while most liquid-liquid interactions are completely accounted for within the drop. The use of lattice summation or reaction field corrections is not useful or desirable for our system, since we are interested in a microscopic drop surrounded by low density vapour, and do not wish to include the image effects.

In the following chapters we investigate the feasibility of using these effectively isolated drops to measure the static and dynamic dielectric constant. We shall compare our results with some of those obtained by other authors, using the more conventional techniques.

## References

1. G.Nienhuis and J.M.Deutch, *J. Chem. Phys.*, vol. 55, p. 4213, 1971.
2. C.J.F.Böttcher, *Theory of Electric Polarization (Vol. 1)*, Elsevier, New York, 1973.
3. L.Onsager, *J. Am. Chem. Soc.*, vol. 58, p. 1486, 1936.
4. J.G.Kirkwood, *J. Chem. Phys.*, vol. 7, p. 911, 1939.
5. H.Fröhlich, *Theory of Dielectrics*, Clarendon Press, Oxford, 1949.
6. G.S.Stell, G.Patey, and J.Høye, *Adv. Chem. Phys.*, vol. 48, p. 183, 1981.
7. G.N.Patey, D.Levesque, and J.J.Weis, *Molec. Phys.*, vol. 38, p. 219, 1979.
8. G.N.Patey, D.Levesque, and J.J.Weis, *Molec. Phys.*, vol. 38, p. 1635, 1979.

9. P.Madden and D.Kivelson, "A consistent molecular treatment of dielectric phenomena," *Adv. Chem. Phys.*, vol. 56, 1984.
10. P.Debye, *Polar molecules*, Dover, New York, 1945.
11. J.G.Powles, *Trans. Faraday Soc.*, vol. 44, p. 802, 1948.
12. R.Kubo, *J. Phys. Soc. Japan*, vol. 12, p. 570, 1957.
13. C.Brot, *Dielectric and related molecular processes*, 2, p. 1, Chemical Society, London, 1975. M.Davis, Ed.
14. E.Fatuzzo and P.R.Mason, *Proc. Phys. Soc. (London)*, vol. 90, p. 741, 1967.
15. M.Neumann and O.Steinhauser, *Chem. Phys. Letters*, vol. 102, p. 508, 1983.
16. D.J.Adams, E.M.Adams, and J.G.Hills, *Molec. Phys.*, vol. 38, p. 387, 1979.
17. J.A.Barker and R.O.Watts, *Molec. Phys.*, vol. 26, p. 789, 1973.
18. P.P.Ewald, *Annlns. Phys.*, vol. 64, p. 253, 1921.
19. H.Kornfeld, *Z. Phys.*, vol. 22, p. 27, 1924.
20. D.J.Adams and I.R.McDonald, *Molec. Phys.*, vol. 32, p. 931, 1976.
21. A.J.C.Ladd, *Molec. Phys.*, vol. 36, p. 1039, 1977.
22. M.Neumann, O.Steinhauser, and G.S.Pawley, *Molec. Phys.*, vol. 52, p. 97, 1984.

## Chapter Seven: Results for the static dielectric constant

### 7.1. Introduction

In this chapter we report results for the mean square moment,  $\langle M^2(r) \rangle$ , within the series of Stockmayer drops that have been studied. It is shown how these measurements can be used to obtain the static dielectric constant of the bulk liquid, using a generalization of the Fröhlich result, equation (6.9). The results will be compared with data due to Adams and Adams<sup>1</sup>, and others, who have performed homogeneous simulations, using Ewald-Kornfeld summations, at similar state points.

The analysis of  $\langle M^2(r) \rangle$  is also extended to treat the drop surface in more detail. While the true form of  $\epsilon_s$  in the liquid vapour interface must strictly require a tensorial representation, it is shown that a simple scalar function for  $\epsilon_s(r)$  can give a satisfactory explanation of most of the observed  $\langle M^2(r) \rangle$  data.

### 7.2. Measuring $\langle M^2(r) \rangle$ within the drops

During most of the longer Stockmayer simulations, detailed in chapter three, the mean square moment,  $\langle M^2(r) \rangle$ , was measured. This quantity was obtained for a number of different sphere radii, each such notional sphere being centred on the centre of mass of the drop. Following the approach used to sample the density profile we chose to use a set of  $N$  sphere sizes, with the radius of the  $i^{\text{th}}$  sphere being  $r_i = i(L/2N)$  where  $L$  is the length of the periodic cell and we took  $N = 50$  (as for  $\rho(r)$ ). To efficiently sample the values of  $M^2(r_i)$ , the vector moment within each shell,  $\mathbf{M}(r_i \rightarrow r_{i+1})$ , is first computed (see listing in appendix for details). Then the total moment of each sphere, and hence  $M^2(r_i)$ , can be obtained by a summation over the appropriate set of shells.

Thus for each drop we have data for the function  $\langle M^2(r) \rangle$ . For comparison with theory it is more convenient here to present values of  $\langle M^2(r) \rangle / (3kTr^3)$  rather than just  $\langle M^2(r) \rangle$ , and we shall refer to this “normalized” quantity as the mean

square moment, or MSM.

Figure (7.1) shows a typical plot of the MSM against  $r$  for the 450 particle S1 system, state (D7). Also shown for comparison on the same figure is the density profile of this drop. It can be seen that the MSM has a relatively low value in the vapour, but that this rises rapidly through the interface region and begins to reach a plateau inside the drop, where the density is approximately constant. However, at very small  $r$  the MSM again decreases quite sharply. A qualitatively similar behaviour was observed in the other drops for which the MSM was measured. Before examining these results in detail it is necessary to discuss the interpretation of this data, which is given in the following sections.

### 7.3. The generalized MSM for a macroscopic dielectric sphere

#### 7.3.1. Derivation of the formula

It was shown in chapter six that the MSM of a sphere immersed in its own medium is directly related to the dielectric constant by the equation (6.9). A similar equation can be derived in the case of an isolated sphere in vacuum<sup>2</sup> which is that,

$$\frac{4\pi}{3} \frac{\langle M^2 \rangle}{3VKT} = \frac{\langle M^2 \rangle}{3R^3kT} (\equiv \text{MSM}) = \frac{\epsilon_s - 1}{\epsilon_s + 2} \quad (7.1)$$

Thus for all  $\epsilon_s > 1$  the vacuum value of the MSM (equation (7.1)) is always less than the immersed value, (6.9). The data shown in figure (7.1) is at least in qualitative agreement with this observation, ignoring the interface region and the data at small  $r$ . A quantitative comparison can be made by calculating the generalization of equations (6.9) and (7.1) to find the MSM of any given sphere of radius  $r'$ , centred within a homogeneous dielectric sphere of radius  $R$ , in vacuum (corrections due to the vapour are considered latter). It is assumed that all parts of the system can be treated macroscopically and that  $\epsilon = \epsilon_s$  for  $r \leq R$  with  $\epsilon = 1$  for  $r > R$ .

Combining equations (6.6) and (6.8) from chapter six gives,

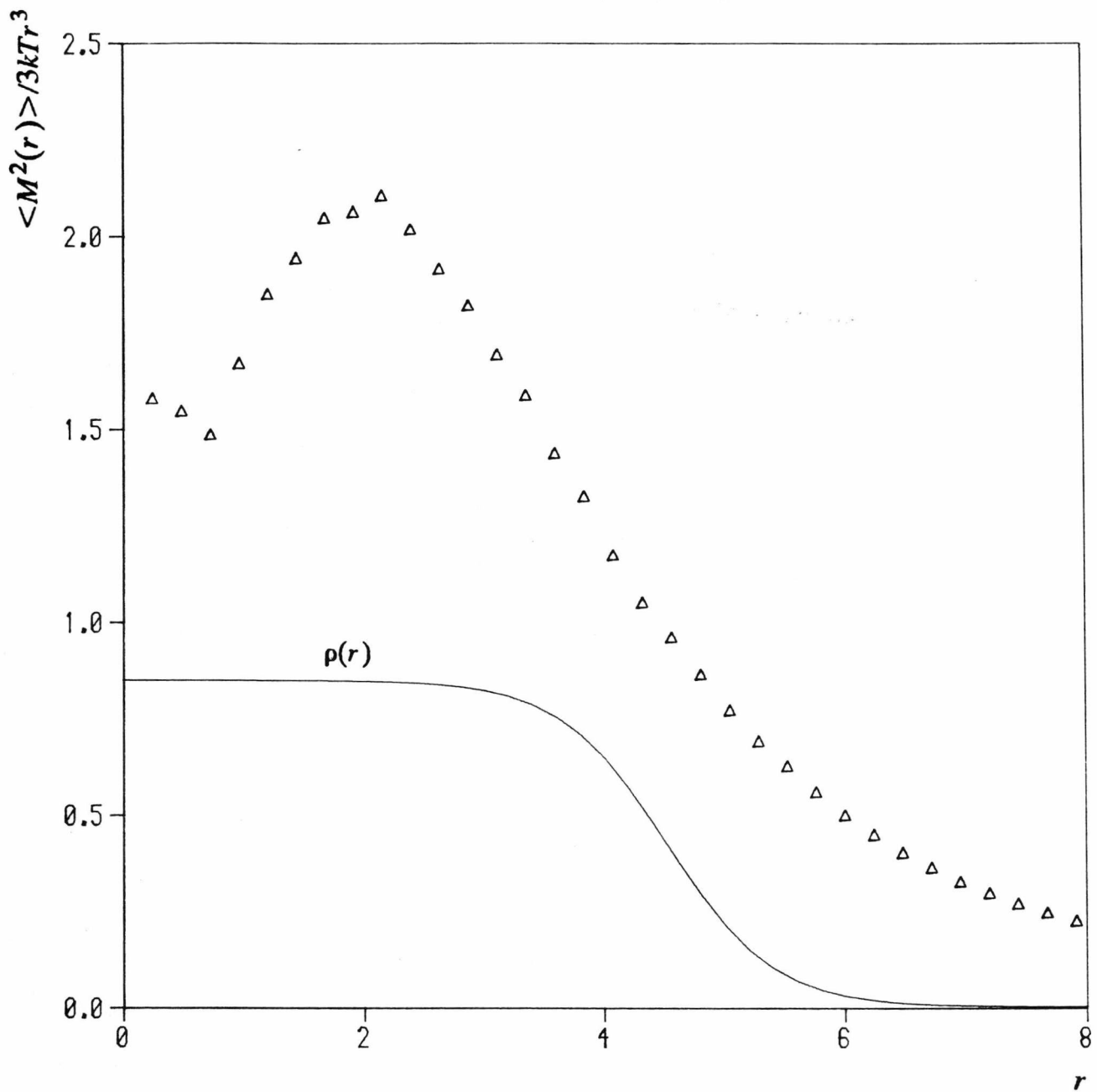


Figure 7.1: The measured MSM ( $= \langle M^2(r) \rangle / 3kTr^3$ ) as a function of sphere radius,  $r$ . The data shown ( $\Delta$ ) is for state (D7), an S1 drop with  $N_p = 450$ , at a temperature of  $T = 0.809$ . The equimolar radius is  $R_e = 4.7$  in this case. For comparison, the density profile of the drop (the tanh fit to  $\rho(r)$ ) is also shown, on the same scale.

$$\frac{\langle M^2(r) \rangle}{3kTr^3} = \frac{(\epsilon_s - 1)}{3} \left( \frac{\partial E_o}{\partial E} \right)^{-1} \quad (7.2)$$

The Maxwell field within the whole sphere (radius  $R$ ) is simply related to the field at infinity ( $E_\infty$ ) by  $E = \frac{3}{\epsilon_s + 2} E_\infty$ . To find the cavity field,  $E_o$ , that acts on the spherical region of radius  $r'$  requires the solution of the Laplace equation for the uniform field inside a dielectric shell (i.e.  $\epsilon = 1$  for  $r < r'$ ) subject to  $E = E_\infty$  at infinity. This can be done using a simple extension of the analysis to find the Maxwell field within a sphere that is given in many texts on dielectrics, e.g. see appendix 2 of reference[2]. The actual calculation is relatively straight forward and yields the result  $E_o = E_\infty 9\epsilon_s / [(\epsilon_s + 2)(2\epsilon_s + 1) - 2(\epsilon_s - 1)^2 (r/R)^3]$ . This allows the determination of  $\left( \frac{\partial E_o}{\partial E} \right)$  and so the more general expression for the MSM is found to be,

$$\frac{\langle M^2(r) \rangle}{3kTr^3} = \frac{\epsilon_s - 1}{9\epsilon_s (\epsilon_s + 2)} \left[ (\epsilon_s + 2)(2\epsilon_s + 1) - 2(\epsilon_s - 1)^2 \frac{r^3}{R^3} \right] \quad (7.3)$$

The limits of  $(r/R) \rightarrow 0$  and  $(r/R) \rightarrow 1$  give the original equations (6.9) and (7.1) respectively, as required.

Equation (7.3) was in fact first obtained by Berendsen<sup>3</sup>. It has also been used by Adams and McDonald<sup>4</sup> in a study of polar lattices and the two dimensional analogue was used by Bossis<sup>5,6</sup> in studies of a 2D Stockmayer system.

In figure (7.2) we plot the MSM as a function of  $(r/R)$ , as given by equation (7.3), for a range of  $\epsilon_s$  values. Beyond  $r = R$  the curves have been extended by plotting  $\langle M^2(R) \rangle / 3kTr^3$ .

An important fact that is illustrated by these curves is that the values of the MSM near  $r = R$  all lie very close together. This effect is most pronounced for the larger values of  $\epsilon_s$ . At the  $r \rightarrow 0$  limit on the other hand, the MSM curves show a much greater separation even for very large values of  $\epsilon_s$ . Thus it is much easier, and more accurate, to calculate  $\epsilon_s$  from measurements of the MSM for an "immersed" system rather than using the "sphere in vacuo" results. This is another argument that has

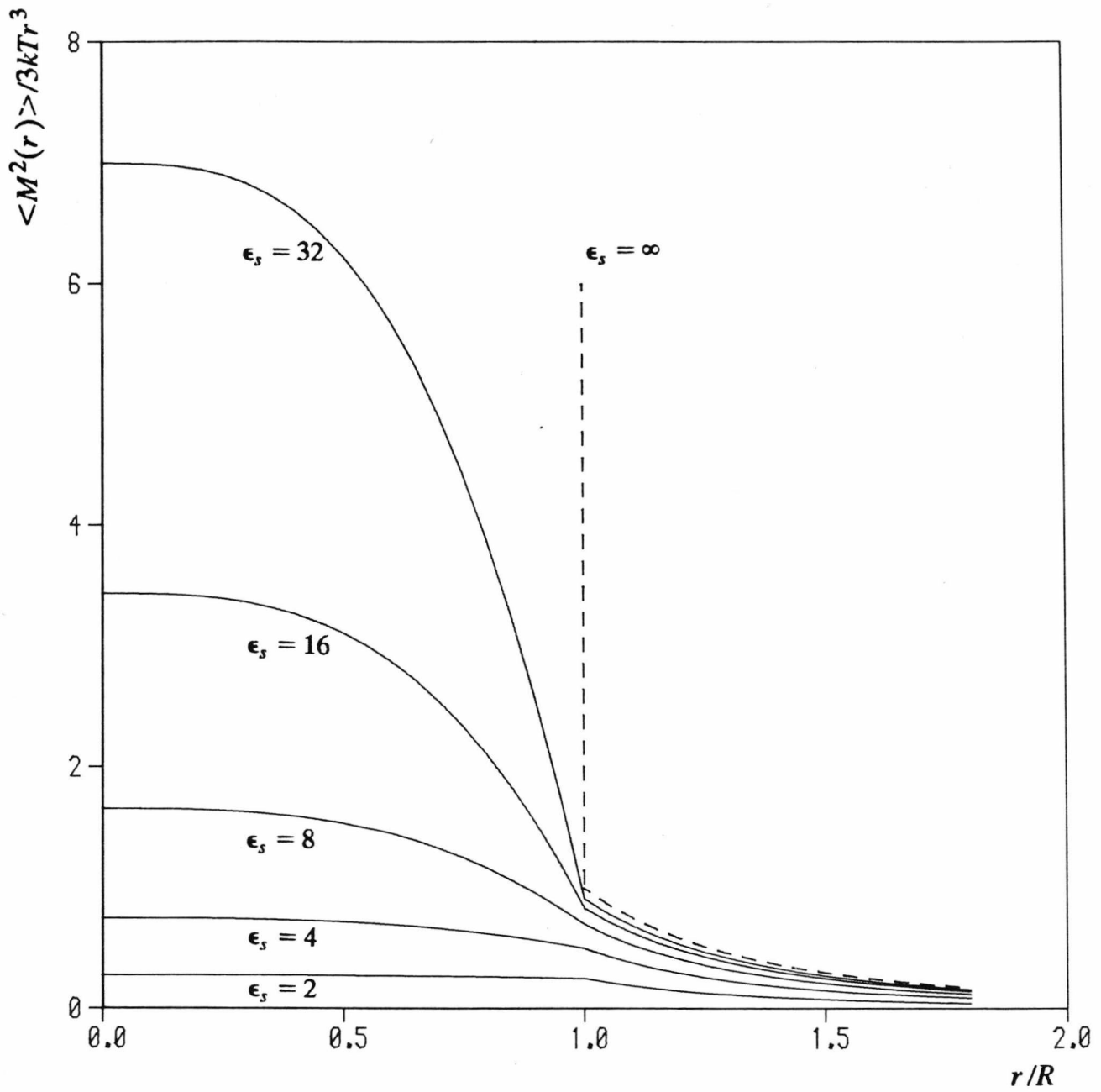


Figure 7.2: The MSM within a macroscopic sphere (sharp surface at  $R$ ) as a function of  $r/R$ , for a range of values of  $\epsilon_s$ .

recently been put forward against using a simple spherical truncation in homogeneous simulations of dipolar fluids<sup>7</sup>.

### 7.3.2. Comparison with simulation data

In this section we shall assume that the dielectric profile of a Stockmayer drop can be adequately approximated by the result obtained above for a macroscopic system with a sharp interface. Simulation data is compared with equation (7.3) by setting the radius  $R$  equal to  $R_e$ , the equimolar radius of the drop, and ignoring the fact that the vapour has a dielectric constant greater than unity.

In figure (7.3) we have again plotted the MSM data of state (D7) but also included is the curve obtained from equation (7.3) for a dielectric constant of  $\epsilon_s = 10.3$ . This particular value was chosen to give a best fit to the data in the approximate range  $2.4 \leq r \leq 4$ . It is clear that the macroscopic theory breaks down at small  $r$  (we discuss this in more detail latter) and this becomes most notable for  $r$  below  $\sim 2.4$ . Also the fact that the interface region is, in reality, quite diffuse means that (7.3) cannot be expected to hold well for  $r \sim R_e$ , and so data above  $r = 4$  was ignored in selecting the best fit for  $\epsilon_s$ .

Within the limited  $r$  region used the agreement between the data and equation (7.3) is quite good. Through the surface of the drop, and also in the vapour, the data indicates rather higher values of the MSM than are predicted by the theory. This is as might be expected since we have ignored the significant number of molecules that lie above  $R_e$ , and the contribution of the vapour region.

### 7.3.3. Importance of surface width

As a first attempt to treat the interface region in a more realistic way, the sharp dielectric profile that was assumed above can be replaced with a "stepped" surface defined by,

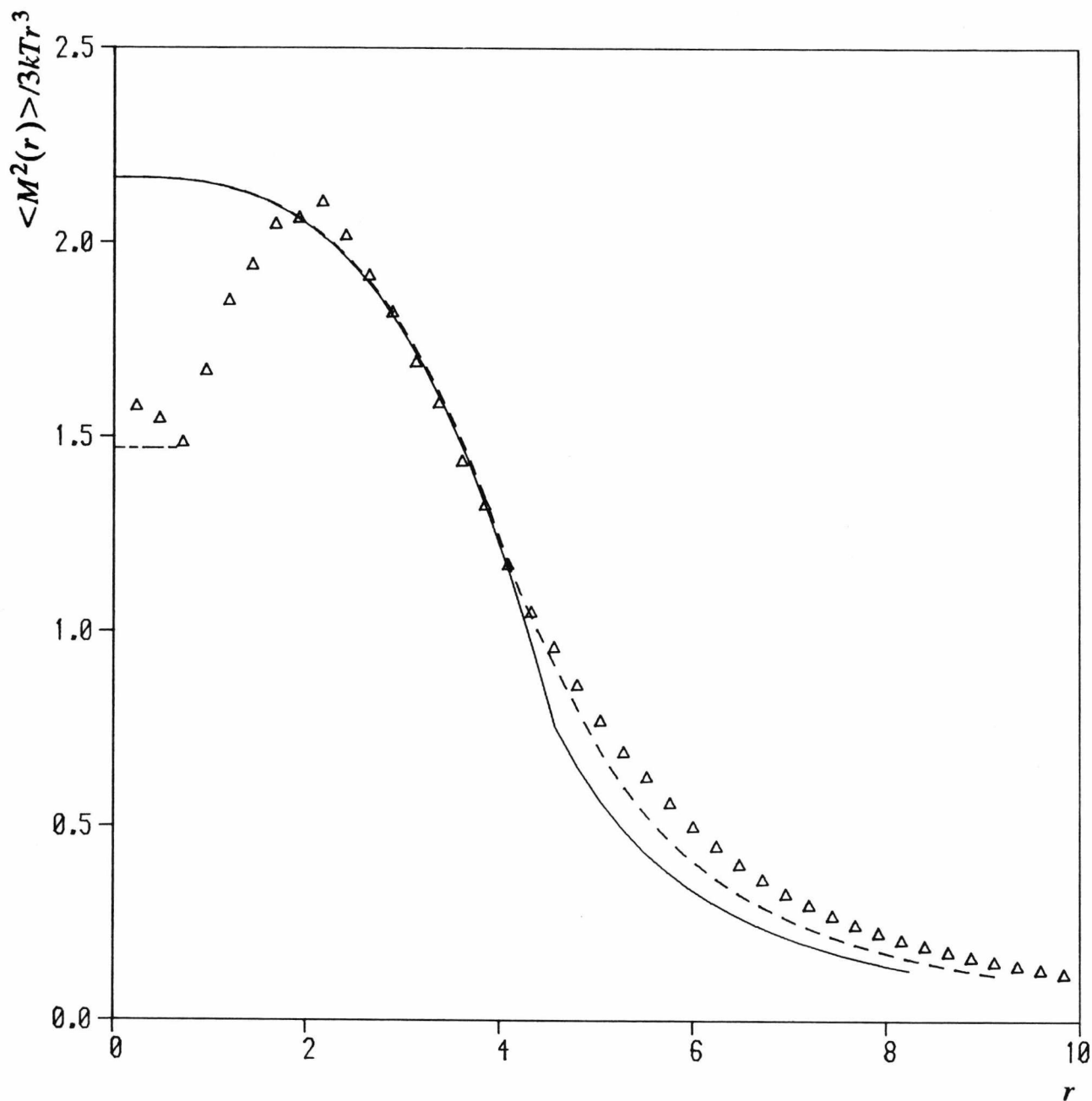


Figure 7.3: A comparison of the simulation data for state (D7) ( $\Delta$ ) with the calculated MSM (solid line) of a macroscopic sphere with a dielectric constant of  $\epsilon_s = 10.3$  and a radius  $R = R_c = 4.7$  in this case. With the “stepped” dielectric profile described in the text ( $\epsilon_s = (10.3+1)/2$  between  $0.9R_c$  and  $1.1R_c$ ) the dashed curve is obtained. The short chained line indicates the “microscopic” limiting value for this particular system, as  $r \rightarrow 0$ .

$$\begin{aligned}
 \epsilon_s(r) &= \epsilon_s && \text{if } r < R(1-\delta) \\
 &= \frac{\epsilon_s + 1}{2} && \text{if } R(1-\delta) \leq r \leq R(1+\delta) \\
 &= 1 && \text{if } r > R(1+\delta)
 \end{aligned} \tag{7.4}$$

where the step has a width of  $2\delta$  (here  $\delta$  is an arbitrary parameter, not to be confused with Tolman's  $\delta$  in chapter four).

The treatment of  $\langle M^2 \rangle$  for such a system is similar to that used for equation (7.3), though slightly more complex because of the extra layer. For any chosen radius  $r$  the cavity field that acts on the particles within the given sphere will be homogeneous as before, so that equation (6.8) is still applicable. For  $r \leq (R-\delta)$  the problem is just one of determining the ratio of the cavity field to the Maxwell field,  $\left(\frac{\partial E_o}{\partial E}\right)$ , as before. While it is feasible to solve the Laplace equation analytically for systems of a few shells, to give expressions like equation (7.3), it is easier to implement a numerical solution which can be extended to treat more complex systems later. The general form of the potential within each shell is  $\Phi_i(r) = -(A_i/r^2 + B_i r)\cos\theta$  and this can be combined with the boundary conditions at  $r = R \pm \delta$  and  $r = 0$  and  $r = \infty$  to find  $\left(\frac{\partial E_o}{\partial E}\right)$ . The details of this method are given in appendix D.

For the case of  $r > (R-\delta)$  we need to find the total MSM due to two regions with different values of  $\epsilon$  and  $E$ . The Maxwell field in the outer shell will in fact have a dipolar component in addition to the homogeneous part (i.e. the  $A_i$  term in the solution for  $\Phi_i(r)$  is non-zero). However this will produce no net moment, by symmetry, and it can be ignored. The total moment in the applied field  $E_o$  is then given by,

$$\langle M(r) \rangle_E = \sum_i (\epsilon_i - 1) \frac{V_i E_i}{4\pi} \tag{7.5}$$

where the sum is over the two separate regions within  $r$ , each of volume  $V_i$  and mean

Maxwell field  $E_i$  (the subscript  $E$  indicates that (7.5) is the mean response in an applied field, as opposed to functions such as  $\langle M^2(r) \rangle$ , which are measured in the absence of any field). The method of solution for the various fields in this case is also given in appendix D.

The resulting MSM that is obtained with such a 'stepped profile' is also shown in figure (7.3). The value of  $\delta$  was chosen to be  $\delta/R_c = 0.1$  to give an interface width of similar magnitude to that found for the density profile.

As can be seen, the agreement between this modified theoretical curve and the MSM data is rather better, at large  $r$  ( $>R-\delta$ ), than was obtained with the simple sharp interface. However the agreement is still not completely satisfactory. More significantly, we note that the values of the MSM for  $r < R-\delta$  are in fact very little different to those obtained without the surface step. Hence it appears that the exact details of the interface region only have a very marginal effect on the MSM well within the drop. Thus it is not necessary to accurately treat the behaviour of the dielectric constant in the surface to measure the dielectric constant of the bulk liquid.

Considering the above, it seems that the original estimate of  $\epsilon_s = 10.3$  that was found for the dielectric constant of the bulk fluid may, therefore, be a reasonably accurate one. From the spread of the data and the uncertainty in the exact range of  $r$  values that should be included in the fit, the error in this result may be of the order of  $\pm 10\%$ , i.e.  $\epsilon_s = 10.3 \pm 1$  at  $T = 0.81$  and a density of  $\rho = 0.85$ .

While it is possible to estimate the bulk liquid dielectric constant for all the studied Stockmayer states by this technique, we chose to first implement a more general treatment of the surface region. The details of this are given in the next section and it is hoped that the ambiguity in deciding which data to omit from the fitting process will be reduced by this more realistic model.

## 7.4. The MSM for a continuous dielectric profile

### 7.4.1. $\langle M^2(r) \rangle$ within the surface

It has been seen, as in figure (7.3), that the plot of the function  $\langle M^2(r) \rangle / 3kTr^3$  against  $r$  is relatively insensitive to the dielectric constant in the surface. However, the  $r^{-3}$  term that is included in this expression emphasizes the data in the bulk (at small  $r$ ) while suppressing the data in the surface and vapour regions. For a better comparison of these results with the macroscopic curves, a graph of just  $\langle M^2(r) \rangle$  against  $r$  can be more useful. Using the same data as before (i.e. state (D7)), such a plot has been drawn in figure (7.4). Also included in this figure are the  $\langle M^2(r) \rangle$  results, as calculated for the sharp interface and the stepped interface. It is clear that the behaviour of these latter curves in the surface and vapour regions is substantially different to that of the simulation data. The stepped profile only makes a marginal improvement to the fit in this figure.

The assumption that  $\epsilon_s = 1$  in the vapour region necessarily leads to the constant values of  $\langle M^2(r) \rangle$  that are shown in (7.4) at large  $r$ . The actual value of  $\epsilon_s$  well outside the drop can be calculated from the known vapour density, using the Onsager equation, (6.3), which is a good approximation at low density. This yields a value of  $\epsilon_s = 1.032$  for this particular state, (D7). It is relatively straightforward to modify the macroscopic theory of the sharp interface to allow for  $\epsilon_s > 1$  outside the drop, and the new curve that is obtained in this way is also shown in figure (7.4). We note that the increase of  $\langle M^2(r) \rangle$  at large  $r$  given by this result is very similar to that of the simulation data, but with the former curve shifted down by a constant amount.

The obvious conclusion from these results is that a better description of the behaviour of the MSM in the surface is required to explain the data. The simplest way to extend this analysis is to increase the number of dielectric shells until we have a virtually continuous profile, the shape of which can be adjusted to fit the observed

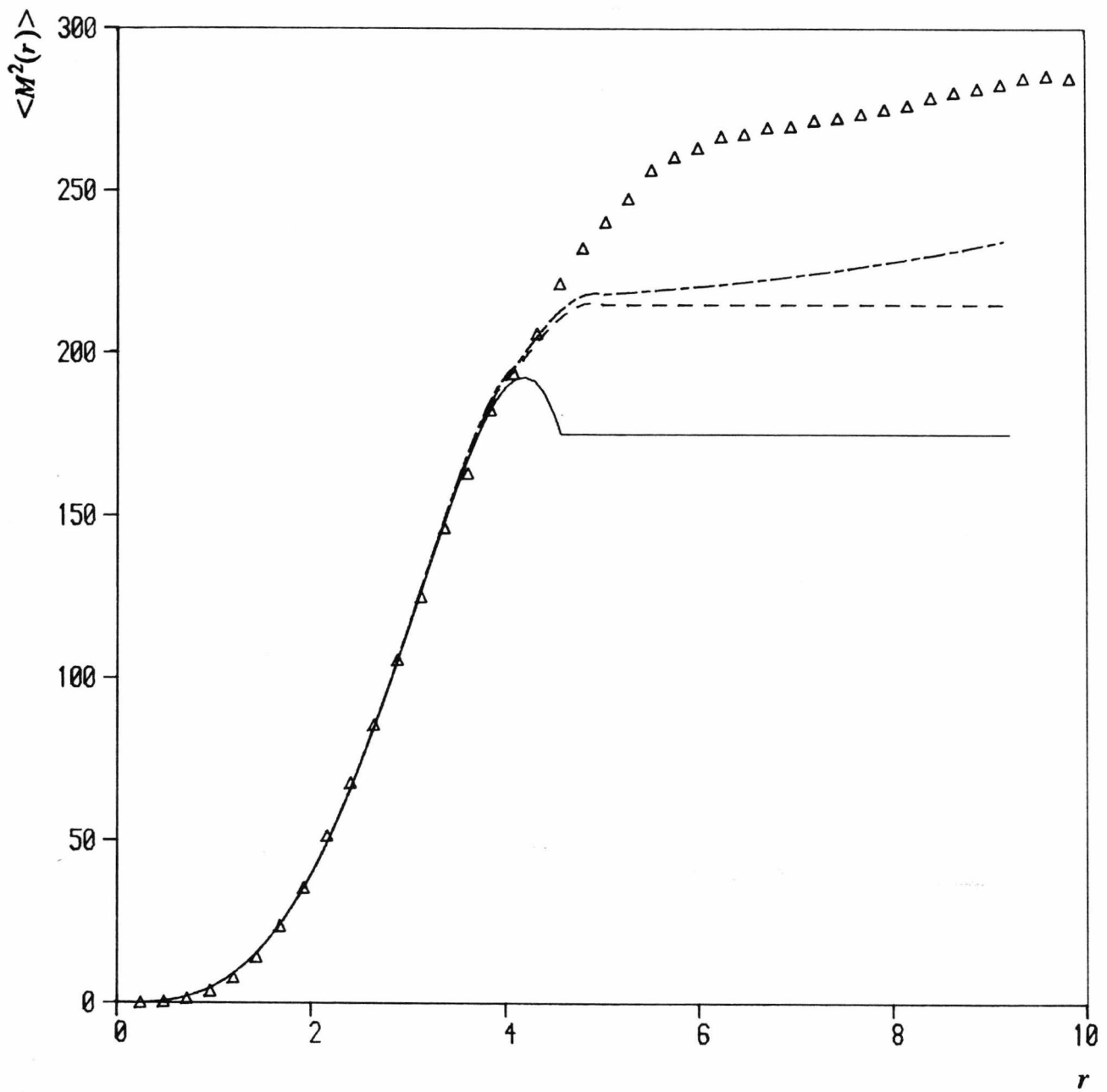


Figure 7.4: The actual function  $\langle M^2(r) \rangle$  as a function of  $r$  for state (D7) ( $\Delta$ ). The result corresponding to a macroscopic dielectric sphere with a sharp surface is given by the solid curve, while that for a stepped surface is shown as a dashed curve. If the vapour dielectric constant is included in the calculations for the stepped surface, the chained curve is obtained.

simulation data. The validity of such an approach, and the methods by which it can be implemented are discussed below.

#### 7.4.2. The general form of the dielectric constant

The most general expression for the dielectric constant is as a tensor<sup>8</sup>,

$$\epsilon(\mathbf{k}, \omega) = \left[ \mathbf{I} + 4\pi\chi(\mathbf{k}, \omega) \right] \quad (7.6)$$

and it is only in the low  $\mathbf{k}$  limit for homogeneous isotropic systems that we can write,

$$\epsilon(\mathbf{k}, \omega) \rightarrow \epsilon(\omega) = \epsilon(\omega)\mathbf{I} \quad (7.7)$$

In the interface region the density is changing very substantially over lengths of the order of a molecular diameter, which is, of course, less than the range of the correlation functions that determine  $\epsilon_s$  (e.g. see values of  $h_{\Delta}(r)$  given by Neumann *et al*<sup>7</sup>). Hence, within the surface the dielectric constant is; (i) likely to require a non-isotropic tensor for its representation, and (ii) the value at a given point within the surface will depend not just on the density,  $\rho(r)$ , but also on the distribution and density of the surrounding fluid. This means that the dielectric constant at any given point in the surface is not necessarily even close to that which would be found for a homogeneous sample at the same density and temperature.

While it would obviously be more correct to treat the dielectric constant as a tensor, in the following analysis we shall just use a scalar function to represent this quantity. This simplifies the necessary calculations significantly, and the methods described in appendix D can be used to find  $\langle M^2(r) \rangle$ . Thus we wish to find the single function  $\epsilon_s(r)$  that will correspond to the measured data from the simulation. If such a scalar function can be found which adequately fits the experimental data then it is probably not worthwhile trying to find the more general tensor expression.

#### 7.4.3. Fitting $\epsilon_s(r)$ to the $\langle M^2(r) \rangle$ data

It would be most desirable to directly calculate the function  $\epsilon_s(r)$  from the

simulation data for  $\langle M^2(r) \rangle$ . However the particular numerical method outlined in appendix D only allows the calculation of the  $\langle M^2(r) \rangle$  from a given dielectric profile<sup>†</sup>.

As far as we know it is not possible to invert the equations to find  $\epsilon_s(r)$  directly, so a fitting process was adopted. Using some functional form for  $\epsilon_s(r)$ , a non-linear least squares fit was performed to find the best parameters for the given function. Since we expect  $\epsilon_s(r)$  to be constant well outside the drop, and also to be tending to a (different) constant value within the drop (we again have to ignore the data at very small  $r$ ), the most obvious choice for this function is a tanh form, analogous to that used for the density profile, i.e.,

$$\epsilon_s(r) = A_\epsilon - B_\epsilon \tanh\left(\frac{2(r-R_\epsilon)}{D_\epsilon}\right) \quad (7.7)$$

where  $A_\epsilon = (\epsilon_{s,l} + \epsilon_{s,v})/2$  and  $B_\epsilon = (\epsilon_{s,l} - \epsilon_{s,v})/2$ . The notation  $\epsilon_{s,l}$  and  $\epsilon_{s,v}$  has been used for the limiting values of the dielectric constant in the liquid and vapour respectively.

Figure (7.5) shows the resultant  $\langle M^2(r) \rangle$  curve that was obtained by fitting such a function for  $\epsilon_s$  to the same data that was used in the previous sections (state (D7)). All data points for  $r \geq 2.4$  were given an equal weight in the fit, while the results for  $r < 2.4$  were excluded as before. The choice of weights is rather arbitrary and to emphasize the data well within the drop, as the method of §7.3 does, one could use weights proportional to  $r^{-3}$ . This might be preferred if the aim is just to maximise the accuracy of the value of  $\epsilon_{s,l}$ .

During the fit  $\epsilon_{s,v}$  was held constant at the value found from the limiting vapour density,  $\epsilon_{s,v} = 1.032$ . The remaining three parameters,  $\epsilon_{s,l}$ ,  $R_\epsilon$  and  $D_\epsilon$  were then

<sup>†</sup> The particular method we have employed is to treat the drop as a system of  $N$  shells, each of the same width, and having a dielectric constant equal to the value of the continuous function  $\epsilon_s(r)$  at the mid-point of the given shell. For large enough  $N$  (we used 50 divisions), the  $\langle M^2(r) \rangle$  profile is independent of  $N$ .

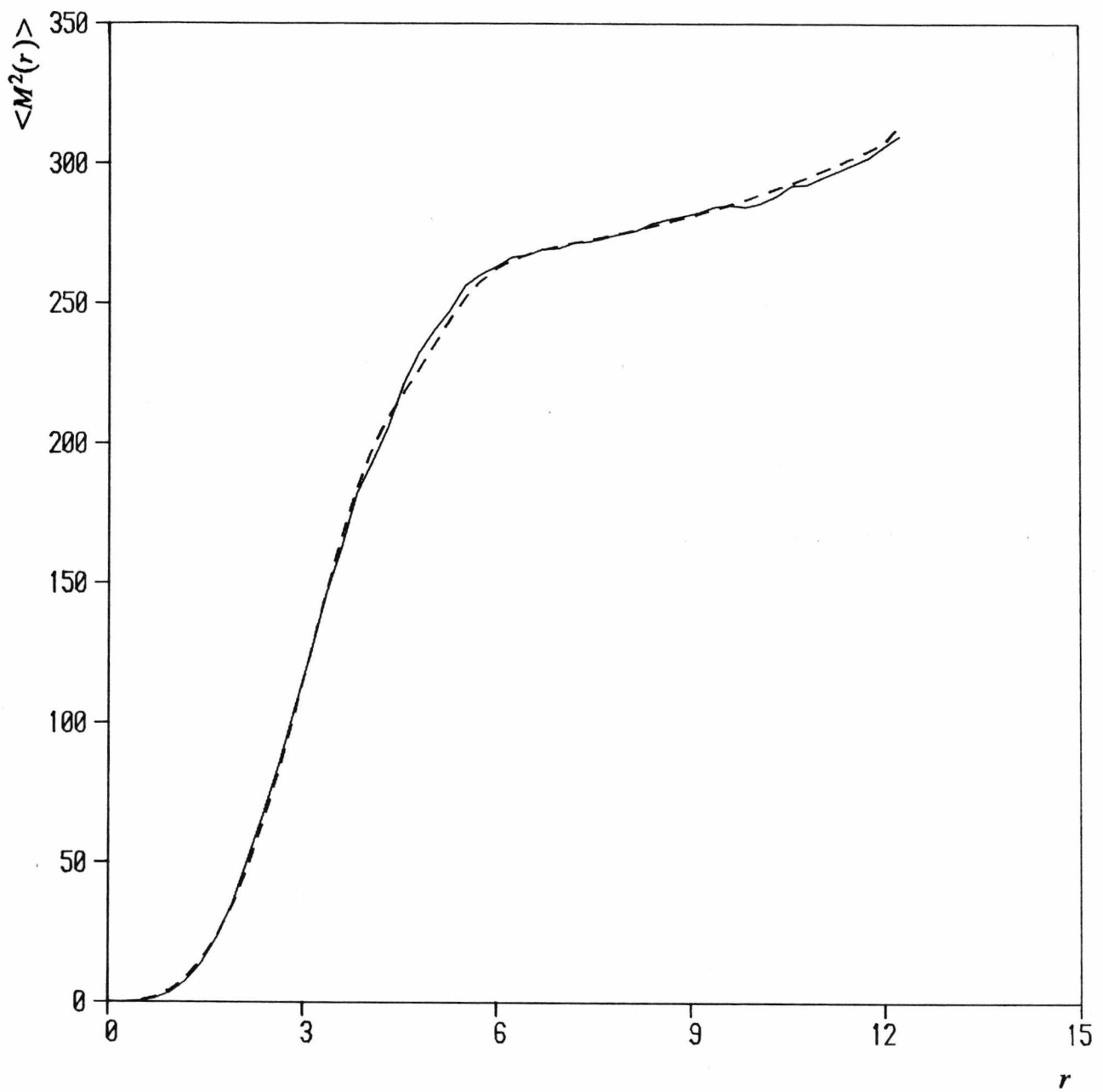


Figure 7.5: The function  $\langle M^2(r) \rangle$  (dashed) that is obtained by fitting to the simulation data, using a tanh form for  $\epsilon(r)$ , with three adjustable parameters. The simulation data for state (D7), to which the fit was made, is shown as the solid curve.

adjusted for the best least-squares fit.

The agreement between this fitted curve and the data from the simulation is seen to be very good. The use of a simple scalar function of tanh form for  $\epsilon_s(r)$  does, therefore, appear adequate to describe our results, at least in this case. This is a vast improvement at large  $r$ , compared to the simple sharp and stepped interface results shown in figure (7.4). At small  $r$ , however, there is very little difference between this new calculation and the previous results.

Similar fits have been performed for a number of the longer Stockmayer runs for which the function  $\langle M^2(r) \rangle$  was measured. In addition to the several S1 drops, fits have also been made for the two S3 states studied. Table (7.1) summarises the results obtained for the various parameters.

Pot.	S1				S3	
State	(D6)	(D10)	(D7)	(D12)	(D13)	(D14)
$N_p$	450	800	450	900	450	450
$T$	0.734	0.744	0.809	0.913	1.20	1.25
$\epsilon_v$	1.018	1.027	1.032	1.048	1.09	1.12
$\epsilon_l$	13.1	13.2	10.2	8.8	29.3	26.2
$R_h$	4.72	5.74	4.57	5.77	4.48	4.30
$R_\epsilon$	4.70	5.64	4.65	5.52	4.42	4.26
$D$	1.52	1.62	1.76	2.10	2.05	2.24
$D_\epsilon$	1.53	1.52	1.47	2.32	1.69	1.75
$\rho_l$	0.879	0.866	0.850	0.812	0.828	0.797

Table 7.1: Results obtained for the dielectric profiles of various drops assuming a hyperbolic tangent form for the function  $\epsilon_s(r)$ . Data for the density profile is also shown for comparison.

The dielectric surface width and “half radius” ( $D_\epsilon$  and  $R_\epsilon$ ) may be compared to the corresponding values obtained for the density profiles of the drops, which are also given in table (7.1). We note that these values are generally very similar. There is a slight tendency for  $R_\epsilon$  to be less than  $R_h$ , but only by  $\sim 0.1$ , and this difference is reversed in one state. The variation between the two sets of surface width parameters is slightly greater, though without any clear trend.

Figures (7.6) to (7.9) illustrate the fits obtained with the parameters given in table (7.1) for a selection of states. As for the previous example, these figures show that the fits are reasonably close to the data. The two S3 drops show slightly poorer agreement than the other S1 results. The higher value of the liquid dielectric constant in the S3 drops means that the function  $\langle M^2(r) \rangle$  has to change more rapidly through the surface region and thus may represent a more severe test of the theory.

We note that, in the case of the S1 drops, the variation of  $\epsilon_s$  through the surface is such that both the fit and the data for  $\langle M^2(r) \rangle$  increase monotonically with  $r$ . However, in the case of the S3 drops, figs. (7.8) and (7.9), there is a significant “bump” in the  $\langle M^2(r) \rangle$  profile. This is probably a vestige of peak that was seen in figure (7.4) for a sharp dielectric profile.

Calculations have been made by Gubbins and Thompson<sup>9</sup> of the anisotropy of dipole orientations in the planar liquid-vapour interface for the Stockmayer fluid. They found only slight anisotropy in the case of the S1 potential, but this effect was much more noticeable with the highly polar S3 potential. Similar correlations can be expected in the curved interfaces of the drops simulated in this work and are likely to be associated with an increase in the anisotropy of the dielectric tensor within the surface as the dipole moment is increased. Hence it might be more useful to investigate the possibility of fitting a tensorial form for the dielectric constant in highly polar drops, such as the S3 ones. This has not however been attempted in this work.

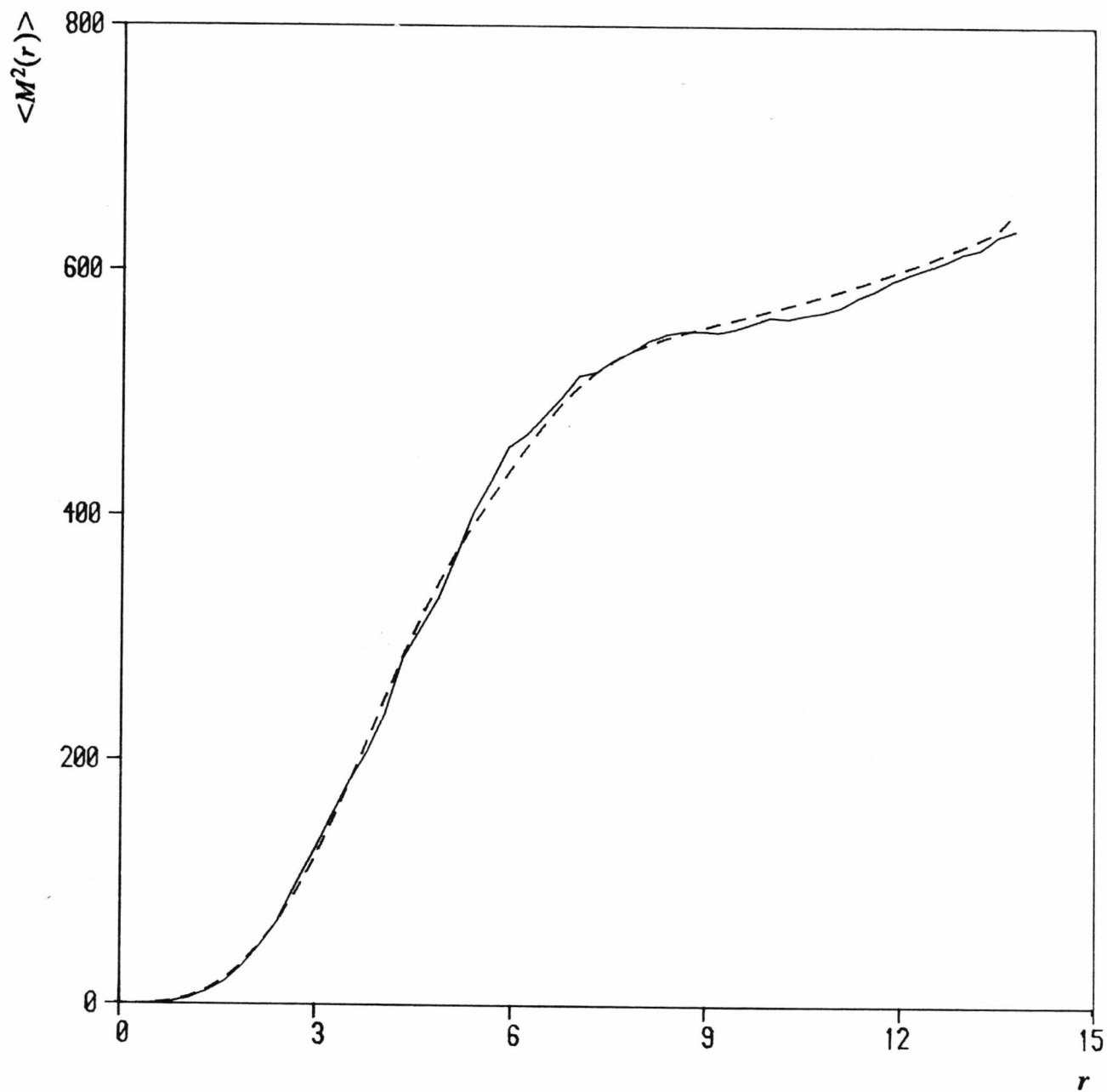


Figure 7.6: As in fig. (7.5), but for state (D12),  $N_p = 900$  and a temperature of  $T = 0.913$ .

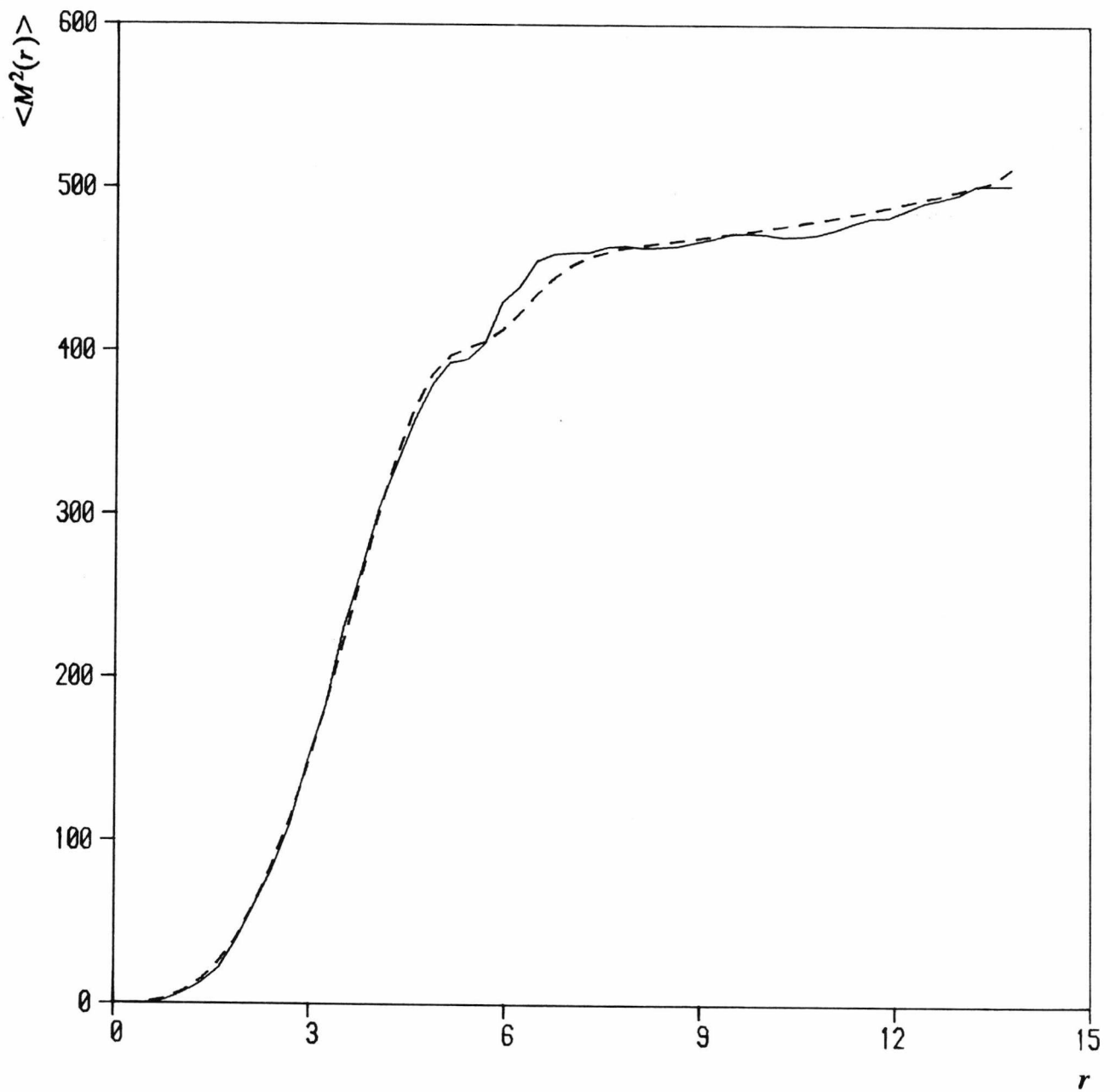


Figure 7.7: As in fig. (7.5), but for state (D10),  $N_p = 800$  and a temperature of  $T = 0.744$ .

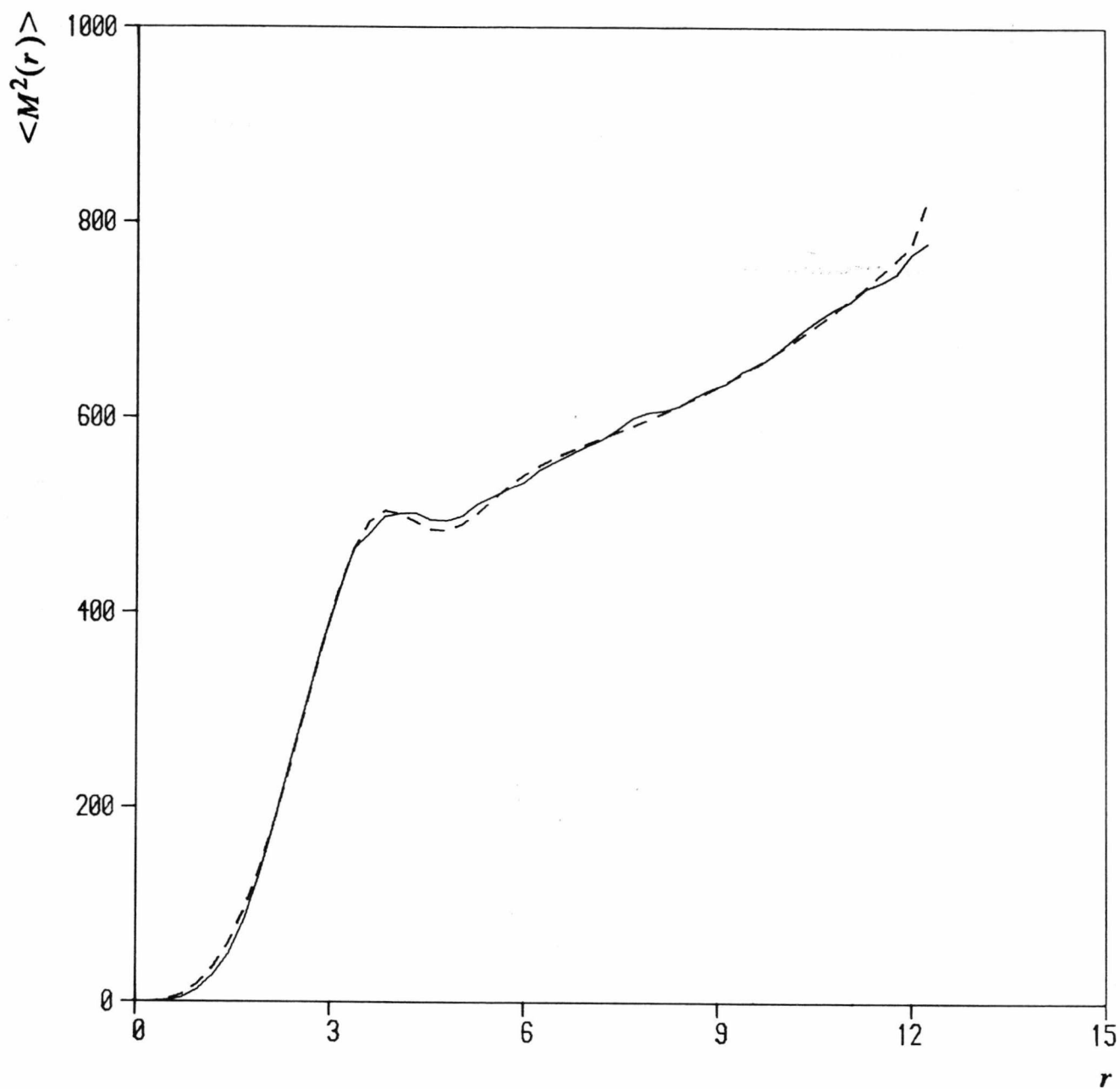


Figure 7.8: As in fig. (7.5), but for state (D14),  $N_p = 450$  and a temperature of  $T = 1.25$ , using the S3 potential ( $\mu^2 = 3$ ).

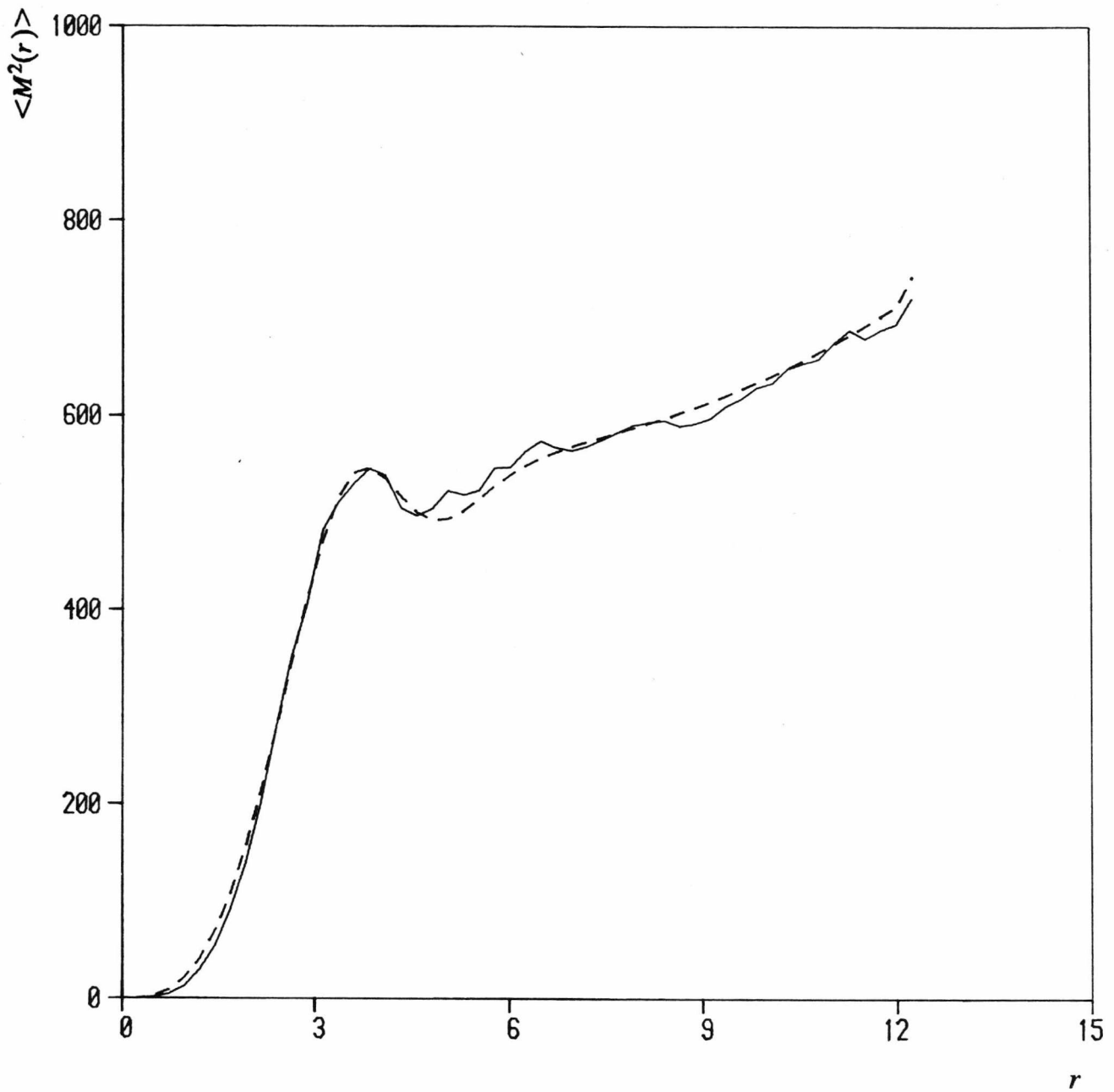


Figure 7.9: As in fig. (7.5), but for state (D13),  $N_p = 450$  and a temperature of  $T = 1.20$ , again for the S3 potential.

#### 7.4.4. An alternative form for $\epsilon_s(r)$

While the results obtained with the tanh form for  $\epsilon_s(r)$  are quite good, this particular choice of function is rather arbitrary. An alternative approach that has been investigated is based on the Kirkwood equation, (6.11), which relates  $\epsilon_s$  to the density and the correlation factor  $g$  in an homogeneous system. The low density of the vapour surrounding the drops will give a value of  $g$  that must be very close to unity, whereas the dielectric constant values for the bulk liquid indicate that  $g$  is of the order of 1.5 to 2.0 within the drops. If, as before, we assume that a simple scalar function,  $\epsilon_s(r)$ , is adequate to describe the surface behaviour, then we can directly define the related function,  $g(r, \rho(r))$  using equation (6.11), in conjunction with the density profile  $\rho(r)$ . For simplicity we shall assume that this *effective*  $g$  factor can be expanded in terms of just the density at  $r$ , i.e.,

$$g(\rho) = 1 + a\rho + b\rho^2 + \dots \quad (7.8)$$

which gives  $g = 1$  in the limit  $\rho \rightarrow 0$ . It must be emphasized that this is an empirical approach and that the function  $g(\rho)$  within the surface cannot be related to the true Kirkwood correlation factor for a homogeneous system at the same density. In fact it might be more correct to include other terms in equation (7.8), such as  $(d\rho/dr)$ , but this has not been investigated.

Thus by using equations (7.8) and (6.11), a form for the dielectric profile,  $\epsilon_s(r)$ , can be obtained in terms of the set of coefficients  $\{a, b, \dots\}$ . Using the same numerical methods as for the tanh curve, a least squares fit can be performed to determine the best values for these coefficients. This has been done <sup>for</sup> a number of states, but here we shall just use the data for drop (D7) as a typical example. Two different expressions were employed for  $g(\rho)$ , a linear one,  $g(\rho) = 1 + a_1\rho$  and a quadratic form,  $g(\rho) = 1 + a_2\rho + b_2\rho^2$ . For this particular state the optimum values found for these coefficients were  $a_1 = 0.747$  for the first fit and  $a_2 = 1.855$ ,  $b_2 = -1.545$  for the second one. In figure (7.10) we compare the simulation data with these linear and

quadratic results for  $\langle M^2(r) \rangle$ . The agreement is quite good in both cases, though slightly better for the quadratic form, as would be expected. The  $\epsilon_s(r)$  profiles given by these fits are shown in figure (7.11), along with the hyperbolic tangent result. We note that all three methods give similar results for the dielectric profile, especially in the surface region. However, the linear expression for  $g$  gives a larger value of  $\epsilon_s$  in the centre of the drop than the other two methods, indicating that a single parameter function may not give adequate flexibility. The estimate of the bulk liquid dielectric constant for the quadratic fit is very close to the value obtained by the tanh method.

It is possible to use more terms in the expansion for  $g(\rho)$ , but it was found that this only gives a slight improvement in the  $\langle M^2(r) \rangle$  fit, and the coefficients themselves tend to change quite significantly as the order of the polynomial is increased. The dielectric profile obtained in the surface and vapour regions is not greatly effected by such changes, but the higher powers can lead to strange behaviour of  $g(\rho)$  for large  $\rho$ .

This method of expressing  $\epsilon_s(r)$  in terms of the density gives results which are consistent with those obtained with the tanh form, but it appears to be slightly less satisfactory. Also, the fit parameters themselves ( $a_1$  and  $a_2$ ,  $b_2$ ) have no clear physical meaning, such as can be associated with the width and radius values of the tanh fit. Hence, we shall limit further discussion to the results given in table (7.1) using the tanh representation for  $\epsilon_s(r)$ .

### 7.5. Comparison with previous dielectric measurements

A number of workers have calculated values of the static dielectric constant at various liquid densities for the S1 and S3 potentials. Computer simulation studies have almost exclusively been based on homogeneous systems with periodic boundary conditions. Long range corrections are applied by either lattice summations techniques or the reaction field method, which are mentioned in chapter six.

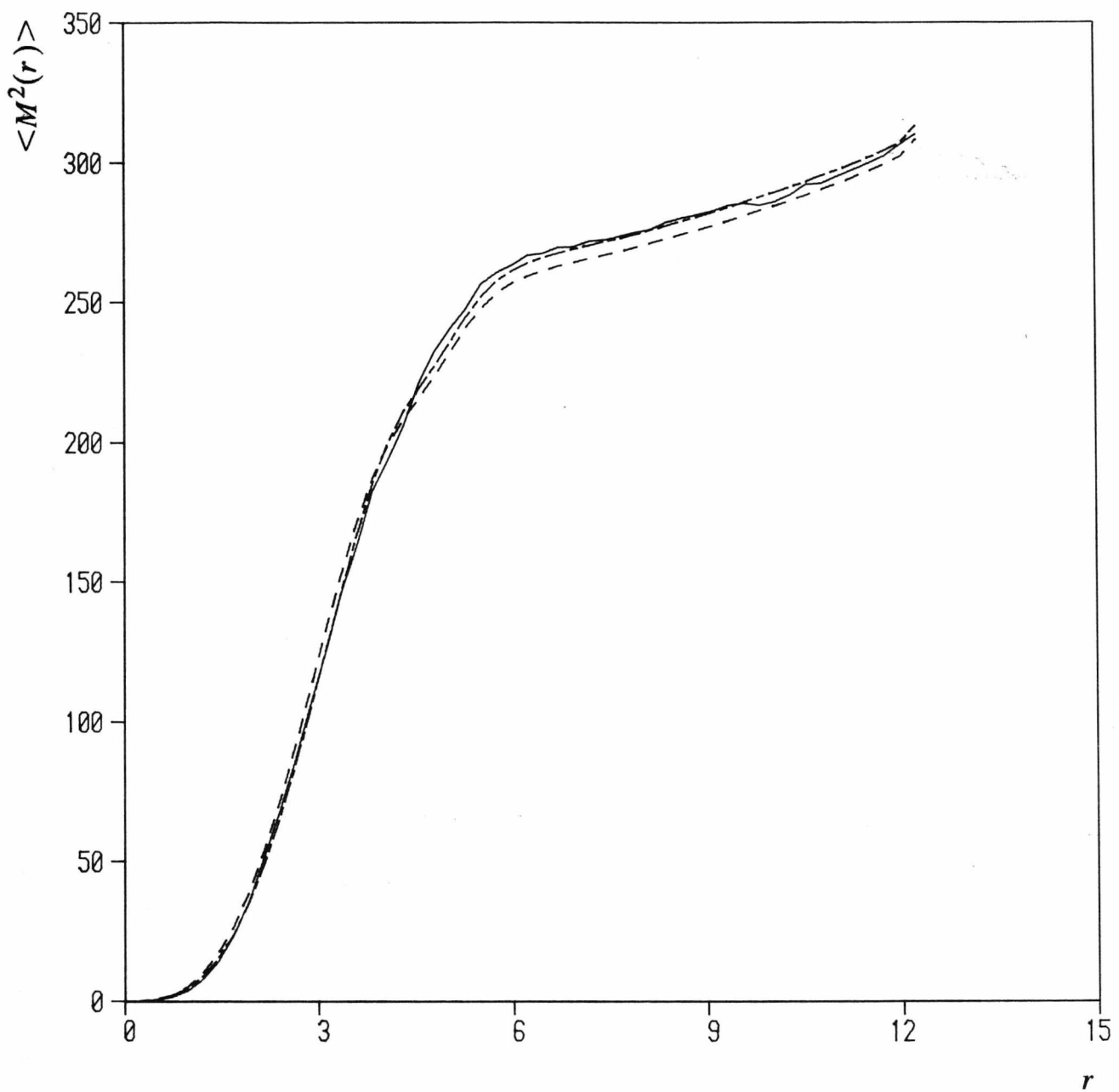


Figure 7.10: The function  $\langle M^2(r) \rangle$  obtained by fits based on the expansion of the Kirkwood  $g$  in terms of the density. The data for state (D7) is again shown as a solid curve, while a linear fit ( $g(\rho) = 1 + a_1\rho$ ) gives the dashed result. The chained curve corresponds to the quadratic fit ( $g(\rho) = 1 + a_2\rho + b_2\rho^2$ ).

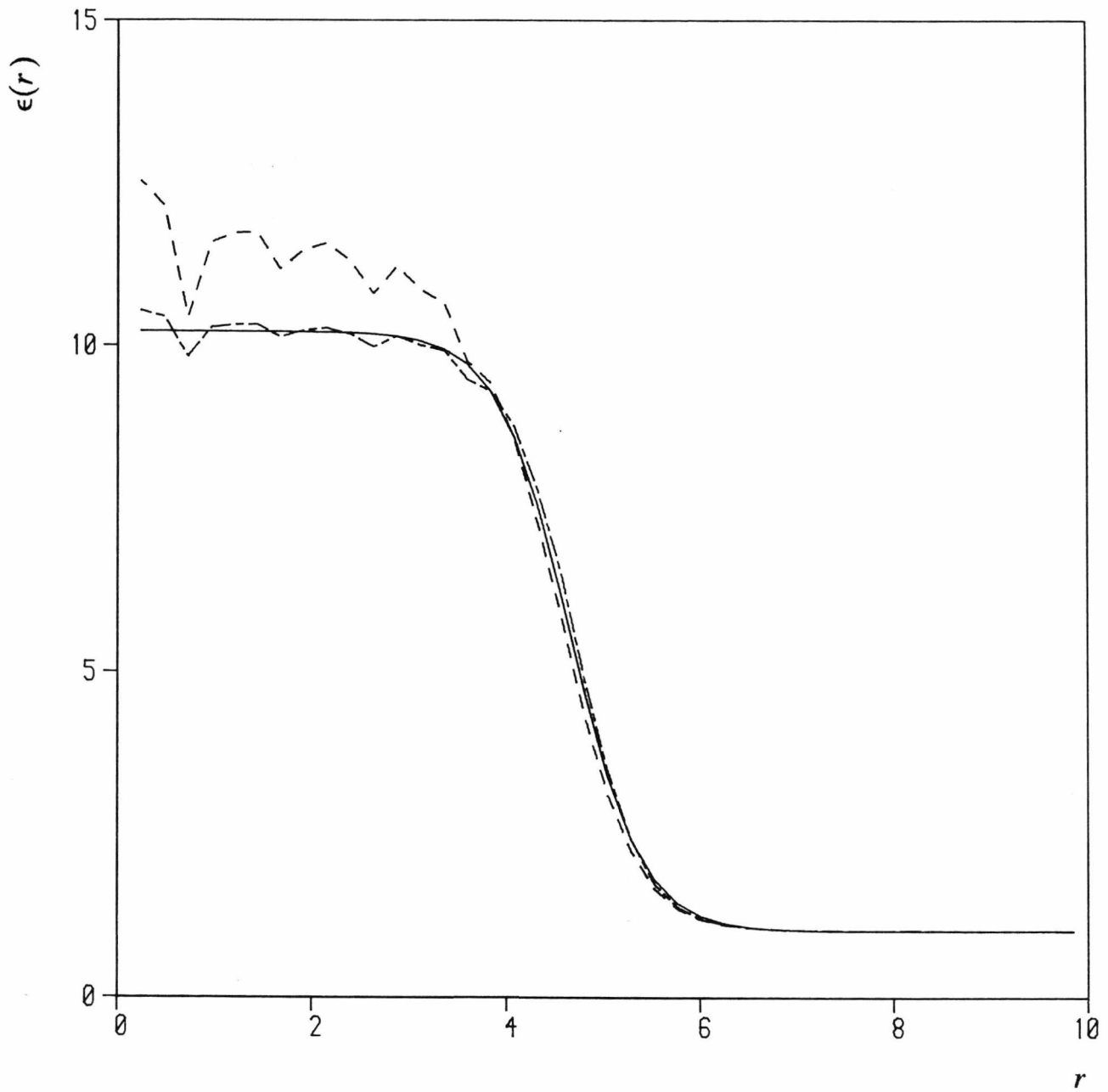


Figure 7.11: The dielectric profiles,  $\epsilon(r)$ , obtained for state (D7) by three different fits to the  $\langle M^2(r) \rangle$  data. The result of using a tanh form for  $\epsilon(r)$  is shown by the solid curve. The dashed curve corresponds to the linear expression for  $g(r)$ , while the quadratic form gives the chained curve.

Adams and Adams<sup>1</sup> give results for  $\epsilon_s$  for the S1 potential at state points close to the values found in the central regions of our drops. In figure (7.12) we have drawn two tentative curves representing the temperature dependence of  $\epsilon_s$  at the two densities  $\rho = 0.8$  and  $\rho = 0.85$ , through the five points given by Adams and Adams. The bulk liquid values,  $\epsilon_{s,l}$ , given in table (7.1), are also marked on the figure. Our results for the S1 states lie between  $\rho = 0.88$  at  $T = 0.735$ , (D6), and  $\rho = 0.812$  at  $T = 0.924$ , (D12), so they do not lie on an isochore, but are close to the coexistence curve.

The drop values for  $\epsilon_s$  are lower than would be indicated by those of Adams and Adams at the three lower temperature points. However, the higher temperature point, state (D12), seems to be above the value than would be expected from Adams and Adams. The accuracy of the results  $\epsilon_s$  given by Adams and Adams is not explicitly stated, but they also report a number of measurements for the same states using an applied electric field, and observing the resultant polarization. The dielectric constant is then obtained directly, using equation (6.2), though the thermal fluctuations of the polarization mean that a very intense field has to be used. Results for  $\epsilon_s$  calculated in this way can vary by more than 20% from the zero applied field values. Part of the difference may be associated with saturation effects, but it seems that there is still a significant uncertainty, even in the zero applied field results.

The two S1 drops at the lowest temperatures, states (D6) ( $N = 450$ ) and (D10) ( $N = 800$ ), were chosen to be as close as possible in temperature to investigate the dependence of our results on system size. It is reassuring to note that the values obtained for  $\epsilon_{s,l}$  are very close, which indicates that a system size of  $N = 450$  should be sufficient, at least for measuring the liquid dielectric constant for the S1 potential. The values for the dielectric surface width,  $D_{\epsilon_s}$ , are also found to be very similar in these two cases.

It was noted earlier that varying the weights used in the fitting process might effect the relative accuracy of  $\epsilon_{s,l}$  and other quantities. However, in practice

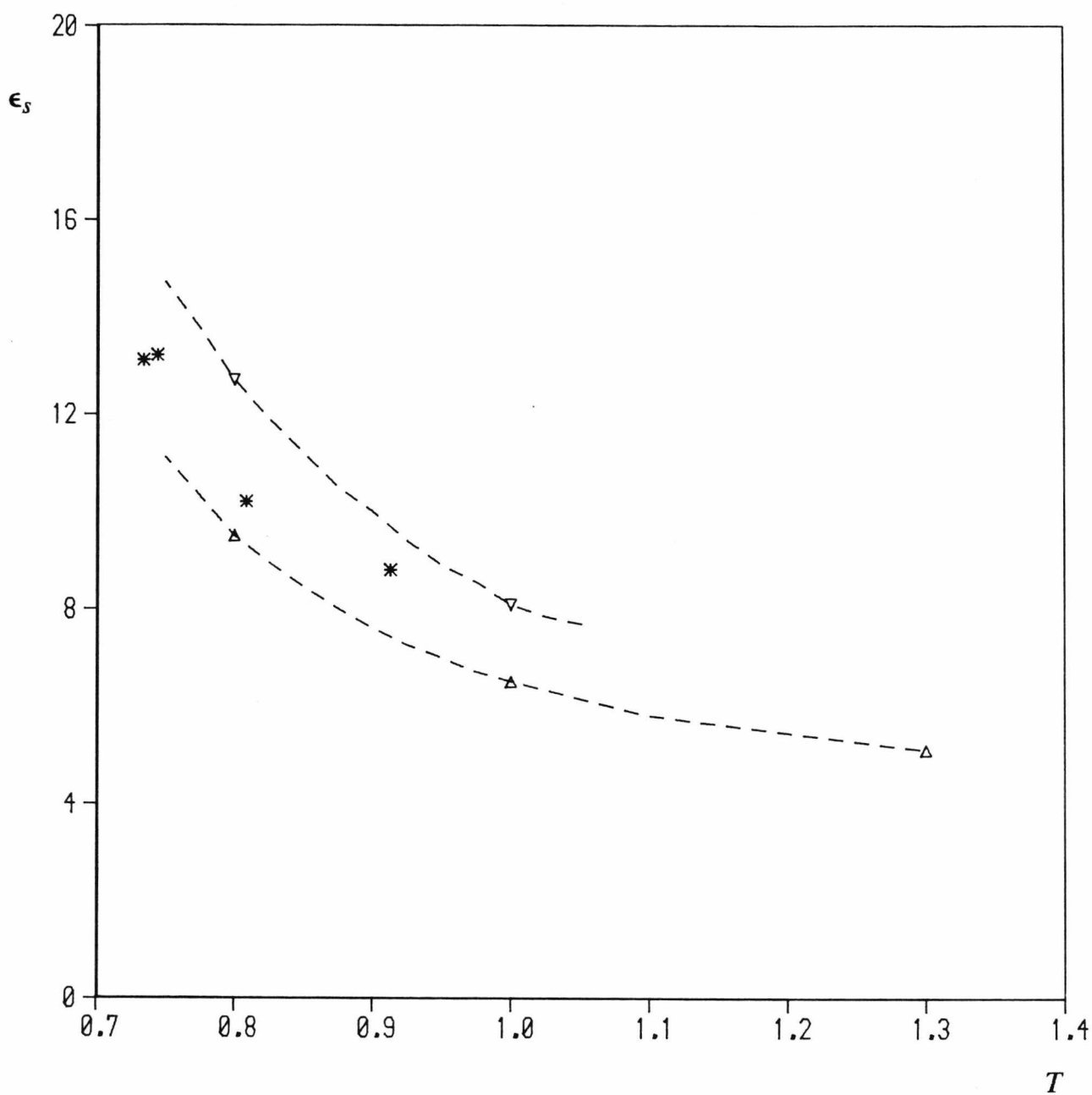


Figure 7.12: The dielectric constant of the S1 liquid as a function of temperature. Five results (due to Adams and Adams) are shown, for the liquid densities of  $\rho = 0.80$  ( $\Delta$ ) and  $\rho = 0.85$  ( $\nabla$ ). The four S1 results reported in table (7.1) are marked as (\*).

increasing the weighting of the data in the bulk liquid only had a quite small effect on the results obtained from the fit. We estimate the accuracy of the values of  $\epsilon_{s,l}$  as about  $\pm 1$  for the S1 drops in table (7.1). This is in addition to the uncertainties mentioned in chapter three for the temperature and liquid density of the drop.

Previous results for the S3 fluid seem to be more restricted. Several workers have reported measurements of  $\epsilon_s$  at the temperature  $T = 1.35$  and a density of  $\rho = 0.8$ . For example, Pollock and Alder<sup>10</sup> found  $\epsilon_s = 38$  for this system, using either 108 or 256 particles. Another S3 state point that has been studied is  $T = 1.15$  and  $\rho = 0.822$ . While Adams and Adams<sup>1</sup> found  $\epsilon_s = 48$  for this state, more recent and extensive simulations of this system by Neumann *et al*<sup>7</sup> yield a value of  $\epsilon_s = 66 \pm 2$ . Moreover they get the same result by both lattice summation and reaction field techniques, and so this value appears more reliable than that of Adams and Adams.

While it is difficult to accurately interpolate the  $\rho$  and  $T$  dependence of  $\epsilon_s$  from just these two points, it is clear that they would suggest values of  $\epsilon_s$  between about 40 and 50 for our S3 drops, at  $T = 1.2$  and  $T = 1.25$  (with  $\rho = 0.83$  and  $\rho = 0.8$  respectively). This is significantly higher than the values of 26 and 29 that are actually found. Hence this method may be inadequate for the highly polar S3 system, when used with only 450 particles. Obviously it would be desirable to investigate larger S3 drops at the same state points, but insufficient time was available to do this.

Hesse-Bezot *et al*<sup>11</sup> have recently published details of a similar method to the one used here, but only for finding the liquid dielectric constant. They use an isolated liquid drop that is contained by a soft wall potential (this introduces some density oscillations near the wall, but they are not very great). The type of method described in §7.3.2 is employed to find  $\epsilon_s$ , assuming a sharp surface. They only report results for one state point, at  $T = 1.35$  and  $\rho = 0.8$ , with  $\mu^2 = 2.7$ . Two large systems were studied, one with  $N = 913$  and the other with  $N = 1472$ . The smaller system gave the result  $\epsilon_s = 22 \pm 6$  where as the larger one gave  $\epsilon_s = 28 \pm 2$ . A conventional

calculation by Pollock and Alder<sup>10</sup> at a very similar state yielded  $\epsilon_s = 29 \pm 1$ . Thus it seems likely that larger drops are required to find the actual *bulk liquid* dielectric constant of highly polar systems.

### 7.6. The MSM at small $r$

The MSM plots such as that shown in figure (7.3), clearly fall well below the macroscopic curve for  $r < \sim 2.4$ . A sphere of radius  $r = 2.4$  at the centre of any given drop will contain a mean number of molecules  $\langle n(r) \rangle = (4\pi/3)r^3\rho \sim 46$ . For  $r = 1$  the expected number of molecules is only 3, and at  $r \sim 0.67$  this value reaches unity. For a spherical volume so small that the probability of two molecules been within it simultaneously is negligible, the value of  $\langle M^2(r) \rangle$  is determined directly from the density as,

$$\langle M^2(r) \rangle = (\boldsymbol{\mu} \cdot \boldsymbol{\mu})\rho V = \frac{4\pi}{3}r^3\rho\mu^2 \quad (7.9)$$

and hence,

$$\frac{\langle M^2(r) \rangle}{3kTr^3} = \frac{4\pi\rho\mu^2}{9kT} \quad (7.10)$$

For state (D7) this gives the limit that the MSM  $\rightarrow 1.47$  as  $r \rightarrow 0$ , and this value is marked in figure (7.3). Considering the statistical uncertainties in the data at small  $r$ , this value agrees well with simulation results.

The behaviour of the MSM in the “transition region”, between the micro and macroscopic limits, is more difficult to calculate, but will clearly depend on the distribution function  $h_{\Delta}(r)$ . If this function were known, the mean moment of any given sphere could be obtained by integration over all possible configurations within the volume. However, there is the complication that  $h_{\Delta}(r)$  may vary with the radial position, and is, in any case, not very well known, so we shall not attempt to calculate this here.

## 7.7. Conclusions

It has been seen that the liquid drop systems used in this work allow the bulk dielectric constant of moderately polar systems to be calculated. For strongly polar fluids it may require drops of significantly more than 450 particles to find the bulk dielectric constant. If this is indeed the case than it may be more economic to use more conventional techniques, such as reaction field methods to find  $\epsilon_r$  at a given density and temperature. It is nevertheless important to show that homogeneous simulations with such artificial long range corrections do give consistent dielectric results, and simulations of large drops represent a good way of avoiding all such corrections.

The analysis of the dielectric surface properties has been made in terms of a simple scalar function,  $\epsilon_s(r)$ . This is clearly an over simplification, but is adequate to describe most of the drop results found here. A surface dielectric profile of similar width and position to the density profile is observed. A better theoretical treatment of the surface, allowing for its microscopic structure, and the fact that the dielectric constant should really be a tensor, may help to remove some of the discrepancies that are found, particularly for the S3 drops.

## References

1. D.J.Adams and E.M.Adams, *Molec. Phys.*, vol. 42, p. 907, 1981.
2. H.Fröhlich, *Theory of Dielectrics*, Clarendon Press, Oxford, 1949.
3. H.J.C.Berendsen, "Molecular dynamics and monte carlo calculations on water," *Cecam report*, p. 21, 1972.
4. D.J.Adams and I.R.McDonald, *Molec. Phys.*, vol. 32, p. 931, 1976.
5. I.G.Bossis, *Molec. Phys.*, vol. 38, p. 2023, 1979.
6. I.G.Bossis, *Molec. Phys.*, vol. 39, p. 1233, 1980.

7. M. Neumann, O. Steinhauser, and G.S. Pawley, *Molec. Phys.*, vol. 52, p. 97, 1984.
8. P. Madden and D. Kivelson, "A consistent molecular treatment of dielectric phenomena," *Adv. Chem. Phys.*, vol. 56, 1984.
9. K.E. Gubbins and S.M. Thompson, *Faraday Symposium*, vol. 16, p. 59, 1981.
10. E.L. Pollock and B.J. Alder, *Physica*, vol. 102A, p. 1, 1980.
11. C. Hesse-Bezot, G. Bossis, and C. Brot, *J. Chem. Phys.*, vol. 80, p. 3399, 1984.

## Chapter Eight: The dynamic dielectric constant

### 8.1. Introduction

In this chapter we present some results for the time correlation functions that have been measured for the Stockmayer drops. It was hoped that the correlation functions (CFs) for the total dipole moment within spheres would allow the calculation of the dynamic dielectric constant, as discussed in chapter six. However theoretical and statistical problems lead to significant difficulties in finding  $\epsilon(\omega)$  reliably in this way and some of the reasons for this are considered.

The procedures used to measure both the single particle and total moment CFs during in the simulations are outlined in §8.2, while some typical results are presented in §8.3. The calculation of  $\epsilon(\omega)$  from this data is examined in section 8.4 and some of difficulties involved are pointed out. The final section discusses this method in relation to some other studies that have been made on  $\epsilon(\omega)$ .

### 8.2. Calculation of the correlation functions

#### 8.2.1. The total moment correlation function

In chapter seven we examined results for the dependence of the mean square dipole moment on the radius of the sphere within which it was measured. For most of our larger drops we also calculated the more general quantity,  $\langle \mathbf{M}(0) \cdot \mathbf{M}(t) \rangle_r$ . This is the time auto correlation function of the total dipole moment within a sphere of radius  $r$ . Extending the notation used in chapter six we shall write the normalised version of this quantity as  $\Phi_r(t) = \langle \mathbf{M}(0) \cdot \mathbf{M}(t) \rangle_r / \langle M^2(r) \rangle$ .

To investigate the  $r$  dependence of  $\Phi_r(t)$ , this quantity was evaluated for 25 separate radii, these being equally spaced, with the largest one equal to half the periodic box side (this gives a resolution of  $\sim 0.48$  in  $r$ ). In the programme a large array was used to store the vector moment within each sphere at every fourth time step

for the last 240 steps of the simulation. These particular sampling frequencies were chosen as a compromise between accurately studying the time and  $r$  dependence of  $\Phi_r(t)$ , while avoiding excessive use of computer resources (in particular the limited disk and memory space). The CFs are obtained by averaging over the appropriate products of vectors from this array.

### 8.2.2. The single particle correlation function

The auto correlation function for individual molecules was also calculated during these simulations. This is just the expectation value  $\langle \boldsymbol{\mu}(0) \cdot \boldsymbol{\mu}(t) \rangle / \mu^2$ . Since this function may, like  $\Phi_r(t)$ , be dependent on the radial position of the molecule, separate averages were evaluated in shells about the drop centre of mass. For convenience the same radial divisions were used as for the total moment CF. However it must be noted that this single particle function, which we denote as  $\Phi_r^s(t) = \langle \boldsymbol{\mu}(0) \cdot \boldsymbol{\mu}(t) \rangle_r / \mu^2$ , refers to just the particles within the shell at  $r$ , whereas  $\Phi_r(t)$  is measured for all the particles in the sphere, radius  $r$ .

## 8.3. Results for the correlation functions

### 8.3.1. The radial dependence of $\Phi_r^s(t)$

Figure (8.1) shows some typical examples of the results obtained for the single particle CFs. These values are for the S1 state (D7),  $N_p = 450$  and  $T = 0.81$ . Only a few of the 25 separate results for  $\Phi_r^s(t)$  are shown, since many of these are similar to one another. As might be expected there is some difference between the CF found in the vapour region and that obtained for the bulk liquid inside the drop. The CF is seen to decay slightly more slowly in the liquid than in the vapour, at least for  $t \leq \sim 1.5$ . At longer times the CF in the vapour also goes quite negative, whereas this feature is much less significant in the liquid. For free reorientation (i.e. the low density limit) the form of this CF is known to be given by Kummer's function<sup>1</sup>, and

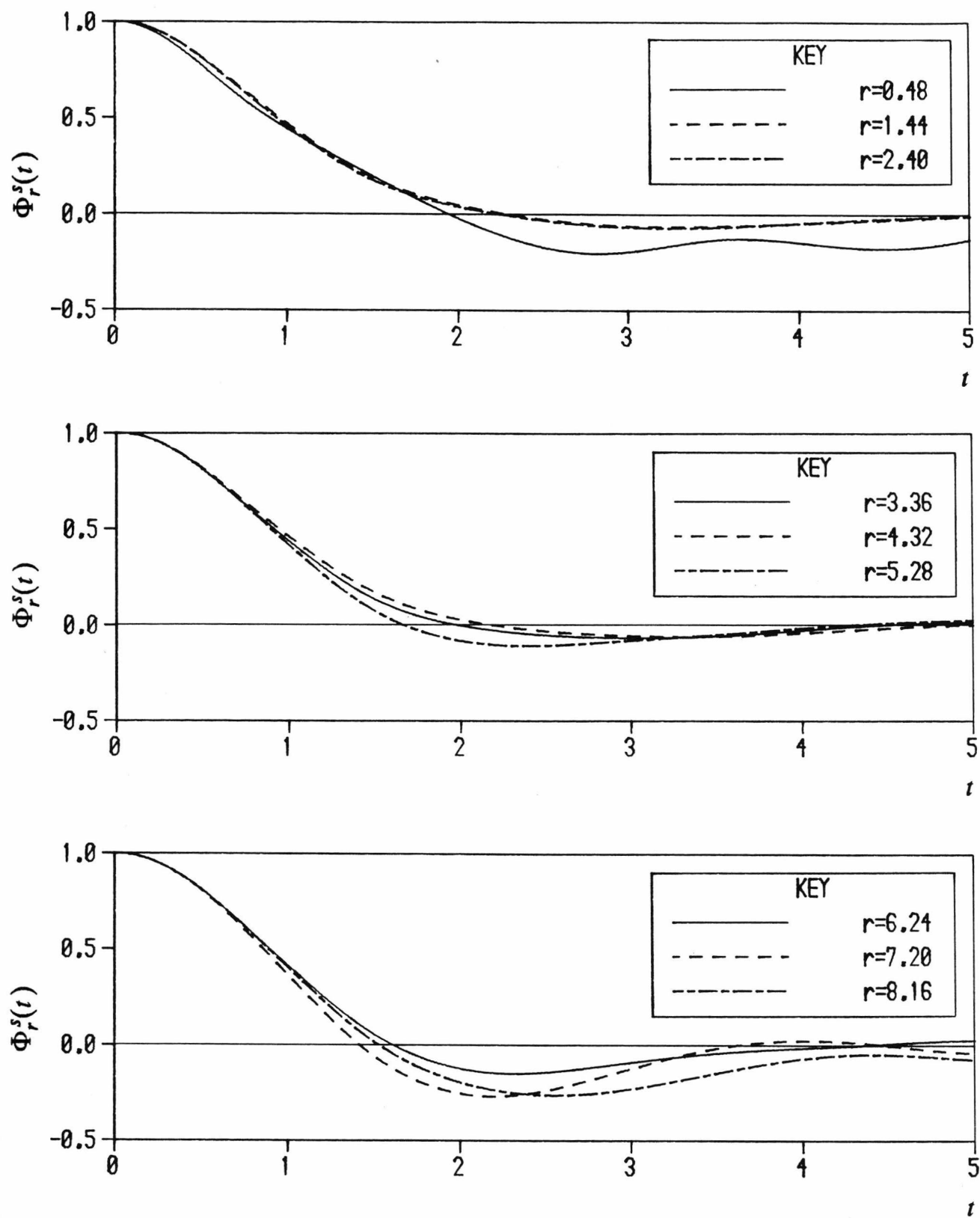


Figure 8.1: Time dependence of the single particle correlation function  $\Phi_r^s(t)$ , measured for a number of spherical shells about the drop centre of mass. Each shell is of width  $\Delta r = 0.48$ , and the  $r$  values given are for the outer radii of the shells. This data is for the S1 state (D7), at  $T = 0.809$ . The equimolar radius is  $R_e = 4.7$ .

the response in the vapour region has been found to be quite close to this limiting form.

### 8.3.2. The radial dependence of $\Phi_r(t)$

Figure (8.2) shows a similar set of curves for the function  $\Phi_r(t)$ , again for the S1 state (D7). At very small  $r$  (e.g. 0.48 - 0.96) this CF decays very rapidly, faster even than the single particle function  $\Phi_r^s(t)$ . This is due to the fact that there are very few molecules within such a volume and those that are present are frequently exchanged with others from the surrounding fluid, so that correlations are "forgotten" sooner than they would otherwise be. Such volumes are obviously not large enough to yield the CFs for a macroscopic sample. As  $r$  is increased the CF decays more slowly (i.e. the correlation time increases). The effect of molecules drifting in and out of the volume then becomes relatively less important.

The form of the CF is found to be approximately constant for  $r$  in the range of about 2 - 2.8, at which point the correlation time reaches a maximum. Beyond this range the CF again changes, presumably due to the effects of the surface region. This variation is most noticeable in the range of  $r$  from about 3.3 to 4.8. The initial decay of the CF again becomes more rapid, and a strong negative feature appears at times above  $t \sim 1.5$ . At larger  $r$  still the CF measured beyond the drop surface seems to show a strongly damped oscillatory form. This changes little with further increase in  $r$ , since the relatively few particles in the vapour have little effect. Similar oscillatory behaviour is predicted by Neumann *et al* for an S3 system<sup>2</sup>.

### 8.3.3. Trends in the correlation functions

The CFs that have been measured are, of course, sensitive to the temperature and density of the drop, and we shall compare some data from a few of the various state points. In figure (8.3) we compare the single particle CFs for three S1 drops. The states (D6) and (D10) are of similar temperature ( $T \approx 0.74$ ) and liquid density, but

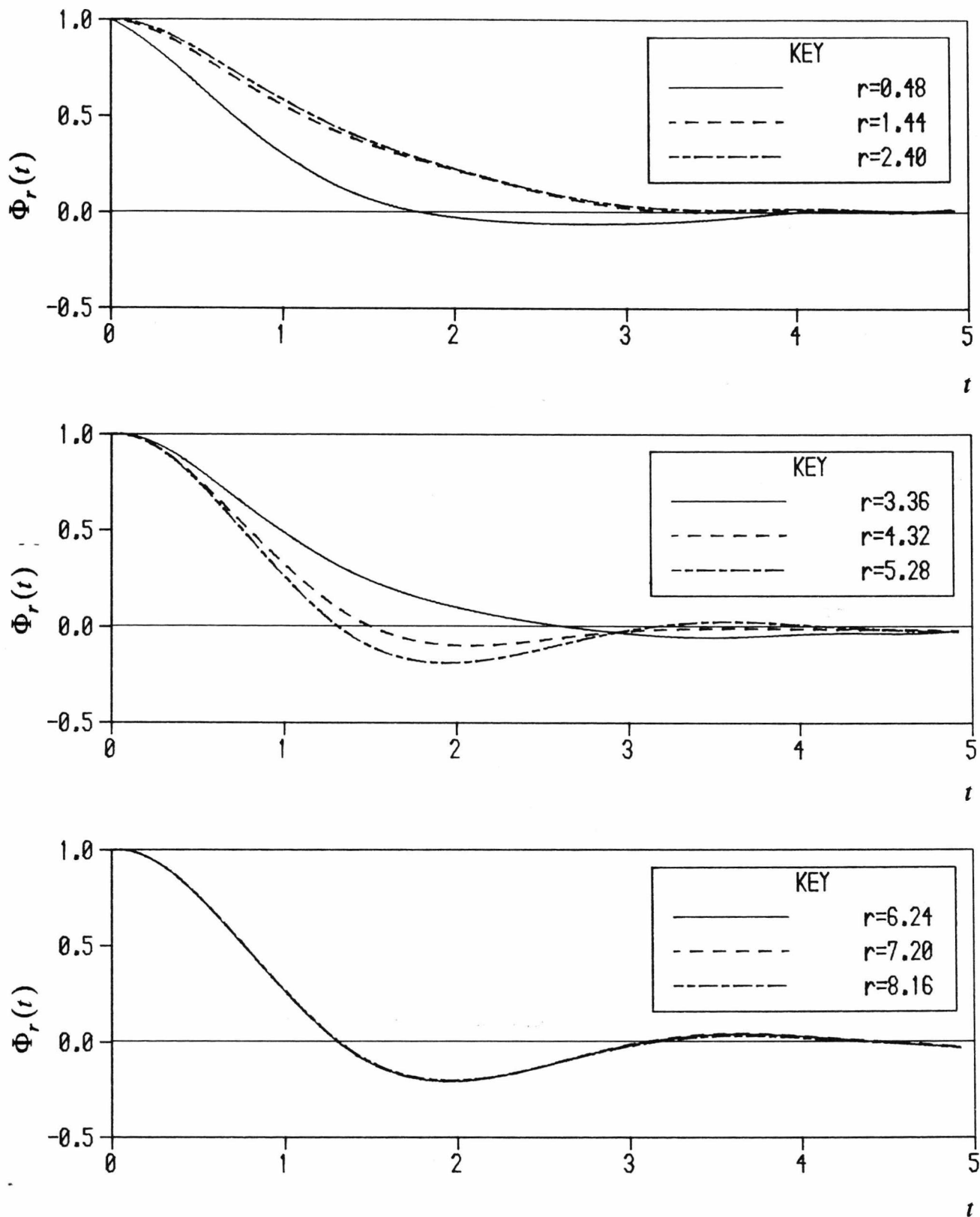


Figure 8.2: As for fig. (8.1), but for the total moment correlation functions,  $\Phi_r(t)$ . These values are measured over all the particles within the given radius,  $r$ .

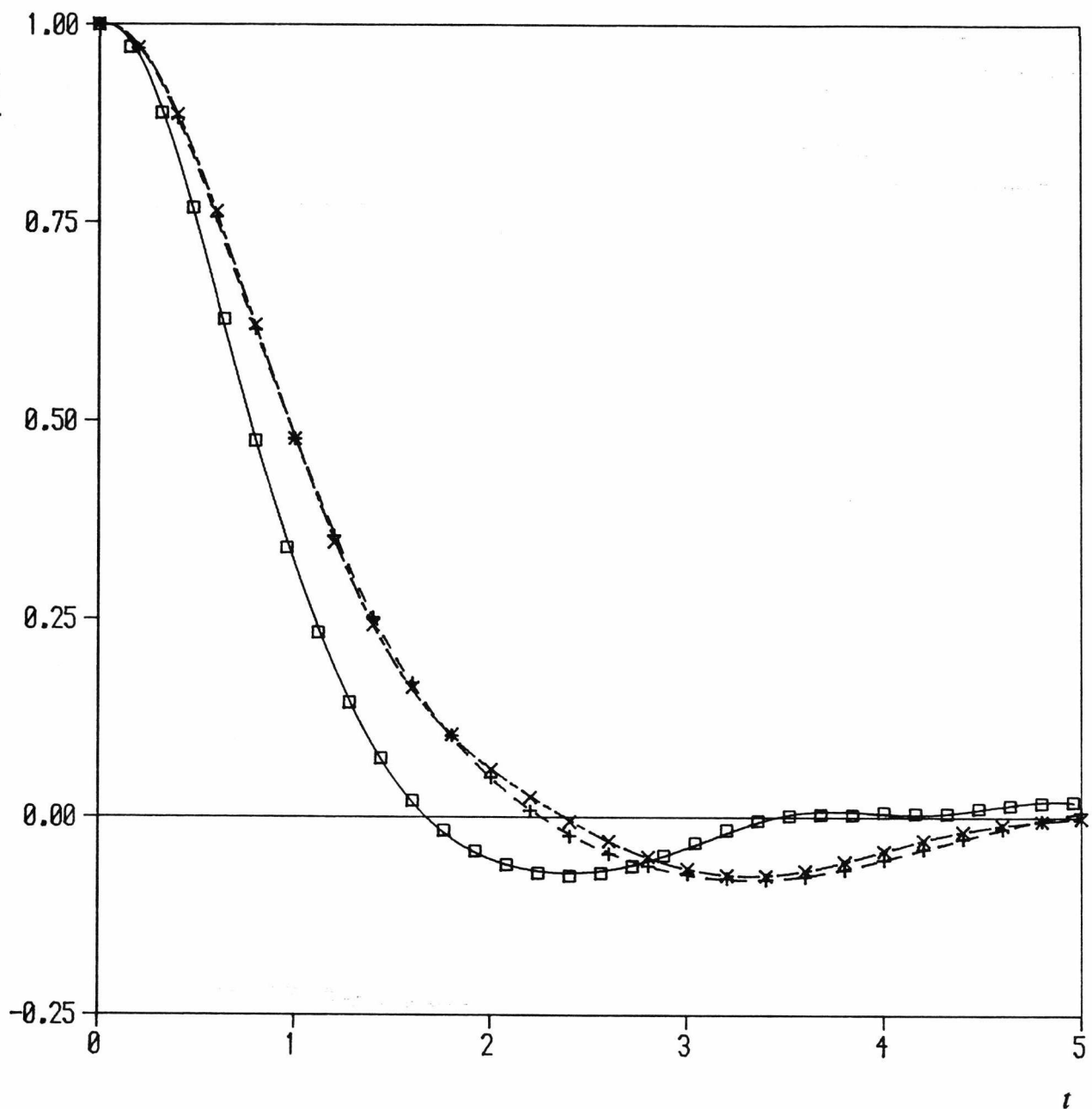


Figure 8.3: The normalized single particle correlation functions  $\Phi_r^s(t) = \langle \boldsymbol{\mu}(0) \cdot \boldsymbol{\mu}(t) \rangle_r / \mu^2$  against time for three S1 states. These are values measured well within the drop ( $r \sim 2.5$ ). The data for the higher temperature state, (D12), with  $N_p = 900$  and  $T = 0.913$ , is marked as ( $\square$ ). The other results are for states (D10),  $N_p = 800$  and  $T = 0.744$  (data as (+)) and (D6),  $N_p = 450$ ,  $T = 0.735$  (data as ( $\times$ )).

differ in size ( $N_p = 450$  and  $N_p = 800$  respectively). The values of  $\Phi_r^s(t)$  shown are for molecules well within the bulk liquid, and it can be seen that the results are very similar for these two states, as would be expected. As the temperature is increased, the correlation times will fall and this is illustrated by the other curve in the figure. This represents  $\Phi_r^s(t)$  within the liquid region of state (D12), which is at the temperature  $T = 0.91$ . The CF in this case decays more rapidly, as expected.

Figure (8.4) makes a similar comparison for the total moment CF,  $\Phi_r(t)$ . These are the results found well within the drops, but not at very small  $r$  where microscopic effects dominate (typically  $r \approx 2.5$ ). The data shown is for the same three states considered above.

As before we find that the CFs measured with the two systems of differing size, but similar temperature, are reasonably consistent with each other. The discrepancies that do occur at longer times are probably due to statistical errors. The higher temperature state again gives a more rapidly decaying CF, as expected.

We note that for the S1 states in general, the single particle correlation function always decays more quickly than the total moment function, at least beyond very short times, where the response is limited by inertia. This is in qualitative agreement with the observations of Pollock and Alder<sup>3</sup>. They have measured similar CFs in the Stockmayer fluid at a temperature of  $T = 1.35$  and density  $\rho = 0.8$  using a range of dipole strengths. Normal periodic boundary conditions plus Ewald summations were employed in their work. The results are not directly comparable due to the higher temperature and the fact that they use a moment of inertia 20% greater than ours. Moreover the total moment CF obtained using Ewald sums is not the same as that for a sphere immersed in its own medium, though it is expected to be similar (see chapter six and Neumann and Steinhauser<sup>4</sup> ).

Figure (8.5) shows some of the CFs that were found for the S3 drops, states (D13) and (D14). The decay is much slower for both the single and multi-particle CFs in

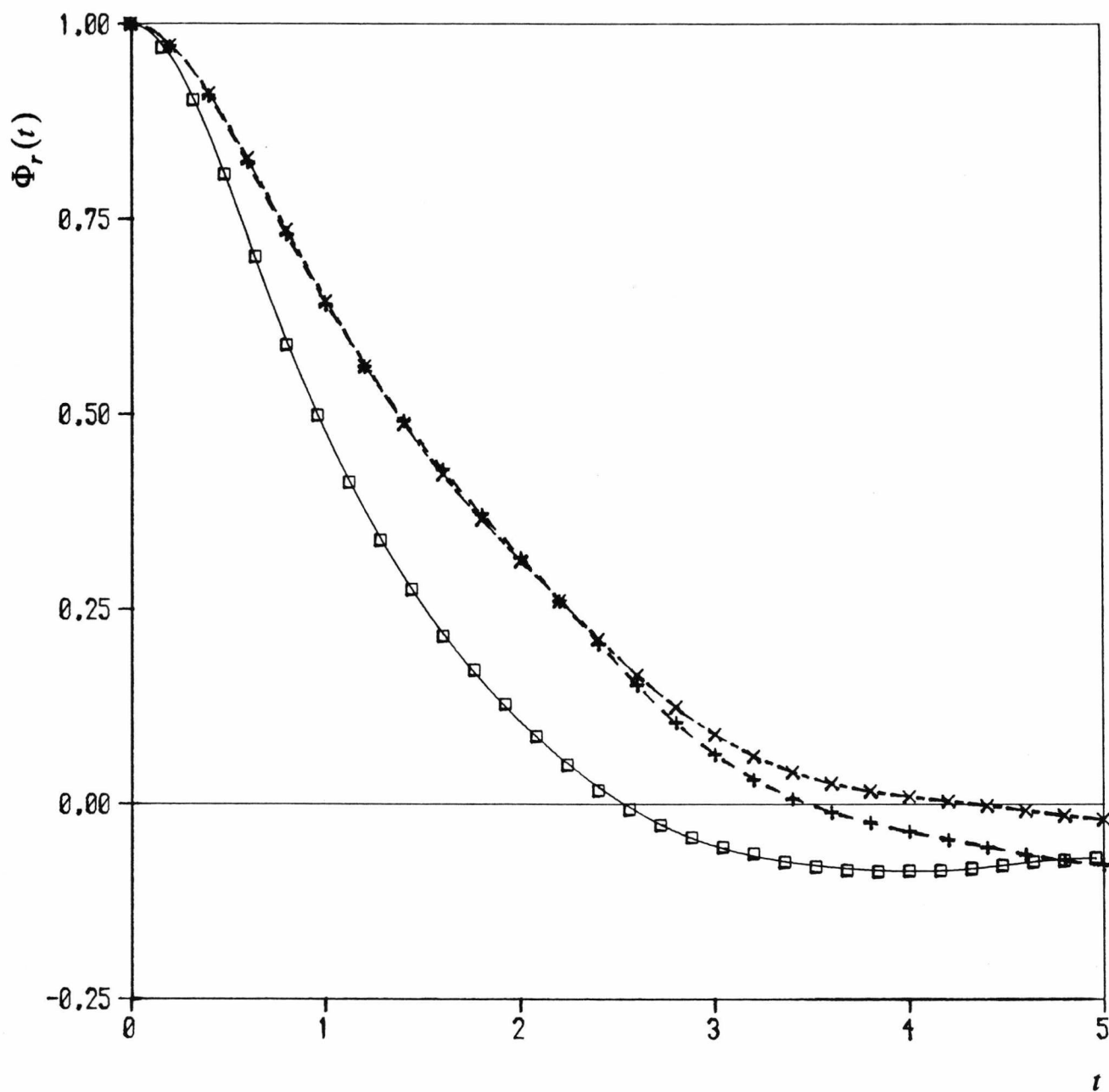


Figure 8.4: As for fig. (8.3), but for the total moment correlation functions,  $\Phi_r(t) = \langle M(0).M(t) \rangle_r / \langle M^2 \rangle$ . These are results measured at  $r \sim 2.5$  so that the spherical region lies well within the drop, but still encloses a significant number of molecules.

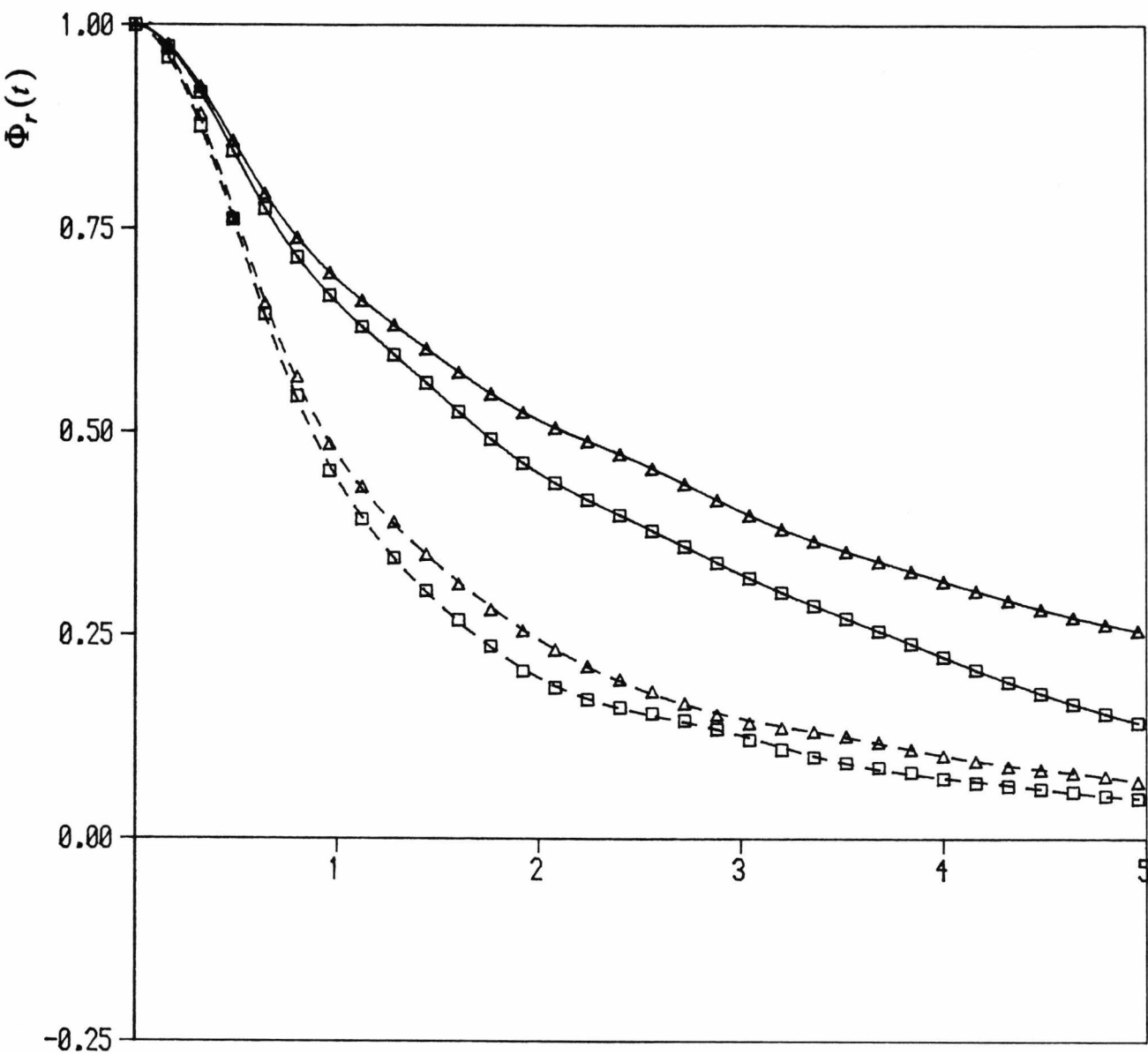


Figure 8.5: The correlation functions  $\Phi_r^s(t)$  (dashed curves) and  $\Phi_r(t)$  (solid curves) for the S3 drops. The CFs of the higher temperature state, (D14) with  $T = 1.25$  (marked as  $\square$ ) are seen to decay more rapidly than the corresponding results for (D13),  $T = 1.20$  (marked as  $\triangle$ ).

this fluid, despite the higher temperatures. As is also apparent in the results of Pollock and Alder, the increased dominance of the dipolar interaction for the S3 potential leads to a greater difference between  $\Phi_r(t)$  and  $\Phi_r^2(t)$ . We again note that the correlation functions decay more rapidly for the higher temperature system, as before. Beyond the short time (inertia) limit, the behaviour is close to exponential, as was found by Pollock and Alder<sup>†</sup>.

#### 8.4. Calculation of $\epsilon(\omega)$

In chapter six some methods for the calculation of  $\epsilon(\omega)$  from the total moment CF were discussed. The two main results are equations (6.21) and (6.22), the first applying to a macroscopic sphere immersed in its own medium and the second to a sphere in vacuum. For sufficiently large drops it should be possible to obtain the CF for an effectively immersed sphere, as long as  $r$  is such that  $(r/R_e)^3 \ll 1$ . However  $r$  must still be large enough that the volume can be treated macroscopically. On the other hand, if the vapour density is very low and the effect of the surface width can be ignored, then we would expect to obtain the CF given by equation (6.22) from measurements made for  $r > R_e$ .

It is not clear how a full generalization, like that used for the function  $\langle M^2(r) \rangle$  in the previous chapter, can be derived for the time CFs that correspond to "partially immersed" spheres. Following the static case, one can derive an analogous formula for a sphere within a larger sphere within a vacuum. However this still requires that  $\epsilon(\omega)$  is independent of  $r$ , within the whole dielectric drop. A more complete macroscopic treatment would require an expression for the dielectric constant as a function of both  $\omega$  and  $r$ , which we do not attempt to find here. Hence we have just

---

<sup>†</sup> In fact it can be shown<sup>5</sup> that the total moment CF for a "Debye dielectric" sphere immersed in its own medium is composed of two exponentials,  $\Phi_r(t) = (2\epsilon_s + 1)^{-1} [2\epsilon_s \exp(-t/\tau_D) + \exp(-\epsilon_s t/\tau_D)]$ , where  $\tau_D$  is the Debye relaxation time. The geometry used by P&A would give a single relaxation time<sup>4</sup>.

examined the results obtained by using equations (6.21) and (6.22) on the appropriate CFs that were measured in the simulations, to see if a consistent form for  $\epsilon(\omega)$  can be found. Because these calculations have not, so far, proved very successful, only a short description is given of the methods used.

Having chosen to use either the immersed sphere or sphere in vacuum relation (or some intermediate version), the first problem is always to calculate the Fourier-Laplace transform which we shall denote as,

$$F_L[-\dot{\Phi}_r(t)] = \left( 1 - i\omega \int_0^{\infty} \Phi_r(t) e^{-i\omega t} dt \right) \quad (8.1)$$

A number of techniques may be used to find this, perhaps the most obvious of which is to employ a numerical FFT on the data. However, due to the noise that arises in the CFs at long times, we instead chose to use a fitting procedure to express the given CF in terms of a series of functions for which the transform in equation (8.1) may be found analytically. The required result can then be calculated directly from the coefficients of the fit. The functional form that we used was,

$$\Phi(t) = e^{-\beta t/2} \left( \sum_{n=1}^N a_n L_n(\beta t) \right) \quad (8.2)$$

where  $L_n(x)$  is the  $n^{\text{th}}$  order Laguerre polynomial (e.g. see Arfken<sup>6</sup>) and the parameters  $\beta$  and  $a_n$  are to be fitted to the data. These functions are orthogonal and their transforms can easily be found. The only difficulty is in constraining the fit to give the correct form of  $\Phi(t)$  in the limit  $t \rightarrow 0$ . It can be shown that the finite inertia,  $I$ , of the molecules requires that  $\dot{\Phi}(0) = 0$  and  $\ddot{\Phi}(0) = -(2\mu^2 NkT/I)/\langle M^2 \rangle$ , where  $N$  is the mean number of molecules within the sphere (for details see e.g. Scaife<sup>7</sup>).

Once such a transform has been made,  $\epsilon(\omega)$  can then be calculated from the data. For the sphere in vacuum CF (eqn. (6.22)) the required formula is,

$$\epsilon(\omega) = \frac{2\alpha(\omega) + 1}{1 - \alpha(\omega)} \quad (8.3)$$

using the notation  $\alpha(\omega) \equiv \frac{(\epsilon_s - 1)}{(\epsilon_s + 2)} F_L[-\dot{\Phi}(t)]$ . In the immersed sphere case (eqn.

(6.22)) we have to solve a quadratic equation for  $\epsilon(\omega)$ ,

$$\epsilon(\omega) = \frac{1 + \alpha(\omega) \pm [(1 + \alpha(\omega))^2 + 8]^{1/2}}{4} \quad (8.4)$$

with in this case,  $\alpha(\omega) \equiv \frac{(\epsilon_s - 1)(2\epsilon_s + 1)}{\epsilon_s} F_L[-\dot{\Phi}(t)]$ , and we have to take the positive root to get  $\epsilon(0) = \epsilon_s$ . This latter form highlighted some of the inadequacy of the method used here, since it generally yielded unphysical results for  $\epsilon(\omega)$  as  $\omega \rightarrow \infty$ . In particular the solution has to obey both the conditions  $\epsilon(0) = \epsilon_s$  and  $\epsilon(\infty) = 1$ . What we found was that, starting from the zero frequency limit and using (8.4) to find  $\epsilon(\omega)$  as  $\omega$  increases, we would end up on the wrong root, with  $\epsilon'(\infty) < 0$ . This is clearly unacceptable and use of the equations for a partially immersed macroscopic drop did not correct this deficiency.

To understand how the above problem can occur, we consider the case of a Debye dielectric, the CF for which is<sup>5</sup>,  $\Phi(t) = (2\epsilon_s + 1)^{-1} [2\epsilon_s e^{-t/\tau_D} + e^{-t\epsilon_s/\tau_D}]$ . Transforming this and using (8.4) leads to two solutions for  $\epsilon(\omega)$ . The first of these gives the expected semi-circle (if plotted in a Cole-Cole plot) which runs from  $\epsilon(0) = \epsilon_s$  to  $\epsilon(\infty) = 1$ . The second, unwanted, solution is a smaller arc from  $\epsilon(0) = -1/(2\epsilon_s)$  to  $\epsilon(\infty) = -1/2$ . Now as the form of the function  $\alpha(\omega)$  departs from the Debye limit these two solutions remain distinct until a "cross-over" point is reached, beyond which the curve starting from  $\epsilon(0) = \epsilon_s$  goes continuously to  $\epsilon(\infty) = -1/2$ . The other solution then goes from  $\epsilon(\infty) = 1$  to  $\epsilon(0) = -1/(2\epsilon_s)$ . This is *not* due to problems as to which value to take for the complex square root. In practice the form of  $\alpha(\omega)$  must be such that this cross-over cannot occur, or if it does then there must be another "cross-over", possibly associated with the long time behaviour of the CF, such that correct limiting values are obtained. Note that this problem does not occur with reaction field or lattice summation simulations, since a linear relation then holds between  $\epsilon(\omega)$  and the appropriate  $\alpha(\omega)$ <sup>4</sup>.

Calculating  $\epsilon(\omega)$  from equation (8.3) using the isolated system CF also avoids the difficulties associated with getting a consistent solution from a quadratic equation, but it is not very satisfactory for other reasons. Apart from the presence of the surrounding vapour, the surface width of the drops used in this work is not negligible in comparison to the radius,  $R_c$ . To see how important this is we can calculate the “mean” density seen by the molecules within the drop, which we define by  $\bar{\rho} = \int_0^R dr 4\pi r^2 \rho^2(r)/N$ ,  $N$  being the number of particles within radius  $R$ . For  $R$  just outside the surface of the drop it is found that this mean density is typically 20 to 40% lower than the measured value at the centre of the drop. Hence the assumption of a uniform system is not a very good approximation.

These problems are illustrated by figure (8.6) which shows the results for  $\epsilon(\omega)$  obtained by the two different methods in the form of a Cole-Cole plot. This data is for state (D7) at  $T=0.81$ , using the S1 potential. The difference between the curves is greater than is immediately apparent from the Cole-Cole plot because the frequencies are not shown. Both cases show a divergence from the Debye result that is more marked than that found by either Hesse-Bezot *et al* or Neumann *et al* for the S3 potential. This casts further doubt on the reliability of our data. We note that there is some indication of a “bump” at high frequencies, at least for the immersed sphere Cole-Cole plot, qualitatively similar to a feature found by Neumann *et al*.

### 8.5. Discussion

No very satisfactory results have been obtained for  $\epsilon(\omega)$  by this method. Part of the problem maybe that our runs were not long enough, and we note that Neumann *et al*<sup>2</sup> used production runs of 100000 steps in their studies of the CF for a homogeneous S3 sample ( $N_p = 512$ ). Nevertheless it seems likely that we would have to use a significantly larger number of particles to be confident of having the true “immersed sphere” CF. To calculate the CF for an isolated sphere it might be better to adopt the

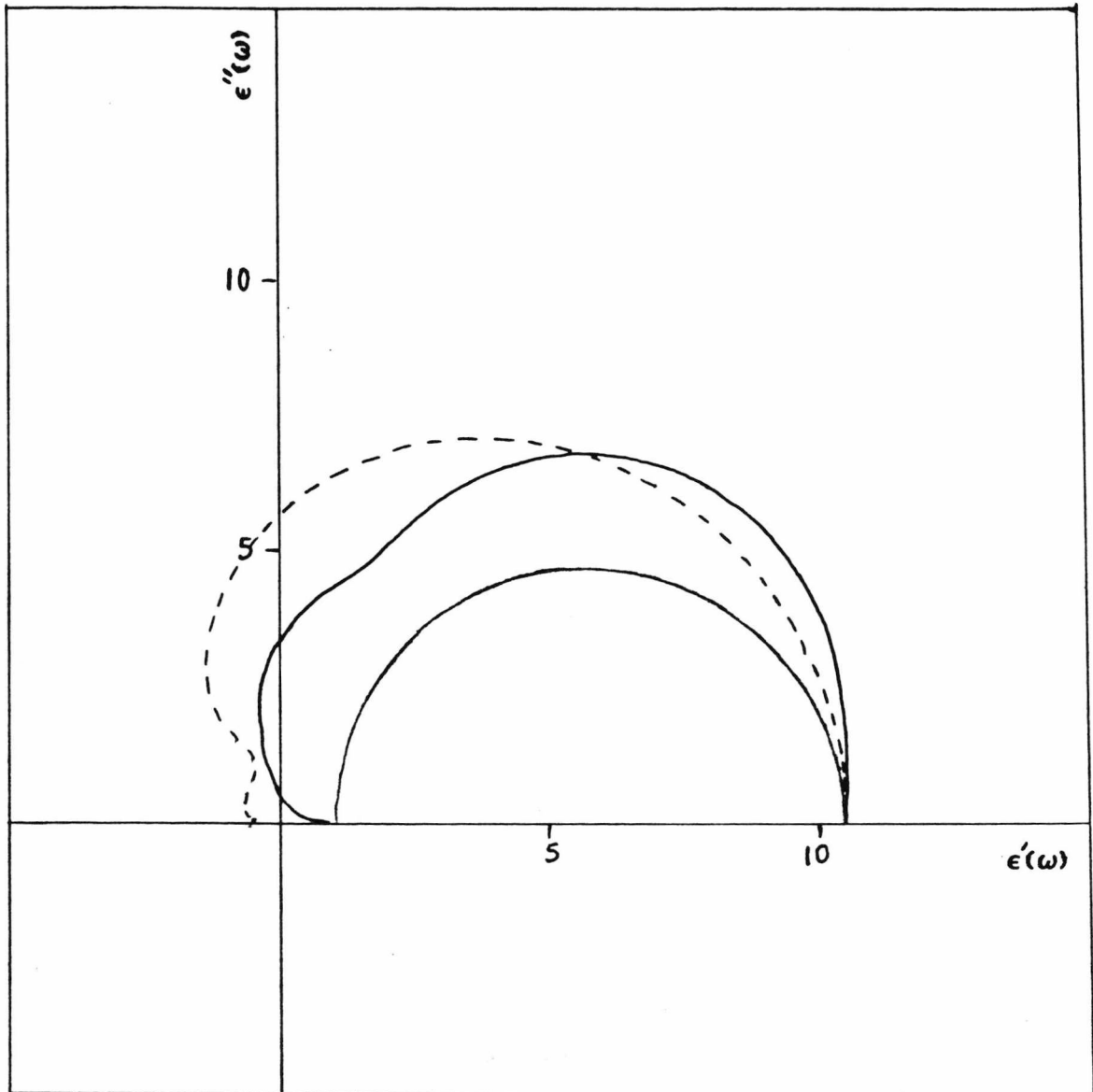


Figure 8.6: Cole-Cole plots for the dynamic dielectric constant  $\epsilon(\omega)$  for state (D7). The dashed curve is the result obtained from the total moment CF within the drop, using the immersed sphere formula. The upper solid curve is that obtained from the CF at large  $r$  assuming the system to be a sphere in vacuum. The Debye semicircle is also shown for comparison.

approach used by Hesse-Bezot *et al*<sup>8</sup>. Their simulation of 1472 particles contained within a spherical "wall" potential avoids any complications due to the vapour, and limits the surface region to some extent. They claim to be able to calculate  $\epsilon(\omega)$  satisfactorily from the CF  $\Phi(t)$  for the whole sphere, though they do not give details of the measured form of the CF and only state that the Fourier-Laplace transform was made numerically. There is some difference between the Cole-Cole plots for  $\epsilon(\omega)$  obtained by Hesse-Bezot *et al* and by the reaction field calculations of Neumann *et al*, though the latter used a larger dipole moment and a lower temperature. It would be interesting to perform calculations of  $\epsilon(\omega)$  for the same state point by both methods to make a better comparison.

Hesse-Bezot *et al* find that their statistics are too poor to allow the calculation of  $\epsilon(\omega)$  from the immersed CFs obtained from their simulations. Their main run was of 7000 steps, with  $\Delta t \approx 0.035$ .

A number of relations that exist between the various correlation times in such systems are also mentioned in the above paper<sup>†</sup>, and for the immersed sphere and sphere in vacuum CFs the ratio is given by,

$$\frac{\tau_{vac}}{\tau_{imm}} = \frac{3\epsilon_s(2\epsilon_s + 1)}{(\epsilon_s + 2)(2\epsilon_s^2 + 1)} \quad (8.5)$$

Some rough calculations for the S3 state (D13) give  $\tau_{imm} = 3.2 \pm 0.2$  and  $\tau_{vac} = 0.65 \pm 0.1$ . Thus the ratio of these correlation times is  $\tau_{imm}/\tau_{vac} \approx 5 \pm 1$ , whereas using the calculated dielectric constant for this state in equation (8.5) implies that this ratio should be  $\sim 10$ . This is a further indication of the discrepancy between the two functions.

Neumann *et al* and Pollock and Alder have given some results for the S3 correlation times at temperatures above and below those of states (D13) and (D14).

---

<sup>†</sup> The definition of the correlation time used is  $\tau = \int_0^{\infty} \Phi(t) dt$

However due to the long range corrections they use, these times are not equivalent to the ones we measure, as is explained by Neumann and Steinhauser<sup>4</sup>. It is possible to predict the true immersed CF from the CFs that they measure, and Neumann *et al* have done this for  $T = 1.15$ , and we estimate the correlation time (from their graph) to be  $\tau_{imm} \approx 6 \pm 1$ . Pollock and Alder's data only allows an upper bound to be easily found for the correlation time at  $T = 1.35$ , which is  $\tau_{imm} < 3.7$ . Thus our result of  $\tau_{imm} = 3.2$  at  $T = 1.2$  is probably too low, but not drastically so. We conclude that longer runs with drops of over  $\sim 1000$  particles may yield more satisfactory results for  $\epsilon(\omega)$ , but that the cost of such simulations would be very great. This has to be contrasted with methods such as that of Neumann *et al*, who used systems of 512 dipoles to find this function.

#### References

1. W.A.B.Evans and J.G.Powles, *Molec. Phys.*, vol. 45, p. 695, 1982.
2. M.Neumann, O.Steinhauser, and G.S.Pawley, *Molec. Phys.*, vol. 52, p. 97, 1984.
3. E.L.Pollock and B.J.Alder, *Phys. Rev. Lett.*, vol. 46, p. 950, 1981.
4. M.Neumann and O.Steinhauser, *Chem. Phys. Letters*, vol. 102, p. 508, 1983.
5. S.H.Glarum, *Molec. Phys.*, vol. 24, p. 1327, 1972.
6. G.Arftken, *Mathematical methods for physicists*, Academic Press, London, 1970.
7. B.K.P.Scaife, *Complex permittivity*, The English University Press, London, 1971.
8. C.Hesse-Bezot, G.Bossis, and C.Brot, *J. Chem. Phys.*, vol. 80, p. 3399, 1984.

## Conclusion

In this work we have investigated a number of different properties of small drops in equilibrium with their own vapour. These highly inhomogeneous systems have been studied over a range of temperatures from just below the triple point to about half way between  $T_t$  and  $T_c$ . It has been found most convenient to work with systems of about 450 particles, since these are large enough to give a significant region of constant density liquid within the drops, while not requiring excessive time to compute. However, a range of system sizes have been used and this enables checks to be made on the sensitivity of measured quantities to the number of particles employed.

The measurement of surface tension in this highly curved system, via use of the Kelvin equation, has been shown to be feasible, at least for large drops at temperatures near  $T_t$ . It seems that the effects of the surface curvature on  $\gamma$  are quite small, even for systems of only  $\sim 1000$  atoms. However, it is necessary to know the coexistence vapour pressure quite accurately as well as making a long simulation to ensure reliable data for the vapour density outside the drop. With the falling cost of computing, and making use of the corrections to the Kelvin equation as suggested by Powles<sup>1</sup>, this could become a viable technique for the determination of  $\gamma$  to moderate accuracy, avoiding the complexities necessary in methods such as that of Miyazaki *et al*<sup>2</sup>. Clearly there is much further work that could be performed on this topic and in particular we would have liked to have investigated the surface tension of the Stockmayer drops, had their been sufficient time. It is possible that  $\gamma$  would show a significantly greater size dependence in such systems due to the long range nature of the dipole interactions.

The study of the surface width of drops has been shown to be consistent with a range of theoretical predictions of this quantity for the LJ12-6 fluid, when the effect of surface oscillations are included. As we noted, there is still some uncertainty as to the exact contribution that capillary waves make to the theoretically calculated widths<sup>3</sup>.

Further simulations to improve the accuracy and range of surface width measurements would be useful in this respect. Also, work on improving the capillary wave analysis for small drops (for example by including the fact that an intrinsic width is already present) would allow better comparisons to be made.

The static dielectric constant of the S1 fluid, as obtained from  $\langle M^2 \rangle$  measurements within drops, is found to be consistent with data from homogeneous simulations that use Ewald summation techniques. However, for the S3 potential the calculated value of  $\epsilon_s$  is rather lower than expected from similar homogeneous simulations. Only systems of 450 particles were employed in the S3 measurements, and this probably indicates that larger samples are required in such strongly polar cases. It would be desirable to make a more detailed study of S3 drops.

The variation of the mean square moment through the surface of drops has been used to find the effective dielectric profiles for a number of states. These results indicate a variation of  $\epsilon(r)$  that is quite similar to that of the measured density profile. A simple scalar function for  $\epsilon(r)$  is found adequate to explain most of our data, though clearly further work is required on the theoretical interpretation of the dielectric constant within the liquid-vapour interface.

Investigations are currently being made in this laboratory by J.G.Powles, M.L.Williams and W.A.B.Evans on the properties of similar isolated drops, but using a hard spherical wall to contain the system. This offers a number of advantages over the systems discussed here. In particular, the necessary equilibration times should be reduced, the need for a truncation of the interaction potential is completely eliminated and it is possible to study densities greater than the coexistence value at the given temperature. The undesirable restriction to temperatures significantly less than  $T_c$  is also removed. Work has been made on the pressure tensor within such systems and on the meaning of virial pressure<sup>4</sup>.

The simulation of drops has proven useful for the calculation of both properties of the surface and of the bulk liquid. With the falling cost of computing power, the range and size of systems that can usefully be simulated is constantly increasing. This will make methods like those discussed here more viable and there is clearly great scope for further work along these lines. One of the most pressing needs is for the use of more realistic interaction potentials. In particular it is known that the Stockmayer model is a far from perfect representation of a real polar liquid and it is desirable to include the effects of molecular shape, polarizability and higher order electric moments. One such model has recently been proposed by Murad<sup>5,6</sup>. Since our ultimate goal is to explain the interactions of real liquids such models must be adopted in future.

#### References

1. J.G.Powles, *J. Phys. A*, vol. 18, p. 1551, 1985.
2. J.Miyazaki, J.A.Barker, and G.M.Pound, *J. Chem. Phys.*, vol. 64, p. 3364, 1976.
3. R.Evans, *Molec. Phys.*, vol. 42, p. 1169, 1981.
4. J.G.Powles, G.Rickayzen, and M.L.Williams, *J. Chem. Phys.*, vol. 83, p. 293, 1985.
5. S.Murad, *Molec. Phys.*, vol. 51, p. 525, 1984.
6. S.Murad, A.Papaioannou, and J.G.Powles, *Molec. Phys.*, vol. 55, 1985. (In press)

## Appendix A: Listing of the LJ simulation programme

This appendix gives a listing of a version of the Fortran-77 programme used in the LJ simulations. The subroutine to locate the cluster (GETDRP) is not included, since this is given in appendix C. To reduce the size of these listings, a shorthand notation is used here, where by a common block is just listed by its name in angle brackets (e.g. <COMMON /VEC/, ..>) after the first occurrence, and all the names within each block are kept the same.

```

PROGRAM LD4
C Liquid drop simulation programme. Uses LJ12-6 interaction
C on drop surrounded by vapour in large periodic cell.
C NP= number of particles; ND= number of divisions for density profile
PARAMETER ( NP = 800 , ND = 50 )
COMMON /VEC/ X0(NP),Y0(NP),Z0(NP),X1(NP),Y1(NP),Z1(NP),X2(NP),
+ Y2(NP),Z2(NP),X3(NP),Y3(NP),Z3(NP),X4(NP),Y4(NP),Z4(NP),
+ X5(NP),Y5(NP),Z5(NP)
COMMON /FORCE/ FX(NP),FY(NP),FZ(NP)
COMMON /NUM/DELTA,FCUT,SIDE,TIME,NCLUST,NINIT,MINSTP,MAXSTP
+ ,IPRFQ,IDMPFQ,IGOPFQ,IDPFQ,IRESFQ,TFIXED
COMMON /SUMS/SUMK,SUMK2,SUMU,SUMU2,NOPROF(0:ND),NDC(0:ND),
+ NCDIST(NP),SUMP
COMMON /RES/ ETOT,EKIN,U,VIR
COMMON /FILES/ FDATA,FLDM,FPROF
CHARACTER*14 FDATA,FLDM,FPROF
LOGICAL OLD
CALL SETUP(OLD)
C For a new run do ten steps at DELTA/10 to get derivatives right.
IF (.NOT.OLD) THEN
CALL SETZER
CALL CHDELTA( DELTA/10. )
DO 35 I=-1,-10,-1
TIME=TIME+DELTA
CALL PREDIC
CALL FORCES
CALL CORREC
CALL DATA(I)
CALL RESCAL(I)
35 CONTINUE
CALL CHDELTA( DELTA*10.)
CALL SETZER
ENDIF
C A negative step number is used to indicate the initialization period.
IF (MINSTP.LE.0) THEN
DO 40 I=MINSTP-1,-NINIT,-1
TIME=TIME+DELTA
CALL PREDIC
CALL FORCES
CALL CORREC
CALL DATA(I)
CALL RESCAL(I)
40 CONTINUE
CALL SETZER
MINSTP=0
ENDIF
C Main production run loop. MINSTP is step at which configuration was saved.
DO 50 I=MINSTP+1,MAXSTP
TIME=TIME+DELTA
CALL PREDIC
CALL FORCES
CALL CORREC

```

```

      CALL DATA(I)
      CALL RESCAL(I)
50  CONTINUE
      WRITE(*,('/' FINISHED'))
      STOP
      END

```

#### SUBROUTINE PREDIC

C Predict new positions and derivatives.

PARAMETER ( NP = 800 )

<COMMON /VEC/, /NUM/ >

```

      DO 10 I = 1, NP
        X0(I) = X0(I)+X1(I)+X2(I)+X3(I)+X4(I)+X5(I)
        Y0(I) = Y0(I)+Y1(I)+Y2(I)+Y3(I)+Y4(I)+Y5(I)
        Z0(I) = Z0(I)+Z1(I)+Z2(I)+Z3(I)+Z4(I)+Z5(I)
        X1(I) = X1(I)+2.*X2(I)+3.*X3(I)+4.*X4(I)+5.*X5(I)
        Y1(I) = Y1(I)+2.*Y2(I)+3.*Y3(I)+4.*Y4(I)+5.*Y5(I)
        Z1(I) = Z1(I)+2.*Z2(I)+3.*Z3(I)+4.*Z4(I)+5.*Z5(I)
        X2(I) = X2(I)+3.*X3(I)+6.*X4(I)+10.*X5(I)
        Y2(I) = Y2(I)+3.*Y3(I)+6.*Y4(I)+10.*Y5(I)
        Z2(I) = Z2(I)+3.*Z3(I)+6.*Z4(I)+10.*Z5(I)
        X3(I) = X3(I)+4.*X4(I)+10.*X5(I)
        Y3(I) = Y3(I)+4.*Y4(I)+10.*Y5(I)
        Z3(I) = Z3(I)+4.*Z4(I)+10.*Z5(I)
        X4(I) = X4(I)+5.*X5(I)
        Y4(I) = Y4(I)+5.*Y5(I)
        Z4(I) = Z4(I)+5.*Z5(I)

```

```

10  CONTINUE
      RETURN
      END

```

#### SUBROUTINE FORCES

C Most time consuming part of the simulation; calculation of all forces.

PARAMETER ( NP = 800 , WTMOL = 48. , ND = 50 )

<COMMON /VEC/, /FORCE/, /NUM/, /RES/ >

```

      U=0.
      VIR=0.
      SIDE2=SIDE/2.
      FCUT2=FCUT*FCUT
      SF=2.*ND/SIDE
      DO 10 I=1, NP
        FX(I)=0.
        FY(I)=0.
        FZ(I)=0.

```

```

10  CONTINUE
      DO 20 I=2, NP
        FXI=0.
        FYI=0.
        FZI=0.
        XI=X0(I)
        YI=Y0(I)
        ZI=Z0(I)
        DO 30 J=1, I-1
          X=X0(J)-XI
          Y=Y0(J)-YI
          Z=Z0(J)-ZI
          R2= X*X+Y*Y+Z*Z
          IF (R2.GT.FCUT2) THEN
            IF (X.GT.SIDE2) THEN
              X=X-SIDE
            ELSE IF (X.LT.-SIDE2) THEN
              X=X+SIDE
            ENDIF
            IF (Y.GT.SIDE2) THEN
              Y=Y-SIDE
            ELSE IF (Y.LT.-SIDE2) THEN
              Y=Y+SIDE
            ENDIF
            IF (Z.GT.SIDE2) THEN
              Z=Z-SIDE
            ELSE IF (Z.LT.-SIDE2) THEN
              Z=Z+SIDE
            ENDIF
          ENDIF
        END DO

```

```

ENDIF
R2= X*X+Y*Y+Z*Z
IF (R2.GT.FOUT2) GOTO 30
ENDIF
RINV2=1./R2
RINV6=RINV2*RINV2*RINV2
U=(RINV6-1.)*RINV6+U
A=(2.*RINV6-1.)*RINV6*RINV2
VIR1=0.
F=A*X
FXI=FXI-F
FX(J)=FX(J)+F
VIR1=VIR1+X*F
F=A*Y
FYI=FYI-F
FY(J)=FY(J)+F
VIR1=VIR1+Y*F
F=A*Z
FZI=FZI-F
FZ(J)=FZ(J)+F
VIR1=VIR1+Z*F
VIR=VIR+VIR1
30 CONTINUE
FX(I)=FX(I)+FXI
FY(I)=FY(I)+FYI
FZ(I)=FZ(I)+FZI
20 CONTINUE
D=12.*DELTA*DELTA/WTMOL
DO 40 I=1,NP
FX(I)=FX(I)*D
FY(I)=FY(I)*D
FZ(I)=FZ(I)*D
40 CONTINUE
U= U*.7/NP
VIR=VIR*.24.
RETURN
END

```

## SUBROUTINE CORREC

C Apply Gear correction step.

PARAMETER ( NP = 800 )

&lt;COMMON /VEC/, /NUM/, /FORCE/ &gt;

DATA F02,F12,F32,F42,F52

+ /.15,.69722222,.61111111,.16666667,.016666667/

DO 10 I=1,NP

XCOR = X2(I)-FX(I)

YCOR = Y2(I)-FY(I)

ZCOR = Z2(I)-FZ(I)

X0(I) = X0(I)-XCOR\*F02

X1(I) = X1(I)-XCOR\*F12

X2(I) = X2(I)-XCOR

X3(I) = X3(I)-XCOR\*F32

X4(I) = X4(I)-XCOR\*F42

X5(I) = X5(I)-XCOR\*F52

Y0(I) = Y0(I)-YCOR\*F02

Y1(I) = Y1(I)-YCOR\*F12

Y2(I) = Y2(I)-YCOR

Y3(I) = Y3(I)-YCOR\*F32

Y4(I) = Y4(I)-YCOR\*F42

Y5(I) = Y5(I)-YCOR\*F52

Z0(I) = Z0(I)-ZCOR\*F02

Z1(I) = Z1(I)-ZCOR\*F12

Z2(I) = Z2(I)-ZCOR

Z3(I) = Z3(I)-ZCOR\*F32

Z4(I) = Z4(I)-ZCOR\*F42

Z5(I) = Z5(I)-ZCOR\*F52

10 CONTINUE

RETURN

END

## SUBROUTINE DATA(I)

C Calculation of all averages and printing of results carried out

C by this subroutine.

```

PARAMETER ( NP = 800 , WTMOL = 48. , ND = 50 )
<COMMON /VEC/, /NUM/, /RES/, /SUNS/, /FILES/ >
CHARACTER*14 FDATA,FLDM,FPROF
INTEGER CLUST(NP)
LOGICAL CAL1
SAVE CLUST,CAL1,XSUM,YSUM,ZSUM
DATA CAL1/.TRUE./,XSUM,YSUM,ZSUM/0.,0.,0./,PI4/12.56637/
SF= 2.*ND/SIDE
IF ( CAL1 ) THEN
  CALL GETDRP( CLUST,LEN,3.61 )
  CAL1=.FALSE.
ENDIF
CALL CMASS( XSUM,YSUM,ZSUM,CLUST,LEN )
V2=0.
C Sample the density profile of the whole system and the cluster
DO 10 JJ=1,NP
  J=CLUST(JJ)
  R= SQRT( (X0(J))**2 + (Y0(J))**2 + (Z0(J))**2 )
  NBOX=SF*R
  IF (NBOX.GT.ND) NBOX=ND
  NDPROF(NBOX)=NDPROF(NBOX)+1
  IF (JJ.LE.LEN) NDC(NBOX)=NDC(NBOX)+1
  V2=V2+X1(J)**2+Y1(J)**2+Z1(J)**2
10 CONTINUE
V2= V2/(NP*DELTA*DELTA)
PRESS=(NP/SIDE**3)*(EKIN**2./3.+VIR/(3.*NP))
SUMP=SUMP+PRESS
EKIN= V2*WTMOL/2.
SUMK= SUMK+EKIN*DELTA
SUMU= SUMU+U*DELTA
SUMU2=SUMU2+U**2*DELTA
SUMK2=SUMK2+EKIN**2*DELTA
IF ( MOD(I,IGDPFQ).EQ.0 ) THEN
  CALL GETDRP( CLUST,LEN,3.61 )
  NCLUST=NCLUST+LEN
ENDIF
IF ( MOD(I,IIPRFQ).EQ.0 ) THEN
  AVCL=REAL( (NCLUST*IGDPFQ) )/I
  AVU= SUMU/TIME
  AVK= SUMK/TIME
  AVE= AVU+AVK
  AVP=SUMP/I
  SIGK= SQRT( SUMK2/TIME-AVK**2 )
  SIGU= SQRT( SUMU2/TIME-AVU**2 )
  OPEN(2,FILE=FLDM)
  CALL FSEEK(2,0,2)
  WRITE(2, '(I5,5F9.5,F9.2,I5,5F8.4,2E11.4E1)') I,AVE,AVK,AVU,
+   SIGU,SIGK,AVCL,LEN,XSUM,YSUM,ZSUM,EKIN,U,PRESS,AVP
  CLOSE(2)
  IF ( MOD(I,IDPFQ).EQ.0 ) THEN
    OPEN(3,FILE=FPROF)
    CALL FSEEK(3,0,2)
    WRITE(3, '(I6,F9.5)') I,SIDE
    WRITE(3, '(17I7)') NDPROF
    WRITE(3, '(17I7)') NDC
    CLOSE(3)
    WRITE(4, '(3I6)') I,IGDPFQ,NP
    WRITE(4, '(10I6)') NCDIST
  ENDIF
ENDIF
IF ( MOD(I,IDMPFQ).EQ.0 ) THEN
  OPEN(8,FILE=FDATA,FORM='UNFORMATTED',STATUS='OLD')
  REWIND(8)
  NPN=NP
  WRITE(8) NPN,ETOT,DELTA,SIDE
  WRITE(8) X0,Y0,Z0,X1,Y1,Z1,X2,Y2,Z2,X3,Y3,Z3,X4,Y4,Z4,
+   X5,Y5,Z5
  WRITE(8) NDPROF,NDC,SUMK,SUMU,SUMK2,SUMU2,
+   SUMP,,TIME,NREF,NCLUST,NCDIST,I
  CLOSE(8)
  IF (IDMPFQ.LT.0) STOP

```

```

ENDIF
RETURN
END

```

```

SUBROUTINE CMASS( XSUM,YSUM,ZSUM,CLUST,LEN )

```

C This routine performs a simple translation on the whole system  
C so that the centre of mass of the cluster is at (0,0,0).

```

PARAMETER ( NP = 800 )

```

```

<COMMON /VEC/, /NUM/ >

```

```

INTEGER CLUST(NP)

```

```

X=0.

```

```

Y=0.

```

```

Z=0.

```

```

SIDE2=SIDE/2.

```

```

DO 10 I=1,LEN

```

```

  I1=CLUST(I)

```

```

  X= X+X0(I1)

```

```

  Y= Y+Y0(I1)

```

```

  Z= Z+Z0(I1)

```

```

10 CONTINUE

```

```

X=X/LEN

```

```

Y=Y/LEN

```

```

Z=Z/LEN

```

```

DO 20 I=1,NP

```

```

  X0(I)=X0(I)-X

```

```

  Y0(I)=Y0(I)-Y

```

```

  Z0(I)=Z0(I)-Z

```

```

  IF (X0(I).GT.SIDE2) THEN

```

```

    X0(I)=X0(I)-SIDE

```

```

  ELSE IF (X0(I).LT.-SIDE2) THEN

```

```

    X0(I)=X0(I)+SIDE

```

```

  ENDIF

```

```

  IF (Y0(I).GT.SIDE2) THEN

```

```

    Y0(I)=Y0(I)-SIDE

```

```

  ELSE IF (Y0(I).LT.-SIDE2) THEN

```

```

    Y0(I)=Y0(I)+SIDE

```

```

  ENDIF

```

```

  IF (Z0(I).GT.SIDE2) THEN

```

```

    Z0(I)=Z0(I)-SIDE

```

```

  ELSE IF (Z0(I).LT.-SIDE2) THEN

```

```

    Z0(I)=Z0(I)+SIDE

```

```

  ENDIF

```

```

20 CONTINUE

```

```

XSUM=XSUM+X

```

```

YSUM=YSUM+Y

```

```

ZSUM=ZSUM+Z

```

```

RETURN

```

```

END

```

```

SUBROUTINE RESCAL(II)

```

C Rescale all velocities to keep total kinetic energy constant.

```

PARAMETER ( NP = 800 , ND = 50 )

```

```

<COMMON /VEC/, /NUM/, /RES/, /FILES/ >

```

```

CHARACTER*14 FDATA,FLDM,FPROF

```

```

LOGICAL TFIXED

```

```

IF (.NOT.TFIXED) THEN

```

```

  DIFF=ETOT-(EKIN+U)

```

```

  IF ( (ABS(DIFF).LT.0.001).AND.(MOD(II,IRESFQ).NE.0) ) RETURN

```

```

  DIFF=DIFF+EKIN

```

```

  IF ( (DIFF).LT.0.0 ) THEN

```

```

    WRITE(*,'('' -SORT '' ,I5)') II

```

```

    SF=0.1

```

```

  ELSE

```

```

    SF= SORT( (DIFF)/EKIN )

```

```

  ENDIF

```

```

ELSE

```

```

  SF= SORT( ETOT/EKIN )

```

```

  IF (MOD(II,IRESFQ).EQ.0) WRITE(2,'(F9.6)') SF

```

```

ENDIF

```

```

DO 10 I=1,NP

```

```

  X1(I)= X1(I)*SF

```

```

  Y1(I)= Y1(I)*SF

```

```

      Z1(I) = Z1(I)*SF
10  CONTINUE
      WRITE(2, '( " EK RES " ,F12.7)')SF
      RETURN
      END

```

#### SUBROUTINE SETZER

C Reset all sums to zero and start averaging from scratch.

PARAMETER ( NP = 800 , ND = 50 )

<COMMON /NUM/, /SUMS/ >

```

      TIME = 0.
      SUMK = 0.
      SUMK2 = 0.
      SUMU = 0.
      SUMU2 = 0.
      SUMP=0.
      DO 10 J= 0,ND
          NPROF(J)=0
          NDC(J)=0
10  CONTINUE
      NCLUST=0
      DO 30 J=1,NP
          NCDIST(J)=0
30  CONTINUE
      RETURN
      END

```

#### SUBROUTINE CHDELTA (DELNEW)

C Change time step

PARAMETER ( NP = 800 )

<COMMON /VEC/, /NUM/ >

```

      X = DELNEW/DELTA
      Y = X
      DELTA = DELNEW
      WRITE(*, '( " DELTA CHANGED TO : " ,F7.4)')DELTA
      DO 10 I = 1,NP
          X1(I) = X1(I)*X
          Y1(I) = Y1(I)*X
          Z1(I) = Z1(I)*X
10  CONTINUE
      X = X*Y
      DO 20 I = 1,NP
          X2(I) = X2(I)*X
          Y2(I) = Y2(I)*X
          Z2(I) = Z2(I)*X
20  CONTINUE
      X = X*Y
      DO 30 I = 1,NP
          X3(I) = X3(I)*X
          Y3(I) = Y3(I)*X
          Z3(I) = Z3(I)*X
30  CONTINUE
      X = X*Y
      DO 40 I = 1,NP
          X4(I) = X4(I)*X
          Y4(I) = Y4(I)*X
          Z4(I) = Z4(I)*X
40  CONTINUE
      X = X*Y
      DO 50 I = 1,NP
          X5(I) = X5(I)*X
          Y5(I) = Y5(I)*X
          Z5(I) = Z5(I)*X
50  CONTINUE
      RETURN
      END

```

#### SUBROUTINE SETUP (OLD)

C Interactively read parameters for run.

PARAMETER ( NP = 800 , ND = 50 )

<COMMON /VEC/, /NUM/, /SUMS/, /RES/, /FILES/ >

CHARACTER SUFFIX\*6,PARAM\*6,FDATA\*14,FLDM\*14,FPROF\*14,FCLUST\*14

```

LOGICAL OLD,TFIXED
PRINT'(/'' LIQUID DROP SIMULATION''')
PRINT'(/'' INPUT SUFFIX FOR FILENAMES''')
READ(*,'(A6)') SUFFIX
FDATA='DD4'//SUFFIX
OPEN(8,FILE=FDATA,FORM='UNFORMATTED',STATUS='OLD')
FLDM='LDM'//SUFFIX
INQUIRE(FILE=FLDM,EXIST=OLD)
OPEN(2,FILE=FLDM)
CALL FSEEK(2,0,2)
FPROF='PROF'//SUFFIX
OPEN(3,FILE=FPROF)
CALL FSEEK(3,0,2)
FCLUST='CLUST'//SUFFIX
OPEN(4,FILE=FCLUST)
CALL FSEEK(4,0,2)
REWIND(8)
READ(8)NIN,ETOT,DELTA,SIDE
FCUT=SIDE/2.
IF(NIN.NE.NP)THEN
  PRINT'(/'' ***** ERROR - INCORRECT DATA FILE'',//
+   '' NP='',I4,''' NIN='',I4)',NP,NIN
  STOP
ENDIF
READ(8) X0,Y0,Z0,X1,Y1,Z1,X2,Y2,Z2,X3,Y3,Z3,X4,Y4,Z4,X5,Y5,Z5
IF(OLD)THEN
  PRINT'('' RUN=OLD '')'
  READ(8) NPROF,NDC,SUMK,SUMU,SUMK2,SUMU2,
+   SUMP,TIME,NREF,NCLUST,NCDIST,MINSTP
  ELSE
  PRINT'('' RUN=NEW '')'
ENDIF
CLOSE(8)
10 PRINT'('' ALTER PARAMETER ?''')
READ(*,'(A6)')PARAM
IF(PARAM.EQ.'ETOT')THEN
  READ*,ETOT
ELSE IF(PARAM.EQ.'SIDE')THEN
  READ*,SIDE
ELSE IF(PARAM.EQ.'FCUT')THEN
  READ*,FCUT
ELSE IF(PARAM.EQ.'NINIT')THEN
  READ*,NINIT
ELSE IF(PARAM.EQ.'MAXSTP')THEN
  READ*,MAXSTP
ELSE IF(PARAM.EQ.'IPRFQ')THEN
  READ*,IPRFQ
ELSE IF(PARAM.EQ.'IDMPFQ')THEN
  READ*,IDMPFQ
ELSE IF(PARAM.EQ.'IGDPFQ')THEN
  READ*,IGDPFQ
ELSE IF(PARAM.EQ.'IDPFQ')THEN
  READ*,IDPFQ
ELSE IF(PARAM.EQ.'IRESFQ')THEN
  READ*,IRESFQ
ELSE IF(PARAM.EQ.'TFIXED')THEN
  TFIXED=.TRUE.
ELSE IF(PARAM.EQ.'DELTA')THEN
  READ*,DELNEW
  CALL CHDELTA(DELNEW)
ELSE IF(PARAM.EQ.'?')THEN
  PRINT'('' ETOT='',F12.6,''' MAXSTP='',I8,''' NINIT='',I8,
+   '' DELTA='',F8.5,''' SIDE='',F8.3,''' FCUT='',F8.3)',
+   ETOT,MAXSTP,NINIT,DELTA,SIDE,FCUT
  PRINT'('' IPRFQ='',I7,''' IDMPFQ='',I6,''' IGDPFQ='',I6,
+   '' IDPFQ='',I7,''' IRESFQ='',I6)',IPRFQ,IDMPFQ,IGDPFQ,
+   IDPFQ,IRESFQ
ELSE IF(PARAM.NE.'NO')THEN
  PRINT'('' ???')'
ENDIF
IF(PARAM.NE.'NO')GOTO 10
IF(OLD)THEN

```

```
      WRITE(2, '(/" RESTART"/)')
ELSE
  WRITE(2, '(/" RUN = ', A6, '" ETOT = ', F8.4)') SUFFIX, ETOT
  WRITE(2, '(/" SIDE = ', F9.4, '" DELTA = ', F8.5)') SIDE, DELTA
  WRITE(2, '(/" TFIXED = ', L2)') TFIXED
ENDIF
CLOSE(2)
RETURN
END

BLOCK DATA
PARAMETER ( NP = 800 )
<COMMON /NUM/ >
LOGICAL TFIXED
DATA NINIT, MINSTP, MAXSTP/800, 0, 10000/ IPRFQ, IDPFFQ, IGPFFQ,
+ IDPFFQ, IRESFQ / 500, 100, 10, 1000, 100 /
+ TFIXED / .FALSE. /
END
```

## Appendix B: Listing of the Stockmayer programme

This appendix gives a listing of the latest version of the Fortran-77 programme used in the Stockmayer simulations. The subroutine to locate the cluster (GETDRP) is omitted, since this is given in appendix C, as is the subroutine CMASS, which is identical with the version in appendix A. Following appendix A, common blocks are represented by the short hand notation <COMMON ...>, after the first occurrence. Running on a VAX 11-780 computer (4.2bsd unix(TM)) a 450 particle simulation required approximately 30 seconds CPU time per step.

```

PROGRAM STOCK
C Stockmayer simulation programme version 3.1 (31/5/84)
C Important parameters:
C NP = number of molecules
C ND = number of divisions used for density profile
C NDM= number of divisions used for correlation functions
C
  PARAMETER ( NP = 450, ND = 50 , NDM = ND/2 , MAXST = 60 )
  COMMON /VEC/ X0(NP),Y0(NP),Z0(NP),X1(NP),Y1(NP),Z1(NP),X2(NP),
+ Y2(NP),Z2(NP),X3(NP),Y3(NP),Z3(NP),X4(NP),Y4(NP),Z4(NP),
+ X5(NP),Y5(NP),Z5(NP)
  COMMON /QUAT/ AX0(NP),AY0(NP),AZ0(NP),AQ0(NP),AX1(NP),AY1(NP),
+ AZ1(NP),AQ1(NP),AX2(NP),AY2(NP),AZ2(NP),AQ2(NP),AX3(NP),
+ AY3(NP),AZ3(NP),AQ3(NP),AX4(NP),AY4(NP),AZ4(NP),AQ4(NP),
+ AX5(NP),AY5(NP),AZ5(NP),AQ5(NP)
  COMMON /DIPOLE/ ALX(NP),ALY(NP),ALZ(NP),WPX(NP),WPY(NP),WPZ(NP)
  COMMON /TORFOR/ TX(NP),TY(NP),TZ(NP),FX(NP),FY(NP),FZ(NP)
  COMMON /NUM/DELTA,FCUT,SIDE,TIME,NCLUST,NINIT,MINSTP,MINSEG
+ ,MAXSEG,NSSEG,IPRFQ,ISGDIE,IGDPFQ,IDPFQ,IRESFQ,IDMTFQ,DIPM
+ ,F1,TFIXED,ICMOTS
  REAL*8  SUNK,SUNKR,SUMUL,SUMUD,SUNK2,SUNKR2,SUMUL2,
+ SUMUD2,SUMP,SUMOM2,SUMCOS,SUMIOT,SUMTM,SUMUOT
  COMMON /SUMS/SUNK,SUNKR,SUMUL,SUMUD,SUNK2,SUNKR2,SUMUL2,SUMUD2,
+ NDFPROF(0:ND),NDC(0:ND),SUMP,SUMCOS(0:ND)
+ ,SUMOM2(0:ND),SUMIOT(0:NDM,0:MAXST),SUMTM(3,0:NDM)
+ ,SUMUOT(0:NDM,0:MAXST)
  COMMON /RES/ ETOT,EKIN,UL,UD,VIR
  COMMON /FILES/ FDATA,FRES,FPROF,FCLUST,FICORR,SUFFIX
  COMMON /ETIM/ CPU,ICSTPS
  CHARACTER*14 FDATA,FRES,FPROF,FCLUST,FICORR,SUFFIX*6
  REAL T(2)
  LOGICAL OLD
  CALL SETUP(OLD)
  CPU=ETIME(T)
  ICSTPS=0
  IF (.NOT.OLD) THEN
    CALL SETZER(0)
    CALL CHDELTA( DELTA/10. )
    DO 35 I=-1,-10,-1
      TIME=TIME+DELTA
      CALL PREDIC
      CALL FORTOR
      CALL CORREC
      CALL DATA(-1,0)
  C Data only called to get ekin etc. for rescale etc.
    CALL RESCAL(I)
  35  CONTINUE
  C Above 10 steps with small delta help predictor/corrector adjust as velocities
  C are rescaled. next is ninit initialisation steps for cluster to reach eqm.
    CALL CHDELTA( DELTA*10.)

```

```

      CALL SETZER(0)
ENDIF
IF (MINSTP.LE.0) THEN
  DO 40 I=MINSTP-1,-NINIT,-1
    TIME=TIME+DELTA
    CALL PREDIC
    CALL FORTOR
    CALL CORREC
    CALL DATA(I,0)
    CALL RESCAL(I)
40  CONTINUE
    CALL SETZER(0)
ENDIF
DO 50 J=MINSEG+1,MAXSEG
  DO 70 I=1,NSSEG
    TIME=TIME+DELTA
    CALL PREDIC
    CALL FORTOR
    CALL CORREC
    CALL DATA(I,J)
    CALL RESCAL(I)
70  CONTINUE
80  CONTINUE
50  CONTINUE
CPU=ETIME(T)-CPU
TOTAL=ICSTPS+.1E-10
PRINT('' FINISHED RUN '',A,' STEPS='',F8.0,' CPU='',F12.3,
+ /'' TIME PER STEP='',F12.3)',SUFFIX,TOTAL,CPU,CPU/TOTAL
STOP
END

```

#### SUBROUTINE PREDIC

C Predict the new set of coordinates and there derivatives

C at the next time step

PARAMETER ( NP = 450 )

<COMMON /VEC/, /QUAT/, /NUM/>

ICSTPS=ICSTPS+1

DO 10 I = 1, NP

X0(I) = X0(I)+X1(I)+X2(I)+X3(I)+X4(I)+X5(I)

Y0(I) = Y0(I)+Y1(I)+Y2(I)+Y3(I)+Y4(I)+Y5(I)

Z0(I) = Z0(I)+Z1(I)+Z2(I)+Z3(I)+Z4(I)+Z5(I)

X1(I) = X1(I)+2.\*X2(I)+3.\*X3(I)+4.\*X4(I)+5.\*X5(I)

Y1(I) = Y1(I)+2.\*Y2(I)+3.\*Y3(I)+4.\*Y4(I)+5.\*Y5(I)

Z1(I) = Z1(I)+2.\*Z2(I)+3.\*Z3(I)+4.\*Z4(I)+5.\*Z5(I)

X2(I) = X2(I)+3.\*X3(I)+6.\*X4(I)+10.\*X5(I)

Y2(I) = Y2(I)+3.\*Y3(I)+6.\*Y4(I)+10.\*Y5(I)

Z2(I) = Z2(I)+3.\*Z3(I)+6.\*Z4(I)+10.\*Z5(I)

X3(I) = X3(I)+4.\*X4(I)+10.\*X5(I)

Y3(I) = Y3(I)+4.\*Y4(I)+10.\*Y5(I)

Z3(I) = Z3(I)+4.\*Z4(I)+10.\*Z5(I)

X4(I) = X4(I)+5.\*X5(I)

Y4(I) = Y4(I)+5.\*Y5(I)

Z4(I) = Z4(I)+5.\*Z5(I)

AX0(I)=AX0(I)+AX1(I)+AX2(I)+AX3(I)+AX4(I)+AX5(I)

AY0(I)=AY0(I)+AY1(I)+AY2(I)+AY3(I)+AY4(I)+AY5(I)

AZ0(I)=AZ0(I)+AZ1(I)+AZ2(I)+AZ3(I)+AZ4(I)+AZ5(I)

AQ0(I)=AQ0(I)+AQ1(I)+AQ2(I)+AQ3(I)+AQ4(I)+AQ5(I)

AX1(I)=AX1(I)+2.\*AX2(I)+3.\*AX3(I)+4.\*AX4(I)+5.\*AX5(I)

AY1(I)=AY1(I)+2.\*AY2(I)+3.\*AY3(I)+4.\*AY4(I)+5.\*AY5(I)

AZ1(I)=AZ1(I)+2.\*AZ2(I)+3.\*AZ3(I)+4.\*AZ4(I)+5.\*AZ5(I)

AQ1(I)=AQ1(I)+2.\*AQ2(I)+3.\*AQ3(I)+4.\*AQ4(I)+5.\*AQ5(I)

AX2(I)=AX2(I)+3.\*AX3(I)+6.\*AX4(I)+10.\*AX5(I)

AY2(I)=AY2(I)+3.\*AY3(I)+6.\*AY4(I)+10.\*AY5(I)

AZ2(I)=AZ2(I)+3.\*AZ3(I)+6.\*AZ4(I)+10.\*AZ5(I)

AQ2(I)=AQ2(I)+3.\*AQ3(I)+6.\*AQ4(I)+10.\*AQ5(I)

AX3(I)=AX3(I)+4.\*AX4(I)+10.\*AX5(I)

AY3(I)=AY3(I)+4.\*AY4(I)+10.\*AY5(I)

AZ3(I)=AZ3(I)+4.\*AZ4(I)+10.\*AZ5(I)

AQ3(I)=AQ3(I)+4.\*AQ4(I)+10.\*AQ5(I)

AX4(I)=AX4(I)+5.\*AX5(I)

AY4(I)=AY4(I)+5.\*AY5(I)

AZ4(I)=AZ4(I)+5.\*AZ5(I)

```

      AQ4(I)=AQ4(I)+5.*AQ5(I)
10  CONTINUE
      RETURN
      END

      SUBROUTINE FORTOR
C Calculate forces and torques acting on all molecules
C - this is the most time consuming part of the programme
      PARAMETER ( NP = 450, WTMOL = 48. , ND = 50 )
<COMMON /VEC/, /TORFOR/, /QUAT/, /DIPOLE/, /NUM/, /RES/ >
      DIPM2C=-3.*DIPM*DIPM/24.
      UL=0.
      UD=0.
      VIR=0.
      SIDE2=SIDE/2.
      FCUT2=FCUT*FCUT
      DO 10 I=1,NP
        FX(I)=0.
        FY(I)=0.
        FZ(I)=0.
        ALX(I)=2.*(AY0(I)*AZ0(I)-AX0(I)*AQ0(I))
        ALY(I)=-2.*(AX0(I)*AZ0(I)+AY0(I)*AQ0(I))
        ALZ(I)=AZ0(I)**2+AQ0(I)**2-AX0(I)**2-AY0(I)**2
        TX(I)=0.
        TY(I)=0.
        TZ(I)=0.
10  CONTINUE
C This double loop runs over all unique pairs of molecules to
C calculate the torques and forces (the long cut-off (FCUT) means
C that the majority of terms have to be included, so neighbour lists
C are used).
      DO 20 I=2,NP
        DO 30 J=1,I-1
          X=X0(J)-X0(I)
          Y=Y0(J)-Y0(I)
          Z=Z0(J)-Z0(I)
          R2= X*X+Y*Y+Z*Z
          IF (R2.GT.FCUT2) THEN
            IF (X.GT.SIDE2) THEN
              X=X-SIDE
            ELSE IF (X.LT.-SIDE2) THEN
              X=X+SIDE
            ENDIF
            IF (Y.GT.SIDE2) THEN
              Y=Y-SIDE
            ELSE IF (Y.LT.-SIDE2) THEN
              Y=Y+SIDE
            ENDIF
            IF (Z.GT.SIDE2) THEN
              Z=Z-SIDE
            ELSE IF (Z.LT.-SIDE2) THEN
              Z=Z+SIDE
            ENDIF
            R2= X*X+Y*Y+Z*Z
            IF (R2.GT.FCUT2) GOTO 30
          ENDIF
          RINV2=1./R2
          RINV6=RINV2*RINV2*RINV2
          UL=UL+(RINV6-1.)*RINV6
          A=(2.*RINV6-1.)*RINV6*RINV2
          VIR=VIR+A*R2
          R=SQRT(R2)
          DNINJ=ALX(I)*ALX(J)+ALY(I)*ALY(J)+ALZ(I)*ALZ(J)
          DNIR =ALX(I)*X+ALY(I)*Y+ALZ(I)*Z
          DNJR =ALX(J)*X+ALY(J)*Y+ALZ(J)*Z
          RINV3=RINV2/R
          RINV5=RINV6*R
          UD=UD+DNINJ*RINV3-3.*DNIR*DNJR*RINV5
          FR=DNINJ-5.*DNIR*DNJR*RINV2
          F=DIPM2C*(FR*X+DNJR*ALX(I)+DNIR*ALX(J))*RINV5-A*X
          FX(I)=FX(I)+F
          FX(J)=FX(J)-F
        
```

```

F=DIPM2C*(FR*Y+DNJR*ALY(I)+DNIR*ALY(J))*RINV5-A*Y
FY(I)=FY(I)+F
FY(J)=FY(J)-F
F=DIPM2C*(FR*Z+DNJR*ALZ(I)+DNIR*ALZ(J))*RINV5-A*Z
FZ(I)=FZ(I)+F
FZ(J)=FZ(J)-F
TX(J)=TX(J)-ALX(I)*RINV3+3.*DNIR*RINV5*X
TY(J)=TY(J)-ALY(I)*RINV3+3.*DNIR*RINV5*Y
TZ(J)=TZ(J)-ALZ(I)*RINV3+3.*DNIR*RINV5*Z
TX(I)=TX(I)-ALX(J)*RINV3+3.*DNJR*RINV5*X
TY(I)=TY(I)-ALY(J)*RINV3+3.*DNJR*RINV5*Y
TZ(I)=TZ(I)-ALZ(J)*RINV3+3.*DNJR*RINV5*Z
30 CONTINUE
20 CONTINUE
DO 40 J=1,NP
  TXX=TX(J)
  TYY=TY(J)
  TZZ=TZ(J)
  TX(J)=ALY(J)*TZZ-ALZ(J)*TYY
  TY(J)=ALZ(J)*TXX-ALX(J)*TZZ
  TZ(J)=ALX(J)*TYY-ALY(J)*TXX
40 CONTINUE
UL=UL*.4./NP
UD=UD*DIPM1*DIPM1/NP
VIR=VIR*.24.
RETURN
END

SUBROUTINE CORREC
C Apply the Gear correction, using the results for the forces and
C torques in the new positions. The Gear coeff.'s are the F02,F12.. etc.
  PARAMETER ( NP = 450 , WTMOL = 48. )
  PARAMETER ( F02 = 3./16. , F12 = 251./360. , F32 = 11./18. ,
+            F42 = 1./6. , F52 = 1./60. )
<COMMON /VEC/, /QUAT/, /DIPOLE/, /NUM/, /TORFOR/ >
REAL TPX(NP),TPY(NP),TPZ(NP),TPQ(NP)
C=(DELTA**2)*(DIPM**2)/(2.*F1)
D=12.*DELTA*DELTA/WTMOL
DO 5 I=1,NP
  FX(I)=FX(I)*D
  FY(I)=FY(I)*D
  FZ(I)=FZ(I)*D
  E11=-AX0(I)**2+AY0(I)**2-AZ0(I)**2+A00(I)**2
  E12=2.*(AZ0(I)*A00(I)-AX0(I)*AY0(I))
  E13=2.*(AY0(I)*AZ0(I)+AX0(I)*A00(I))
  E21=-2.*(AX0(I)*AY0(I)+AZ0(I)*A00(I))
  E22=AX0(I)*AX0(I)-AY0(I)*AY0(I)-AZ0(I)*AZ0(I)+A00(I)*A00(I)
  E23=2.*(AY0(I)*A00(I)-AX0(I)*AZ0(I))
  TPX(I)=(E11*TX(I)+E12*TY(I)+E13*TZ(I))*C
  TPY(I)=(E21*TX(I)+E22*TY(I)+E23*TZ(I))*C
  TPZ(I)=0.
  TPQ(I)=- (AX1(I)**2+AY1(I)**2+AZ1(I)**2+AQ1(I)**2)
5 CONTINUE
DO 10 I=1,NP
  XCOR = X2(I)-FX(I)
  YCOR = Y2(I)-FY(I)
  ZCOR = Z2(I)-FZ(I)
  X0(I) = X0(I)-XCOR*F02
  X1(I) = X1(I)-XCOR*F12
  X2(I) = X2(I)-XCOR
  X3(I) = X3(I)-XCOR*F32
  X4(I) = X4(I)-XCOR*F42
  X5(I) = X5(I)-XCOR*F52
  Y0(I) = Y0(I)-YCOR*F02
  Y1(I) = Y1(I)-YCOR*F12
  Y2(I) = Y2(I)-YCOR
  Y3(I) = Y3(I)-YCOR*F32
  Y4(I) = Y4(I)-YCOR*F42
  Y5(I) = Y5(I)-YCOR*F52
  Z0(I) = Z0(I)-ZCOR*F02
  Z1(I) = Z1(I)-ZCOR*F12
  Z2(I) = Z2(I)-ZCOR

```

```

Z3(I) = Z3(I) - ZCOR*F32
Z4(I) = Z4(I) - ZCOR*F42
Z5(I) = Z5(I) - ZCOR*F52
AXCOR=AX2(I)-0.5*(-AZ0(I)*TPX(I)-AQ0(I)*TPY(I)+AX0(I)*TPQ(I))
AYCOR=AY2(I)-0.5*( AQ0(I)*TPX(I)-AZ0(I)*TPY(I)+AY0(I)*TPQ(I))
AZCOR=AZ2(I)-0.5*( AX0(I)*TPX(I)+AY0(I)*TPY(I)+AZ0(I)*TPQ(I))
AQCOR=AQ2(I)-0.5*(-AY0(I)*TPX(I)+AX0(I)*TPY(I)+AQ0(I)*TPQ(I))
AX0(I) = AX0(I) - AXCOR*F02
AX1(I) = AX1(I) - AXCOR*F12
AX2(I) = AX2(I) - AXCOR
AX3(I) = AX3(I) - AXCOR*F32
AX4(I) = AX4(I) - AXCOR*F42
AX5(I) = AX5(I) - AXCOR*F52
AY0(I) = AY0(I) - AYCOR*F02
AY1(I) = AY1(I) - AYCOR*F12
AY2(I) = AY2(I) - AYCOR
AY3(I) = AY3(I) - AYCOR*F32
AY4(I) = AY4(I) - AYCOR*F42
AY5(I) = AY5(I) - AYCOR*F52
AZ0(I) = AZ0(I) - AZCOR*F02
AZ1(I) = AZ1(I) - AZCOR*F12
AZ2(I) = AZ2(I) - AZCOR
AZ3(I) = AZ3(I) - AZCOR*F32
AZ4(I) = AZ4(I) - AZCOR*F42
AZ5(I) = AZ5(I) - AZCOR*F52
AQ0(I) = AQ0(I) - AQCOR*F02
AQ1(I) = AQ1(I) - AQCOR*F12
AQ2(I) = AQ2(I) - AQCOR
AQ3(I) = AQ3(I) - AQCOR*F32
AQ4(I) = AQ4(I) - AQCOR*F42
AQ5(I) = AQ5(I) - AQCOR*F52
WPX(I) = 2.*(-AZ0(I)*AX1(I)+AQ0(I)*AY1(I)+AX0(I)*AZ1(I)
+
  -AY0(I)*AQ1(I))/DELTA
WPY(I) = 2.*(-AQ0(I)*AX1(I)-AZ0(I)*AY1(I)+AY0(I)*AZ1(I)
+
  +AX0(I)*AQ1(I))/DELTA
C   Ensure that sum of squares=1 & wpx=0 for all molecules
WPZ(I)=0.
Q=AX0(I)**2+AY0(I)**2+AZ0(I)**2+AQ0(I)**2
Q=SQRT(Q)
AX0(I)=AX0(I)/Q
AY0(I)=AY0(I)/Q
AZ0(I)=AZ0(I)/Q
AQ0(I)=AQ0(I)/Q
AX1(I)=-DELTA*((AZ0(I)*WPX(I)+AQ0(I)*WPY(I))/2.)
AY1(I)= DELTA*((AQ0(I)*WPX(I)-AZ0(I)*WPY(I))/2.)
AZ1(I)= DELTA*((AX0(I)*WPX(I)+AY0(I)*WPY(I))/2.)
AQ1(I)= DELTA*((-AY0(I)*WPX(I)+AX0(I)*WPY(I))/2.)
ALX(I)=2.*(AY0(I)*AZ0(I)-AX0(I)*AQ0(I))
ALY(I)=-2.*(AX0(I)*AZ0(I)+AY0(I)*AQ0(I))
ALZ(I)=AZ0(I)**2+AQ0(I)**2-AX0(I)**2-AY0(I)**2
10 CONTINUE
RETURN
END

SUBROUTINE DATA(ISTEP,JSEG)
C This routine deals with the calculation of the various averages
C in the course of the simulation and the regular dumping of data
C in case a crash occurs.
PARAMETER ( NP = 450,WTMOL = 48.,ND = 50,NDM = ND/2,ISMTFQ=4 )
PARAMETER ( MAXST = 60 )
COMMON /VEC/, /QUAT/, /DIPOLE/, /NUM/, /RES/ >
REAL*8 SUMK,SUMKR,SUMUL,SUMUD,SUMK2,SUMKR2,SUMUL2,
+
  SUMUD2,SUMP,SUMDM2,SUMCOS,SUMM0T,SUMM1,SUMM0T
CHARACTER*14 FDATA,NRES,FPROF,FCLUST,FMCORR,SUFFIX*6
INTEGER CLUST(NP),NHELL(NP)
REAL*8 SX,SY,SZ,DMX(0:ND),DMY(0:ND),DMZ(0:ND)
LOGICAL CAL1,SAMPMT
SAVE CLUST,TRUE, XSUM, YSUM, ZSUM
DATA CAL1/.TRUE./,XSUM,YSUM,ZSUM/0.,0.,0./
SF= 2.*ND/SIDE
IF ( CAL1.OR. ISTEP.EQ.1 ) THEN
  CALL GETDRP ( CLUST,LEN,3.61,X0,Y0,Z0 )

```

```

      CAL1=.FALSE.
    ENDIF
    I=ISTEP
    IF (I.GT.0) I=I+(JSEG-1)*NSSEG
    IF (MOD(I,IGOPFQ).EQ.0) THEN
      CALL GETDRP ( CLUST,LEN,3.61,X0,Y0,Z0 )
      NCLUST=NCLUST+LEN
    ENDIF
    CALL CMASS ( XSUM,YSUM,ZSUM,CLUST,LEN )
    V2=0.
    W2=0.
    RV=0.
    DO 9 J=0,ND
      DMX(J)=0.
      DMY(J)=0.
      DMZ(J)=0.
9  CONTINUE
    DO 10 JJ=1,NP
      J=CLUST(JJ)
      R= SQRT ( (X0(J))**2 + (Y0(J))**2 + (Z0(J))**2 )
      NBOX=SF*R
      IF (NBOX.GT.ND) NBOX=ND
      NSHELL(J)=NBOX/2
      NDPROF(NBOX)=NDPROF(NBOX)+1
      IF (JJ.LE.LEN) THEN
        NDC(NBOX)=NDC(NBOX)+1
      ENDIF
      SUMCOS(NBOX)=SUMCOS(NBOX)+(X0(J)*ALX(J)+Y0(J)*ALY(J)+
+ Z0(J)*ALZ(J))**2/(R**2)
      DMX(NBOX)=DMX(NBOX)+ALX(J)
      DMY(NBOX)=DMY(NBOX)+ALY(J)
      DMZ(NBOX)=DMZ(NBOX)+ALZ(J)
      V2=V2+X1(JJ)**2+Y1(JJ)**2+Z1(JJ)**2
      W2=W2+WPX(JJ)**2+WPY(JJ)**2+WPZ(JJ)**2
10  CONTINUE
      SX=0.
      SY=0.
      SZ=0.
      DO 12 J=0,ND
        SX=SX+DMX(J)
        SY=SY+DMY(J)
        SZ=SZ+DMZ(J)
        SUMDM2(J)=SUMDM2(J)+SX*SX+SY*SY+SZ*SZ
12  CONTINUE
      V2= V2/(NP*DELTA*DELTA)
      W2=W2/NP
      EKINT= V2*W2*TMOL/2.
      EKINR= W2*FI/2.
      EKIN=EKINR+EKINT
      PRESS=(NP/(SIDE)**3)*(EKIN**2./5.+VIR/3./NP+UD)
      SUMK= SUMK+EKINT*DELTA
      SUMKR= SUMKR+EKINR*DELTA
      SUMUL= SUMUL+UL*DELTA
      SUMUL2=SUMUL2+UL**2*DELTA
      SUMUD= SUMUD+UD*DELTA
      SUMUD2=SUMUD2+UD**2*DELTA
      SUMK2=SUMK2+EKINT**2*DELTA
      SUMKR2=SUMKR2+EKINR**2*DELTA
      SUMP=SUMP+PRESS*DELTA
C Sample the time correlation functions
      IF (MOD(I,4).EQ.0.AND.I.GT.0) THEN
        SAMPMT=(MOD(I,ISMTFQ).EQ.0)
        CALL MSQM( NSHELL,SAMPMT )
        IF (SAMPMT) ICMTS=ICMTS+1
      ENDIF
C print running averages
      IF (MOD(I,IPRFQ).EQ.0) THEN
        AVCL=REAL ( (NCLUST*IGOPFQ) )/I
        AVUL= SUMUL/TIME
        AVUD= SUMUD/TIME
        AVK= SUMK/TIME
        AVKR=SUMKR/TIME

```

```

AVE= AVUL+AVUD+AVK+AVKR
AVP=SUMP/TIME
SIGK= SORT( SUMK2/TIME-AVK**2 )
SIGKR= SORT( SUMKR2/TIME-AVKR**2 )
SIGUL= SORT( SUMUL2/TIME-AVUL**2 )
SIGUD= SORT( SUMUD2/TIME-AVUD**2 )
WRITE (2, '(I5,5F9.5,E10.3E1,F8.1,I5,4F8.4)') I, AVE, AVK, AVKR,
+ AVUD, AVUL, AVP, AVCL, LEN, EKINT, EKINR, UL, UD
WRITE (2, '(7F10.6)') SIGK, SIGKR, SIGUL, SIGUD, XSUM, YSUM, ZSUM
C write density profile and other data out
IF ( MOD(I, NSSEG*IDPFQ).EQ.0.AND.I.GT.0 ) THEN
WRITE (3, '(I6,F9.5)') I, SIDE
WRITE (3, '(17I7)') NDPROF
WRITE (3, '(17I7)') NDC
WRITE (3, '(17 COS)')
WRITE (3, '(10E12.5E1)') (SUMCOS(J)/(NDPROF(J)+1.E-7), J=0, ND)
WRITE (3, '(17 <M2>')')
X=DIPM*DIPM/(JSEG*NSSEG)
WRITE (3, '(10E12.5E1)') (SUMM2(J)*X, J=0, ND)
ENDIF
IF ( MOD(I, IDMTFQ).EQ.0.AND.I.GT.0.AND.ICM0TS.GT.0 ) THEN
WRITE (7) I, SIDE, ICM0TS
WRITE (7) SUMM0T
WRITE (7) SUMM1
WRITE (7) SUMM0T
ENDIF
ENDIF
C save the current configuration in case of system crash
C old data over written
IF (MOD(ISTEP, NSSEG).EQ.0.OR. ISTEP.EQ.-NINIT) THEN
REWIND(8)
NPI=NP
WRITE (8) NPI, ETOT, DELTA, SIDE, F1, DIPM
WRITE (8) X0, Y0, Z0, X1, Y1, Z1, X2, Y2, Z2, X3, Y3, Z3, X4, Y4, Z4,
+ X5, Y5, Z5
WRITE (8) AX0, AY0, AZ0, AQ0, AX1, AY1, AZ1, AQ1, AX2, AY2, AZ2, AQ2, AX3,
+ AY3, AZ3, AQ3, AX4, AY4, AZ4, AQ4, AX5, AY5, AZ5, AQ5
WRITE (8) NDPROF, NDC, SUMK, SUMKR, SUMUL, SUMUD, SUMK2,
+ SUMKR2, SUMUL2, SUMUD2, SUMP, SUMM2,
+ SUMCOS, SUMM0T, SUMM0T, SUMM1,
+ ICM0TS, TIME, NCLUST, ISTEP, JSEG, SUFFIX
CALL DDUMP
ENDIF
RETURN
END

SUBROUTINE DDUMP
C Ensure all data written to files by opening and closing them
<COMMON /FILES/>
CHARACTER*14 FDATA, FRES, FPROF, FCLUST, FDCORR, SUFFIX*6
CLOSE (8)
OPEN (8, FILE=FDATA, FORM='UNFORMATTED', STATUS='OLD')
CLOSE (2)
OPEN (2, FILE=FRES)
CALL TEOF (2, 1)
CLOSE (3)
OPEN (3, FILE=FPROF)
CALL TEOF (3, 1)
CLOSE (4)
OPEN (4, FILE=FCLUST)
CALL TEOF (4, 1)
CLOSE (7)
OPEN (7, FILE=FDCORR, FORM='UNFORMATTED')
CALL TEOF (7, 0)
END

SUBROUTINE TEOF (ICH, IFMT)
C Position file at end - system dependent routine
CALL FSEEK (ICH, 0, 2)
END

SUBROUTINE CMASS ( XSUM, YSUM, ZSUM, CLUST, LEN )

```

```

PARAMETER ( NP = 450 )
C This routine is identical to that used in the LJ programme,
C so we omit the listing here.
...
END

SUBROUTINE RESCAL (II)
C rescale velocities to keep total energy constant - rescale factors recorded
PARAMETER ( NP = 450, ND = 50 )
<COMMON /VEC/, /QUAT, /DIPOLE/, /NUM/, /RES/ >
LOGICAL TFIXED
IF (.NOT.TFIXED) THEN
  DIFF=ETOT-(EKIN+UL+UD)
  IF ( ABS(DIFF).LT.0.001).AND.(MOD(II,IRESFQ).NE.0) RETURN
  DIFF=DIFF+EKIN
  IF ( (DIFF).LT.0.0 ) THEN
    WRITE(*,('' -SORT '' ,15)') II
    SF=0.1
  ELSE
    SF= SORT( (DIFF)/EKIN )
  ENDIF
ELSE
  SF=SQRT(ETOT/EKIN)
ENDIF
IF (MOD(II,IRESFQ).EQ.0) WRITE(2,'(F9.6)') SF
DO 10 I=1,NP
  X1(I)= X1(I)*SF
  Y1(I)= Y1(I)*SF
  Z1(I)= Z1(I)*SF
  WPX(I)=SF*WPX(I)
  WPY(I)=SF*WPY(I)
  AX1(I)=AX1(I)*SF
  AY1(I)=AY1(I)*SF
  AZ1(I)=AZ1(I)*SF
  AQ1(I)=AQ1(I)*SF
10 CONTINUE
RETURN
END

SUBROUTINE SETZER (ISUMEF)
PARAMETER ( NP = 450, ND = 50 , NDM = ND/2 , MAXST = 60 )
<COMMON /NUM/, /SUMS/ >
REAL*8 SUMK, SUMKR, SUMUL, SUMUD, SUMK2, SUMKR2, SUMUL2,
+ SUMUD2, SUMP, SUMDM2, SUMCOS, SUMT0T, SUMM1, SUMUL2
TIME = 0.
SUMK = 0.
SUMK2 = 0.
SUMKR = 0.
SUMKR2 = 0.
SUMUL = 0.
SUMUL2 = 0.
SUMUD = 0.
SUMUD2 = 0.
SUMP=0.
NCLUST=0
ICM0TS=0
DO 10 J= 0,ND
  NPROF(J)=0
  NDC(J)=0
  SUMCOS(J)=0.
  SUMDM2(J)=0.
10 CONTINUE
DO 20 J=0,NDM
  SUMM1(1,J)=0.
  SUMM1(2,J)=0.
  SUMM1(3,J)=0.
  DO 20 JJ=0,MAXST
    SUMT0T(J,JJ)=0.
20 SUMM0T(J,JJ)=0.
RETURN
END

```

```

SUBROUTINE CHDELTA(DELNEW)
PARAMETER ( NP = 450 )
<COMMON /VEC/, /QUAT, /NUM/ >
X = DELNEW/DELTA
Y = X
DELTA = DELNEW
WRITE (*, '( " DELTA=" ,F7.5 )' )DELTA
DO 10 I = 1, NP
  X=Y
  X1(I) = X1(I)*X
  Y1(I) = Y1(I)*X
  Z1(I) = Z1(I)*X
  AX1(I)=AX1(I)*X
  AY1(I)=AY1(I)*X
  AZ1(I)=AZ1(I)*X
  AQ1(I)=AQ1(I)*X
  X=X*Y
  X2(I) = X2(I)*X
  Y2(I) = Y2(I)*X
  Z2(I) = Z2(I)*X
  AX2(I)=AX2(I)*X
  AY2(I)=AY2(I)*X
  AZ2(I)=AZ2(I)*X
  AQ2(I)=AQ2(I)*X
  X=X*Y
  X3(I) = X3(I)*X
  Y3(I) = Y3(I)*X
  Z3(I) = Z3(I)*X
  AX3(I)=AX3(I)*X
  AY3(I)=AY3(I)*X
  AZ3(I)=AZ3(I)*X
  AQ3(I)=AQ3(I)*X
  X=X*Y
  X4(I) = X4(I)*X
  Y4(I) = Y4(I)*X
  Z4(I) = Z4(I)*X
  AX4(I)=AX4(I)*X
  AY4(I)=AY4(I)*X
  AZ4(I)=AZ4(I)*X
  AQ4(I)=AQ4(I)*X
  X=X*Y
  X5(I) = X5(I)*X
  Y5(I) = Y5(I)*X
  Z5(I) = Z5(I)*X
  AX5(I)=AX5(I)*X
  AY5(I)=AY5(I)*X
  AZ5(I)=AZ5(I)*X
  AQ5(I)=AQ5(I)*X
10 CONTINUE
RETURN
END

```

#### SUBROUTINE SETUP (OLD)

C Read configuration file and prompt for run parameters interactively

```

PARAMETER ( NP = 450, ND = 50, NOM = ND/2, MAXST = 60 )
<COMMON /NUM/, /SUMS/, /RES/, /FILES/ >
REAL*8 SUMK, SUMKR, SUMUL, SUMUD, SUMK2, SUMKR2, SUMUL2,
+ SUMUD2, SUMP, SUMDM2, SUMCOS, SUMM0T, SUMM1, SUMM0T
CHARACTER*14 SUFFIX*6, PARAM*6, FDATA, FRES, FPROF, FCLUST, FMDCORR
LOGICAL OLD, TFIXED
PRINT' (/" LIQUID DROP SIMULATION" )'
PRINT' (/" INPUT SUFFIX FOR FILENAMES" )'
READ (*, '( A6 )' ) SUFFIX
FDATA='SFD'//SUFFIX
OPEN(8, FILE=FDATA, FORM='UNFORMATTED', STATUS='OLD')
FRES='RES'//SUFFIX
OPEN(2, FILE=FRES)
CALL TOEOF(2, 1)
FPROF='PROF'//SUFFIX
OPEN(3, FILE=FPROF)
CALL TOEOF(3, 1)
FCLUST='CLUST'//SUFFIX

```

```

OPEN(4,FILE=FCLUST)
CALL TOEOF(4,1)
FMCORR='MCCORR'//SUFFIX
OPEN(7,FILE=FMCORR,FORM='UNFORMATTED')
CALL TOEOF(7,0)
CALL INDATA(OLD,SUFFIX,0)
FCUT=SIDE/2.
IF (OLD) THEN
  PRINT('' RUN=OLD '')
ELSE
  PRINT('' RUN=NEW '')
ENDIF

```

C Long if loop to allow interactive selection of parameters

```

10 PRINT('' ALTER PARAMETER ?'')
  READ(*,'(A6)')PARAM
  IF (PARAM.EQ.'ETOT ') THEN
    READ*,ETOT
  ELSE IF (PARAM.EQ.'TFIXED') THEN
    TFIXED=.TRUE.
  ELSE IF (PARAM.EQ.'NEW ') THEN
    OLD=.FALSE.
  ELSE IF (PARAM.EQ.'OLD ') THEN
    OLD=.TRUE.
  ELSE IF (PARAM.EQ.'SIDE ') THEN
    READ*,SIDE
  ELSE IF (PARAM.EQ.'FCUT ') THEN
    READ*,FCUT
  ELSE IF (PARAM.EQ.'NINIT ') THEN
    READ*,NINIT
  ELSE IF (PARAM.EQ.'MAXSEG') THEN
    READ *,MAXSEG
  ELSE IF (PARAM.EQ.'NSSEG') THEN
    READ *,NSSEG
  ELSE IF (PARAM.EQ.'IPRFQ ') THEN
    READ*,IPRFQ
  ELSE IF (PARAM.EQ.'IGOPFQ') THEN
    READ*,IGOPFQ
  ELSE IF (PARAM.EQ.'IDPFQ ') THEN
    READ*,IDPFQ
  ELSE IF (PARAM.EQ.'IRESFQ') THEN
    READ*,IRESFQ
  ELSE IF (PARAM.EQ.'IDMTFQ') THEN
    READ*,IDMTFQ
  ELSE IF (PARAM.EQ.'DELTA ') THEN
    READ*,DELNEW
    CALL CHDELTA(DELNEW)
  ELSE IF (PARAM.EQ.'DIPM ') THEN
    READ*,DIPM
  ELSE IF (PARAM.EQ.'FI ') THEN
    READ*,FI
  ELSE IF (PARAM.EQ.'? ') THEN
    PRINT('' ETOT='',F12.6,/'' MAXSEG='',I8,/'' NINIT='',I8,
+   /'' DELTA='',F8.5,/'' SIDE='',F8.3,/'' FCUT='',F8.3,)'
+   ETOT,MAXSEG,NINIT,DELTA,SIDE,FCUT
    PRINT('' DIPM ='',F12.7,/'' FI ='',F12.7,
+   )',DIPM,FI
    PRINT('' IPRFQ ='',I7,/'' IGOPFQ ='',I6,
+   /'' IDPFQ ='',I7,/'' IRESFQ ='',I6)',IPRFQ,IGOPFQ,
+   IDPFQ,IRESFQ
    PRINT('' NSSEG ='',I5,/'' TFIXED ='',L1)',NSSEG,TFIXED
  ELSE IF (PARAM.NE.'NO ') THEN
    PRINT('' ???'')
  ENDIF
  IF (PARAM.NE.'NO ') GOTO 10
  IF (OLD) THEN
    WRITE(2,'(/'' RESTART'',2I6)') MINSTP,MINSEG
  ELSE
    WRITE(2,'(/'' RUN = '',A6,/'' ETOT = '',F8.4)')SUFFIX,ETOT
    WRITE(2,'(/'' SIDE = '',F9.4,/'' DELTA = '',F8.5)')SIDE,DELTA
    WRITE(2,'(/'' DIPM = '',F9.4,/'' FI = '',F8.5)')DIPM,FI
    WRITE(2,'(/'' TFIXED = '',L2)') TFIXED
    MINSEG=0
  
```

```

      MINSTP=0
    ENDIF
    RETURN
  END

  SUBROUTINE INDATA( OLD,SUFFIX,ICALL )
C Actual routine to read configuration file
  PARAMETER ( NP = 450, ND = 50, NDM = ND/2, MAXST = 60 )
<COMMON /VEC/, /QUAT/, /NUM/, /SUMS/ >
  REAL*8 SUNK,SUNKR,SUMUL,SUMUD,SUMK2,SUNKR2,SUMUL2,
+   SUMUD2,SUMP,SUMDM2,SUMCOS,SUMM0T,SUMM1,SUMU0T
  CHARACTER SUFFIX*6,OLDSUF*6
  LOGICAL OLD
  REWIND(8)
  READ(8)NIN,ETOT,DELTA,SIDE,FI,DIPM
  IF(NIN.NE.NP)THEN
    PRINT' (/' '* ERROR - INCORRECT DATA FILE',//
+   ' ' NP=',I4,' ' NIN=',I4)',NP,NIN
    STOP
  ENDIF
  READ(8) X0,Y0,Z0,X1,Y1,Z1,X2,Y2,Z2,X3,Y3,Z3,X4,Y4,Z4,X5,Y5,Z5
  READ(8)AX0,AY0,AZ0,AQ0,AX1,AY1,AZ1,AQ1,AX2,AY2,AZ2,AQ2,AX3,
+   AY3,AZ3,AQ3,AX4,AY4,AZ4,AQ4,AX5,AY5,AZ5,AQ5
  READ(8,(IOSTAT=IERR) NDPROF,NDC,SUNK,SUNKR,SUMUL,SUMUD,SUMK2,
+   SUNKR2,SUMUL2,SUMUD2,SUMP,SUMDM2,
+   SUMCOS,SUMM0T,SUMU0T,SUMM1,
+   ICM0TS,TIME,NCLUST,MINSTP,MINSEG,OLDSUF
  IF(ICALL.EQ.1.AND.IERR.NE.0) THEN
    PRINT' ('' IO ERROR IN INDATA'')'
    STOP
  ENDIF
  OLD=(IERR.EQ.0).AND.(SUFFIX.EQ.OLDSUF)
  RETURN
  END

  BLOCK DATA
<COMMON /NUM/ >
  LOGICAL TFIXED
  DATA NINIT,MINSTP,MINSEG,MAXSEG/800,0,0,100/ NSSEG,IPRFQ,
+   IGDPFQ,IDPFQ,IRESFQ,IDMTFQ / 150,500,10,5,10,1000 /
+   ISGDIE/0/
  DATA DIPM,FI/1.,1./ TFIXED /.FALSE./
  END

  SUBROUTINE MSQM( NSHELL,SAMPMT )
C Subroutine to measure time dependent corr. fn's for the total moment
C <M(t).M(t)> and single particle <J(t).U(t)>
  PARAMETER ( NP = 450, ND = 50, NDM = ND/2, MAXST = 60 )
<COMMON /SUMS/, /DIPOLE/ >
  INTEGER NSHELL(NP),LSHELL(NP)
  REAL*8 SUNK,SUNKR,SUMUL,SUMUD,SUMK2,SUNKR2,SUMUL2,
+   SUMUD2,SUMP,SUMDM2,SUMCOS,SUMM0T,SUMM1,SUMU0T
  REAL MT(3,0:NDM,0:MAXST),AL0(3,NP)
  LOGICAL MTFULL,SAMPMT
  SAVE MTFULL,IPTH,AL0,LSHELL
  DATA MTFULL /.FALSE./ IPTH /0/
  IF(IPTH.EQ.MAXST+1) THEN
    MTFULL=.TRUE.
    IPTH=0
  ENDIF
  IF(IPTH.EQ.0) THEN
    DO 4 J=1,NP
      AL0(1,J)=ALX(J)
      AL0(2,J)=ALY(J)
      AL0(3,J)=ALZ(J)
      LSHELL(J)=NSHELL(J)
4    CONTINUE
  ENDIF
  DO 5 J=0,NDM
    MT(1,J,IPTH)=0.
    MT(2,J,IPTH)=0.
    MT(3,J,IPTH)=0.
  END

```

```

5  CONTINUE
   DO 10 J=1,NP
     MT(1,NSHELL(J),IPTH)=MT(1,NSHELL(J),IPTH)+ALX(J)
     MT(2,NSHELL(J),IPTH)=MT(2,NSHELL(J),IPTH)+ALY(J)
     MT(3,NSHELL(J),IPTH)=MT(3,NSHELL(J),IPTH)+ALZ(J)
10  CONTINUE
   DO 15 J=1,NOM
     MT(1,J,IPTH)=MT(1,J,IPTH)+MT(1,J-1,IPTH)
     MT(2,J,IPTH)=MT(2,J,IPTH)+MT(2,J-1,IPTH)
     MT(3,J,IPTH)=MT(3,J,IPTH)+MT(3,J-1,IPTH)
15  CONTINUE
   DO 17 J=1,NP
     I=LSHELL(J)
     SUMJ0T(I,IPTH)=SUMJ0T(I,IPTH)+AL0(1,J)*ALX(J)+AL0(2,J)*ALY(J)+
+    AL0(3,J)*ALZ(J)
17  CONTINUE
     IF (MTFULL.AND.SAMPMT) THEN
       DO 20 J=0,MAXST
         JJ=MOD(IPTH+J+1,MAXST+1)
         DO 30 I=0,NOM
           SUMJ0T(I,J)=SUMJ0T(I,J)+MT(1,I,JJ)*MT(1,I,IPTH)+
+          MT(2,I,JJ)*MT(2,I,IPTH)+MT(3,I,JJ)*MT(3,I,IPTH)
           SUMM(1,I)=SUMM(1,I)+MT(1,I,JJ)
           SUMM(2,I)=SUMM(2,I)+MT(2,I,JJ)
           SUMM(3,I)=SUMM(3,I)+MT(3,I,JJ)
30         CONTINUE
20       CONTINUE
     ELSE
       SAMPMT=.FALSE.
     ENDIF
     IPTH=IPTH+1
     RETURN
   END

```

## Appendix C: Determination of the drop location

### 1. Introduction

In the simulation of small droplets in equilibrium with their vapour it is often necessary to accurately locate the centre of the droplet, which can drift away from its original position. If the number of particles in the vapour phase is significant, the centre of mass of the whole system is not an accurate guide to the center of the droplet.

We assume spherically symmetric particles, and say that any two are “neighbours” if their center to center separation is less than some value  $R_n$ . Then particle B is in the same group as A if they are neighbours, or a neighbour of A is in the same group as B. With a suitable choice of  $R_n$ , the largest of these groups defines the droplet. The center of mass of the droplet is then readily found. For the Lennard-Jones 12-6 interaction it was found that the largest cluster size was virtually independent of  $R_n$  for  $R_n$  in the region of  $1.9 \sigma$  (see figure (C.1)) and so that was taken as the criterion for separating the drop from its vapour and in defining the center of the drop. The difference between the center of mass of the whole system, and that of the cluster is of the order  $0.3 \sigma$  for a 260 particle system.

### 2. Simple-minded sorting

At first we used a simple-minded routine for finding the largest cluster, which is listed in section 4. This assumes that one particle (number IC) is already known to be within the cluster. We then search for the nearest neighbours of IC, according to the distance criterion  $R_n$ , and any that are found are recorded in the array NCL. The search then proceeds to find the neighbours of these that are not already recorded in NCL, and repeats this until the size of the cluster in NCL does not increase. The first NC elements of the array NCL then contain the index numbers of atoms within the

cluster. This method has been found to be extremely slow and takes many times longer to compute than one simulation step. Since we need to relocate the cluster fairly frequently (say every ten steps) to follow changes, it slows the simulation to an intolerable degree. The coding given in section 5 is more complex, but is about 50 times faster. No doubt experts on sorting could improve this further, but as the routine takes rather less than the time for a simulation step, such improvements would have little effect on the total time taken.

### 3. More sophisticated sorting

This FORTRAN77 subroutine is composed of three parts:

- (1) For each atom, find all the unique neighbours (i.e. if 2 is a neighbour of 1, do not count 1 as a neighbour of 2). All the neighbours are stored in the large array LIST.
- (2) Go through the list obtained above assigning "group numbers" to each atom such that two atoms have the same group number if they are linked via neighbours.
- (3) Find the largest group and return the members of it in the array ICLUST.

In more detail the sections work as follows:

- (1) The loops DO10 and DO20 run over all possible pairs. RCUTSQ is the square of  $R_n$ . Any neighbours that are found for a given atom I are stored in the array LIST, with the "pointer" array elements IPTT(I) and IPTH(I) giving the start (Head) and end (Tail) of its neighbours.
- (2) The integer array IGROUP contains a "group number" for each atom that is initialised to zero, indicating no neighbours. The loop DO40 then processes each atom and its neighbours. The code up to label 50 stores any non-zero group numbers that these atoms have in the array IGNU, with IPTGN giving the top element. If more than one group number has been found, then these groups are all linked together by the present atom. Hence the loop DO70 makes all the

other group numbers equal to the first one. If no group numbers are found, a value of I is used. The loop DO90 ensures that all the neighbours have the correct group number.

- (3) The final loop DO100 finds the first group to contain more than one third of the total number of atoms (NP), and returns them as the first LEN elements of the array ICLUST. The choice of one third is arbitrary, but works at most reasonable temperatures.

Note that the size of NLIST required depends on NP and the value of  $R_n$  used.

#### 4. Simple subroutine

```

..
C positions of particles are in arrays X,Y,Z
  NC=1
  NCL(1)=IC
  2  NCP=NC
     DO 10 II=1,NC
        I=NCL(II)
        DO 20 J=1,NP
           DO 21 JJ=1,NC
              21  IF (J.EQ.NCL(JJ)) GOTO 20
                 R2=(X(I)-X(J))**2+(Y(I)-Y(J))**2+(Z(I)-Z(J))**2
                 IF (R2.GT.RCUTSQ) GOTO 20
                 NC=NC+1
                 NCL(NC)=J
              20  CONTINUE
             10  CONTINUE
                 IF (NC.GT.NCP) GOTO 2
..

```

#### 5. More sophisticated subroutine

```

SUBROUTINE GETDRP( ICLUST,LEN,RCUTSQ )
PARAMETER(NP = 900,NLIST = 12000 )
COMMON /POS/ X(NP),Y(NP),Z(NP)
INTEGER ICLUST(NP)
INTEGER LIST(NLIST),IPTH(NP),IPTT(NP),IGNUM(50),IGROUP(NP)
LCOUNT=1
DO 10 I=1,NP-1
  IPTH(I)=LCOUNT
  DO 20 J=I+1,NP
    R2=(X(J)-X(I))**2+(Y(J)-Y(I))**2+(Z(J)-Z(I))**2
    IF (R2.LT.RCUTSQ) THEN
      LIST(LCOUNT)=J
      LCOUNT=LCOUNT+1
    ENDIF
  20  CONTINUE
  IPTT(I)=LCOUNT-1
  10  CONTINUE
DO 30 I=1,NP

```

```

30  IGROUP(I)=0
    DO 40 I=1,NP-1
      IPTGN=0
      IF (IGROUP(I).NE.0) THEN
        IPTGN=IPTGN+1
        IGNU(IPTGN)=IGROUP(I)
      ENDIF
      DO 50 J=IPTH(I),IPTT(I)
        NJ=LIST(J)
        IF (IGROUP(NJ).NE.0) THEN
          DO 60 K=1,IPTGN
            IF (IGNUM(K).EQ.IGROUP(NJ)) GOTO 50
            IPTGN=IPTGN+1
            IGNU(IPTGN)=IGROUP(NJ)
          ENDIF
        CONTINUE
      IF (IPTGN.GT.0) THEN
        DO 70 K=2,IPTGN
          KG=IGNUM(K)
          DO 80 KK=1,NP
            IF (IGROUP(KK).EQ.KG) IGROUP(KK)=IGNUM(1)
          CONTINUE
        ELSE
          IGNU(1)=I
        ENDIF
        IGROUP(I)=IGNUM(1)
        DO 90 J=IPTH(I),IPTT(I)
          NJ=LIST(J)
          IGROUP(NJ)=IGNUM(1)
        CONTINUE
      CONTINUE
    CONTINUE
40  LEN=0
    DO 100 I=1,NP
      IF (IGROUP(I).GT.0) THEN
        ICOUNT=1
        IG=IGROUP(I)
        IGROUP(I)=-IG
        DO 110 J=I+1,NP
          IF (IGROUP(J).EQ.IG) THEN
            ICOUNT=ICOUNT+1
            IGROUP(J)=-IGROUP(J)
          ENDIF
        CONTINUE
      IF (ICOUNT.GT.NP/3) THEN
        LEN=ICOUNT
        IG=-IG
        DO 120 J=1,NP
          IF (IGROUP(J).EQ.IG) THEN
            ICLUST(ICOUNT)=J
            ICOUNT=ICOUNT-1
          ENDIF
        CONTINUE
      ENDIF
    ENDIF
  ENDIF
100 CONTINUE
  IF (LEN.EQ.0) THEN
    WRITE(*,('** ***** NO CLUSTER > NP/3**'))
    STOP
  ENDIF
  RETURN
END

```

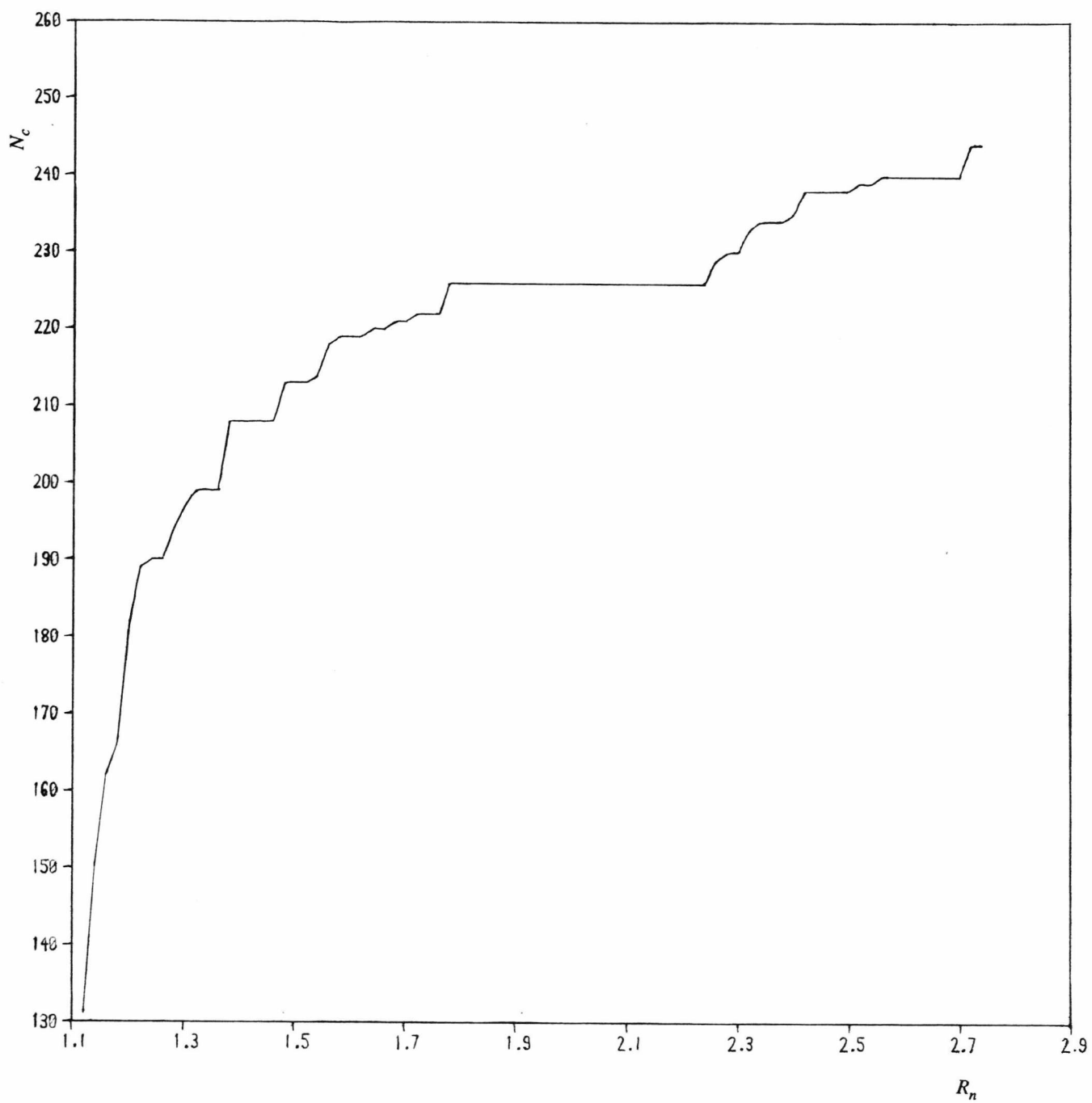


**Figure C.1:** The number of particles that are included in the definition of the cluster, as a function of the distance used for  $R_n$ , the maximum distance between “neighbours”.

## Appendix D: Method of calculating the MSM

In chapter seven it was shown how the mean square moment (MSM) could be found at any radius within a uniform macroscopic dielectric sphere. To treat the surface in more detail, the case of a drop composed of a number of shells is considered. These shells are also assumed to be uniform and isotropic, the  $i^{\text{th}}$  one having a dielectric constant  $\epsilon_i$ .

Given such systems, we need to find the Maxwell field within each shell, and also the cavity field that exists within any chosen radius  $r$ , in terms of the applied field at infinity ( $E_\infty$ ). We write,  $E = \psi E_\infty$  for the Maxwell field and  $E_o = \phi E_\infty$  for the cavity field (in the notation of chapter seven,  $(\partial E_o / \partial E) = \phi / \psi$ ). For a few dielectric layers,  $\phi$  and  $\psi$  can be found analytically, but a general solution is more easily found numerically.

The potential within each shell must satisfy the Laplace equation and for this geometry the potential in shell  $i$  is of the form  $\Phi_i(r) = -(A_i/r^2 + B_i r) \cos\theta$ . At each boundary the tangential component of  $\mathbf{E}$  ( $E_t = -r^{-1}(\partial\Phi/\partial\theta)$ ) and the radial component of  $\mathbf{D}$  ( $D_r = -\epsilon(\partial\Phi/\partial r)$ ) must be continuous, which requires that,

$$\frac{A_i}{r^2} + B_i r = \frac{A_{i+1}}{r^2} + B_{i+1} r \quad (\text{D.1})$$

and,

$$\epsilon_i \left( \frac{2A_i}{r^3} - B_i \right) = \epsilon_{i+1} \left( \frac{2A_{i+1}}{r^3} - B_{i+1} \right) \quad (\text{D.2})$$

where  $r$  is the radius of the dividing surface between shells  $i$  and  $i+1$ . These can be rearranged to give,

$$A_{i+1} = \frac{1}{3} \left[ \frac{\epsilon_{i+1} + 2\epsilon_i}{\epsilon_{i+1}} A_i + r^3 \frac{\epsilon_{i+1} - \epsilon_i}{\epsilon_{i+1}} B_i \right] \quad (\text{D.3})$$

$$B_{i+1} = \frac{1}{3} \left[ \frac{2}{r^3} \left( \frac{\epsilon_{i+1} - \epsilon_i}{\epsilon_{i+1}} \right) A_i + \left( \frac{2\epsilon_{i+1} + \epsilon_i}{\epsilon_{i+1}} \right) B_i \right] \quad (\text{D.4})$$

Thus we take the components of the solution in the central region (including  $R = 0$ ) to be,  $A_1 = 0$  and  $B_1 = 1$ , since the potential must be finite at the origin. Then (D.3) and (D.4) allow us to work outwards through the shells to find all the other components. This allows the required ratios to be obtained, since the value of  $\psi$  for shell  $i$  is just  $\psi_i = E_i/E_\infty = B_i/B_N$ , if the outermost shell is the  $N^{\text{th}}$  one. The same approach works for the cavity field, just by taking the dielectric constant as unity for the inner shells.

The actual equation for the MSM at a given shell boundary follows quite straight forwardly from the equations of chapters six and seven. From the analysis used to find (6.8), the total moment of the sphere bounded by  $r_j$ ,

$$\frac{\langle M^2(r_j) \rangle}{3kT} = \frac{\langle \mathbf{M}(r_j) \cdot \hat{\mathbf{e}} \rangle}{E_0} = \frac{\langle \mathbf{M}(r_j) \cdot \hat{\mathbf{e}} \rangle}{\phi_j E_\infty} \quad (\text{D.5})$$

The total moment of all the shells within this radius is given by equation (7.5) as,

$$\langle \mathbf{M}(r_j) \cdot \hat{\mathbf{e}} \rangle = \sum_{i \leq j} (\epsilon_i - 1) \frac{V_i E_i}{4\pi} \quad (\text{D.6})$$

where  $V_i$  is the volume of shell  $i$ . Finally this gives,

$$\frac{\langle M^2(r_j) \rangle}{3kT} = \frac{1}{\phi_j} \sum_{i \leq j} (\epsilon_i - 1) \frac{V_i \psi_i}{4\pi} \quad (\text{D.7})$$

This allows the calculation of the MSM for any arbitrary set of concentric dielectric shells.

In the case of a continuous dielectric profile,  $\epsilon(r)$ , two coupled differential equations are obtained for the components  $A_i$  and  $B_i$ , which then also become continuous functions. However, we can obtain the MSM for a given form of  $\epsilon(r)$  by just using a large number of shells, each of dielectric constant  $\epsilon(r_i)$ , which is equivalent to a step-wise solution of the differential equations.